Graduate Student Theses, Dissertations, & Professional Papers	Graduate School

2022

EMISSION AND CHEMISTRY OF VOLATILE ORGANIC COMPOUNDS IN WESTERN U.S. WILDIFRE SMOKE

Wade Jeremy Permar

EMISSION AND CHEMISTRY OF VOLATILE ORGANIC COMPOUNDS IN

WESTERN U.S. WILDIFRE SMOKE

By

WADE JEREMY PERMAR

B.S. Environmental Chemistry, Northern Arizona University, Flagstaff, AZ, 2010

Dissertation

presented in partial fulfillment of the requirements
for the degree of

Doctor of Philosophy
in Chemistry

The University of Montana
Missoula, MT

December 2022

Approved by:

Scott Whittenburg, Dean of The Graduate School
Graduate School

Dr. Lu Hu, Committee Chair
Department of Chemistry and Biochemistry

Dr. Robert Yokelson
Department of Chemistry and Biochemistry

Dr. Christopher Palmer
Department of Chemistry and Biochemistry

Dr. Michael DeGrandpre
Department of Chemistry and Biochemistry

Dr. Tony Ward
School of Public and Community Health Sciences

Permar, Wade, PhD, November 2022   *Chemistry*

Emission and chemistry of volatile organic compounds in western U.S. wildfire smoke

Advisor: Dr. Lu Hu, Department of Chemistry and Biochemistry

Abstract

Wildfires are a significant source of volatile organic compounds (VOCs) in the western U.S., emitting hundreds to thousands of different species that play key roles in tropospheric oxidation, ozone production, and secondary organic aerosol formation. Many of these VOCs have only recently been identified and quantified in laboratory burning experiments. Consequently, little is known about their emissions from wildfires, which species are most important for plume OH oxidation chemistry, and how they evolve as smoke plumes age. This dissertation aims to improve our understanding of the emissions and chemistry of VOCs in wildfire smoke using detailed *in situ* measurements made during the summer 2018 Western Wildfire Experiment for Cloud Chemistry, Aerosol Absorption, and Nitrogen (WE-CAN) field campaign.

WE-CAN sampled wildfire smoke across seven western states and is one of the most comprehensive field studies of smoke emissions and aging to date. During the campaign, VOCs were measured by four complementary instruments, which were all found to agree within their stated uncertainties for most co-measured species. Leveraging these measurements, we report emission factors (EFs) and emission ratios (ERs) for 161 VOCs measured from 24 individual fires (Permar et al., 2021). OH reactivity (OHR) was used to determine which species are most important for daytime plume OH chemistry, and therefore should be included in next generation atmospheric chemistry models. From this, the master chemical mechanism was determined to contain chemistry for most reactive species. However, ~50 % of the emitted VOC OHR is not currently implemented in the commonly used GEOS-Chem chemical transport model. Implementing chemistry for furan-containing species, butadienes, and biomass burning monoterpenes would greatly improve model representation (Permar et al., 2023).

As smoke plumes age, formic acid was rapidly produced at rate of 2.7 ppb ppm_{CO}^{-1} h^{-1}, resulting in it and acetic acid become an increasingly important OH sink in aged smoke. GEOS-Chem generally underestimates their enhancement during WE-CAN, likely due to missing secondary production from wildfire and biogenic emissions. Collectively, this work significantly expands our understanding of western U.S. wildfire emissions while providing direction for future model and emission inventory development.

Acknowledgments

Table of contents

List of figures

Figure S2.4. Correlations of WE-CAN furfural EFs versus MCE, along with EFs for one field campaigns (Müller et al., 2016) and coniferous fuels measured during three laboratory burns (Koss et al., 2018; Selimovic et al., 2018; Stockwell et al., 2015).

Figure S3.1: WE-CAN research flight tracks colored by the total calculated OH reactivity (tOHR, s^{-1}) for free troposphere and aged smoke sampling periods.

Figure S3.2. Total gas OH reactivity profiles for 24 fires reported in this work.

Figure S3.3. The proportion of VOC groups comprising the non-implemented VOC OHR fraction shown in Figure 4c. These groups represent those species that were measured during WE-CAN but are not implemented for biomass burning in the GEOS-Chem CTM.

Figure S4.1. Flight tracks for WE-CAN research flights colored by formic acid (I^- CIMS) and acetic acid (PTR-ToF) mixing ratios (ppb).

Figure S4.2. Formic and acetic acid sensitivity in PTR-ToF as a function of the internal humidity proxy $H_2O \cdot H_3O^+$ to H_3O^+ ([*m/z* 39]/[*m/z* 21]).

Figure S4.3. Correlations between I^- CIMS and PTR-ToF 1 Hz FA measurements during WE-CAN for all research flights, filtered to remove cloud sampling.

Figure S4.4. Emission factors of formic and acetic acid from WE-CAN PTR-ToF observations, I^- CIMS , and literature values.

Figure S4.5. Box-and-whisker plot of WE-CAN and literature formic and acetic acid EFs by the type of fuel burned.

Figure S4.6. Acetic acid NEMRs compared to various gas phase species measured in 5 smoke plumes with more than 10 pseudo-Lagrangian plume transects.

Figure S4.7. Vertical profiles of the median acetic acid mixing ratio measured during the full WE-CAN and FIREX-AQ field campaigns, binned at 33 hPa.

Figure S4.8. Vertical profiles of the median CO, benzene, and acetone mixing ratios measured during the full WE-CAN and FIREX-AQ field campaigns, binned at 33 hPa.

Figure S4.9. Vertical profiles of the median formic acid enhancement ratios to CO, benzene, and acetone during the full WE-CAN and FIREX-AQ field campaigns, binned at 33 hPa.

List of tables

1 Introduction

Wildfires are increasing in both size and intensity in the western United States (U.S.) due to historic forest management practices and global climate change (Bowman et al., 2017; Flannigan et al., 2013; Groot et al., 2013; Higuera et al., 2021; Jolly, 2015; Littell et al., 2018; Rocca et al., 2014; Westerling, 2016, 2006; Westerling et al., 2011; Yue et al., 2013). Consequently, regional air quality is degrading relative to the rest of the country (McClure and Jaffe, 2018; O'Dell et al., 2019). As exposure to wildfire smoke has been linked to numerous negative health outcomes (Liu et al., 2015; Reid et al., 2016), it is important to better understand wildfire emissions and subsequent downwind plume chemistry in order to better predict their impacts on air quality.

Wildland fires are a significant source of volatile organic compounds (VOCs) to the atmosphere (Akagi et al., 2011; Atkinson and Arey, 2003). Atmospheric VOCs are a key ingredient in the formation of tropospheric ozone (O_3) and secondary organic aerosol (SOA), influence greenhouse gas lifetime by changing tropospheric oxidation potential, and are often themselves hazardous air pollutants (O'Dell et al., 2020). However, global and regional VOC emissions from fires are highly uncertain due in part to a scarcity of field measurements, particularly for the hundreds of species that have only recently been identified in laboratory burning experiments (Gilman et al., 2015; Hatch et al., 2017; Koss et al., 2018; Stockwell et al., 2015). By extension, the importance of these recently identified species as a hydroxyl radical (OH) sink is poorly constrained. Consequently, we do not understand how well current global chemical transport models (CTMs) and explicit chemical mechanisms represent biomass burning (BB) VOCs, the amount of reactive carbon they may be missing, and which species should be prioritized to incorporate into the next generations of air quality models. Similarly, the fate of individual atmospherically important species in BB smoke, such as formic acid and acetic acid, are not well understood nor well represented by models.

This dissertation aims to improve our understanding of wildfire emissions and smoke plume chemistry using *in-situ* measurements made during the Western Wildfire

Experiment for Cloud Chemistry, Aerosol Absorption, and Nitrogen (WE-CAN) field campaign (https://www.eol.ucar.edu/field_projects/we-can). WE-CAN sampled wildfire plumes across seven western U.S. states from 24 July to 1 September 2018 using the NSF/NCAR C-130 research aircraft, with a payload designed to measure most known gas, particle, and physical parameters in smoke plumes. During WE-CAN, I lead the installation, daily operation, and data management of the University of Montana proton-transfer-reaction time-of-flight mass spectrometer (PTR-ToF-MS 4000, Ionicon Analytik, Innsbruck, Austria) on the C-130 research aircraft. Additionally, I designed and built the zero air/calibration unit and inlet system that was used by our PTR-ToF-MS on the plane during the campaign.

PTR-Tof-MS is capable of measuring a full mass spectrum of hundreds of VOCs at greater than 1 Hz resolution, providing high spatial temporal resolution of smoke plumes sampled from air airborne platforms (Müller et al., 2016). In addition to the PTR-ToF-MS, three other complementary VOC instruments were operated on the C-130, resulting in a rich dataset that characterizes most known BB VOCs. Using these four different instruments, I have done extensive validation of their co-measured species and ultimately compiled a master list of 161 individual and isomeric VOCs measured during the campaign. Leveraging this extensive VOC dataset, I set out to investigate the following guiding questions:

- What VOCs are emitted by wildfires and how are their emissions influence by combustion efficiency?

- What VOC species are the most important for plume mediate OH chemistry, and are these species implemented in current CMTs and explicit chemical mechanisms?

- How do wildfires contribute to formic acid and acetic acid enhancement in the western U.S.?

The following chapters in this dissertation are broken into three self-sufficient parts (Chapters 2-4), each containing an abstract, introduction, methods, results/discussion, and conclusion corresponding to their published form. Consequently, much of the introductory material is repeated throughout this work, while the corresponding manuscript for each chapter is available through their following citations. Chapter 2 focuses on validating WE-CAN VOC measurements before providing emissions estimates for most of the measured gas phase species (Permar et al., 2021). Chapter 3 further investigates the VOC emissions during WE-CAN to assess which compounds are the most important for daytime plume oxidation chemistry and therefore should be implemented in next generation atmospheric chemical mechanisms (Permar et al., 2023). Chapter 4 shifts focus away from the bulk VOC analysis done in the previous sections to investigate plume aging through two key VOCs, formic and acetic acid.

2 Emissions of trace organic gases from western U.S. wildfires based on WE-CAN aircraft measurements

2.1 Abstract

We present emissions measurements of volatile organic compounds (VOCs) for western U.S. wildland fires made on the NSF/NCAR C-130 research aircraft during the Western Wildfire Experiment for Cloud Chemistry, Aerosol Absorption, and Nitrogen (WE-CAN) field campaign in summer 2018. VOCs were measured with complementary instruments onboard the C-130, including a proton-transfer-reaction time-of-flight mass spectrometer (PTR-ToF-MS) and two gas chromatography (GC)-based methods. Agreement within combined instrument uncertainties (< 60 %) was observed for most co-measured VOCs. GC-based measurements speciated the isomeric contributions to selected PTR-ToF-MS ion masses and generally showed little fire-to-fire variation. We report emission ratios (ERs) and emission factors (EFs) for 161 VOCs measured in 31 near-fire smoke plume transects of 24 specific individual fires sampled in the afternoon when burning conditions are typically most active. Modified combustion efficiency (MCE) ranged from 0.85–0.94. The measured campaign-average total VOC EF was 26.1 ± 6.9 g kg-1, approximately 67 % of which is accounted for by oxygenated VOCs. The 10 most abundantly emitted species contributed more than half of the total measured VOC mass. We found that MCE

alone explained nearly 70 % of the observed variance for total measured VOC emissions ($r^2 = 0.67$) and > 50 % for 57 individual VOC EFs representing more than half the organic carbon mass. Finally, we found little fire-to-fire variability for the mass fraction contributions of individual species to the total measured VOC emissions, suggesting that a single speciation profile can describe VOC emissions for the wildfires in coniferous ecosystems sampled during WE-CAN.

2.2 Introduction

Wildland fires are a significant source of non-methane volatile organic compounds (VOCs) to the atmosphere, impacting downwind air quality, public health, and the formation of secondary pollutants such as ozone (O_3), and secondary organic aerosol (SOA) (Akagi et al., 2011; Crutzen and Andreae, 1990; Hatch et al., 2017; Koss et al., 2018; Liu et al., 2017). However, their global and regional emissions are highly uncertain, in part reflecting the scarcity of field measurements to constrain VOC emissions from biomass burning. As the size and intensity of wildfires in the western United States (U.S.) have increased due to historic forest management practices and climate change (Bowman et al., 2017; Jolly, 2015; Westerling, 2016, 2006), regional air quality is degrading relative to the rest of the country (McClure and Jaffe, 2018; O'Dell et al., 2019). These issues motivated comprehensive smoke characterization measurements from the National Science Foundation / National Center for Atmospheric Research (NSF/NCAR) C-130 research aircraft for western U.S. wildfires during the 2018 Western Wildfire Experiment for Cloud Chemistry, Aerosol Absorption, and Nitrogen (WE-CAN) field campaign (https://www.eol.ucar.edu/field_projects/we-can).

Biomass burning emission factors (EFs, g compound emitted per kg biomass burned) are a critical input to emissions inventories that are derived from vegetation/compound specific EFs and burned area, fuel consumption per unit area, or fire radiative power (Kaiser et al., 2012; Larkin et al., 2014; Urbanski, 2014; van der Werf et al., 2017; Wiedinmyer et al., 2011). Global and regional emissions estimates for biomass burning are subject to large uncertainties, often at a factor of 4–10, given the difficulty of

estimating burned area and fuel consumption (Carter et al., 2020; Pan et al., 2020; Zhang et al., 2014) along with large fire-to-fire variability and generally limited observational constraints in many wildfire-prone regions, including the western U.S. (Jaffe et al., 2020; Prichard et al., 2020). For example, in a recent synthesis of field-measured temperate forest EFs, many species that are important in plume SOA and O_3 formation such as furans and terpenes (Coggon et al., 2019; Hatch et al., 2019), have only been reported in 7 western U.S. wildfires (Andreae, 2019; Friedli et al., 2001; Liu et al., 2017). The large natural fire-to-fire variability of some commonly measured VOC emissions can be partially explained by modified combustion efficiency (MCE), which is a simple proxy of "flaming" and "smoldering" combustion processes readily calculated from observations of carbon monoxide (CO) and carbon dioxide (CO_2) (Akagi et al., 2013; Andreae and Merlet, 2001; Ferek et al., 1998; Guérette et al., 2018; Liu et al., 2017; Urbanski, 2014; Yokelson et al., 1999). However, the extent that MCE describes many of the rarely measured and reported compounds in wildfire smoke remains unknown.

To better constrain VOC and other air pollutant emissions from western U.S. fires, several recent large laboratory burn experimental studies have been conducted for representative fuels (Gilman et al., 2015; Hatch et al., 2017; Koss et al., 2018; Selimovic et al., 2018; Stockwell et al., 2015, 2014; Yokelson et al., 2013). Laboratory experiments attempt to simulate real-world burning conditions using fuels selected to replicate at least partially authentic fires, sometimes resulting in good agreement between field and laboratory measured EFs and emission ratios (ERs) of overlapping species (Akagi et al., 2013; Christian et al., 2003; Selimovic et al., 2018; Yokelson et al., 2013, 2008). However, laboratory burning experiments are imperfect proxies for the complexity of the dynamic burning processes, meteorological conditions, and varying fuels present in wildland fires. Meanwhile, many field emission measurements, either using ground- or airborne-based platforms, are limited by how near a wildfire they can sample due to safety and logistical constraints. As chemical processes take place in the smoke plume within tens of minutes between emission and sampling by research aircraft (Akagi et al., 2012; Hobbs et al., 2003; Lindaas et al., 2021b; Peng et al., 2020), field emission measurements reflect some removal of highly reactive species along with formation of

5

secondary products. Airborne measurements may also miss emissions from residual smoldering combustion (Bertschi et al., 2003), which tend to not be lofted into the main convective column of the plume, while near-field ground-based measurements reflect the opposite problem as they are often unable to sample portions of the smoke most impacted by flaming emissions (Akagi et al., 2013; Ottmar, 2014; Prichard et al., 2020; Yokelson et al., 2013). Additionally, laboratory studies can allow for a large suite of analytical instrumentation to sample smoke within meters of a fire, from ignition to extinction. Field measurements are often limited by instrument payload and include emissions from a variety of burning conditions. Consequently, to most accurately characterize wildfire emissions, insights gained from laboratory studies are useful in the interpretation of field measurements (Selimovic et al., 2019).

Hundreds, if not thousands, of VOCs are known to be present in biomass burning smoke (Bruns et al., 2017; Hatch et al., 2017; Koss et al., 2018; Müller et al., 2016; Stockwell et al., 2015). Characterization of these VOCs remains a challenge though, with no single technique best suited to measure such a large variety of compounds, particularly at the temporal resolution needed for aircraft sampling. Chemical ionization mass spectrometry (CIMS), such as proton-transfer-reaction time-of-flight mass spectrometry (PTR-ToF-MS), is capable of measuring hundreds of VOCs at < 1 s, but does not provide isomer speciation without co-deployed auxiliary techniques. Gas chromatography (GC)-based systems are highly complementary to CIMS instruments, providing speciated VOC measurements with low ppt detection limits at lower temporal resolution. During the recent Fire Influence on Regional to Global Environments Missoula Fire Lab experiment (FIREX-MFL, https://www.esrl.noaa.gov/csl/projects/firex/firelab), Koss et al. (2018) identified the VOC contributors to more than 150 ions detected by PTR-ToF-MS (~90 % of the total detected VOC mass) through a combination of approaches including gas chromatography pre-separation, two chemical ionization methods, literature review, and time series correlation. Additionally, Sekimoto et al. (2017) showed that sensitivities for many VOCs without direct calibrations in PTR-ToF-MS can be calculated to within an uncertainty of $\pm$ 50 % using readily available molecular properties such as polarizability, dipole moment, and functionality.

In this work, we utilize data from the co-deployed GC-based Trace Organic Gas Analyzer (TOGA) and the Advanced Whole Air Sampler (AWAS), while building extensively off previous identification, calibration, and validation efforts for PTR-ToF-MS, to report emissions for 161 individual VOCs and ion masses, plus five non-VOCs (CO_2, CO, CH_4, BC, and OC) for western U.S. wildfires. This represents nearly double the number of VOCs reported for temperate forests in the most recent synthesis study by Andreae (2019), offering more complete measurements of the total VOC emissions from wildfires. To the best of our knowledge, it is also the first time many of the VOCs recently identified in laboratory studies have been measured and assessed in the field under real-world fire conditions. Additionally, the unprecedented large number of wildfires sampled during WE-CAN doubles the number of western U.S. airborne samples for near-field fire emissions, allowing us to explore the variability of VOC emissions and how they are related to combustion processes.

2.3 Methods

2.3.1 WE-CAN field campaign

The WE-CAN field campaign was based in Boise, ID, from 24 July to 31 August 2018 and Broomfield, CO from 1 September to 13 September 2018 (https://www.eol.ucar.edu/field_projects/we-can). Nineteen flights were conducted by the NSF/NCAR C-130 research aircraft approximately every 1–3 days and sampled smoke from fires across seven western states (Juncosa Calahorrano et al., 2021; Lindaas et al., 2021b). Smoke plumes were typically sampled between 14:00 and 19:00 local time when burning conditions were most active. Most sampled smoke plumes were emanating from wildfires located in mixed coniferous ecosystems primarily dominated by pine, fir, and spruce trees (http://catalog.eol.ucar.edu/we-can/tools/fccs). Sampling of fresh emissions was done by flying perpendicular transects through each smoke plume as near to the source as was allowed by safety and logistical constraints.

Emissions were assessed using transects that proceeded as follows. The C-130 entered into each plume after sampling background air as determined by real-time CO observations in flight and continued through the plume until the CO mixing ratios reached regional background levels (generally 75–175 ppb), ideally similar to the mixing ratios observed prior to entering the plume. During WE-CAN, the C-130 also sampled smoke plumes in a pseudo-Lagrangian fashion to characterize smoke evolution (Akagi et al., 2012); other portions of the flights were devoted to sampling cloud-smoke mixtures and aged regional smoke plumes in specific locations. In this analysis, we focus on the WE-CAN VOC emission factors while emission information for NH_3, NO_x, and other reactive nitrogen species can be found in Lindaas et al. (2021b) and Peng et al. (2020), and emission ratios for organic aerosol are available in Garofalo et al. (2019).

2.3.2 Proton-transfer-reaction time-of-flight mass spectrometer

We deployed the University of Montana proton-transfer-reaction time-of-flight mass spectrometer (PTR-ToF-MS 4000, Ionicon Analytik, Innsbruck, Austria) aboard the NSF/NCAR C-130 during WE-CAN. This represents only the second time a PTR-ToF-MS had been used to measure smoke from an aircraft and the first where smoke sampling was the primary mission objective. The PTR-ToF-MS is custom-built into a standard NSF/NCAR HIAPER Gulfstream-V (GV) rack with the mass spectrometer separately vibration dampened. Drift tube conditions were maintained at 3.00 mbar, 810 V, and 60 °C, resulting in E/N of 130 Td for the duration of the campaign. Ion m/z from 15–400 were measured at 2 or 5 Hz frequency with a mass resolution of 2250 $m/\Delta m$ at m/z 33.033 to 4000 $m/\Delta m$ at m/z 330.842, where Δm is the full width at half mass for an ion peak of mass m.

The PTR-ToF-MS inlet was positioned below the instrument rack, mid-cabin underneath the aircraft. Ambient air was drawn into the cabin at 10–15 lpm, dependent on altitude, via a heated (60 °C) NCAR HIAPER Modular Inlet (HIMIL) attached to a downstream pump (KNF Neuberger Inc., Trenton, NJ). From the HIMIL to the instrument rack, sampled air traveled a distance of ~3 m through a 3.175 mm I.D. PFA tubing maintained

at ~55 °C by a self-regulating heat cable. At the rack, the sample stream was subsampled by the PTR-ToF-MS through ~100 cm of 1.588 mm O.D. PEEK tubing maintained at 60 °C. The residence time from outside the plane to the drift tube was less than 2 seconds. A detailed schematic of our instrument inlet and sampling setup is provided in Figure S2.1.

For a typical research flight, the PTR-ToF-MS was powered on and allowed to pump down starting 3 hours prior to takeoff. Instrument background was checked approximately every hour by measuring VOC-free air generated from a heated catalytic converter (375 °C, platinum bead, 1 % wt. Pt, Sigma Aldrich) for 3 minutes. Real-time mass calibrations were performed every 5 seconds using an internal 1,3-diiodobenzene ($C_6H_4I_2$) reference standard added directly to the drift tube from an adjacent heated permeation device.

Mass spectra were analyzed using Ionicon's PTR-MS Viewer software (version 3.2.8.0, Ionicon Analytik, Innsbruck, Austria). Postflight mass calibrations were done to further refine the real-time mass calibration using 5 ion peaks: *m/z* 18.0338 [NH_3H^+], 29.9971 [NO^+], 59.0491 [$C_3H_6OH^+$], 203.943 [$C_6H_4IH^+$], and 330.848 [$C_6H_4I_2H^+$]. Chemical formulas for each ion mass were assigned using a peak list native to the software as well as derived from the growing PTR-ToF-MS literature (Koss et al., 2018; Pagonis et al., 2019). A high-resolution peak fitting algorithm was then manually adjusted for individual peak shapes and PTR-MS Viewer calculated ion counts for each peak, performing a baseline correction, and correcting for mass discrimination in the time-of-flight following common standard PTR-ToF-MS data analysis procedures (Yuan et al., 2017).

Mass transmission corrected raw instrument signals were exported for post-processing in R (R Core Team, 2019), using the open source software RStudio with the dplyr and ggplot2 packages (RStudio Team, 2020; Wickham, 2016; Wickham et al., 2019). Ion masses were first background corrected by subtracting the linearly interpolated instrument background measured in-flight. Ion counts were then normalized to the

primary ion signal and a humidity correction factor was applied for those VOCs which were calibrated by the gas standard (de Gouw et al., 2003). PTR-ToF-MS data in normalized counts per second (ncps) were averaged to 1 Hz and converted to mixing ratios as described in Section 2.3.4 for all subsequent analyses.

2.3.3 Identification and speciation of PTR-ToF-MS ion masses

Overlapping speciated VOC measurements available on the C-130 during WE-CAN (Section 2.4) allow us to identify and assign isomeric fractional contributions to four PTR-ToF-MS ions masses (Table S2.1): m/z 59.049, m/z 71.049, m/z 107.086, and m/z 137.132. For the remaining ions, we applied available isomeric contributions measured during the FIREX-MFL study, which burned similar western U.S. fuel types and speciated PTR-ToF-MS ion peaks for an instrument with a similar mass resolving power to the one deployed during WE-CAN (Koss et al., 2018). Although the actual isomeric contributions may differ, especially for relatively reactive species, the consistent treatment of PTR-ToF-MS measurements between FIREX-MFL and WE-CAN allows for a more direct comparison of the emission factors determined in the laboratory to our field observations (Section 2.7). The overall measurement uncertainty caused by assumptions in isomeric contributions are mostly governed by the instrument sensitivities for all isomers which differ by less than 50 % at any given ion mass, indicating that the impact on mixing ratio is within the error of the calculated sensitivities (see Section 2.3.4)

During WE-CAN, we quantified 125 of 154 identified ions (excluding ammonia, NH_3, and nitrous acid, HONO) reported during FIREX-MFL (Koss et al., 2018). The remaining 29 ions accounted for less than 2 % of the FIREX-MFL PTR-ToF-MS total measured VOC mass (sum of VOC EFs). Additional quantification in the laboratory resulted largely from Fourier-transform infrared spectroscopy (FTIR) co-measured data for NH_3 and HONO (Selimovic et al., 2018) and the fact that laboratory burning experiments measure emissions at ~10 times higher sample concentrations than field observations (e.g., Figure 2, Stockwell et al., 2014). In later sections, we discuss if the identification and speciation of ion masses from laboratory studies are represented in the

field as constrained by the limited co-measured VOCs onboard the C-130 aircraft (Section 2.4), and describe how the difference of plume aging between laboratory and field measurements may affect emission factors (Section 2.7).

2.3.4 Calibration

For each flight, we calibrated the instrument 3 times: 10 minutes before takeoff, in-flight when in transit to/from a fire, and immediately after landing. Instrument calibrations were carried out by the dynamic dilution and subsequent addition of 25 distinct VOCs from two compressed gas standard cylinders (stated accuracy 5 % at ~1 ppmv; Apel-Riemer Environmental Inc., Miami, FL; species listed in Figure S2.2) to the VOC-free air described above. The standard gas cylinders were filled in June 2017 and were re-analyzed for selected VOCs before and after the WE-CAN campaign with the permeation device described below. Calibrations were carried out in the range of 1–10 ppb. Typical r^2 values for the 4-point calibration curve of all species were greater than 0.99 with average residual standard errors less than 10 % (in almost all cases < 3 %). The standard error (95 % confidence interval) of sensitivities for all calibrated VOCs was found to be < 9 % during WE-CAN, thus the campaign averaged sensitivities were applied to all flights. The overall uncertainty for gas standard calibrated species is < 15 %, which is based on the quadrature addition of the individual errors including mass flow controllers, standard accuracy, peak fitting, and calibration.

Additionally, we calibrated formaldehyde (HCHO) post WE-CAN using a gas standard (accuracy 5 % at 420 ppbv reanalyzed by FTIR in October 2019). We quantified the humidity dependent sensitivity by varying the water vapor in the zero air to the range observed during WE-CAN (i.e., [*m/z* 39]/[*m/z* 21], an internal humidity proxy, spanning 0–2 %) (Vlasenko et al., 2010; Warneke et al., 2011), and accounted for a possible sensitivity drift since WE-CAN based on other gas standard calibrations. The formaldehyde measurement uncertainty is estimated to be 40 %, mostly contributed by instrument sensitivity drift since WE-CAN.

11

We also calibrated acetic acid (CH_3COOH) and formic acid ($HCOOH$) before and after the campaign using a custom built permeation system (Baasandorj et al., 2015; Haase et al., 2012; Veres et al., 2010). Here, a constant flow of 20 sccm of ultrapure zero air was passed over a PFA permeation tube (fabricated in-house), which was maintained at a constant temperature. The VOC mixing ratio from the permeation source was stoichiometrically determined by converting to CO_2 via passing through a heated catalyst (400 °C, platinum bead, 1 % wt. Pt, Sigma Aldrich) and subsequently measuring enhancement by a CO_2 detector (LI-840A, LI-COR Inc, Lincoln, NE). Analytes were then added into the PTR-ToF-MS via the above dynamic dilution calibration. The performance of the permeation system was verified by both certified permeation tubes and the multi-component gas standards. The uncertainty in the permeation calibrations is generally less than 30 %, contributed mostly by the LI-COR.

For the remaining ~180 identified VOCs that are not directly calibrated, we estimated their instrument sensitivities using the method developed by Sekimoto et al. (2017). Briefly, molecular dipole moments and polarizability for each species are used to calculate a proton capture coefficient, k_{cap}, for the reaction with H_3O^+. k_{cap} was shown to be linearly correlated to sensitivity for most VOCs:

$$Sensitivity_{calculated,i} = a \times k_{cap,i} \tag{2.1}$$

where the coefficient a is experimentally determined from calibrated VOCs and their k_{cap} ($a = 5.00 \times 10^9$ for the instrument setting in WE-CAN). Chemical properties used here, including functional groups, polarizabilities, and dipole moments, are from the compiled PTR-ToF-MS Library (www.tinyurl.com/PTRLibrary; Pagonis et al., 2019).

The overall uncertainty for this method is estimated to be 50 % for most species and may be higher for select groups of VOCs (Sekimoto et al., 2017). The calculated and measured sensitivity for 26 directly calibrated VOCs are compared in Figure S2.2,

showing agreement within the stated uncertainty. Sensitivity estimates are further verified for co-measured VOCs onboard the C-130 in Section 2.5.

Average sensitivities for each ion mass were subsequently determined using the weighted sensitivity of the known isomers following:

$$sensitivity_{average} = \left(\Sigma \frac{contribution_i}{sensitivity_i} \right)^{-1} \tag{2.2}$$

where *contribution$_i$* is the isomeric contribution of VOC isomers to an ion mass (Section 2.3.3) and *sensitivity$_i$* is the corresponding instrument calibration factor either from direct calibrations using gas standards or calculated using molecular properties. The overall uncertainty is then estimated by adding in quadrature errors from involved sensitivities weighted by isomeric contributions. Table S2.1 lists the sensitivities for 180 VOCs, along with their uncertainties, isomeric contributions to each mass, and calibration methods.

2.3.5 TOGA, AWAS, I⁻ CIMS, and other supporting instrumentation

In addition to PTR-ToF-MS, we report VOCs measured by the Trace Organic Gas Analyzer (TOGA) (Apel et al., 2015, 2010, 2003; Hornbrook et al., 2011), Advanced Whole Air Sampler (AWAS) (Andrews et al., 2016), and iodide (I⁻) adduct high-resolution time-of-flight chemical-ionization mass spectrometer (I⁻ CIMS) (Lee et al., 2014; Palm et al., 2019; Peng et al., 2020). The TOGA and AWAS measurements greatly extend the emission analysis here to include many species not detected by PTR-ToF-MS, while also adding isomer contributions for several ion masses. During WE-CAN, TOGA sampled ambient air for 28–33 seconds to a liquid nitrogen cooled cryogenic preconcentrator, which was then analyzed for 72 VOCs every 100–105 seconds via a gas chromatography-mass spectrometer (GC-MS). The collection of AWAS canister samples was manually initiated based on inflight measured CO mixing ratios targeting both edges and the center of a plume. Typically, 1–3 canister samples were collected per emission transect in addition to background samples collected either just outside a smoke plume or

behind the fire. Each canister was filled for 3–7 s and analyzed for 58 individual VOCs (C_1-C_{10} hydrocarbons, C_1-C_5 alkyl nitrates, and oxygenated VOCs) using a five-channel gas chromatography system equipped with three flame ionization detectors, one electron capture detector, and one mass spectrometer (Benedict et al., 2020, 2019; Russo et al., 2010; Zhou et al., 2010). Measurement uncertainties for TOGA and AWAS vary by compound but are typically between 15 and 50 % (TOGA) and < 10 % (AWAS). We also report HCOOH measured by I^- CIMS because of its high sensitivity. I^- CIMS HCOOH calibration uncertainty is 30 % and was measured at 2 Hz (Palm et al., 2019; Peng et al., 2020).

CO, measured at 1 Hz (accuracy 1 ppb, 2σ) by quantum cascade laser spectrometry (CS-108 miniQCL, Aerodyne Inc., Billerica, MA), was used for all analyses except for fires sampled on 13 August 2018 (RF10), where we used a cavity ring down spectrometer (G2401-m WS-CRD, Picarro, Santa Clara, CA) which also measured CO_2 (accuracy 100 ppb, 2σ) and CH_4 (accuracy 3 ppb, 2σ) at 1.3 Hz for the duration of the campaign.

Black carbon (mass equivalent diameter ~90–500 nm) was measured by a single particle soot photometer (SP2) (Liu et al., 2017; Schwarz et al., 2008) and averaged to a 10 s sampling frequency. When in a plume, the SP2 sample was diluted with HEPA-filtered ambient air to prevent signal saturation (Garofalo et al., 2019) and has an uncertainty of 40 % when on the dilution system. Organic carbon (OC) was determined by high-resolution aerosol mass spectrometry (HR-AMS; Aerodyne Inc., Billerica, MA). HR-AMS operation during WE-CAN is described in Garofalo et al. (2019) and OA:OC ratios were determined via improved ambient elemental analysis for AMS (Canagaratna et al., 2015). For the analysis shown here, OC was calculated in the nascent HR-AMS time resolution (5s) from the simultaneously measured OA mass concentration and OA:OC ratio. When OA:OC was unavailable due to OA being below the instrument detection limit during background sampling, we used the average background OA:OC ratio of 2.02. HR-AMS measured OA with vacuum aerodynamic diameter of ~70–1000 nm and

uncertainty of 35 %, while the OA:OC uncertainty is 8 %. The average OA:OC ratio for the emissions transects used in this work is 1.73.

2.3.6 Co-measured VOCs and data reduction

Of the 161 VOC species reported in this work, 34 were co-measured PTR-ToF-MS, TOGA, and/or AWAS. For overlapping VOC measurements, we used similar criteria as in Yokelson et al. (2013) to determine which measurement to report. Selection criteria are hierarchically described below.

1) Species that PTR-ToF-MS is known to have difficulty measuring because of low sensitivities or interfering fragments were removed from the analysis and the appropriate TOGA or AWAS measurement was used instead. These include hydrogen cyanide (HCN), ethane (C_2H_6), ethanol (C_2H_5OH), and dimethyl sulfide (DMS, $(CH_3)_2S$). Similarly, we removed PTR-ToF-MS measured isoprene (C_5H_8) due to possible fragment interference as discussed in Section 2.5.

2) When selecting between species co-measured by TOGA and AWAS, we retained the measurement reporting the most isomers for a given chemical formula. When the number of observed isomers was equal, we report the measurement with the greater campaign average ER for that chemical formula in order to account for potential unidentified species.

3) VOCs directly calibrated by the PTR-ToF-MS (Figure S2.2) were selected over TOGA or AWAS measurements to preserve the high time resolution of the measurement. It also helps minimize possible errors from (1) background correcting discrete samples, (2) misalignment of the discrete data to the high-frequency CO measurements, and (3) the potential for discrete samples only capturing part of a plume. For VOCs with known isomers or fragments in PTR-ToF-MS, we also report the TOGA or AWAS measurement as described in

criteria 2. However, to prevent double counting, additional speciated information was not used in the EF mass balance or total emitted VOC calculations.

For example, PTR-ToF-MS measures the total of methyl vinyl ketone (MVK), methacrolein (MACR), and 2-butenal at m/z 71.049 ($C_4H_6OH^+$; Table S2.1). TOGA and AWAS both report individual MVK and MACR, with TOGA also measuring 2-butenal. For the EF calculations here, we used the PTR-ToF-MS measurement for m/z 71.049. Additionally, we report the TOGA MVK, MACR, and 2-butenal measurements in Table S2.2 to provide more detailed speciation, and because TOGA observed more isomers than AWAS. When totaling carbon, EFs, or ERs, only the PTR-ToF-MS measurement was used.

4) For VOCs with calculated sensitivities, we used the PTR-ToF-MS measurement when campaign-average emission transect mixing ratios agree within 50 % of the sum of TOGA or AWAS isomers for that mass. Additionally, if the PTR-ToF-MS does not agree within 50 % but there are known isomers not reported by TOGA or AWAS, we again report the PTR-ToF-MS measurement with TOGA or AWAS speciation as described in criteria 3. For the remaining species where the PTR-ToF-MS does not agree within 50 %, we again report the appropriate TOGA or AWAS measurement following criteria 2.

2.3.7 Calculations of emission factors, emission ratios, and modified combustion efficiency

We calculated WE-CAN EFs and ERs for 31 emission transects of 13 wildfires and 1 prescribed burn. Plume transects were chosen for inclusion based on the criteria of being from well-defined smoke plumes traceable to a single emission source, being the nearest transects to said source, and having physical age less than 130 minutes as calculated by wind speeds measured aboard the C-130 and fire locations reported by the U.S. Forest Service (http://catalog.eol.ucar.edu/we-can/tools/fuels). The latter criterion was chosen to

reflect aging times in similar studies (Liu et al., 2017) and maximize the number of plume transects available to improve statistics. Recent studies have shown that rapid chemistry occurs within minutes after emission (Akagi et al., 2012; Hobbs et al., 2003; Lindaas et al., 2021b; Peng et al., 2020); later we discuss how this may affect the emission factors for some very reactive VOCs that we report here. For repeated sampling, we aggregate those plume transects which were performed in succession for the same fire within 30 minutes and treat those that are more than 30 minutes apart as 'unique fires'. This results in 24 fires used in the emission analysis here (denoted a, b, c, etc.; Table 2.1).

Table 2.1. Details of Fires Sampled During the WE-CAN Field Campaign Used in this Work.

Fire name[a]	Date (2018)	Flight	State	Num. passes[b]	Lat.	Lon.	Distance sampled downwind (km)	Physical age (minutes)	Burned area (ha)[c]
Carr (a, b)	July 26	RF02	CA	1, 1	40.63°	-122.52°	32.8–33.6	64–106	92,939
Taylor Creek	July 30	RF03	OR	2	42.47°	-123.69°	11.5–13.7	22–27	21,383
Sharps (a, b)	July 31	RF04	ID	2, 1	43.59°	-114.16°	18.4–19.9	50–85	26,209
Rabbit Foot (a, b, c)	Aug. 3 Aug. 13 Aug. 15	RF06 RF10 RF11	ID	1 1 5	44.86°	-114.27°	11.2–29.8	22–78	14,570
Donnell (a, b)	Aug. 6	RF07	CA	1, 2	38.36°	-119.88°	35.7–45.5	66–106	14,751
Bear Trap (a, b)	Aug. 9	RF09	UT	1, 1	39.29°	-109.87°	11.5–30.6	30–74	4,955
Dollar Ridge	Aug. 9	RF09	UT	1	40.14°	-110.88°	29.6	118	27,870
Monument	Aug. 13	RF10	MT	1	45.00°	-111.82°	15.2	27	2,676
Wigwam	Aug. 13	RF10	MT	1	45.14°	-111.89°	14.4	18	1,654
Goldstone (a, b)	Aug. 13 Aug. 15	RF10 RF11	MT/ID	1 1	45.11°	-113.56°	13.8–51.9	19–121	3,787
Beaver Creek (a, b)	Aug. 15	RF11	MT	1, 1	45.94°	-113.51°	27.3–56.2	57–127	845
Mendocino Complex	Aug. 20	RF13	CA	1	39.43°	-122.84°	57.1	120	185,804
Red Feather Prescribed Burn (a, b)	Sep. 10	RF18	CO	1, 1	40.85°	-105.58°	3.5–4.8	17–17	1,759
Silver Creek (a, b)	Sep. 13	RF19	CO	1, 1	40.23°	-106.60°	24.7–27.3	23–28	8,142

[a]Letters in parentheses denote smoke plumes sampled more than 30 minutes apart, where each is treated separately in emission factor calculations (Section 2.3.7). [b]Number of emission transects per fire as denoted by a, b, or c. Emission transect times can be found in Table S2.3. [c]Total area burned by the fire before being extinguished, sourced from https://www.fireweatheravalanche.org.

Excess mixing ratios (Δ) for high rate measurements were determined per transect by subtracting the linearly interpolated background between air measured immediately outside both edges of the plume transect as determined by CO and acetonitrile levels. For lower rate measurements by TOGA and AWAS, Δ was calculated using the average background of the samples taken nearest one or both edges of a plume transect.

ERs were calculated by integrating the background-corrected in-plume measurements and dividing by the plume-integrated excess CO mixing ratio (averaged over each measurement's sampling time). We note that ERs here are calculated by integrating PTR-ToF-MS and CO real-time plume measurements, rather than using the slope of the least-squares regression of ΔVOC versus ΔCO, to minimize potential biasing of ERs by the center or edge of plume measurements and limit potential error caused by discrepancies in instrument timing (Garofalo et al., 2019).

EFs were calculated using the carbon mass balance method, assuming all burnt carbon is volatilized and detected following (Yokelson et al., 1999):

$$EF_{VOC} = F_c \times 1000 \left(\frac{g}{kg}\right) \times \frac{MW_{VOC}}{12} \times \frac{\frac{\Delta VOC}{\Delta CO}}{\sum_{i=1}^{n}\left(NC_i \times \frac{\Delta VOC_i}{\Delta CO}\right)}$$ (2.3)

Where F_c is the mass fraction of carbon in the fuel (0.457), MW_{VOC} is the molecular mass of a given VOC, 12 is the atomic mass of carbon, $\frac{\Delta VOC}{\Delta CO}$ is the ER of VOC to CO in ppb ppb⁻¹, NC_i is the number of carbon atoms in VOC$_i$, and the sum is over all carbon containing species including 161 ions and individual VOCs measured by PTR-ToF-MS, AWAS, TOGA, and I⁻ CIMS, along with organic carbon (OC), black carbon (BC), CO, CO_2, and CH_4. We use 45.7 % for the percent carbon of western U.S. fuels (Santín et al., 2015) as justified by Liu et al. (2017) for computing EFs (Section 2.7).

Additionally, to explore the dependence of EFs on the combustion efficiency (Section 2.8), we calculated the modified combustion efficiency (MCE) for each emission transect using the plume integrated excess CO and CO_2 mixing ratios:

$$MCE = \frac{\Delta CO_2}{\Delta CO_2 + \Delta CO} \qquad (2.4)$$

2.4 Inferred isomeric contribution to PTR-ToF-MS ion masses in fire smoke

The TOGA instrument aboard the C-130 during WE-CAN provides sufficient constraints to quantify the isomeric fractional contributions for four PTR-ToF-MS ion masses using 12 TOGA speciated VOCs measured in 20 emission transects (Figure 2.1; Table S2.1). Such isomeric information fills a gap in PTR-ToF-MS measurements and is rarely available due to limited co-deployed instruments, especially in fire smoke with complex mixtures of VOCs (Section 2.3.4). Koss et al. (2018) found that the isomeric fractional contributions tended to be similar across different fire burns and fuel types during FIREX-MFL. Here we use TOGA measurements to constrain the isomeric contribution to PTR-ToF-MS ion masses and examine consistency with laboratory studies and their natural variability in wildfires.

Figure 2.1 and Table S2.1 shows the isomeric contributions for m/z 59.049 (acetone and propanal), m/z 71.049 (MVK, MACR, and 2-butenal), m/z 107.086 (*m*-, *p*-, *o*-xylenes and ethylbenzene), and m/z 137.132 (monoterpenes). Two additional ion masses at m/z 69.070 and m/z 73.065 are also shown. Both the WE-CAN field and FIREX-MFL laboratory measurements indicate MVK is the largest contributor at m/z 71.049 (60 ± 9 % (1σ) WE-CAN, 48 % FIREX-MFL) and acetone at m/z 59.049 (83 ± 6 % WE-CAN, 100 % FIREX-MFL). The WE-CAN isomeric contributions of m/z 107.086 differ the most from FIREX-MFL, but still show some consistency: (*m*, *p*)-xylenes are the major contributor (46 % ± 5 % WE-CAN, 68 % FIREX-MFL) followed by ethylbenzene (36 % ± 6 % WE-CAN, 10 % FIREX-MFL) and *o*-xylene (18 % ± 10 % WE-CAN, 23 % FIREX-MFL) .

At *m/z* 137.132, four monoterpenes (camphene, α-pinene, β-pinene + myrcene, and tricylene) were measured by TOGA on the C-130. We approximately speciate *m/z* 137.132 using WE-CAN measurements (Section 2.3.3) but note that laboratory burn studies have recently identified more than 30 monoterpene isomers. Among them, the most dominant compounds vary by fuel type, generally including β-pinene, 3-carene, limonene, α-pinene, and camphene (Hatch et al., 2019, 2017). Though we are likely missing key information to fully assign isomeric fractions for monoterpenes measured by PTR-ToF-MS, we do not expect additional speciation to change the total PTR-ToF-MS monoterpene measurement since the calculated sensitivities for additional isomers would be the same due to their identical chemical formula and functionalities (Sekimoto et al., 2017).

We do not attempt to fully speciate *m/z* 73.065 because only methyl ethyl ketone (MEK) and butanal were measured by TOGA during WE-CAN, while Koss et al. (2018) suggests a non-negligible amount of 2-methylpropanal (14 %) may be present at this mass in the laboratory burn experiment. Nonetheless, both studies agree that MEK is the dominant species at *m/z* 73.065 contributing 80 % ± 2 % during WE-CAN and 85 % during FIREX-MFL.

PTR-ToF-MS measured isoprene (*m/z* 69.070) is known to have interfering fragments from 2-methyl-3-buten-2-ol (MBO), which is potentially emitted in more abundance biogenically than isoprene in western U.S. coniferous forests (Karl et al., 2012). Figure 2.1 shows the fractional contribution of isoprene and MBO for the hypothetical case of all MBO fragmenting and being detected at *m/z* 69.069 (i.e., their ratio to the sum of isoprene and MBO). In this scenario *m/z* 69.069 would be 93 ± 9 % isoprene, suggesting that in western U.S. wildfire emissions, MBO may not be a significant interfering fragment.

We find isomeric fractional contributions vary relatively little from fire-to-fire during WE-CAN, with standard deviations across 20 emission transects less than 10 % for half of the isomers shown in Figure 2.1. Monoterpenes (31–60 %) and MBO (96 %) fractional contribution standard deviations vary the most between emission transects, likely reflecting changing background levels in the lofted air above the forests. Though these above six ion masses constrained by TOGA are a small sample of all isomeric fractional information needed for PTR-ToF-MS measurements, the small observed fire-to-fire variation hints that the ratios of isomers measured in the laboratory are comparable to similar fuels measured in the field.
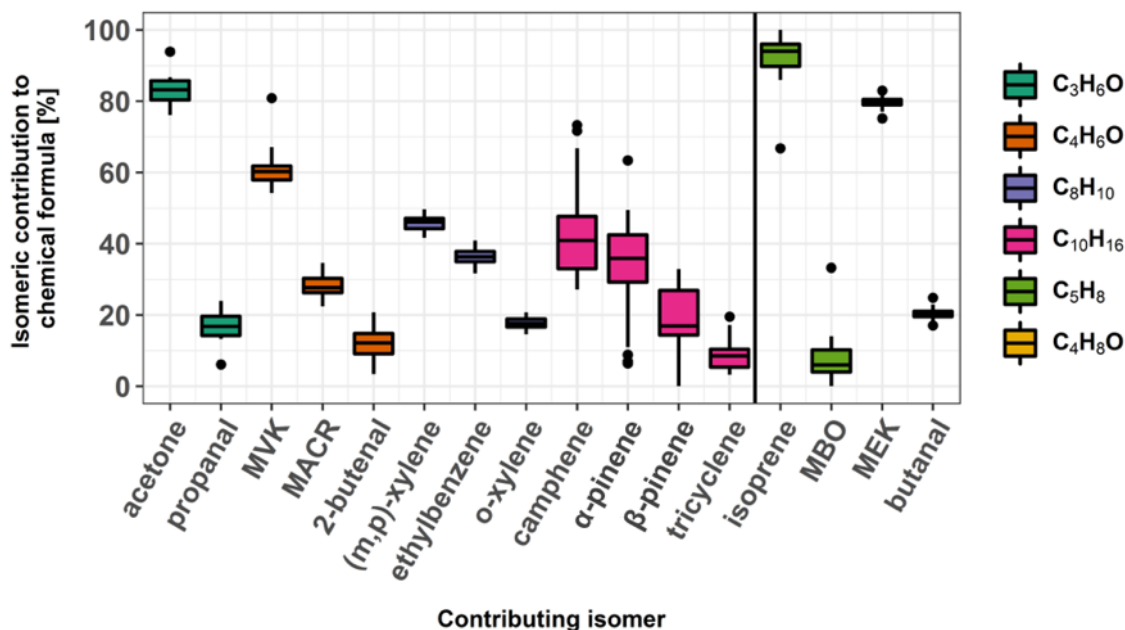
Figure 2.1: Individual isomer contributions to PTR-ToF-MS ions as measured by TOGA from 20 emission transects during WE-CAN. Box and whisker plots (boxes: 25th and 75th percentiles, horizontal line: median, whiskers: 1.5x the inter quartile range, points: > 1.5x inter quartile range) are grouped by color corresponding to a single chemical formula. VOCs to the left of the vertical line were used to speciate four PTR-ToF-MS ion masses in this work. Isoprene and MBO are not isomers but are included due to the potential for MBO to contribute a significant interfering fragment to *m/z* 69.070 in coniferous forests (Karl et al., 2012). MEK and butanal, *m/z* 73.065, are not used for speciation because ~14 % of the signal may be from 2-methylpropanal (Koss et al., 2018), which was not measured aboard the C-130. Note that β-pinene also includes myrcene.

2.5 Instrument intercomparison

Here we compare the co-deployed PTR-ToF-MS, TOGA, and AWAS VOC observations during WE-CAN. Though at lower sampling frequencies (Section 2.3.5), both TOGA and AWAS GC-based measurements observe many VOCs not detected by PTR-ToF-MS while providing additional analytical separation power. We focus on the 24 'unique fire' emission transects and assess the implications for instrument uncertainties for measuring wildfire emissions. Whenever possible, multiple isomers measured by each method are summed together for comparison.

Figure 2.2 summarizes intercomparison results from the reduced major axis regression between PTR-ToF-MS and the two GC-based instruments. Most of the VOCs directly calibrated by PTR-ToF-MS, with only a single known isomer, and little interference due to fragments (formaldehyde, methanol, acetonitrile, acetaldehyde, benzene, and toluene) agree within combined measurement uncertainties with the GC instruments, typically < 30 %. PTR-ToF-MS calibrated masses with identified contributing isomers or interfering fragments including butenes, acetone/propanal, MVK/MACR/2-butenal, MEK/butanal/2-methylpropanal, ethylbenzene/(*m,p*)- and *o*-xylenes (*m/z* 57.070, 59.049, 71.049, 73.064, and 107.085, respectively) also agree within ± 30%.
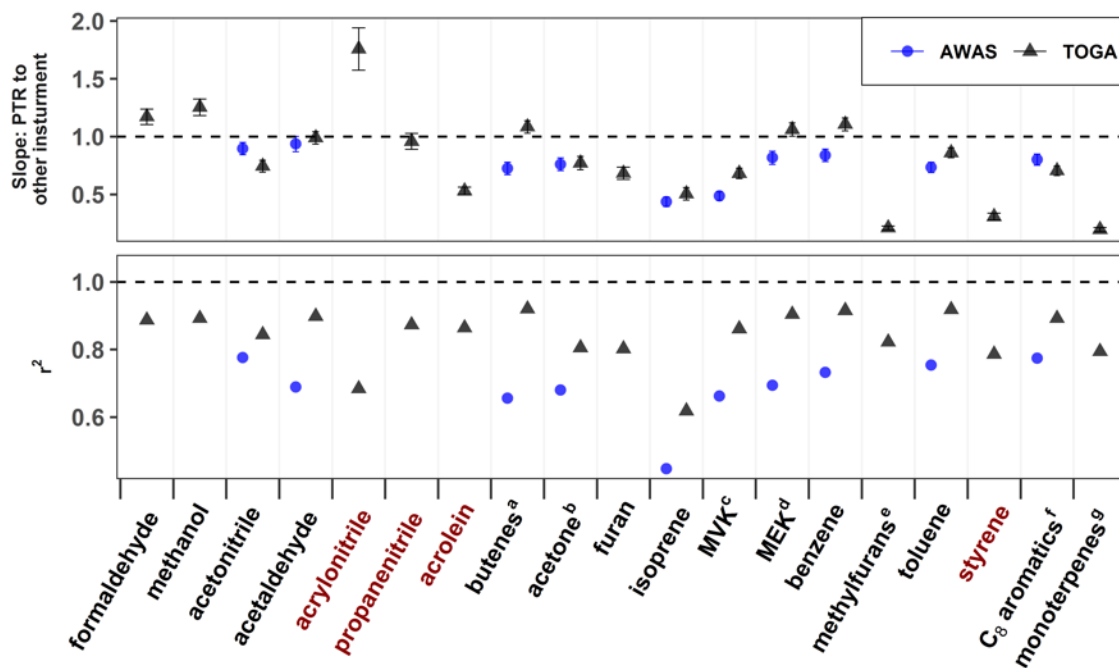
Figure 2.2. Slope and correlation coefficients (r^2) of the reduced major axis regression of PTR-ToF-MS versus TOGA (blue circles) and AWAS (black triangles) mixing ratios for all available emission transect measurements used in this work (~34 TOGA samples and ~40 AWAS samples). Slopes < 1 mean that PTR-ToF-MS measured values are higher than TOGA or AWAS values. Error bars show the standard error of the slope, often too small to be discernible behind the points. VOCs in red have calculated PTR-ToF-MS calibration factors (Sekimoto et al., 2017), while VOCs in black have at least one directly calibrated isomer. Names for the most abundant VOC for each chemical formula are shown while superscripts denote VOCs where multiple isomers measured by TOGA or AWAS are summed together for comparison to the PTR-ToF-MS measurement. [a]TOGA: isobutene, 1-butene; AWAS: 1-butene, cis-2-butene, and trans-2-butene. [b]TOGA: acetone and propanal; AWAS: acetone. [c]TOGA: MVK, MACR, 2-butenal; AWAS: MVK and MACR. [d]TOGA: MEK and butanal; AWAS: MEK. [e]TOGA: 2-methylfuran and 3-methylfuran. [f]TOGA: (*m,p*)-xylenes, ethylbenzene, and *o*-xylene; AWAS: (*m,p*)-xylenes, ethylbenzene, and *o*-xylene. [g]TOGA: camphene, α-pinene, β-pinene + myrcene, and tricylene.

Notable disagreement is found for five ion masses. PTR-ToF-MS measured isoprene is ~2 times higher than either TOGA or AWAS during smoke sampling. However, when sampling over forested regions with relatively little smoke influence, TOGA, AWAS, and PTR-ToF-MS isoprene agree within the combined uncertainty (not shown). Additionally, the PTR-ToF-MS isoprene shows poor correlation with the two GC instruments while in smoke ($r^2 = 0.43$), which suggests further fragment interference while in a plume than the

37 % that we removed based on FIREX-MFL results (Koss et al., 2018). As mentioned in Section 2.4, TOGA typically measured little MBO relative to isoprene in WE-CAN emission transects, thus its fragments are not likely to be the major contributor. Additionally, cyclohexane fragments could play a role (Gueneron et al., 2015; Yuan et al., 2014), though their contribution in wildfire smoke is likely small as TOGA measured isoprene ERs were nearly 12 times higher than cyclohexane measured by AWAS during WE-CAN. Subsequently, the source of any additional fragments in fire smoke is currently unknown.

Total monoterpene abundance measured by PTR-ToF-MS is ~5 times higher than the sum of camphene, α-pinene, β-pinene/myrcene, and tricyclene measured by TOGA. This is likely due to a combination of factors. First, over 30 different monoterpene isomers have been detected in smoke, with the dominant isomers being highly variable between fuels (Hatch et al., 2019, 2017), while only four monoterpene isomers were reported by TOGA during WE-CAN (Figure 2.1). It is likely a large proportion of monoterpenes were not measured here (Section 2.4). Second, the PTR-ToF-MS monoterpene sensitivity is weighted by a speciation profile from TOGA measurements (Section 2.3.4; Eq. (2.2)). However, the factor of 5 difference here is much larger than can reasonably be explained by differences in calibration factor alone as it would require unrealistic sensitivities. Finally, in addition to other monoterpene isomers, the high PTR-ToF-MS monoterpene measurement may have a contribution from interfering fragments from higher-mass species such as bornyl acetate (Hatch et al., 2017).

PTR-ToF-MS measured furan ~1.5 times higher than TOGA with an r^2 of 0.814, potentially suggesting an unknown additional isomer detected by PTR-ToF-MS or a loss in the GC system. Methylfurans were measured by PTR-ToF-MS to be ~15 times greater than the sum of isomers measured by TOGA. Though the PTR-ToF-MS measurement was corrected for being 37 % fragmentary at this mass following Koss et al. (2018), the cause of this discrepancy is currently unknown. Finally, the sum of C_9 aromatics measured by AWAS was found to be ~4 times greater than PTR-ToF-MS (not shown in

Figure 2.2 to preserve y-axis scale). As the PTR-ToF-MS was calibrated using 1,3,5- and 1,2,4-trimethylbenzene, this may indicate a significant proportion of other substituted C_9 aromatics undergo fragmentation in the drift tube, potentially biasing the PTR-ToF-MS C_9 aromatic measurement low.

For PTR-ToF-MS ion masses with only calculated calibration factors, acrylonitrile, propanenitrile, and acrolein measured by TOGA were found to agree within the combined measurement uncertainty of < 60 %. AWAS measured propene was observed to be 2.5 times higher than measured by PTR-ToF-MS, potentially due to overcorrecting the amount of that mass attributed to fragments (not shown in Figure 2.2 to preserve the y-axis scale). TOGA-measured styrene was found to be ~4 times lower than PTR-ToF-MS, and the reason for this discrepancy is currently unknown. AWAS propene and TOGA styrene are reported in this work rather than PTR-ToF-MS (Section 2.3.6).

Due to different sampling frequencies, TOGA and AWAS mixing ratios cannot be directly compared as in Figure 2.2. Instead, we compare ERs for 15 'unique fires' where both TOGA and AWAS capture the same plume transect (Figure S2.3). All TOGA and AWAS co-measured ERs except 3-methylpentane agree within < 50 %, with most < 30 %. The poor slope comparison for 3-methylpentane is due in part to it being only slightly enhanced in the wildfires compared to the other observed alkanes. Though slopes for the reduced major axis regression between TOGA and AWAS ERs agree well, correlation coefficients and standard errors are generally worse than in Figure 2.2 due to added uncertainty from the CO measurement, background corrections, and sampling of different locations within a plume.

During WE-CAN, 48 % of the measured mass (sum of VOC emission factors) was directly calibrated in the PTR-ToF-MS, emphasizing that the strength of the technique is largely dependent on the ability to get accurate sensitivities for non-directly calibrated VOCs. PTR-ToF-MS is further challenged by a lack of speciation information for

25

wildfire smoke, which likely contributes to discrepancies when comparing to TOGA or AWAS measurements (Figure 2.2). However, the high temporal resolution (< 1 s) of PTR-ToF-MS allows for narrow smoke plumes with rapid changes in VOC concentrations to be captured (Müller et al., 2016), while TOGA is constrained by the time needed for gas chromatography separation (~100 s). Though AWAS theoretically has little temporal limitations between filling consecutive canisters, the discrete number of canisters available per flight makes it difficult to capture every plume transect while still sufficiently characterizing background air. As most plumes were crossed in 1–4 minutes at the emission transect and most flights had tens or more transects through smoke, of the 31 emission transects identified in this work only 20 were sampled by TOGA and 20 by AWAS. Together, the large number of VOCs measured by PTR-ToF-MS, coupled with the speciation power, low detection limits, and characterization of alkanes, alkenes, nitrogen containing VOCs, and halides of AWAS and TOGA greatly improves our ability to characterize wildfire emission during WE-CAN. If each instrument were deployed to sample fire emissions alone, a PTR-ToF-MS would capture 87 % of the measured VOC mass during WE-CAN (Section 2.8.2), while AWAS and TOGA capture 34 % and 38 % respectively. These proportions are somewhat consistent with the proportions reported from laboratory burns (Hatch et al., 2017). Of the fraction captured by AWAS, 65 % are alkenes, aldehydes, and alkanes. Similarly, 65 % of the TOGA fraction consists of aldehydes, alcohols, and aromatics.

2.6 Emission factors for speciated and total VOCs

Table S2.2 shows WE-CAN campaign-averaged emission ratios and emission factors for 161 VOCs/ion masses, OC, BC, CH_4, CO, and CO_2. Additional speciation is also provided for 30 isomers known to contribute to PTR-ToF-MS ions masses (Section 2.3.6). Fire-to-fire variability is reflected by the standard deviation of the study average (1σ). One challenge of airborne emission sampling is that the nearest plume transect to a given fire is often tens of minutes or more from the source due to plane safety and firefighting traffic concerns (average aging 60 ± 40 min in WE-CAN; Table 2.1). For reactive species that are not photochemically produced in the outflow from fires such as

monoterpenes or furan, the EF is likely a lower limit. For reactive species that are both directly emitted and photochemically produced in the outflow such as formaldehyde or acetaldehyde, the EF reported here represents the sum of the fraction remaining after decay experienced before the time of analysis and the fraction formed in the plume from precursors. To maximize sample numbers and improve statistics, here we choose to include all emission transects available and focus on discussing the campaign-average with the potential aging effect reflected in part by the deviation. Additionally, EFs that include slight aging may be more appropriate for the spatial and temporal resolution in many models (Lonsdale et al. 2020). A more detailed breakdown of EFs and ERs by fire with corresponding estimated physical age and MCE can be found in Permar et al. (2021).

For the western U.S. wildfires sampled during WE-CAN, the total measured mass of VOCs emitted per fire (expressed as the total emission factor of all measured VOCs, or tVOC$_{EF}$) ranges from 9.8 g kg^{-1} to 35.9 g kg^{-1}, with a mean emission factor of 26.1 $\pm$ 6.9 g kg^{-1} (1σ). Our average tVOC$_{EF}$ is consistent with many previous studies including (1) an early estimate of total non-methane organic gases (NMOG) for temperate forest fires (23.7 g kg^{-1}) from Akagi et al. (2011), (2) total NMOG for pine-forest understory prescribed fires (27.6 g kg^{-1}) from Yokelson et al. (2013), (3) total NMOG from FLAME-4 laboratory coniferous canopy fires (23.9 g kg^{-1}) in Stockwell et al. (2015; Table 2.1), and (4) the total PTR-ToF-MS measured NMOG for carefully simulated wildfires in FIREX-MFL (25.0 g kg^{-1}; Koss et al., 2018).

On a molar basis, the total measured VOC emitted by western U.S. wildfires relative to CO (sum of ERs) ranges from 90.0 ppbv ppmv^{-1} to 206.1 ppbv ppmv^{-1}, with an average of 148.3 $\pm$ 29.6 ppbv ppmv^{-1}. This sum of ERs is also similar to the laboratory-determined sum of 144.5 ppbv ppmv^{-1} for western U.S. fuels (Koss et al., 2018). We later conduct a detailed comparison with previous field and laboratory studies exploring the ability of flaming versus smoldering combustion processes to explain variability in total measured VOC emissions (Section 2.8).

On average, the top 10 most abundantly emitted species (discussed collectively as individual isomers measured by GC and speciated ion masses representing 1–3 isomers measured by PTR-ToF-MS) account for ~53 % of the $tVOC_{EF}$ in western U.S. wildfire smoke, or ~68 % on a molar basis (Figure 2.3). The remaining 47 % of VOC mass is represented by at least 151 species each individually contributing less than 2 % to the overall $tVOC_{EF}$. In contrast, 15 species were needed to reach 50 % of the total measured VOC emission factor in FIREX-MFL (Koss et al., 2018), likely due to the inclusion of ethane in this work, as well as the higher acetaldehyde, ethene, formic acid, and acetone EFs observed during WE-CAN relative to FIREX-MFL. Many of the most abundantly emitted VOCs have also been reported as top emissions in other field and laboratory studies, though some may be in varying orders of abundance (Akagi et al., 2011; Hatch et al., 2017; Koss et al., 2018; Liu et al., 2017; Müller et al., 2016; Selimovic et al., 2018). For example, Akagi et al. (2011) reported the sum of acetic acid and glycolaldehyde (2.22 g kg^{-1}) essentially equal with formaldehyde as the most abundant VOC from temperate forest fires, similar to FIREX-MFL (2.6 g kg^{-1}) (Selimovic et al., 2018) and WE-CAN (2.4 ± 0.59 g kg^{-1}).

Of important exception, total monoterpenes have been measured in laboratory burns as among the most abundantly emitted VOCs (Akagi et al., 2011; Hatch et al., 2017; Koss et al., 2018), however, they do not rank in the top 30 WE-CAN EFs (0.2 g kg^{-1}), nor the top 10 reported in another aircraft study of western fires (Liu et al., 2017) or one southeastern U.S. prescribed fire (Müller et al., 2016). Akagi et al. (2013) observed large monoterpene emissions from airborne measurements directly over prescribed fires, but also noted that some major monoterpene airborne EFs were significantly lower than those from ground-based samples of the same fires. This may be in part because these monoterpenes tend to be produced from fuels (e.g., dead/down logs) that release emissions with less tendency to be lofted into the main convective column of the plume and sampled by aircraft. Additionally, airborne measurements by larger aircraft such as the NSF/NCAR C-130, may only be possible several minutes downwind of the flame front, thus highly reactive

species such as monoterpenes could have undergone some extent of chemical removal before being sampled.
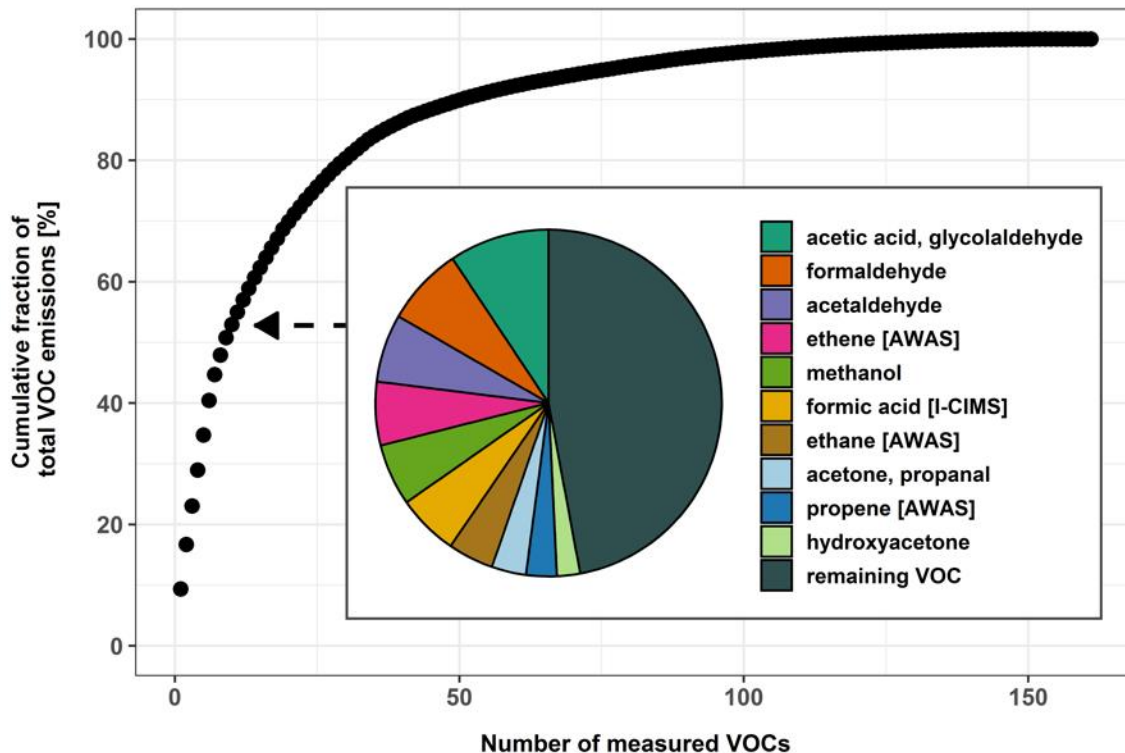
Figure 2.3. The cumulative mass fraction of the total measured VOC emissions as a function of measured VOCs during WE-CAN. 76 VOCs account for 95% of the total measured VOC mass, and 117 VOCs account for 99 % of the total measured VOC mass. The inset pie chart shows the ten most abundantly emitted VOCs which account for ~53 % of the total mass emitted, while the remaining mass consists of 151 species. Reported species not measured by PTR-ToF-MS are identified by corresponding instrument in the legend (i.e., Ethene [AWAS]). Note that hydroxyacetone also includes methyl acetate and ethyl formate isomers (Koss et al., 2018).

Oxygen containing VOCs were found to contribute 67 % of the tVOC$_{EF}$ (or 61% on a molar basis). It is approximately 5–10 % higher than previous comprehensive laboratory studies of western U.S. fuels (51–57 % of the total on a molar basis; Gilman et al., 2015; Hatch et al., 2017; Koss et al., 2018), potentially reflecting oxidation of VOC emissions before being sampled by the C-130 or differences in the fuel components between studies.

2.7 Comparison to previous studies

In this section, we compare the WE-CAN campaign-averaged individual EFs to past studies. Five relevant studies were selected: two PTR-ToF-MS laboratory studies of simulated burns representative of western U.S. fuels (Koss et al., 2018; Stockwell et al., 2015), airborne measurements of wildfire EFs (Liu et al., 2017), a compilation of temperate forest fire EFs based mainly on pine understory prescribed fires (Akagi et al., 2011), and a compilation of > 70 field studies of various temperate fuels (Andreae, 2019). Here we examine differences between field and laboratory measured EFs across individual species in the context of natural fire-to-fire variability and later explore potential explanations for the observed variability in Section 2.8.

Figure 2.4 compares WE-CAN EFs for the top 20 most abundantly emitted VOCs (~70 % of the measured tVOC$_{EF}$) and the sum of remaining VOCs for the 24 'unique fires' sampled more than 30 minutes apart (Table 2.1). The WE-CAN VOC EFs in a logarithmic scale reveals the large species-to-species and fire-to-fire variability of observed EFs, which except for formic acid and acrolein, overlap the literature values for similar fuels. Formic acid EFs measured by both I$^-$ CIMS and PTR-ToF-MS (not shown) were higher than the laboratory and synthesis studies, which may be related to the rapid formation in fresh fire plumes (Akagi et al., 2012; Chaliyakunnel et al., 2016; Goode et al., 2000; Pommier et al., 2017; R J Yokelson et al., 2009). WE-CAN acrolein EFs are consistently lower than in the laboratory, which may reflect chemical loss prior to airborne sampling. Though WE-CAN EFs largely overlap literature values, there are many individual data points where one or more studies are > 1.5 times the interquartile range of the WE-CAN EF, emphasizing the need for multiple biomass burning emission measurements to improve EF statistics.
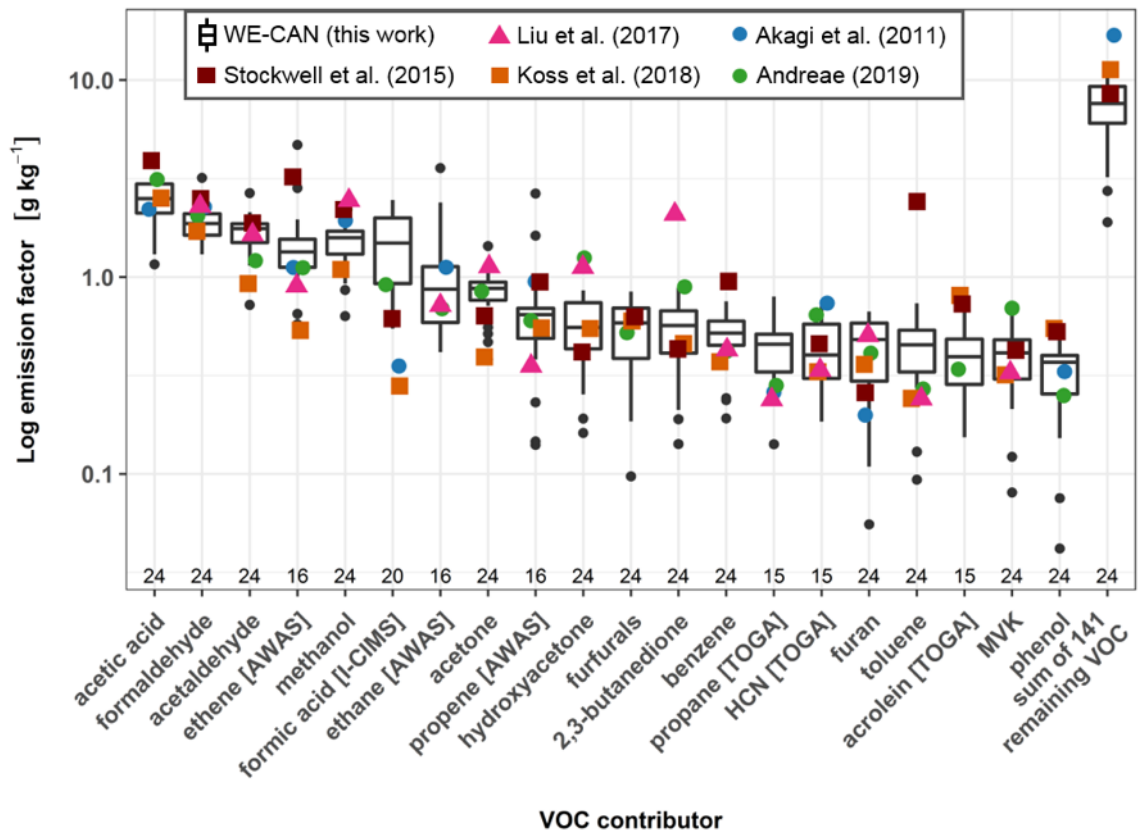
Figure 2.4. Box plot of emission factors for the 20 most abundantly emitted and remaining VOCs by mass during WE-CAN. The number of 'unique fire' EFs (Table 2.1) used for each box is shown at the bottom of the plot. Also shown are relevant literature values for western U.S. fuel types with round points denoting synthesis studies and squares representing laboratory burns. Specifically, the Akagi et al. (2011) value shown with the "sum of 147 remaining VOC" is the total non-methane organic carbon (NMOC) for temperate forests, excluding the EFs shown for individual VOCs. Andreae (2019) EFs are for temperate forests. The Stockwell et al. (2015) values are the average EFs for relevant western U.S. fuels measured by PTR-ToF-MS and Fourier-transform infrared spectroscopy (FTIR; 4 black spruce, 2 juniper, and 7 ponderosa pine fueled laboratory burning experiments), weighted by the number of reported burns. The Koss et al. (2018) values are FIREX-MFL western U.S. fuel type study averages, while Liu et al. (2017) reports average EFs of three western U.S. wildfires sampled during the Biomass Burning Observation Project (BBOP) and the Studies of Emissions and Atmospheric Composition, Clouds, and Climate Coupling by Regional surveys (SEAC[4]RS) aircraft campaigns. TOGA, AWAS, and I[-] CIMS measurements are noted in brackets. PTR-ToF-MS measured species names reflect the most abundant isomer at that mass (Koss et al., 2018), and is consistent with the compared literature. Note that $C_2H_4O_2$: acetic acid includes glycolaldehyde, C_3H_6O: acetone includes propanal, $C_3H_6O_2$: Hydroxyacetone includes methyl acetate and ethyl formate, $C_5H_4O_2$: furfurals include 2-furfural and 3-furfural, $C_4H_6O_2$: 2,3-butanedione includes methyl acrylate, and C_4H_6O: MVK, MACR

includes 2-butenal. Detailed speciation information is available in Table 2.1.

EFs for many of the VOC species in this work have rarely, if ever, been compared between field and laboratory studies. Figure 2.5 summarizes how WE-CAN EFs for 116 species measured by PTR-ToF-MS compare to the FIREX-MFL laboratory experiment average (Koss et al., 2018). Reduced major axis regression between the two campaign averages shows overall good agreement with a slope of 0.93 and r^2 of 0.82. Average EFs for 73 species agree within a factor of two between studies. Most species outside of this range when FIREX-MFL EFs are greater than observed during WE-CAN (16 out of 22) have lifetimes < 3 hours against oxidation by OH (assuming 1×10^6 molec cm^{-3}), such as vanillin, monoterpenes, eugenol, syringol, and sesquiterpenes. This again suggests the potential role of aging and missed emissions from residual smoldering combustion in the field data. Interestingly, in the opposite case when FIREX-MFL average EFs are more than a factor of 2 lower than WE-CAN, 18 out of 21 species are nitrogen containing VOCs (NVOCs). Recently, NVOC emissions have been associated with low temperature pyrolysis (Roberts et al., 2020), which is a loose proxy of lower MCE. More NVOC emissions during WE-CAN relative to FIREX-MFL may be due to the lower MCEs observed in the field relative to laboratory burns (Roberts et al., 2020) or fuel nitrogen differences. Additionally, this could also reflect lager error of PTR-ToF-MS kinetically calculated sensitivities for NVOCs. In Figure 2.5, the large fire-to-fire variability of WE-CAN measured EFs is again apparent, with many WE-CAN individual fire EFs potentially lower than the FIREX-MFL average.

To quantify the fire-to-fire EF variability, we focus on PTR-ToF-MS (and I⁻ CIMS) measurements to prevent statistical bias from the smaller TOGA and AWAS sample sizes. Of these, the median fire-to-fire EF coefficient of variation (COV, standard deviation divided by the mean) is 43 % (45 % mean; Table S2.2). Nitromethane, formaldehyde, isocyanic acid, and acetic acid have the least variable EFs with COVs of 11–25 % for the campaign and ranges varying by less than a factor of 3. Conversely, the most variable species are some of the most reactive (monoterpenes, creosol, vanillin, and sesquiterpenes; COV 73–108 %), suggesting a potential role of rapid early plume

chemistry in the observed variability. The "sum of remaining VOCs" further characterizes the variability, ranging by nearly a factor of 4 across all fires with 29 % COV (a factor of 2 and 23 % COV on a molar basis).
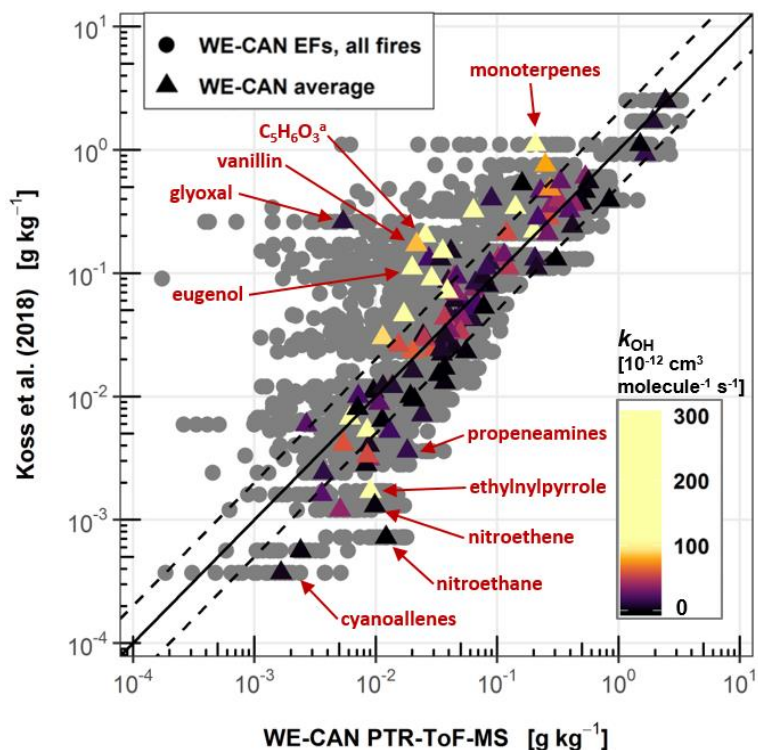
Figure 2.5: WE-CAN campaign averaged (triangles) and individual fire (grey points) EFs compared to study average EFs reported by Koss et al. (2018) for 116 species measured by PTR-ToF-MS. Campaign averages are colored by each VOC's rate constant for the reaction with OH (k_{OH}) and the scale saturated at 100×10^{12} cm^3 molecules^{-1} s^{-1}. The solid black line represents one-to-one agreement, while the dashed lines represent $\pm$ 100 %. Additional labels are provided for the five species with the worst agreement when FIREX-MFL average EFs are more than a factor of 2 higher and lower than WE-CAN. [a]5-hydroxymethyl-2[3H]-furanone (Koss et al., 2018).

2.8 Dependence of emission factors on the modified combustion efficiency

Though direct comparisons of campaign averaged EFs as in Figures 2.4 and 2.5 are common in the literature for showing agreement between studies, such comparisons largely ignore the dependence of EFs on combustion processes. In this section, we explore the relationship between MCE and EFs for all measured VOCs in an attempt to

explain some of the observed variability and relate WE-CAN observations to the growing EF literature with the simple combustion proxy that is readily measured in the field.

2.8.1 Individual VOC emission

Figure 2.6 shows that 98 out of 151 reported VOC EFs, measured in at least 10 of the 24 fires, correlate to MCE with p-values < 0.05, indicating that 76 % of the average $tVOC_{EF}$ has statistically significant dependence on burning conditions. Of these, correlation coefficients range from 0.23 for quinone to 0.91 for benzene and all slopes are negative. The wide range of correlation coefficients suggests MCE is not the only contributor to the emission variability, with fuel types/conditions (decomposition, elemental chemistry, geometry, and moisture), plume aging, surface wind, and pyrolysis temperature likely playing a role (Roberts et al., 2020; Sekimoto et al., 2018). Still, the correlations obtained by WE-CAN can provide observational constraints on uncertainties for predicting VOC emissions with MCE, particularly for those species that are rarely measured in the field. Overall, we find that MCE can explain at least 50 % of the variance for 57 individual VOC EFs, representing 54 % of the $tVOC_{EF}$. Equations and coefficients for these 151 correlations are listed in the supplement (Table S2.4).
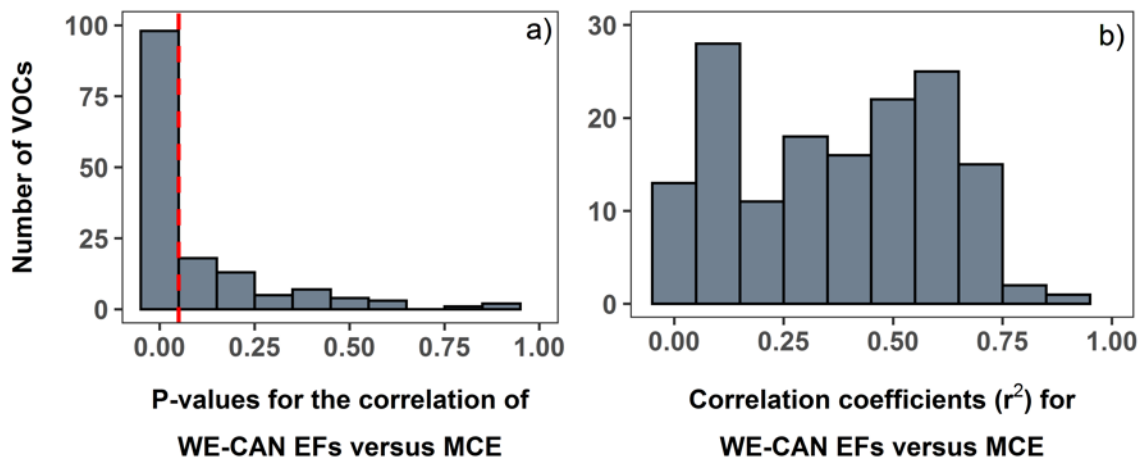
Figure 2.6: a) Histogram of p-values from the least squares regression of EF versus MCE for 151 VOCs. Among them, 98 VOC EFs have a statistically significant correlation with MCE, p-values < 0.05, represented by the red dashed line. b) The same as Panel a) except for correlation coefficients (r^2) of the least squares regression of EF versus MCE.

We compare WE-CAN EFs to previous studies in terms of their dependence on MCE for CH$_4$ and five VOCs selected for their representativeness as discussed below. Figure 2.7 shows that when MCE is considered, WE-CAN EFs show good agreement with both laboratory and field measurements, with slightly better agreement with field data. This may reflect chemical aging effects or under-representation of emissions from residual smoldering combustion in the field relative to the laboratory. Benzene, methanol, and CH$_4$ represent long-lived species with minimal degradation in the plume aging times characteristic of the WE-CAN emission transects. Interestingly, the spread in the laboratory benzene EFs are larger than the field data, the reason for which is currently unknown. Furan represents shorter-lived species, while acetaldehyde and formaldehyde are a photochemical product of many VOCs. Finally, the figure highlights the agreement between EFs as a function of MCE for CH$_4$ measurements obtained by the NCAR Picarro instrument and literature values. A few notable outliers are also present. The outlying point from Stockwell et al. (2015) represents a ponderosa pine lab burn. Furan's outlier is from combustion of Jeffrey pine duff (Koss et al., 2018), and is also present in the comparison of furfural EFs vs MCE (Figure S2.4).

Although the comparison of these six species is not inherently representative of the other 156 VOCs reported in this work, they do suggest that WE-CAN measured EFs agree with previous studies when compared in the context of MCE. Additionally, Figure 2.7 highlights that despite complex fuels and combustion chemistry, the simple MCE index explains a significant amount of the study-to-study variability. The remaining variance is expected due to fuel chemistry, moisture, geometry, or measurement uncertainty (Yokelson et al., 1996), and should be further explored as more field data become available.

35
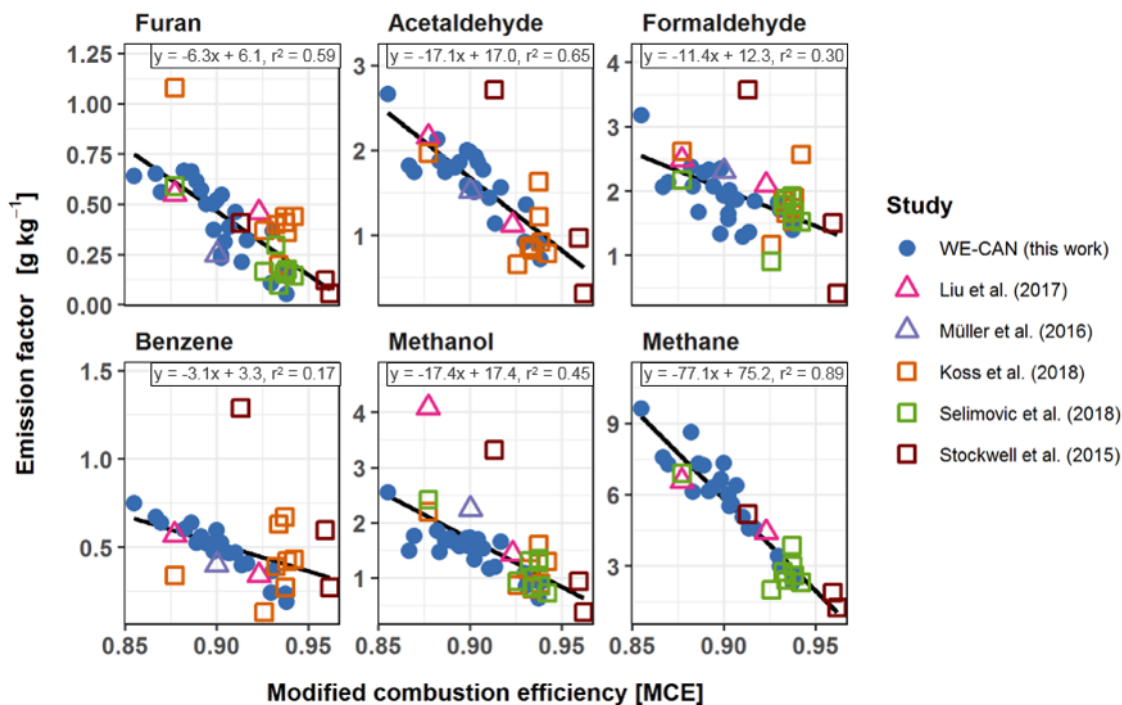
Figure 2.7: Correlations of EFs versus MCE for methane and a subset of VOCs (furan, acetaldehyde, formaldehyde, benzene, and methanol) commonly reported in the literature. Also shown are additional EFs for two field campaigns (Liu et al., 2017; Müller et al., 2016) and averaged coniferous fuel EFs measured during three laboratory burn experiments (Koss et al., 2018; Selimovic et al., 2018; Stockwell et al., 2015). We also show the same figure for furfurals in Figure S2.4 as an additional short lived VOC. Black lines represent the least squares regression for all studies. Regression statistics of all 151 VOC EFs with MCE measured in at least 10 fires during WE-CAN are available in Table S2.4.

2.8.2 Total measured VOC emissions

WE-CAN total measured VOC emissions strongly correlate with MCE ($r^2 = 0.67$; Figure 2.8), indicative of less VOC being produced relative to CO_2 as fuels burn more efficiently and that nearly 70% of the tVOC$_{EF}$ can be explained by MCE alone. Total measured VOC emissions for western U.S. fuels measured during combined laboratory burns also show a strong negative correlation with MCE ($r^2 = 0.72$), however with a much steeper slope and approximately 2 times greater tVOC$_{EF}$ than WE-CAN at similar MCEs. Overall, such strong correlations observed both in the field and laboratory studies suggest that total measured VOC emissions could be predicted when the MCE information is

36

available, and individual VOC emission could be subsequently derived using emission profiles (Section 2.9), similar to the wildland fire portion of the EPA's National Emission Inventory (Baker et al., 2016; U.S. Environmental Protection Agency, 2020)

There are a few potential reasons for the differences between the WE-CAN and laboratory measured $tVOC_{EF}$. First, rapid chemistry taking place in the wildfire plumes prior to their sampling by the C-130 could result in lower EFs compared to laboratory studies particularly for shorter-lived species, which also tend to have high molecular weights. Similarly, condensation of lower volatility species between emission and sampling may also account for some of the mass difference. Ground-based studies of wildfire $\Delta PM_{2.5}/\Delta CO$ ratios show that considerable evaporation of biomass burning organic aerosol occurs at the warmer temperatures typical of ground-level and laboratory burn environments relative to aircraft sampling (Selimovic et al., 2019). Including the WE-CAN average OA ($\sim$19 g kg^{-1}) in the $tVOC_{EF}$ would help achieve agreement, but not all OA evaporates at room temperature so this does not fully resolve the differences between studies. Second, a forced flow directly to the sample inlets during laboratory burns likely means that they capture some emissions from smoldering combustion which may not be as efficiently lofted in the wildfire plume and thus underreported in the field. Third, in this work we assume 45.7 % emitted carbon in our carbon mass balance for deriving EFs following other field studies in the western U.S., which contrasts with the $\sim$50 % used during the laboratory studies (Koss et al., 2018; Stockwell et al., 2015), meaning WE-CAN EFs are generally expected to be $\sim$10 % lower (Eq. 2.3). Additionally, WE-CAN emission factors were calculated using the sum of carbon from 161 ions and individual VOCs, along with OA, BC, CO, CO_2, and CH_4 for the total carbon term of the mass balance equation (Eq. 2.3), which is expected to result in slightly lower individual EFs than if a smaller sampling of VOCs, CO, CO_2, and CH_4 are only used. Finally, the data available to calculate MCE differs substantially between laboratory and field experiments. In the lab, the full progression of a fire from ignition to completion is measured, and MCE is therefore calculated using the fire integrated CO and CO_2 measurements, providing the fire's overall MCE for the entirety of the burn. While this includes both flaming and smoldering time periods, the laboratory integrated MCE

remains higher than in the field due to a number of factors including drier fuels and more optimize burning conditions (Christian et al., 2003; Holder et al., 2017; Selimovic et al., 2018; Yokelson et al., 2013). In the field, MCE is calculated from a single transect through a smoke plume which is assumed to contain all the stages of burning. It is likely a combination of the above factors contributes to the difference in $tVOC_{EF}$ versus MCE between field data and laboratory burns. While we cannot ascertain the exact reasons for lab field differences, the comparison highlights the importance of field measurements of authentic fires.
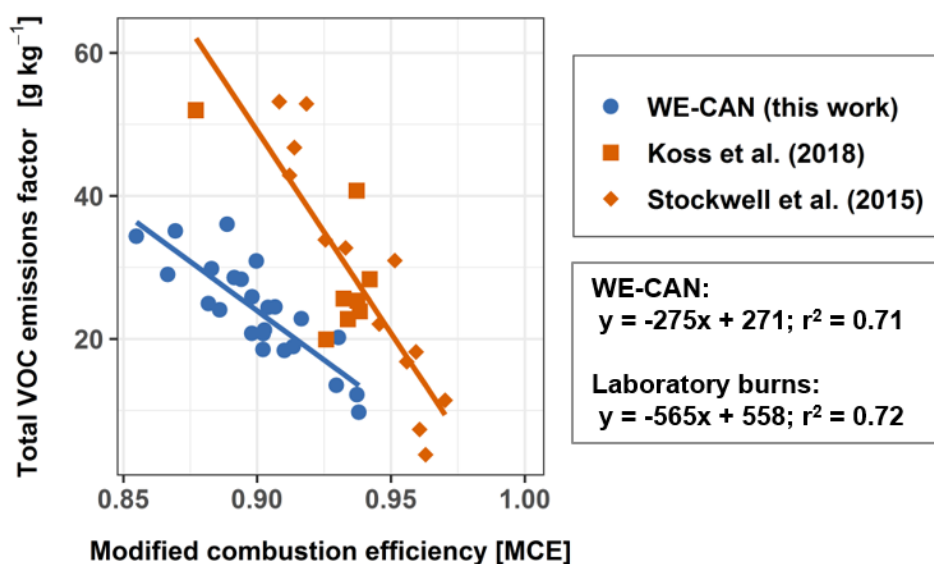
Figure 2.8: Relationship between total measured VOC emissions and MCE observed in WE-CAN. Also shown are data from laboratory burns for similar fuels during FLAME-4 and FIREX-MFL. The solid lines are corresponding least squares regression fits. WE-CAN total measured VOC emissions include the 161 VOC EFs reported in this work. Koss et al. (2018) total VOC include ~154 PTR-ToF-MS measured ions, excluding ammonia and nitrous acid, from individual burns of ponderosa pine, lodgepole pine, Douglas fir, subalpine fir, Engelmann spruce, loblolly pine, Jeffrey pine, and juniper fuel types. Stockwell et al. (2015) total measured VOC emissions include ~55 PTR-ToF-MS measured ions reported as positively identified and 10 VOCs measured by Fourier-transform infrared spectroscopy (FTIR) during 4 black spruce, 2 juniper, and 7 ponderosa pine fueled laboratory burning experiments.

Rapid early plume chemistry can cause aircraft-measured EFs of reactive primary VOCs to be lower than at the source, while simultaneously increasing EFs for secondary

species. Field and laboratory measured MCEs also differ, making the decision of which EFs to use in models unclear. Generally, laboratory burns may better capture the emissions and evolution of reactive VOCs throughout fires, including smoldering combustion, or provide an opportunity to control variables. However, WE-CAN sampled western U.S. wildfires mid-afternoon during the summer, when presumably the fires are burning at their highest emissions production level. Within this dataset, only 4 out of the 24 'unique fires' were characterized by MCE > 0.92, which is near the lower end of MCEs typically reported for laboratory burns of similar fuels. Airborne measurements would be expected to favor flaming combustion if they have a bias, so a lower MCE in the air suggests a tendency towards unrepresentative high MCE in many lab burns. For this reason, many laboratory studies provide EFs adjusted to reflect the field average MCE (Selimovic et al., 2018). Interestingly, aging effects may change the airborne EFs to levels that are perhaps more appropriate for the spatial and temporal resolution of many regional to global models (Lonsdale et al., 2020), but it is not simple to rule out the loss of smoldering emissions in airborne sampled fires (Akagi et al., 2014; Bertschi et al., 2003). Overall, using data from real wildfires makes sense, but lab studies can help characterize species rarely or not measured in the field, especially if they are adjusted to match field MCE or other steps are taken to increase representativeness (Selimovic et al., 2018; Yokelson et al., 2013).

2.9 VOC emission profiles for emissions speciation

Rather than using correlations with MCE to predict individual VOC EF, another approach to get speciated emissions is by applying a flaming or smoldering profile to the total VOC emissions (U.S. Environmental Protection Agency, 2020). Here, we calculate VOC emission profiles by dividing individual VOC EFs by the $tVOC_{EF}$ to get the mass fraction of each species to the total emissions. Mass fractions for the five highest and five lowest MCE fires sampled during WE-CAN were then binned into a "high" and "low" MCE profile. A Wilcox rank-sum test comparing the two profiles shows that only 26 VOCs, ~18 % of the $tVOC_{EF}$, are statistically different between the profiles (p-values < 0.05); among them, only 3 VOCs (methylpyridines, isocyanic acid, and toluene) have p-values < 0.01. This suggests that for the majority of VOCs (> 80 % by mass) emitted in western U.S. wildfires, mass fractions of individual VOCs significantly overlap for the

MCE range sampled during WE-CAN. As such, separated high and low MCE profiles cannot be clearly defined here and a single campaign averaged VOC emission profile best describes the data for all but a few species (Table S2.2).

To examine the role of MCE on emission profiles, we further investigate the dependence of the mass fraction on MCE for the same 151 species, measured in 10 or more fires, as in Section 2.8.1. In contrast to EF versus MCE correlations, we find that the mass fractions of only 44 of the 151 species have a statistically significant dependence on MCE (p-values < 0.05) with correlation coefficients ranging from 0.17 to 0.62. These 44 VOCs account for 31 % of the average tVOC$_{EF}$. Additionally, 11 of these correlations have positive slopes, with three of the steepest being for formic acid, formaldehyde, and isocyanic acid, indicating that these VOCs account for more of the tVOC$_{EF}$ as combustion efficiency increases.

Recently it has been shown that laboratory biomass burning VOC emissions could be described by two positive matrix factorization (PMF) factors related to high and low temperature pyrolysis, where pyrolysis is one component of smoldering combustion (Sekimoto et al., 2018; Yokelson et al., 1996). One possible explanation for the lack of distinct high and low MCE emission profiles in this work is that emissions from all types of burning (including flaming, gasification, and high and low temperature pyrolysis) are lofted into the large wildfire plumes sampled during WE-CAN, which likely results in the high and low MCE emissions intermixing such that the measured VOC profile regresses towards a mean. This is in contrast to laboratory burns where both "pure" and mixed combustion processes can be observed as the burn progresses from ignition to completion. Consequently, these results may be different if airborne data are obtained over a broader range of MCEs, such that similar direct comparison between smoldering and flaming emissions can be done.

2.10 Conclusions

We present emission factors and emission ratios for 161 isomeric and individual VOCs for western U.S. wildfires measured by complementary instruments onboard the NSF/NCAR C-130 aircraft during the WE-CAN field campaign. *In situ* emission measurements were made during 31 emission transects of 24 'unique' wildfires, significantly expanding the number of observations of many VOCs rarely reported in the field and allowing us to assess the large natural variability of wildfire emissions. Across all fires, measured MCEs ranged from 0.85 to 0.94 when they were typically burning most actively in the mid-to-late afternoon.

Using co-deployed TOGA measurements for 13 speciated VOCs, we found that the fractional contribution of isomers to four PTR-ToF-MS measured ions (*m/z* 59.049, 71.049, 107.086, and 137.132) had relatively little fire-to-fire variability and were comparable to results in previous laboratory burn experiments for similar fuels. Among 45 co-measured VOCs, 36 showed agreement within combined instrument uncertainties (< 60 %). Disagreement was found between five PTR-ToF-MS ion masses and the two GC-based measurements (*m/z* 69.069 isoprene, *m/z* 69.033 furan, *m/z* 83.049 methylfurans, *m/z* 121.061 C_9 aromatics, and *m/z* 137.132 monoterpenes), likely reflecting additional unknown isomers or fragment products detected by PTR-ToF-MS in fire smoke. Given that these ions represent several reactive VOCs, their further identification could help improve PTR-ToF-MS measurements and better understand their implications for air quality. TOGA and AWAS measurements agree between all co-measured species with the exception of 3-methylpentane.

The total observed VOC emissions averaged 26.1 ± 6.9 g kg^{-1} (148.3 ± 29.6 ppbv ppmv^{-1}) for western U.S. wildfires, consistent with previous studies. The top 10 most abundant VOCs accounted for 53 % of the total measured VOC mass; while the remaining 47 % was represented by at least 151 species, each contributing less than 2 % to the total. Oxygenated VOCs contributed to 67 % of the measured total VOC emissions by mass, or 61 % on a molar basis.

When MCE is considered, we found overall good agreement between individual VOC EFs and previous laboratory and field studies. However, for a given MCE, total measured VOC emissions are nearly 2 times lower than measured in two recent laboratory experiments utilizing similar instrumentation and nominally similar fuels. The source of this difference may reflect aging effects, fuel differences, under-sampling of smoldering emissions by aircraft, or different integration of combustion processes. WE-CAN observations reveal 98 species, accounting for 76 % of the average total measured VOC mass, have statistically significant and negative dependences on MCE. VOC mass fractions show much less MCE dependence with significant overlap within the observed MCE range, suggesting that a single speciation profile can describe VOC emissions for the western U.S. coniferous forest wildfires sampled during WE-CAN.

Overall, WE-CAN field observations nearly double the number of measured VOC emission ratios and emission factors for wildfires compared to the most recent synthesis study, and double the number of western U.S. airborne samples for near-field fire emissions, providing better constraints for air quality models. However, plane safety and logistical concerns limited WE-CAN measurements to sampling plumes mid-to-late afternoon and tens of minutes downwind of a fire. Future studies of wildfire emissions from the less active (and possibly lower MCE) burning conditions typical of nighttime and early morning would complement the WE-CAN dataset. Additionally, more work connecting ground-based studies to laboratory and aircraft observations would better inform how smoldering combustion emissions, not lofted into the main plume, may bias airborne measurements. Finally, future model and observational plume aging studies are needed to improve our understanding of how rapid early plume chemistry in wildfires may impact comparisons between laboratory and field-measured EFs for reactive VOCs and the total organic emissions.

3 Atmospheric OH reactivity in the western United States determined from comprehensive gas-phase measurements during WE-CAN

3.1 Abstract

Wildfire smoke contains numerous different reactive organic gases, many of which have only recently been identified and quantified. Consequently, their relative importance as an oxidant sink is poorly constrained, resulting in incomplete representation in both global chemical transport models (CTMs) and explicit chemical mechanisms. Leveraging 160 gas-phase measurements made during the Western Wildfire Experiment for Cloud Chemistry, Aerosol Absorption, and Nitrogen (WE-CAN) aircraft campaign, we calculate OH reactivities (OHRs) for western U.S. wildfire emissions, smoke aged > 3 days, smoke-impacted and low/no smoke-impacted urban atmospheres, and the clean free troposphere. VOCs were found to account for ~80 % of the total calculated OHR in wildfire emissions, with at least half of the field VOC OHR not currently implemented for biomass burning (BB) emissions in the commonly used GEOS-Chem CTM. To improve the representation of OHR, we recommend CTMs implement furan-containing species, butadienes, and monoterpenes for BB. The Master Chemical Mechanism (MCM) was found to account for 88 % of VOC OHR in wildfire emissions and captures its observed decay in the first few hours of aging, indicating that most known VOC OH sinks are included in the explicit mechanisms. We find BB smoke enhanced the average total OHR by 53 % relative to the low/no smoke urban background, mainly due to the increase in VOCs and CO thus promoting urban ozone production. This work highlights the most important VOC species for daytime BB plume oxidation and provides a roadmap for which species should be prioritized in next-generation CTMs to better predict the downwind air quality and health impacts of BB smoke.

3.2 Introduction

Wildfires are a major source of volatile organic compounds (VOCs) to the atmosphere (Akagi et al., 2011; Andreae and Merlet, 2001; Crutzen and Andreae, 1990), emitting hundreds to thousands of different organic gas-phase species (Hatch et al., 2019; Koss et al., 2018; Permar et al., 2021). Many of the VOCs emitted by wildfires are known hazardous air pollutants, play an integral role in the formation of secondary organic

aerosol (SOA) and ozone (O_3) as smoke plumes age, and have long-range impacts on tropospheric oxidation potential (Atkinson and Arey, 2003; O'Dell et al., 2020; Palm et al., 2020; Xu et al., 2021). Increasing evidence has suggested that wildfires can bring VOC-rich air into VOC-limited cities resulting in enhanced ozone production in urban atmospheres (Liang et al., 2022; Ninneman and Jaffe, 2021; Xu et al., 2021). Although many VOC species have recently been identified and quantified in biomass burning (BB) smoke, their roles as a hydroxyl radical (OH) sink are poorly constrained. Consequently, we do not understand how well current global chemical transport models (CTMs) and explicit chemical mechanisms represent BB VOCs, the amount of reactive carbon they may be missing, and which species should be prioritized to incorporate into the next generations of air quality models. In this work, we use comprehensive VOC and other trace gas measurements made during the Western Wildfire Experiment for Cloud Chemistry, Aerosol Absorption, and Nitrogen (WE-CAN) field campaign to examine the major daytime OH radical sinks over the western United States (U.S.) during an active wildfire season.

Both plume scale and global chemical transport models have difficulty predicting the evolution and downwind air quality impacts of BB on NO_x (Peng et al., 2021), VOCs (Müller et al., 2016), O_3 (Bourgeois et al., 2021), and SOA in smoke-impacted environments. During the day, OH radicals are the primary oxidant in BB smoke, though O_3 can also play an important role in alkene and terpene oxidation, while in optically dense plumes NO_3 is a competitive oxidant of phenolics (Decker et al., 2021a). Major BB OH sources include photolysis of HONO (Peng et al., 2020), O_3, and formaldehyde (Liao et al., 2021; Robinson et al., 2021). The major sinks include primary and secondary VOCs, NO_x, and CO (Decker et al., 2019, 2021a; Liang et al., 2022). As the global mean OH concentration is consistently overestimated across CTMs (Murray et al., 2021; Naik et al., 2013), it is likely that significant OH sinks are missing in models (Mao et al., 2009; Travis et al., 2020). This in turn affects the overall simulated oxidation chemistry and may partly explain why CTMs underestimate O_3 enhancement from BB (Bourgeois et al., 2021).

OH reactivity (OHR) is a measure of the total amount of reactive gases in the atmosphere on the scale of reactivity (Di Carlo et al., 2004; Kovacs et al., 2003; Sanchez et al., 2021) and can be calculated from field measurements of speciated reactive gases or directly measured. The calculated OHR is defined as,

$$OHR = k_{OH_X}[X] \tag{3.1}$$

where k_{OH} is the rate constant for the reaction of species X with the OH radical and $[X]$ is the measured species concentration. Total calculated OH reactivity (tOHR) is then the sum of all individual species' OH reactivities. Because the directly measured OHR (mOHR) describes the total reactive burden in an air mass, the difference between the measured and calculated OHR, ofeten called the missing OHR, constitutes reactive gases not measured by the deployed instrumentation for speciated compounds. In this work, we do not have a direct OHR measurement and therefore do not speculate about the missing OHR fractios. Instead, we focus our analysis on the calculated OHR as a tool to describe the relative importance of different measured species as an OH sink, with larger OHRs representing those gases more likely to react with OH radicals. Consequently, the species that make up the largest fraction of tOHR play the largest role in daytime OH-mediated oxidation chemistry and are therefore some of the most important measured compounds to include in atmospheric chemical models.

The major trace gas contributors to the tOHR can vary significantly between environments, resulting in distinct OHR speciation profiles. For example, a majority of the tOHR in biogenic emissions is accounted for by isoprene, monoterpenes, 2-methyl-3-buten-2-ol (MBO), and isoprene oxidation products such as methyl vinyl ketone (MVK) and methacrolein (MACR) (Heald et al., 2020; Hunter et al., 2017; Millet et al., 2018; Sinha et al., 2010), while the tOHR in urban environments is typically dominated by NO_x, CO, and petroleum-linked hydrocarbons such as light alkenes and aromatics (Heald et al., 2020; Lou et al., 2010; Mao et al., 2010; Ren et al., 2003). Though less reactive than many primarily-emitted VOCs, formaldehyde and acetaldehyde have also been shown to be substantial OH sinks in most environments. To date, the most

comprehensive characterizations of OHR in BB emissions come from laboratory experiments and suggest a much more diverse OHR speciation profile than urban or forest atmospheres due to the large number of reactive organic gases that are emitted. Even though BB emits large amounts of CO_2, NO_x, CO, and CH_4, VOCs are the major OH sink, contributing 80 % of the initial tOHR in laboratory burning experiments, despite comprising less than 1 % of emissions by mass (Gilman et al., 2015). Many highly reactive individual VOCs or groups have been found to significantly contribute to OHR upon emission, including terpenes, alkenes, furan-containing species (collectively referred to here as furans), formaldehyde, and acetaldehyde (Decker et al., 2019, 2021a; Gilman et al., 2015; Hatch et al., 2019; Koss et al., 2018). The OHR profile of aged smoke has been less described in the literature and is often mixed with other emission sources, but typically is characterized by oxygenated VOCs (OVOCs), furans, aromatics, and aliphatic hydrocarbons (Kumar et al., 2018; Liang et al., 2022).

Currently, CTMs such as the commonly used GEOS-Chem, are ultimately limited on the number of VOCs they can explicitly describe due to computational constraints. Consequently, CTMs only implement simplified chemistry for a handful (typically < 30) of the most studied individual and lumped species, which were often developed and evaluated for relatively well-studied environments such as urban areas, forests, and to a lesser extent the remote/clean troposphere (Carter et al., 2022; Ferracci et al., 2018; Lelieveld et al., 2016; Millet et al., 2018; Safieddine et al., 2017; Travis et al., 2020). Recent work suggests the GEOS-Chem CTM underpredicts biogenic VOC reactivity flux by 40–60 % in forest environments, with major uncertainties related to a few select known/modeled VOCs, rather than unrepresented species (Millet et al., 2018). How well these modeled species represent the most important individual OH sinks in wildfire smoke has yet to be assessed.

Alternatively, box models such as the Framework for 0-D Atmospheric Modeling (F0AM) can simulate chemistry in BB plumes for tens of thousands of reactions and species using detailed explicit chemical mechanisms such as the Master Chemical

Mechanism (MCM) (Liao et al., 2021; Peng et al., 2021; Robinson et al., 2021). How well these models represent the tOHR and its evolution downwind is bound by the number of reactive species included in the chemical mechanisms, how well we understand their cascade oxidation, and whether these species are included in model initialization. The extent to which the MCM incorporates most of the reactive species emitted from wildfires is not well known due to historically scarce field observations that fully characterize BB smoke. Laboratory burning experiments suggest that the MCM captures 75 % of the initial VOC tOHR in BB emissions measured by the mass spectrometry techniques used in that study, while the remaining missing reactivity likely stems from species whose chemistry has not been extensively studied such as oxygenated aromatics and less abundant furans (Coggon et al., 2019). Here, we use a similar suite of instrumentation to build on the laboratory work done by Coggon et al. (2019) evaluating how the MCM represents OHR in wildfire emissions, while expanding the analysis to examine how the MCM captures OHR as wildfire smoke ages.

To the best of our knowledge, no other studies have employed such a comprehensive suite of gas-phase measurements to examine speciated OHR in various environments affected by wildfire smoke. By leveraging the detailed gas-phase measurements made during WE-CAN we assess major OH sinks using the metric of calculated OHR in fresh wildfire emissions, smoke aged > 3 days, smoke-impacted and low/no smoke-impacted urban environments, and the clean free troposphere over the western U.S. during a wildfire season. WE-CAN was designed to measure most known reactive gases and constituted one of the most comprehensive field measurements of trace gases in these environments to date. Using calculated OHR speciation profiles we highlight the most important daytime plume OH initialized oxidation sinks and then examine how much of the field calculated OHR may be missing in current iterations of the GEOS-Chem CTM and MCM. We later use the Taylor Creek Fire as a case study to evaluate the ability of the F0AM model (using MCM chemistry) to simulate changes in plume OHR as smoke ages. These analyses are used to examine the current knowledge of BB VOC representations in models and provide a roadmap for which VOCs should be incorporated into the next generations of chemical transport models for BB applications.

3.3 Methods

3.3.1 WE-CAN aircraft campaign and relevant instruments

The Western Wildfire Experiment for Cloud Chemistry, Aerosol Absorption, and Nitrogen (WE-CAN) field campaign deployed a comprehensive payload of instrumentation aboard the NSF/NCAR C-130 research aircraft to investigate near-field smoke plume chemistry and cloud smoke interactions in the western U.S. from 24 July to 13 September 2018 (https://www.eol.ucar.edu/field_projects/we-can). During the campaign, more than 22 hours of *in situ* BB plume measurements were made across seven states mostly between 14:00 and 19:00 local time when burning conditions were most active. As part of normal operations, the C-130 also sampled various other environments including 1.2 hours of observations of smoke estimated to have aged > 3 days, 4.8 hours of clean free troposphere, and 32 vertical profiles of urban/smoke interaction in Boise, ID (metropolitan area population 750,000). In this work, we use OH reactivity (the inverse of the lifetime of OH) calculated for 160 trace gases measured aboard the C-130 to explore the major daytime OH radical sinks in the western U.S. during a wildfire season.

Table 3.1 summarizes the trace gas measurements used in this work, including methodology, accuracies, sampling intervals, and references. Organic gases were measured by four complementary instruments during WE-CAN: a proton-transfer-reaction time-of-flight mass spectrometer (PTR-ToF-MS), the Advanced Whole Air Sampler (AWAS), the NCAR Trace Organic Gas Analyzer (TOGA), and an iodide adduct chemical-ionization mass spectrometer (I^- CIMS). Here, we utilize 154 measured VOCs following the data selection and data reduction criteria in Permar et al. (2021) with a few exceptions discussed below.

Table 3.1. Summary of instrumentation for 160 trace gas species used in this work.

Species	Instrument	Accuracy	Sample Interval	References
VOCs and OVOCs	PTR-ToF-MS[a]	15 % for directly calibrated species, 50 % for species calibrated based on molecular properties	0.2 or 0.5 s	(Permar et al., 2021)
VOCs	NCAR TOGA[b]	15–50 %.	28–33 s integrated samples every 100–105 s	(Apel et al., 2015, 2010, 2003; Hornbrook et al., 2011)
VOCs	AWAS[c]	10 %	3–7 s canister samples triggered manually	(Andrews et al., 2016; Benedict et al., 2020, 2019; Russo et al., 2010; Zhou et al., 2010)
Formic acid, phenol, HCN, HONO	I⁻ CIMS[d]	30 %	0.5 s	(Lee et al., 2018; Palm et al., 2019; Peng et al., 2020)
CO	QCL[e]	1 ppb (2σ)	1 s	(Lebegue et al., 2016)
CH$_4$	WS-CRD[f]	3 ppb (2σ)	1.3 s	-
NO, NO$_2$, O$_3$	Chemiluminescence Detector	3 %, 4 %, and 2 %		(Ridley et al., 1992; Ridley and Grahek, 1990)
PAN	NCAR-PAN-CIMS	12 % or 25 ppt	2 s	(Slusher et al., 2004; Zheng et al., 2011)

[a]Proton-transfer-reaction time-of-flight mass spectrometer. [b]Trace organic gas analyzer. [c]Advanced whole air sampler. [d]Iodide adduct chemical-ionization mass spectrometer. [e]Quantum cascade laser instrument. [f]Cavity ring down spectrometer.

Permar et al. (2021) found notable disagreement between PTR-ToF-MS, TOGA, and AWAS measurements of five species relevant to the OHR in BB smoke: isoprene, propene, furan, methyl furans, and monoterpenes. To limit the error from potentially interfering fragments while preserving temporal resolution in this work, PTR-ToF-MS isoprene and propene measurements were calibrated using TOGA and AWAS mixing ratios, resulting in near 1:1 agreement during the campaign. Similarly, TOGA furan and methyl furans are used for OHR calculations due to TOGA's lower detection limits and lack of potential interfering isomers. As the PTR-ToF-MS measured furan and methyl furans approximately 1.5 and 15 times higher than TOGA, the OHR of these two species

in this work may represent a lower bound, while use of PTR-ToF-MS data would result in furans being an even larger OH sink. Finally, we note that PTR-ToF-MS measures the sum of monoterpenes at m/z 137.13, which is ~5 times higher than sum of camphene, α-pinene, β-pinene/myrcene, and tricyclene measured by TOGA, likely representing missing speciated isomers (Hatch et al., 2019; Permar et al., 2021). Further details of the measurements used in this work, the corresponding instrument, measurement uncertainty, assumed speciation of PTR-ToF-MS measured ions based on Koss et al. (2018), and OH rate constants are in Table S3.1 and discussed in more detail in Permar et al. (2021).

3.3.2 Data selections and definitions

We focus our analyses on 5 different environments sampled during WE-CAN, including 1) wildfire emissions near the source, 2) aged wildfire smoke with physical age greater than 3 days, 3) smoke-impacted urban atmospheres, 4) low/no smoke urban atmospheres, and 5) free tropospheric clean conditions. Constraints for each of these environments are as follows.

WE-CAN wildfire emission transects are defined as the perpendicular plume transects nearest to a given fire as described in Permar et al. (2021). This results in OHR calculations for 24 unique fires using 31 emission transects and allows for direct comparisons to the emission factors and emission ratios presented therein. Emissions range in physical age from 27–130 minutes downwind from the source due to plane logistical and safety constraints. While those transects represent the freshest smoke sampled during the campaign, there is sufficient time for some photochemical processing to have occurred between emission and sampling (Akagi et al., 2012, 2012; Hobbs et al., 2003; Lindaas et al., 2021c; Peng et al., 2020). Consequently, for very reactive primary emitted species such as monoterpenes, the calculated OHR for WE-CAN emission transects reported here is likely a lower bound. For OVOCs that are both primary emissions and photochemical products, the calculated OHR represents the culmination of production and loss processes between when smoke was emitted and when it was first sampled by the C-130.

For all smoke plumes analyzed in this work, OH reactivity was calculated from the plume center average mixing ratios determined as the top 5 % of CO observations for each transect. This metric was chosen to get a better estimate of the freshest smoke by excluding the more aged plume edges while also remaining consistent with previous WE-CAN literature (Decker et al., 2021b; Palm et al., 2021; Peng et al., 2021). Discrete TOGA or AWAS measurements were often not available during this period. In this case, we calculated the plume average normalized excess mixing ratio (NEMR) from the available measurements for each transect and then scaled NEMRs to the center of the plume by multiplying by the average top 5% CO abundance. Absolute mixing ratios at the plume center were then determined by adding back in regional background concentrations.

For the discussion in Sections 3.4 and 3.5, plume center mixing ratios are not background corrected and therefore discussed in terms of absolute reactivity, allowing for more direct comparison to other environments sampled during the campaign. The average tOHR during plume background periods is 1.7 ± 2.5 s^{-1} or 17 % of the average total plume OHR. When comparing to emission speciation profiles in CTMs and box model results in Sections 3.7 and 3.8, OHR is calculated from plume excess mixing ratios. Here, transect excess mixing ratios were determined by subtracting the interpolated background measured on both edges of the plume. Physical ages for each transect were calculated based on the fire location and average wind speeds measured in the plume upwind of that transect.

To investigate the effects of photochemical aging on OH reactivity, a > 3 days aged smoke profile was calculated according to the plume aging criteria in O'Dell et al. (2020). Briefly, ~1.2 hours of smoke plume measurements were identified and classified as being well-aged based on 2-methylfuran < 0.7 ppt, acrolein < 7.4 ppt, and acrylonitrile > 2.9 ppt. An approximate age of > 3 days was calculated for these plumes based on the predicted loss of these tracers against OH (assuming regional background of 2×10^6

51

molecules cm^{-3}), assuming initial concentrations equal to emission transect observations. The altitudes of the aged smoke samples range from 850 to 5300 m above sea level. Though the calculated smoke age generally agrees well with physical age estimates, this method is sensitive to variability in fire emissions, dilution rates, and oxidant concentrations (O'Dell et al., 2020). Consequently, the aging time is a best estimate and reflects smoke having undergone significantly more photochemical processing than the fresh emissions.

In addition to sampling in wildfire plumes, the C-130 sampled vertical profiles during ascents and descents at the Boise, ID, airport (KBOI) where the campaign was based. During WE-CAN, Boise was often impacted by mixed aged smoke transported 1–3 days from regional fires, resulting in the enhancement of many pollutants over the anthropogenic emissions (Lill et al., 2022). Here, we calculate OHR speciation profiles for the average of 16 smoke-impacted and 16 low/no-smoke ascents/descents following the selection criteria described in Lill et al. (2022). Ascent and descent start and stop times were defined as the period between the C-130 being in contact with the runway and within the boundary layer as identified from temperature gradients. Ascents and descents were defined as smoke-impacted based on mean mixing ratios of hydrogen cyanide (HCN) > 300 ppt and acetonitrile (CH$_3$CN) > 200 ppt. Note that we use the term low/no smoke to describe the ascents/descents that are below this threshold as some smoke influence is expected in these profiles due to a large number of fires in the region during WE-CAN.

Free troposphere measurements were collected while in transit to and from fires. OH reactivities were calculated for non-smoke impacted free troposphere samples, defined as periods with HCN < 250 ppt, CH$_3$CN < 150 ppt, and altitudes > 4000 m asl. The altitude criteria were selected based on the maximum observed boundary layer height as determined by vertical temperature profiles. This results in ~4.8 hours of clean free troposphere data allowing for the impacts of wildfire smoke on regional atmospheric composition to be assessed by comparison. Sampling locations for the aged smoke and

clean free troposphere observations are shown in Figure S3.1 and are generally well distributed across the northwestern U.S.

3.3.3 OH reactivity calculations

Rate constants for the reaction of individual VOCs with the OH radical (k_{OH}) were assigned for PTR-ToF-MS measured masses, with OH rate constants normalized by the fraction of contributing isomers to each ion mass as determined during laboratory burning experiments following Koss et al. (2018). Rate constants for the other measured species were retrieved from the NIST chemical kinetics database (https://kinetics.nist.gov). Standard temperature and pressure (STP) conditions were assumed for all k_{OH} values, while trace gas mixing ratios were converted to molecules cm^{-3} using the field-measured temperature and pressure. OH reactivities for the major OH reactive gases measured during WE-CAN were subsequently calculated following Eq. 3.1, with tOHR defined as the sum of all individual species' OH reactivities during a given measurement period. Similarly, the sum of all VOC OH reactivities is defined as the total calculated VOC OHR (tOHR$_{voc}$). When applicable, OHRs are normalized to the observed CO mixing ratio to account for dilution effects in BB plumes.

Uncertainty in the total calculated OHR for BB has been estimated as 25 % when using PTR-ToF-MS, and is mostly dependent on the speciation of ions and the subsequent assignment of rate constants to each mass (Liang et al., 2022). Specifically, in addition to uncertainties in the measurements and OH rate constants, many of the ion masses measured by PTR-ToF-MS are attributed to one or more potential isomers. Most isomers have similar chemical structures and therefore similar reaction rates with OH. However, if the isomers have very different chemical structures, their k_{OH} may also vary significantly. As a result, uncertainty in the OH reactivity is dependent on the correct weighting of OH rate constants to each ion mass based on the expected fractional contribution of each isomer. As the identification and rate constants for the major contributors to the total OHR are mostly well-defined, the impacts on the total OHR are

small. However, the uncertainty in the calculated OHR for individual species, especially those rarely reported, may be 100 % or more.

3.3.4 BB emissions implemented in GEOS-Chem CTM

To assess how well typical global CTMs represent wildfire emissions, we compare the average VOC OHR speciation profile calculated for WE-CAN emissions with that from the Global Fire Assimilation System version 1.2 (GFAS) inventory as implemented in GEOS-Chem version 13.3.2 (GEOS-Chem + GFAS; Bey et al., 2001; Kaiser et al., 2012). GFAS emissions were retrieved for the 2018 fire season (June – September) over the western U.S. domain (36° N-127° W, 49.5° N-105° W) with updated emission ratios for lumped aldehydes, MEK, formic acid, and acetic acid following Permar et al. (2021). Only those species implemented in GEOS-Chem were included for further comparison, resulting in 18 explicitly implemented VOCs along with three lumped species (21 GEOS-Chem VOC species are listed in Table S3.2 with their emission estimates and k_{OH} values). OHR speciation profiles were calculated from GFAS emissions estimates in GgC by converting to molecules cm^{-3} assuming STP conditions, then dividing each species by the total implemented OHR. k_{OH} values were the same as those used in the observations for consistent comparisons. Additionally, k_{OH} was calculated for the three lumped species by weighting the k_{OH} of corresponding WE-CAN measured species by their emission ratios.

3.3.5 The Framework for 0-D Atmospheric Modeling driven by MCM (F0AM + MCM)

To explore how explicit chemical mechanisms represent BB OHR upon emission and as smoke plumes age, we use the F0AM box model (Wolfe et al., 2016) to simulate the Taylor Creek Fire sampled during WE-CAN. The Taylor Creek Fire was selected as a case study because it has been well described in the WE-CAN literature (Garofalo et al., 2019; Lindaas et al., 2021a; Palm et al., 2021, 2020; Peng et al., 2021, 2020), was well sampled in a pseudo-Lagrangian fashion, and had well-defined plume edges with no or minimal mixing of regional smoke and other anthropogenic emissions.

F0AM was run using the Master Chemical Mechanism (MCM, v3.3.1), augmented with recently developed furans and phenolic chemistry (Coggon et al., 2019; Decker et al., 2019). Initial conditions, observational constraints, and model setup generally followed those described in detail by Peng et al (2021). Briefly, physical parameters such as photolysis frequencies, temperature, and pressure were constrained to measured values at each model step while CO observations were used to derive a plume dilution correction factor. F0AM was initialized using 50 VOCs in addition to NO, NO_2, HONO, O_3, and CO. To facilitate consistent model/observation comparison in this work, minor updates were made to approximately half of the initial VOC concentrations in Peng et al.(2021) to incorporate campaign measured values for species that were unavailable at the time of their study. When using PTR-ToF-MS data to initialize F0AM, individual VOC mixing ratios were estimated using the fractional contribution of known isomers to the total ion signal in BB emissions (Table S3.1) (Koss et al., 2018; Permar et al., 2021). Initialized values are available in Table S3.3. Our model updates do not significantly alter the model results presented by Peng et al. (2021). The simulation of the detailed gas photochemistry then includes 5,832 species in 17,224 reactions. The top 100 species contributing to the total model OHR are retrieved and compared to the field calculated OHR in Section 3.8. These top 100 species comprise > 99 % of the total model OHR.

3.4 Atmospheric OH reactivity in various western U.S. environments

3.4.1 Fresh and aged wildfire smoke

Figure 3.1 shows the total calculated OHR for five different environments sampled during WE-CAN. It includes a total of 160 gas-phase species, representing 86 oxygenated and 68 non-oxygenated VOCs, in addition to NO_2, NO, HONO, O_3, CH_4, and CO. Note that we do not include organic aerosols in our OHR calculations as their reaction rate with OH is uncertain and they are expected to contribute < 5 % to the tOHR (Heald et al., 2020). Similarly, PAN was found to account for < 0.01 % (range $7x10^{-5}$ to $2x10^{-3}$ s^{-1}) of the tOHR in all environments in this work and is consequently not treated separately in our analysis. Despite VOCs comprising less than 1 % of the total emitted mass from a fire (Permar et al., 2021), they collectively represent the largest sink for OH radicals in

WE-CAN sampled emissions, averaging 80 ± 7 % (1σ, representing fire-to-fire variability) of the total calculated OH reactivity. OHR speciation profiles for each of the 24 emission transects in Permar et al. (2021) are shown in Figure S3.2. The VOC proportion to the tOHR in WE-CAN sampled wildfire emissions is in good agreement with laboratory emission measurements (70–90 %) (Gilman et al., 2015) and laboratory-measured VOC emission ratios scaled with field CO observations (88 %) (Decker et al., 2021a). The remaining calculated OH reactivity in western U.S. wildfire emissions is mostly accounted for by NO_x and CO (8.7 ± 2.5 % and 8.2 ± 6.4 % respectively), reflecting their large enhancements in smoke. CH_4 and O_3 play insignificant roles in OHR in fire emissions, though they become more important in other environments after the fresh smoke is chemically aged and diluted into the regional background or other sources.

In emission transects the plume center tOHR ranges from 9–199 s^{-1} (mean 73.6 s^{-1}; Figure S3.2), and plume excess tOHR normalized to CO ranges from 12–41 s^{-1} ppm_{CO}^{-1} (mean 27.5 s^{-1} ppm_{CO}^{-1}). This is at the lower end of laboratory emissions scaled with field observations (98–450 s^{-1}) (Decker et al., 2021a) reflecting higher initial CO mixing ratios during the lab study. Previously reported total mOHR values in urban plumes (10–130 s^{-1}) and forested regions (1–70 s^{-1}) vary greatly between environments (Yang et al., 2016), but are generally similar to or lower than wildfire emissions. This is further illustrated in Figure 3.1 where the tOHR of low/no smoke and smoke-impacted urban emissions in Boise, ID, is 16–25 times lower than in wildfire emissions. As discussed in more detail below, wildfire emissions also consist of many different reactive VOCs and consequently have a markedly different OHR speciation profile than urban and forested regions.

The fraction of VOC OHR in aged smoke is ~26 % lower than in the BB emissions (Figure 3.1). This loss of the fraction of VOC reactivity is mainly driven by the oxidation of many primarily emitted hydrocarbons (HCs) including propene, ethene, monoterpenes, and C_2 substituted furans. The proportion of OVOC OHR remains nearly the same between emissions and aged speciation profiles (~50 %), bolstered in part by the increase in reactivity from formaldehyde and acetic acid. As a result, CO makes up a significantly

larger proportion of the plume OHR, from 7.8 % of the tOHR in wildfire emissions to 32 % in aged smoke, suggesting the increased role of CO in photochemistry in aged smoke.

The amount of missing OHR varies by source and is dependent on the deployed speciated measurements. Using modern analytical instrumentation selected to characterize known gas-phase species, studies have found 25 % missing OHR in the global marine boundary layer (Thames et al., 2020) and 0–30 % missing OHR in urban environments (Hansen et al., 2015; Heald et al., 2020; Mao et al., 2010; Ren et al., 2003; Shirley et al., 2006; Yoshino et al., 2006). Forested environments have a generally larger missing fraction of 0–75 % (Di Carlo et al., 2004; Hunter et al., 2017; Nölscher et al., 2016; Sinha et al., 2010). These studies often have pointed to unmeasured VOCs, particularly OVOCs, as the main contributor to the missing OHR. For BB, Kumar et al. (2018) suggested 40 % missing OHR in the only study to date to report direct OHR field measurements in an agricultural fire-influenced environments, hypothesizing that unmeasured nitrogen-containing VOCs (NVOCs), specifically alkylamines were likely the main contributor to the missing fraction. During WE-CAN, missing 40 % of the OHR in fresh and aged smoke would suggest increases of the average tOHR by 30 s^{-1} and 2 s^{-1} respectively. However, 34 NVOCs including 4 alkylamines, account for only 2 % of the tOHR and 2.5 % of the tOHR$_{voc}$ (Section 3.5) in WE-CAN emissions, suggesting that in western U.S. wildfires NVOCs may not be a major contributor to the tOHR. This could point to much greater NVOC emission from agricultural BB because of the higher nitrogen content in crop biomass (Kumar et al., 2018). However, due to the high uncertainty in PTR-ToF-MS NVOC measurements more detailed speciation and better quantification of NVOCs in BB is needed to fully understand their role as an OH sink.
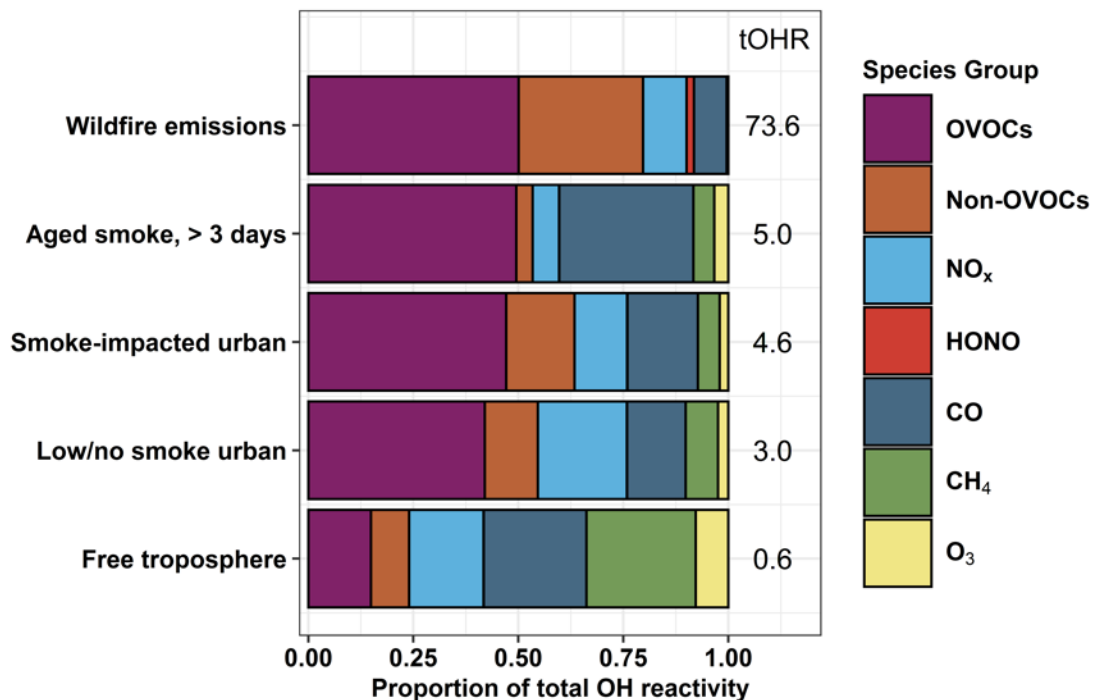
Figure 3.1: The percent contribution of major reactive gas species/groups to the total calculated OH reactivity for wildfire emissions (31 transects of 24 fires), aged smoke with chemical age > 3 days (1.2 hours of samples), atmospheric boundary layer in Boise, ID, separated by smoke-impacted and low/no smoke conditions (32 takeoff/landing profiles), and clean free tropospheric conditions (4.8 hours of data) sampled by the C-130 during WE-CAN. Average calculated OH reactivities (s^{-1}) are shown for each sampling condition to the right of the bars. Note that the low/no smoke profile still likely contains small smoke impacts due to regional fires.

3.4.2 Clean free troposphere

Figure 3.1 also includes OHR speciation profiles for ~4.8 hours of free troposphere clean samples, and 16 smoke-impacted and 16 low/no smoke ascents and descents at the Boise, ID, airport made during WE-CAN. In the clean free troposphere, CH_4 and relatively long-lived species like CO and O_3 account for 53 % of the tOHR during WE-CAN (collectively 0.37 s^{-1}, Figure 3.1), consistent with current knowledge of tropospheric chemistry in clean environments. We find that VOCs are also a significant contributor to the tOHR accounting for nearly one third of the OH sink (31 %, 0.22 s^{-1}). In comparison, CO accounts for less of the tOHR during WE-CAN (25 %) than at similar altitudes over the Pacific Ocean off the North American coast during the INTEX-B aircraft campaign

(60 %) (Mao et al., 2009) and over the continental U.S. during the DC3 (30-40 %) campaign (Brune et al., 2018). Conversely, VOCs and CH_4 makes up a higher proportion of the free troposphere tOHR during WE-CAN (VOCs: 31 %, CH_4: 25 %) than during both INTEX-B (VOCs: 20 %, CH_4: 10 %) (Mao et al., 2009) and DC3 (VOCs: 17 %, CH_4: 10) (Brune et al., 2018) The fractional difference between these studies can likely be contributed to the additional 121 VOCs measured during WE-CAN, as well as a general increase in background OVOCs, CO, and CH_4 from regional wildfires during the 2018 summer. Additionally, the average calculated free troposphere tOHR during WE-CAN of 0.7 s^{-1} (0.4–0.9, 5th and 95th percentiles) is ~2.5× lower than the mOHR (~1.7 s^{-1}) at similar altitudes during INTEX-B (Mao et al., 2009), but approximately the same as the mOHR in the free troposphere during the ATom-1 (~0.4–0.9 s^{-1}) (Thames et al., 2020; Travis et al., 2020) and DC3 (< 1 s^{-1}) (Brune et al., 2018) aircraft campaigns. However, the free troposphere OHR calculated during WE-CAN is likely a lower bound due to missing measurements, with additional variance likely due to differences in seasonality and latitude between studies. For example, methyl hydroperoxide was suggested to account for 17 % of the calculated OHR above the Pacific Ocean during ATom-1 (Travis et al., 2020) and is elevated over North America and in aged BB smoke (Snow et al., 2007).

3.4.3 Urban atmosphere

Boise, ID is a midsize city located in a metropolitan area of ~750 thousand people and is commonly impacted by smoke during the summer fire season (McClure and Jaffe, 2018; O'Dell et al., 2020). Vertical profiles of the atmospheric boundary layer collected during takeoff and landing at the Boise airport allow for the impacts of smoke mixing with anthropogenic emissions to be explored. During WE-CAN, BB smoke increased the average tOHR in Boise by 1.6 s^{-1}, or 53 % enhancement relative to the typical low/no smoke urban background of 3.0 s^{-1}. This increase in reactivity is largely driven by the increase in BB VOCs and CO, which make up approximately 9 % and 3 % more of the tOHR during smoke-impacted days relative to low/no smoke days.

BB has little impact on the NO_x OHR in Boise, with smoke-impacted profiles having slightly lower NO_x OHR than low/no smoke ones (0.58 s^{-1} vs. 0.64 s^{-1}). As a result, the low/no smoke urban atmosphere has a higher fraction of NO_x OHR than during smoke-impacted days (21 % vs. 13 %). This is consistent with our general understanding of aged smoke, where NO_x is rapidly depleted due to fast reactions with OH and other primary VOCs (i.e., furans or phenolic compounds) or converted to PAN during transport (Jaffe and Wigder, 2012; Xu et al., 2021).

3.5 OH reactivity of VOCs

Here, we use the detailed speciated VOC measurements available during WE-CAN to investigate the contribution of individual VOC species to the OHR speciation profiles discussed above. Our previous work using this dataset found that, in western U.S. wildfires, the 20 most abundantly emitted species account for ~70 % of the total VOC emissions by mass, and ~81 % on a molar basis (Permar et al., 2021). However, in this study, we find that they account for only 51 % of the $tOHR_{voc}$.

The plume center $tOHR_{voc}$ for western U.S. wildfire emissions averaged 58 s^{-1} during WE-CAN, with a range of 7–170 s^{-1}, largely representing different extents of dilution between sampled smoke plumes. Total VOC OHR normalized to CO was found to average 23.5 s^{-1} ppm$_{CO}^{-1}$ (range 8.6–31.8 s^{-1} ppm$_{CO}$ $^{-1}$), which is lower than observed in previous laboratory studies of biomass burning emissions (61 ± 10 s^{-1} ppm$_{CO}^{-1}$) (Gilman et al., 2015). Since laboratory studies sample BB smoke only a few seconds after emission while WE-CAN emission transects are 27-130 minutes downwind from each fire, this may represent a loss of the most reactive primary VOCs between emission and sampling by the C-130 as well as differences between laboratory and field burning conditions (typically drier fuels, higher combustion efficiency, and simpler fuel mixtures in the lab) (Permar et al., 2021). The $tOHR_{voc}$ during WE-CAN then is likely a lower bound due to rapid oxidation of short-lived species such as monoterpenes, isoprene, and many furan containing compounds. Consequently, these species may make up a larger

proportion of the tOHR in emissions sampled nearer to the source, while the contribution of photochemically produced OVOCs may be reduced.
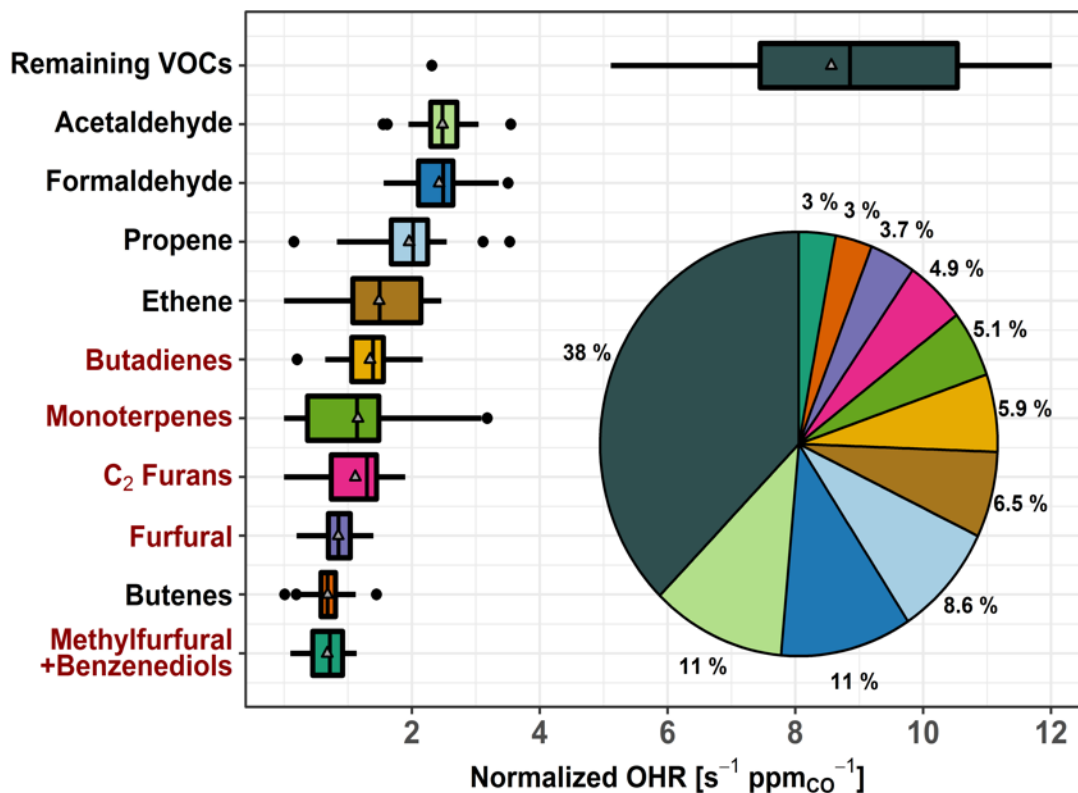
Figure 3.2: Box and whisker plots of the 10 largest contributors to the total calculated VOC OHR of western U.S. wildfire emissions during WE-CAN. The OHR is normalized to CO to account for BB plume dilution effects. The inset pie chart shows the fraction of plotted species contribution to the total VOC OHR. The remaining VOCs include 143 species not explicitly shown. Pie chart colors correspond to the box plots. Red VOC names correspond to those BB emissions not implemented in the standard GEOS-Chem CTM. Boxes represent the 25th and 75th percentiles, vertical lines as median, whiskers as 1.5× the interquartile range, points as > 1.5× interquartile range, and triangles as mean. Butadienes include 1,3- and 1,2-butadiene isomers. Monoterpenes are the sum of all ionizable isomers (α-pinene, β-pinene, camphene, etc.). C2 furans include 2,5-dimethylfuran, 2-ethylfuran, and other unidentified C2 substituted furan isomers. Furfurals include 2- and 3-furfural. Methylfurfural and benzenediol isomers are expected to each make up ~50 % of the mass (Table S3.1).

Figure 3.2 shows the normalized OHR (s^{-1} ppm_{CO}^{-1}) of the top 10 trace organic gas contributors to the calculated $tOHR_{voc}$ in western U.S. wildfire emissions (CO abundance for the fire emissions is 2.6 ± 1.7 ppm during WE-CAN). These 10 VOCs account for 62 % of the $tOHR_{voc}$, while 143 species comprise the remaining 38 %. Three VOCs (acetaldehyde, formaldehyde, and propene) each have similar or slightly larger normalized OHR as NO_x, collectively accounting for ~25 % of the total calculated trace gas OHR (Section 3.4), and 30 % of the $tOHR_{voc}$. Importantly, the $tOHR_{voc}$ of the remaining 143 species/groups not explicitly shown in Figure 3.2 is larger than any individual contributor, further emphasizing the complexity of wildfire emissions and the challenge of implementing all observed OHR in atmospheric models.

Figure 3.3 shows the proportion of individual and grouped VOCs to the $tOHR_{voc}$. Furan-containing species, alkenes, and aldehydes each make up ~20 % of the plume $tOHR_{voc}$ upon emission, similar to the VOC OHR profile found by Xu et al. (2021) during the Fire Influence on Regional to Global Environments and Air Quality (FIREX-AQ) aircraft campaign. Furans, representing 19 species in this work, are important OH sinks in fresh laboratory biomass burning emissions (Gilman et al., 2015; Hatch et al., 2017; Koss et al., 2018), contributing up to 10 % of O_3 production in the first four hours since emission (Coggon et al., 2019). Alkene OHR is largely from propene and ethene (15 % of the $tOHR_{voc}$), while aldehyde OHR is from formaldehyde and acetaldehyde (21 %), which are in turn the two largest individual contributors to the plume $tOHR_{voc}$. Figure 3.3 also shows that reactivity in wildfire emissions is relatively uniformly spread amongst the major contributing groups. This contrasts with more well-studied VOC sources such as biogenic emissions where isoprene, monoterpenes, and isoprene oxidation products such as MVK and MACR are the primary contributors to the tOHR (Millet et al., 2018; Sanchez et al., 2021; Sinha et al., 2010). Similarly, urban tOHR is primarily comprised of ~50 % NO_x and CO (Figure 3.1), while aromatic and other hydrocarbons make up most of the urban VOC OHR fractions.
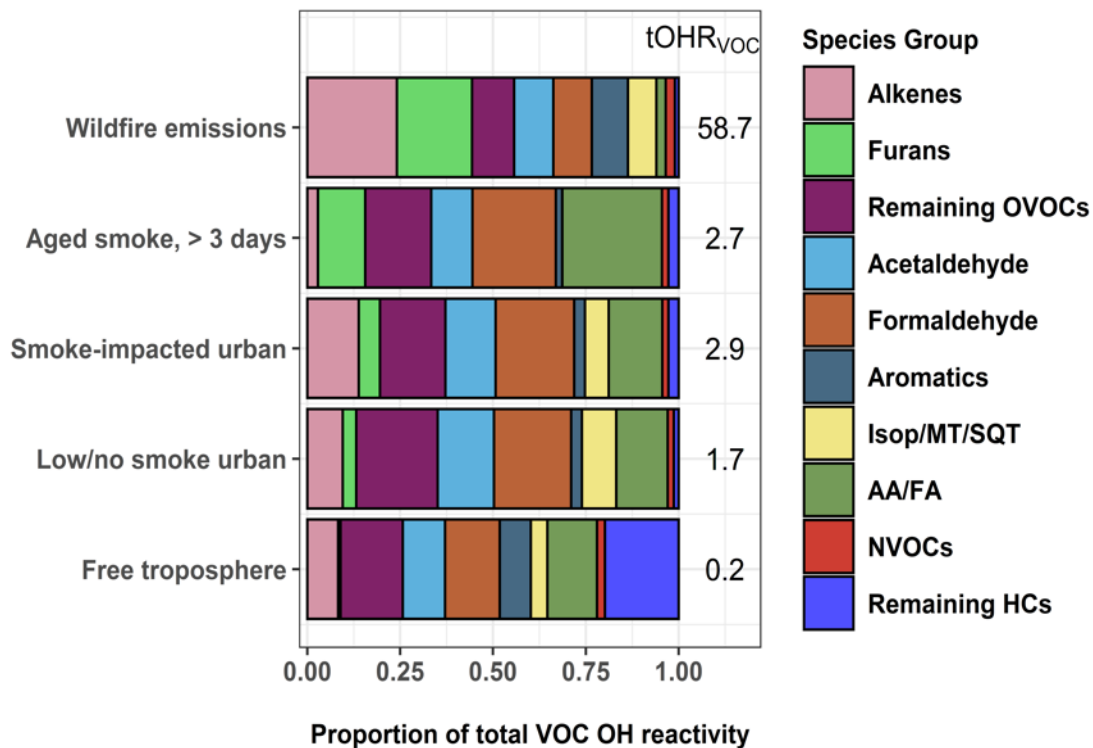
Figure 3.3: The percent contribution of individual and VOC groups to the total calculated VOC OHR during WE-CAN. WE-CAN wildfire emission average, smoke-impacted urban, low/no smoke urban, and clean free troposphere periods are the same as described in Figure 3.1. The Isop/MT/SQT grouping includes isoprene, monoterpenes, and sesquiterpenes. AA/FA are acetic and formic acids.

As smoke plumes age and directly emitted non-methane hydrocarbons are oxidized, OVOCs become an even more dominant OH sink in aged smoke (Figure 3.1). In smoke sampled during WE-CAN that had aged > 3 days, formaldehyde (23 %), acetic acid (measured with glycolaldehyde; 21 %), and acetaldehyde (11 %) are the largest individual contributors to the $tOHR_{voc}$, reflecting their growing importance as an OH sink as smoke is transported downwind and primary VOCs are oxidized. Additionally, formic and acetic acids collectively make up a quarter of the aged smoke $tOHR_{voc}$, emphasizing the importance of BB as a source of organic acids and the need to better understand the chemistry leading to their formation and loss. The remaining OVOC fraction in Figure 3.3 consists of 36 species contributing 18 % of the plume $tOHR_{voc}$, with the top 3 VOCs being methylmethacrylate, methanol, and hydroxyacetone (~13 % of the $tOHR_{voc}$).

Interestingly, furans still account for 13 % of the aged smoke tOHR$_{voc}$ (Figure 3.3), despite their generally short atmospheric lifetime. A closer examination of the aged smoke profile shows that 97 % of the furans OHR is accounted for by five species/groups: 5-hydroxy-2-furfural/2-furoic acid ($C_5H_4O_3$), succinic anhydride ($C_4H_4O_3$), furanone ($C_4H_4O_2$), 5-(hydroxymethyl)-2-furfural ($C_6H_6O_3$), and maleic anhydride ($C_4H_2O_3$). Maleic and succinic anhydride are long-lived species (> 5 days assuming OH concentrations of 1.5×10^6 molecules cm^{-3}) and are known oxidation products of furans and oxygenated aromatics (Coggon et al., 2019; Jiang et al., 2020). Measurement of these anhydrides in the aged plumes sampled during WE-CAN further confirms their relevance as tracers for aged biomass burning plumes as proposed by Coggon et al. (2019). The remaining three species are generally not well described in the BB literature. We speculate they are likely all photochemically produced from the oxidation of furans though we do not know their exact precursors and chemical pathways. Additionally, speciation of the PTR-ToF-MS measured $C_5H_4O_3$, $C_4H_4O_3$, $C_4H_4O_2$, $C_6H_6O_3$, and $C_4H_2O_3$ was based on laboratory BB emissions, meaning that there may be additional isomers and interfering fragments in aged smoke. However, the contribution of these species to the aged plume OH reactivity suggests that furans and their oxidation products could play a sizable role in plume chemistry even far downwind of fires, highlighting the need for further investigations to improve our ability to measure and understand their chemical transformations.

The tOHR$_{voc}$ in Boise during the aircraft takeoffs/landings was 50 % higher (1.6 s^{-1} to 2.9 s^{-1}) on smoke-impacted days. On these days, the fraction of alkenes and furans were both elevated relative to the urban background, in agreement with our knowledge of BB emissions. Biogenic species including monoterpenes and isoprene make up a larger proportion of the OHR on low/no smoke days due to local and regional biogenic emissions, though they are only a small fraction of the tOHR$_{voc}$ in Boise (10 %). Additionally, on low/no smoke days, formaldehyde and organic acids are significant

contributors to the tOHR$_{voc}$, suggesting that even during minimal BB impacted periods they play an important role in the local chemistry.

Clean free tropospheric VOC OHR during the study period is largely dominated by OVOCs, including formaldehyde (13 %), acetaldehyde (11 %), acetic acid/glycolaldehyde (10 %), methanol (6 %), MVK/MACR/2-butenal (2 %), and acetone/propanal (2 %), in good agreement with previous studies of the free tropospheric OH budget (Chen et al., 2019; Travis et al., 2020). Longer lived alkanes make up most of the remaining hydrocarbons ("Remaining HCs" in Figure 3.3), and consequently account for 20 % of the tOHR$_{voc}$ in the free troposphere. Methylhexanes, methylheptanes, and propane are the top 3 contributors (50 %) of the remaining HCs fraction.

3.6 Implications for urban O$_3$ chemistry

BB has generally been shown to increase O$_3$ production in urban environments, though decreased production may occur under significantly smoky conditions (Jaffe and Wigder, 2012; McClure and Jaffe, 2018; McKeen et al., 2002). One way to predict how smoke will impact O$_3$ production is by investigating the O$_3$ production regime of an air mass. Kirchner et al. (2001) proposed the metric $\theta = tOHR_{NOx}/tOHR_{VOC}$, where t$OHR_{NOx}$ and $tOHR_{VOC}$ are the total NO$_x$ and VOC OH reactivity, to define the O$_3$ production regime. When θ is > 0.2, O$_3$ production is classified as VOC-limited (or NO$_x$ saturated), θ < 0.01 indicates a NO$_x$-limited regime, and θ between 0.01 and 0.2 indicates transitional conditions. Using this metric, Liang et al. (2022) showed that smoke altered the ozone formation regime in Berkeley, CA and that O$_3$ production was higher during BB-influenced periods as BB VOCs lowered θ below the 0.2 threshold.

For the Boise vertical profiles presented here, the influx of BB smoke causes the O$_3$ production regime to shift from being VOC-limited during low/no smoke periods (θ = 0.39) toward a more optimal O$_3$ production regime (θ = 0.20) on smoke-impacted days. This is due to BB smoke adding VOCs and CO to the urban atmosphere, but little

additional NO_x due to its rapid removal in BB plumes and relatively consistent urban emissions. This impact on O_3 production is corroborated by the measured O_3 mixing ratio averaging 50 ppb on low/no smoke days and 63 ppb on smoke-impacted days. Recent box modeling work suggests that such urban O_3 production on smoky days is largely driven by local photochemistry (Ninneman and Jaffe, 2021).

Wildfire emissions during WE-CAN are typically in the optimal O_3 production regime with θ equal to 0.15, while θ in smoke aged > 3 days was 0.12. Consequently, fresh and aged wildfire smoke is generally in a more optimal O_3 production regime and becomes more NO_x-limited with aging and diluting, in agreement with recent studies of BB plume O_3 formation (Robinson et al., 2021; Xu et al., 2021). Incidentally, this analysis suggests that the impact of BB smoke on urban O_3 production is in part dependent on the smoke's age. For example, very fresh fire emissions would greatly increase the VOC OHR due to reactive primary species while simultaneously enhancing NO_x, whereas more aged smoke adds less VOC OHR but also little to no NO_x. As urban environments are traditionally VOC-limited, the influx of BB smoke will likely enhance ozone production in urban centers which would otherwise typically stay VOC-limited. However, the real-world impacts of BB smoke on urban O_3 production could be further complicated due to factors such as smoke-altered photolysis rates (Buysse et al., 2019; Selimovic et al., 2020), temperature, and conversion of PAN back to NO_x (*i.e.*, PAN mixing ratios increased from 350 ppt on low/no smoke days to 600 ppt on smoke impacted days in Boise during WE-CAN).

3.7 Biomass burning emissions as implemented in the GEOS-Chem CTM
In this section, we probe if any significant initial OH reactivity from BB is missing in current CTM VOC representations to help guide future model development for both modeled and unrepresented VOCs in BB-influenced environments. To this end, we compare the average VOC OHR speciation profiles calculated from WE-CAN wildfire emissions with GFAS emission estimates. We focus on the 21 individual and lumped VOCs included in BB emissions in GEOS-Chem, referred to here as "implemented

VOCs". Using other BB emission inventories including GFED (Global Fire Emissions Database), FINN (FIre INventory from NCAR), and QFED (Quick Fire Emissions Dataset) does not change the conclusions of this work due to emission ratios being mostly between the inventories. Note that by using OHR speciation profiles we are not comparing the absolute OHR, which would require further constraints on the BB emission amount. Rather, we assess whether the fractional distribution of OHR agrees between WE-CAN and GEOS-Chem + GFAS emissions and if the 21 implemented species constitute a majority of the field calculated tOHR upon emission.

Figure 3.4a shows the OHR profile calculated from GEOS-Chem + GFAS emissions. Lumped alkenes are the largest contributor to the calculated OHR (30 %), followed by formaldehyde (21 %), ethene, (17 %), and acetaldehyde (13 %). Cumulatively, these 4 species make up 81 % of the GEOS-Chem + GFAS OHR. Figure 3.4b shows the average WE-CAN emission OHR profile filtered to only include implemented/modeled VOCs. We find that field measurements for 17 of the 21 implemented species agree within 3σ of the GEOS-Chem + GFAS OHR proportions, where σ represents the WE-CAN fire-to-fire variability of each VOC's proportion to the tOHR$_{voc}$. These 17 species accounts for 93 % of the implemented tOHR$_{voc}$ and indicate that the implemented GFAS species capture the OHR profile observed in wildfire emissions well, in part representing good relative agreement between emission factors (EFs). As mentioned previously, we do not attempt to compare absolute OHR between WE-CAN and GEOS-Chem + GFAS emissions. However, the similar OHR speciation profiles shown here suggest that agreement between the absolute OHR of these 21 implemented species is likely to be most dependent on the amount of dry mass burned rather than EFs. A more detailed analysis of the total BB emission is needed to better quantify how well emission inventories represent absolute wildfire OHR.

Three of the four species that do not agree in the observed fire-to-fire variability have higher OHR fractions in the observations than in GFAS likely due to the mismatch of measured isomers and model VOC speciation. These include xylenes, MACR, and MEK

67

which are implemented separately in GEOS-Chem (Figure 3.4a) but are measured as the sum of C_8 aromatics, MACR/MVK/2-butenal, and MEK/butanal/2-methylpropanal during WE-CAN (Figure 3.4b). Conversely, the OHR fraction of methanol is lower in the field observations (1.4 %) than in GFAS (2.8 %).

Although the GEOS-Chem + GFAS OHR profile agrees well with the WE-CAN constraints, Figure 3.4c shows that the 21 implemented species account for only ~50 % of the $tOHR_{voc}$ in western U.S. wildfire emissions. OHR in the non-implemented VOCs is spread across 104 species, with the largest individual contributors being butadienes (12 % of the non-implemented fraction), monoterpenes (10 %; note that GEOS-Chem does include monoterpene chemistry but only simulates their biogenic emissions), C_2 substituted furans (10 %), furfural (7 %), and methylfurfurals (6 %). These species make up 21% of the average $tOHR_{voc}$ and are the only ones among the top 10 most reactive VOCs in wildfire emissions (Figure 3.2) not currently represented in GEOS-Chem.

Grouping the non-implemented fraction discussed above by the same criteria as in Figure 3.2 finds that furans comprise 41 % of the non-implemented fraction in Figure 3.4c, followed by aromatics (18 %), other OVOCs (12 %), butadienes (12 %), and monoterpenes (10 %; Figure S3.3). The lack of reactive primary BB VOCs would constitute a missing OH sink in smoke-impacted environments, which is consistent with independent studies suggesting the global model OH is generally too high (Mao et al., 2009; Murray et al., 2021). Consequently, implementing butadienes, BB monoterpenes, and speciated or lumped furans is likely to improve model performance, particularly in BB-impacted environments and when the proper model resolution is used.

68
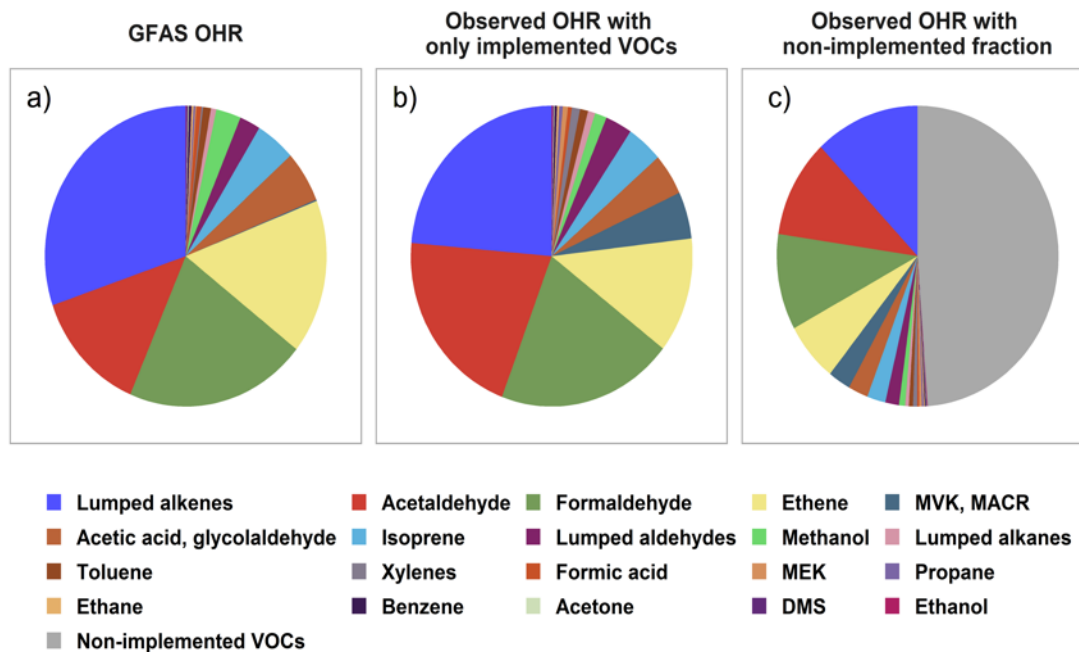
Figure 3.4. a) The calculated OHR profile of the 21 GEOS-Chem + GFAS species implemented as biomass burning emissions, estimated as the total regional GFAS emissions during the WE-CAN campaign. b) The WE-CAN-measured OHR profile for wildfire emissions calculated using only the implemented species in panel a. c) OHR profile calculated from all VOCs measured during WE-CAN. Colored slices correspond to the implemented VOCs in panels a and b, representing that the 21 implemented species account for 50 % of the total VOC OHR in wildfires, while the gray slice is OHR from non-implemented species. The composition of the non-implemented fraction (gray slice) is shown in Figure S3.3. Note that acetic acid and glycolaldehyde emissions in GFAS are summed for better comparison to the field PTR-ToF-MS measurements.

3.8 Field OH reactivity observations vs F0AM + MCM, a case study

To assess how well our current knowledge of smoke plume chemistry agrees with field observations, we compare the field-calculated OHR (OHR_{field}) to the OHR predicted by the F0AM + MCM (OHR_{mod}) for a pseudo-lagrangian sampled wildfire plume. Unlike CTMs, box models such as the F0AM are less computationally limited and therefore can represent the chemistry of thousands of gases at a time. We use the Taylor Creek Fire (flight track shown in Figure 3.5) sampled during WE-CAN as a case study to investigate: 1) to what extent the modeled initial OHR accounts for the observed OHR in

wildfire emissions, 2) how well the model captures the observed change in tOHR$_{voc}$ as plumes age, and 3) if any significant OHR is contributed by secondary species predicted by the model but missing from the field measurements.

Figure 3.5 shows the calculated (shaded regions) and modeled (dashed lines) OH reactivity normalized to CO for the Taylor Creek Fire. The combined green, blue, and purple shading shows the field calculated OHR for acetaldehyde, formaldehyde, and the sum of VOCs that are both measured in the field and present in the top 100 contributors to the OHR$_{mod}$ (implemented VOCs). The red shaded region then represents the combined OHR of species measured in the field but not present in the OHR$_{mod}$ (non-implemented VOCs). Green, blue, and purple dashed lines represent the model OHR for the corresponding VOCs. Similarly, the red dashed line indicates VOCs present in the OHR$_{mod}$ but not measured in the field (non-measured VOC).

F0AM + MCM generally reproduces the OHR of formaldehyde and acetaldehyde well as the plume ages, with their OHR$_{field}$ and OHR$_{mod}$ agreeing within 2 % and 6 %, respectively, at initialization and 38 % and 30 % after 2.5 hours of plume aging (Figure 3.5). As the model and field k_{OH} values for these two species are the same, this indicates that the model is simulating their mixing ratios correctly, though maybe under-estimating formaldehyde after 1 hour of aging, in good agreement with previous studies (Peng et al., 2020; Wolfe et al., 2022). Additionally, the field calculated OHR for the two aldehydes can be seen to stay nearly constant with plume age. For formaldehyde, a similar steady state was also observed in some FIREX-AQ sampled plumes, where the plume-to-plume variability was found to be dependent on OH concentrations, with OH-initialized VOC oxidation and photolysis being the main (nearly equal) production and loss pathways (Liao et al., 2021; Wolfe et al., 2022). Conversely, acetaldehyde loss is primarily from reaction with OH radicals (Wolfe et al., 2022). Given that acetaldehyde's atmospheric lifetime against OH is ~1 day, minimal loss is expected within ~2.5 hours of plume aging (Millet et al., 2010), thus its near constant OHR in Figure 3.5 suggests that it is likely from direct emissions. Due to formaldehyde and acetaldehyde being products of many

different VOC oxidation pathways, their accurate representation in the model suggests that much of the overall VOC oxidation chemistry is being simulated correctly.

Upon initialization, the OHR_{mod} is expected to be equal to the OHR_{field} if all measured species were initialized in the model and k_{OH} values agree between the MCM and weighted rate constants used to calculate the field OHR. Because F0AM is initialized with only 50 of the 154 VOCs used to calculate the OHR_{field}, excess OHR_{field} at model initialization represents OH reactivity from species unimplemented in the model and thus constitutes a missing OH sink in the model. Figure 3.5 shows that upon initialization the MCM contains 88 % of the total field measured VOC OHR, indicating that the MCM is not missing a significant fraction of the initial OHR_{field} and that most of the known VOC OH sinks are included in the model. This is in good agreement with similar analysis done using FIREX-AQ laboratory measurements that found the MCM captures 75 % of the $tOHR_{voc}$ (Coggon et al., 2019). The slightly higher percentage during WE-CAN is likely explained by the model being initialized by a few additional VOCs during WE-CAN, instrument uncertainty, and potential loss of some reactive species before the C-130 first intercepted the plume. Additionally, when comparing only implemented species, the OHR_{mod} accounts for 95 % of OHR_{field} (purple shading vs. the purple dashed line), which is well within the uncertainty of the field calculated OHR ($\pm$ 25 %) and suggests the speciation of PTR-ToF-MS ions and subsequently weighting of k_{OH} values is valid.

Figure 3.5 demonstrates that as BB plumes age, oxidation of primary VOCs results in a net decrease in normalized plume OHR, indicative of the oxidation products being generally less reactive towards OH. Good agreement ($\pm$ 20 %) between the decay rate of the field calculated and modeled $tOHR_{voc}$ then suggests that the MCM is accurately representing the bulk of VOC OH oxidation chemistry. Additionally, in the aged plume transects OHR from non-implemented VOCs is seen to decrease slightly (red shading), again pointing to the model capturing most of the OHR_{field}.
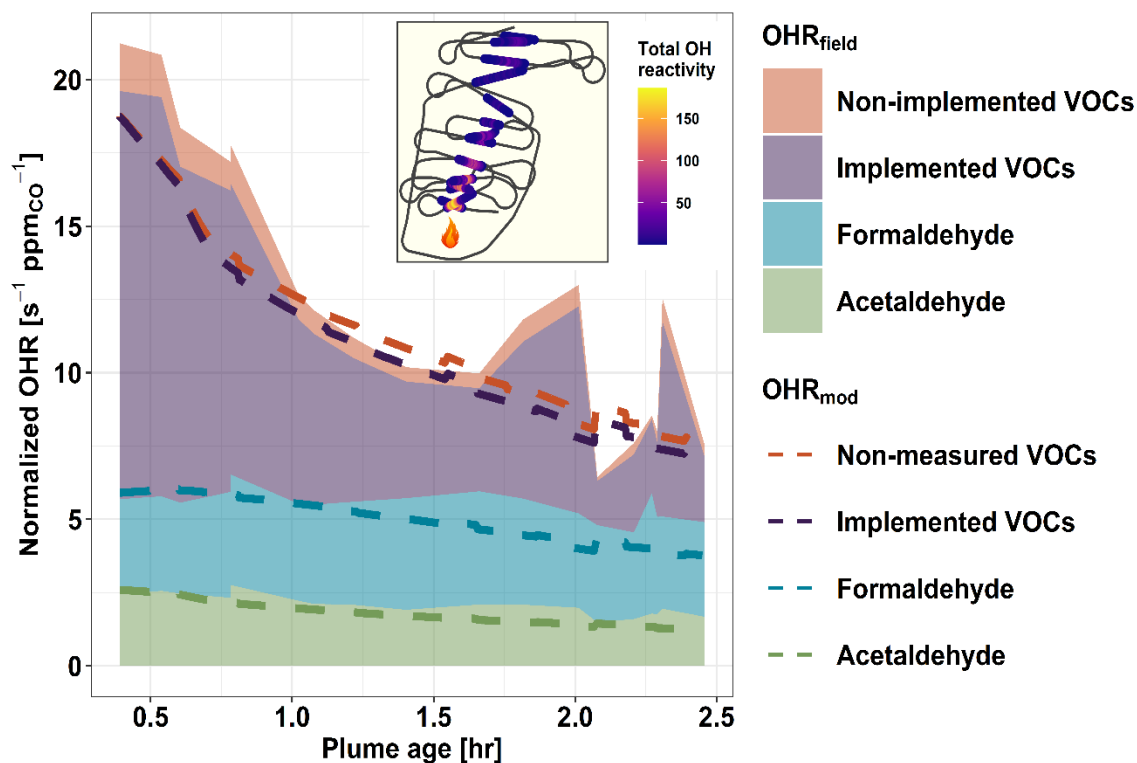
Figure 3.5: Field and modeled normalized OHR (s^{-1} ppm_{CO}^{-1}) for the Taylor Creek Fire sampled during WE-CAN with the inset plot showing the corresponding flight track shaded by the total OHR for each plume transect. Shaded regions represent the total calculated OHR from observations, while dashed lines are the model predicted OHR. Formaldehyde and acetaldehyde are shown separately as they are two of the largest contributors to the VOC OHR and important model diagnostics. The purple shading and dashed line represent VOC measured in the field which are also included in the model. The red shading and dashed line is the combination of measured but not modeled plus modeled but not measured VOCs and show their combined impact is relatively insignificant.

The MCM contains thousands of oxidation products and intermediate species which are formed during the simulation but were not quantified in the field. Deviation of the dashed purple and red lines in Figure 3.5 thus represents OHR from secondary VOCs predicted by the MCM but not measured in the field. As the plume ages, this proportion (difference between purple and red dashed lines) increases slightly from 0.5 % at t_0 to 7.4 % at 2.5 hours of aging. This implies that the non-measured modeled OHR is primarily due to oxidation products rather than missing measurements of primary VOC emissions and that the MCM does not generate a significant OH sink of non-measured oxidation products in

72

the plume aging times sampled during WE-CAN. An important implication is that the species used to initialize the model determines the total OH sink for at least the first few hours of plume aging. However, because this may not be sufficient time for the model to generate a sizeable unmeasured pool of OH reactive species, we are unable to extend this analysis to predict whether the WE-CAN payload is missing a reservoir of OH reactive species further downwind. Rather, this analysis shows that the MCM contains chemistry for most of the field-measured OHR, while future studies comparing field-calculated and direct OHR measurements are needed to better understand if there is still significant unmeasured OHR in wildfire smoke.

3.9 Conclusions

OH reactivity was calculated using 154 VOCs, in addition to NO_2, NO, HONO, O_3, CH_4, and CO measured during the WE-CAN aircraft campaign and assessed in different environments including western U.S. wildfire emissions, smoke aged > 3 days, smoke-impacted and low/no smoke urban atmospheres, and the clean free troposphere. Plume center tOHR for wildfire emissions ranges from 9–198 s^{-1} (12–41 s^{-1} ppm_{CO}^{-1}), with VOCs accounting for 80 ± 7 % of the tOHR. In contrast to more well-studied VOC emission sources, VOC OHR is relatively well spread across many species and groups, with furans, alkenes, and aldehydes each accounting for ~20 % of the $tOHR_{voc}$.

In smoke aged > 3 days, primarily emitted hydrocarbons were found to make up 26 % less of the tOHR due to the oxidation of reactive primary emitted species. OVOC and CO become the dominant OH sinks in aged smoke, accounting for 50 % and 32 % of the tOHR, respectively. Formaldehyde (23 % of the $tOHR_{voc}$), acetic acid (21 %), and acetaldehyde (11%) are the largest individual contributors to the aged smoke $tOHR_{voc}$. Notably, furan oxidation products were also found to account for 13 % of the aged smoke $tOHR_{voc}$, suggesting that furans and their oxidation products play an important role in plume chemistry far downwind of fires. However, the lack of detailed speciation of PTR-ToF-MS data in aged smoke makes it difficult to fully characterize these species,

highlighting the need for further investigations of furan oxidation products to improve analytical skills and understanding of their chemistry.

The average calculated clean free troposphere OHR during WE-CAN is 0.7 s^{-1}, with the relatively long-lived species CH$_4$, CO, and O$_3$ accounting for 53 % of tOHR. VOCs, mainly formaldehyde, acetaldehyde, acetic acid, and methanol, make up an additional 31 % of the tOHR.

Vertical profiles collected during take-off and landing at the Boise, ID, airport allowed for the impacts of smoke on anthropogenic emissions to be explored. During smoke impacted periods, the average tOHR in Boise increases by 53 % relative to the typical low/no smoke urban background (from 3.0 s^{-1} to 4.6 s^{-1}), mainly due to the increase in BB VOCs and CO. NO$_x$ OHR remains similar between profiles, consistent with our general understanding of aged BB smoke being NO$_x$ depleted and VOC rich. Consequently, the influx of BB smoke shifts the urban O$_3$ production regime from being VOC-limited during low/no smoke periods to a more optimal O$_3$ production regime on smoke-impacted days.

We use our field results to evaluate how well current iterations of the GEOS-Chem CTM and MCM represent the field-calculated OHR for wildfire emissions. The fractional OHR distribution of 17 of the 21 implemented explicit and lumped VOCs in GEOS-Chem were found to agree well with wildfire emissions measured during WE-CAN, indicating good agreement between the field and inventory emission factors. However, methanol, xylenes, MACR, and MEK distributions did not agree within 3σ likely due to the latter three being implemented separately in GEOS-Chem but measured with their isomers by PTR-ToF-MS. Additionally, the 21 implemented species were found to account for only 50 % of the measured tOHR$_{voc}$, indicating that even if the model BB emission estimates are correct, they will miss half of the emitted VOC OHR. As the lack of reactive primary BB VOCs would constitute a missing OH sink in smoke-impacted environments,

74

implementation of furan-containing species, butadienes, and monoterpenes (collectively accounting for 62 % of the non-implemented VOC OHR) into GEOS-Chem for BB would likely improve model performance.

Using a pseudo-lagrangian sampled smoke plume as a case study, we find that the F0AM + MCM initiated with 50 field measured VOCs, accounts for ~90 % of the $tOHR_{voc}$, suggesting that the MCM is not missing a significant fraction of the $tOHR_{voc}$ in BB emissions and that most of the known VOC OH sinks are included in the model. Additionally, the F0AM + MCM model was able to simulate the observed decay of the normalized plume $tOHR_{voc}$ generally within ± 20 %, suggesting that the MCM is accurately representing the bulk VOC OH oxidation chemistry.

Our analysis highlights the most important VOC species for daytime BB plume oxidation and assesses how well the current standard GEOS-Chem CTM and MCM capture the observed OHR of wildfire emissions. The results presented here provide a roadmap for which individual VOCs and groups should be prioritized in next-generation air quality models to better predict the downwind air quality and subsequent public health impacts of BB smoke.

4 Formic acid and acetic acid in western U.S. wildfire smoke

4.1 Abstract

Formic acid and acetic acid are the two of the most abundant organic acids in the atmosphere. However, models typically underestimate their enhancement relative to observations likely due to missing secondary sources. In this work we use detailed gas phase measurements of formic and acetic acid made during the WE-CAN field campaign to investigate their emissions and chemistry in western U.S. wildfire smoke. The GEOS-Chem chemical transport model is then used to assess the representation of both acids during the WE-CAN and FIREX-AQ campaigns. Comparison of formic acid measured by two complementary instruments during WE-CAN indicates large uncertainty in its

measurement by chemical ionization mass spectrometry due to calibration error and inlet artifacts. Formic acid emission ratios (ERs) and emission factors (EFs) during WE-CAN were found to be 3.5 time higher than the literature average, with little to no dependence on fuel type or modified combustion efficiency (MCE). One potential reason for the higher formic acid ERs measured during WE-CAN is that it is rapid produced at an average rate of 2.7 ppb ppm_{CO}^{-1} h^{-1}. Conversely, acetic acid ERs and EFs agree well between WE-CAN and the literature, with a modest negative correlation with MCE (r^2=0.52) and some fuel type dependence. Additionally, acetic acid normalized excess mixing ratios remain within the range of observed ERs during the first 8 hours of plume aging, suggesting little to no production in the time scales sampled during WE-CAN. The observed formic acid and acetic acid trends are not captured by the Framework for 0-D Atmospheric Modeling (F0AM) with MCM chemistry, which mainly predicts their loss through OH oxidation. Similarly, the GEOS-Chem chemical transport model was found to be biased low for both acids during WE-CAN and FIREX-AQ, likely due to missing secondary chemistry in BB smoke and/or coniferous forest biogenic emissions. This work improves our understanding of formic acid and acetic acid in biomass burning smoke such that they can be better predicted by next generation models.

4.2 Introduction

Formic acid (FA) and acetic acid (AA) are the two most abundant organic acids in the troposphere, influencing aqueous-phase chemistry (Jacob, 1986) and gas-aerosol partitioning (Metzger et al., 2006) by controlling pH levels in cloud droplets and aerosols (Andreae et al., 1988; Galloway et al., 1982; Keene et al., 1983; Millet, 2012; Stavrakou et al., 2012). Multiple studies have shown that various models continuously underestimate both FA and AA abundance compared to ground, airborne, and satellite observations, reflecting an incomplete knowledge of their global budget (Alwe et al., 2019; Cady-Pereira et al., 2014; Chaliyakunnel et al., 2016; Le Breton et al., 2012; Millet et al., 2015; Paulot et al., 2011; Stavrakou et al., 2012; Yuan et al., 2015). This underestimation is particularly prevalent in regions with significant biogenic or biomass burning emissions, indicating potential missing primary or secondary sources.

Formic and acetic acid are two of the most abundantly emitted VOCs from biomass burning (BB), accounting for 16 % of the average VOC emissions by mass in western U.S. wildfires (Permar et al., 2021). As smoke plumes age, substantial secondary production of FA and AA may occur (Akagi et al., 2012; Goode et al., 2000; Grutter et al., 2010; R. J. Yokelson et al., 2009; Yokelson et al., 1999), resulting in them being one of the largest OH sinks in aged smoke, accounting for 23 % of plume OH reactivity (Permar et al., 2023). However, analytical challenges measuring FA, along with an incomplete understanding of chemical processes in smoke (Akagi et al., 2013) has made it difficult to accurately model FA and AA evolution in BB plumes (Chaliyakunnel et al., 2016; Trentmann et al., 2005).

FA and AA both have multiple known primary and secondary sources, though their relative contributions to their global budget are not well defined (Franco et al., 2021; Glasius et al., 2000; Link et al., 2020; Millet et al., 2015; Paulot et al., 2011; Stavrakou et al., 2012). Primary emission sources include anthropogenic waste, soil, cattle, biomass burning, and terrestrial vegetation. As the two simplest organic acids, FA and AA may also be produced from the oxidation of many different VOCs including isoprene, terminal alkenes, monoterpenes, glycolaldehyde, aromatics, acetone, and acetaldehyde (Baltensperger et al., 2005; Bossolasco et al., 2014; Millet et al., 2015; Müller et al., 2019; Paulot et al., 2011; Wyche et al., 2009; Yuan et al., 2015). Additionally, heterogeneous formation of FA in aerosols and cloud droplets has recently been identified as a potential major FA source (Cope et al., 2021; Franco et al., 2021).

The primary sinks of FA and AA include wet and dry deposition, photochemical oxidations by OH radicals, and the irreversible uptake on dust resulting in atmospheric lifetimes of 2–4 days for FA and ~2 days for AA (Chebbi and Carlier, 1996; Millet et al., 2015; Paulot et al., 2011; Stavrakou et al., 2012).

It has been well described that GEOS-Chem underpredicts formic and acetic acid abundances in the atmosphere. Secondary production from biogenic emissions is likely the largest reason for the low model bias, though a few studies point to missing emissions sources and/or the overall model sink being too large. By updating FA chemistry in GEOS-Chem Chen et al. (2019) was able to improve GC representation of the remote free troposphere relative to field observations during the Atmospheric Tomography (ATom) aircraft campaign. However, even with the updated chemistry the model was unable to capture the enhancement of FA in plumes traced to BB and anthropogenic sources.

In this work, we use measurements made during both the Western Wildfire Experiment for Cloud Chemistry, Aerosol Absorption, and Nitrogen (WE-CAN) and Fire Influence on Regional to Global Environments and Air Quality (FIREX-AQ) field campaigns to examine the emissions, secondary chemistry, and model representation of FA and AA in the western United States (U.S.) during wildfire season.

4.3 Methods

4.2.1 WE-CAN and FIREX-AQ campaign overviews and sampling approach

Comprehensive gas and aerosol measurements were made in wildfire smoke plumes across seven western U.S. states from 24 July to 13 September 2018 during the WE-CAN aircraft campaign (https://www.eol.ucar.edu/field_projects/we-can). *In situ* smoke plume sampling was carried out aboard the NSF/NCAR C-130 research aircraft based out of Boise, ID, typically between 14:00 and 19:00 local time when burning conditions were most active. Figure S4.1 depicts the C-130 flight tracks during WE-CAN, colored by the observed formic and acetic acid mixing ratios. Upon arriving at a fire, the C-130 would typically sample fire emissions by flying perpendicular transects through the plume, as near to the source as was allowed by firefighting operations and plane safety constraints. To investigate plume aging, most plumes were subsequently sampled using a pseudo-Lagrangian approach where perpendicular transects were performed in a stepwise pattern

starting near a fire and continuing as far downwind as possible (seen as the zig-zag pattern in Figure S4.1). In total, WE-CAN sampled more than 22 hours of wildfire smoke, including 31 emission transects of 24 unique fires, along with 4.8 hours of clean free troposphere, and 1.2 hours of smoke estimated to have aged >3 days (Permar et al., 2023).

The FIREX-AQ aircraft campaign sampled biomass burning plumes across the western and southeastern U.S. from July–September 2019 (https://csl.noaa.gov/projects/firex-aq). In this work, we use both the western and southeastern U.S. portion of the FIREX-AQ data to assess FA and AA representation in the GEOS-Chem CTM across multiple fire seasons and regions. As the total emissions in the western U.S. during the 2018 WE-CAN campaign were ~10 × higher than during the 2019 FIREX-AQ campaign (190 GgC *vs.* 20 GgC) (Jin et al., 2022), these two datasets provide complementary representation of a wide range of seasonal fire activity allowing for the model to be assessed under varying real-world conditions.

4.2.2 Measurements of Formic and Acetic Acid
Formic and acetic acid were both measured by a proton-transfer-reaction time-of-flight mass spectrometer (PTR-ToF) and an iodide adduct chemical-ionization mass spectrometer (I^- CIMS) during the WE-CAN and FIREX-AQ campaigns. The PTR-ToF (Permar et al., 2021) and I^- CIMS (Lee et al., 2018, 2014; Palm et al., 2019; Peng et al., 2020) operated during WE-CAN and used in this work have been extensively described by the cited literature, while here we include those details most relevant to their measurements of FA and AA.

4.2.3 PTR-ToF
During WE-CAN, the PTR-ToF measured at 2 or 5 Hz frequency with drift tube conditions maintained at 3.00 mbar, 810 V, and 60°C, resulting in an E/N of 130 Td. Sampling was done by drawing ambient air into the cabin at 10–15 lpm through 3.175 mm I.D. PFA tubing, maintained at ∼55°C. This sample stream was then subsampled by the PTR-ToF drift tube through ∼100 cm of 1.588 mm O.D. PEEK tubing (60°C),

resulting in a total inlet residence of less than 2 s. Three-minute instrument zeroes were performed every hour by sampling VOC free air generated via a platinum bead catalyst heated to 375°C.

Calibrating FA and AA is analytically challenging due to their instability in gas standards and known humidity-dependent sensitivities in PTR-ToF measurements (Baasandorj et al., 2015). To overcome these challenges, humidity-dependent FA and AA sensitivities were determined in the laboratory post-campaign using a commercial Liquid Calibration Unit (LCU; Ionicon Analytik). Here, analytical grade FA and AA are volatilized in the LCU and dynamically diluted into zero air. The humidity in the zero air is then varied by adjusting water flow in the LCU to within the range observed during WE-CAN as determined by the internal humidity proxy of $H_2O \cdot H_3O^+$ to H_3O^+ ([m/z 39]/[m/z 21], 0–6 %) (Baasandorj et al., 2015; de Gouw and Warneke, 2007). The resulting calibration curves for FA and AA sensitivities as a function of the percent [m/z 39]/[m/z 21] are shown in Figure S4.2 and were applied to all WE-CAN FA and AA PTR-ToF measurements. The resulting uncertainty is 50 %, mostly from potential 40 % instrument drift between WE-CAN and the laboratory calibrations, determined from the observed sensitivity change of gas standards, with 3 sigma detection limits of 1.2 ppb for FA and 0.5 ppb for AA.

In PTR-ToF, formic acid (HCOOH) and acetic acid (CH_3COOH) are detected at their protonated masses, m/z 47.013 and m/z 61.028 respectively. The corresponding mass resolution during WE-CAN are 2120 $m/\Delta m$ at m/z 47 and 3060 $m/\Delta m$ at m/z 61, where Δm is the full width at half mass for the ion peak. FA has three major potential interfering ions: dimethyl ether (DME, m/z 47.077), ethanol (m/z 47.050), and $N_2H_3O^+$ (m/z 47.024) (Baasandorj et al., 2015; Koss et al., 2018). The mass resolution during WE-CAN was high enough to separate DME and ethanol signals from FA, with ethanol also expected to be ~4 × lower than FA in BB smoke (Koss et al., 2018). The $N_2H_3O^+$ signal, which was not fully resolved from FA, was observed to stay constant regardless of emission source strength throughout the campaign and was therefore classified and corrected as

instrumental background. Consequently, we treat the *m/z* 47 signal as being primarily FA in agreement with previous literature (Baasandorj et al., 2015; de Gouw and Warneke, 2007; Yuan et al., 2017).

Potential interferences of AA in PTR-TOF measurements include 2-propanol and n-propanol (*m/z* 61.065), peroxyacetic acid (PAA fragments, *m/z* 61.028), ethyl acetate fragments (*m/z* 61.028), methyl formate (*m/z* 61.028), and glycolaldehyde (*m/z* 61.028) (Baasandorj et al., 2015; Fortner et al., 2009; Gilman et al., 2015; Koss et al., 2017; Španěl et al., 2003; Yuan et al., 2017). Propanol was resolved from AA during WE-CAN, while PAA fragments, ethyl acetate fragments, methyl formate, and glycolaldehyde are all isomers. PAA is formed by the reaction of $CH_3C(O)O_2$ radicals with HO_2, which may be important in low NOx conditions (Baasandorj et al., 2015) but is unlikely to be present in smoke plumes (Koss et al., 2018). Ethyl acetate is used in coatings, adhesives, cosmetics, and as a process solvent, resulting in it being most prevalent in anthropogenically polluted areas and thus not expected at significant concentrations during WE-CAN. For methyl formate, a small peak can be seen in the GC-MS during the FIREX-AQ laboratory burning experiment, but FTIR comparison suggests its contribution is negligible (Koss et al., 2018). Due to interference from these isomers being unlikely in BB smoke, we do not attempt to correct for their presence, and assume m/z 61 to be predominantly AA and glycolaldehyde in wildfire emissions.

Based on the FIREX-AQ Missoula fire laboratory burning experiments, the *m/z* 61 signal is 67 % AA and 33 % glycolaldehyde in fresh emissions from western U.S. fuels (Koss et al., 2018; Selimovic et al., 2018). However, the glycolaldehyde contribution in aged smoke is not well described. As glycolaldehyde's atmospheric lifetime of 1 day (Bacher et al., 2001) is approximately half of that of AA (Paulot et al., 2011), it is likely *m/z* 61 becomes more predominantly AA in aged airmasses, though glycolaldehyde production could offset its loss. Given that the relative contribution of glycolaldehyde to *m/z* 61 was not constrained during WE-CAN, we do not attempt to correct for the potential glycolaldehyde interference and apply only the humidity dependent AA sensitivity to *m/z*

61. Though we treat and discuss the PTR-ToF *m/z* 61 as AA in this work, the reported values may reflect the combined AA and glycolaldehyde isomers and therefore likely represent an upper bound for AA.

4.2.4 I⁻ CIMS

I⁻ CIMS operates by colliding iodide ions (I⁻) with neutral analytes inside of an ion-molecule reaction region (IMR), forming clusters which are then analyzed by a time-of-flight mass spectrometer. During WE-CAN, ambient air was sampled at 20 slpm through a 40 cm, 18 mm O.D., Teflon tube before being subsampled into the IMR. Between the inlet and IMR, the residence time was < 0.7 seconds.

Two different instrument zeros were performed by the I⁻ CIMS during WE-CAN to better correct for sample line losses. To characterize the persistent instrument background signal, a full inlet zero was done every 20 minutes by flowing ultra-high purity N_2 through the entire inlet and IMR for 10 seconds. Additionally, the I⁻ CIMS employed a fast-zeroing approach described in Palm et al. (2019) where a 6 second background concentration within the IMR was found every minute. The 6 second zeros are then used to determine the background-subtracted signal by isolating the effects of adsorb and desorption of 'sticky' molecules on the inlet surfaces. This zero occurred both in and out of smoke plumes to account for the changes in background signal with varying sampled concentrations.

The I⁻ CIMS detects FA as a cluster with iodide at *m/z* 172.911. For WE-CAN, FA was calibrated in the lab prior to the campaign by flowing pure air over heated permeation tubes with gravimetrically determined permeation rates. Although I⁻ CIMS measures AA, it was not calibrated for during WE-CAN and therefore we only report AA from PTR-ToF. Recent work has shown that one potential source of error for the I⁻ CIMS FA measurement is that its sensitivity to FA decreases with increasing IMR temperature (Robinson et al., 2021). The I⁻ CIMS deployed during WE-CAN did not directly regulate

temperature in the IMR, though the region was insulated. Cabin temperatures measured near the I⁻ CIMS ranged 18–34 °C (10th and 90th percentiles: 21–29 °C). Robinson et al. (2021) showed that a 16 °C change in IMR temperature could correspond to a 60 % change in sensitivity, though IMR temperatures in their study were all higher than the cabin temperatures observed during WE-CAN. It is unlikely that the IMR temperature fluctuated as widely as the cabin temperature, though a lack of data makes it difficult to constrain the actual IMR temperature during WE-CAN or during the laboratory calibrations. Consequently, we conservatively estimate the I⁻ CIMS FA measurement to be a likely upper bound, with 70 % uncertainty and 30 ppt detection limit, based on calibration uncertainties and potential variation in IMR temperature.

4.4 GEOS-Chem chemical transport model

GEOS-Chem nested grid simulations (version 12.5.0) (Bey et al., 2001) over North America were run for the WE-CAN (24th July–14th September 2018) and FIREX-AQ periods (22nd July–5th September 2019) using the model conditions described in Chen et al. (2019). Simulations were carried out using Goddard Earth Observation System Forward Processing, (GEOS-FP) assimilated meteorological with detailed HO_x, NO_x, VOC, ozone, halogen, and aerosol chemistry. Model runs were conducted at $0.25° \times 0.3125°$ (~25 km) resolution with time steps of 15 min (transport/convection) and 30 min (chemistry/emission). Emissions were kept the same as in Chen et al. (2019) with the notable exception of using Global Fire Assimilation System version 1.2 (GFAS) biomass burning emissions with FA and AA emission ratios updated based on Permar et al. (2021), which in turn reflect the WE-CAN averages discussed in Section 4.6. GEOS-Chem was subsequently sampled along both campaign flight tracks for comparison to the observations.

The GEOS-Chem simulations also reflect updated FA chemistry including photochemical FA production based on OH initiated oxidation of alkynes, monoterpenes, isoprene, and CH_3O_2, ozonolysis of terminal alkenes (e.g. ethene, propene, isoprene), keto-enol tautomerization (Millet et al., 2015; Paulot et al., 2011), and phototautomerization of acetaldehyde (Shaw et al., 2018). Based on these updates, Chen et al. (2019) found that

GEOS-Chem accurately simulated FA concentrations in the remote free troposphere during the Atmospheric Tomography (ATom) aircraft campaign, indicating that GEOS-Chem is not missing any significant FA sources in the remote free troposphere. However, the model was found to significantly underestimate FA mixing ratios in 1–10 days aged plumes attributed to both anthropogenic and biomass burning sources. In this work, we investigate how GOES-Chem with updated FA and AA by chemistry by Chen et al. (2019) represents FA and AA in the western U.S. under heavily smoke impacted conditions.

4.5 Formic acid measurement intercomparison

Formic acid is analytically challenging to measure due to its 'stickiness' in sample inlets and its having humidity dependent sensitivities in PTR-ToF (Baasandorj et al., 2015; Müller et al., 2016) and I^- CIMS (Lee et al., 2014). Figure 4.1 shows the 1 Hz time series and cumulative mixing ratios of FA measured by PTR-ToF and I^- CIMS during five near plume transects (< 20 km downwind) of the Taylor Creek (TC) fire sampled during WE-CAN (Research Flight #3). When corrected for inlet residence times the two measurements show good temporal agreement, capturing the real-time plume variability. However, the PTR-ToF consistently measures ~2 × lower maximum FA concentrations than the I^- CIMS during the plume transects likely representing 1) sample retention in the inlet, 2) a base line offset due to background correction differences, and/or 3) calibration errors. Each is discussed in more detail below.
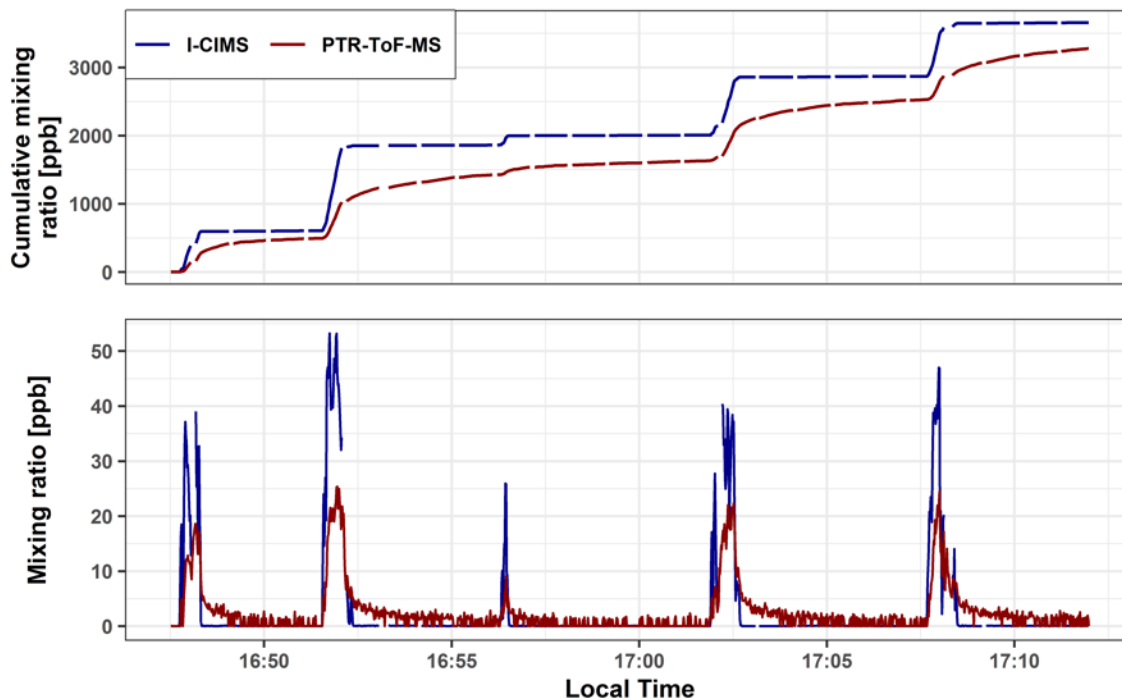
Figure 4.1. Time series of 1 Hz PTR-ToF and I⁻ CIMS formic acid mixing ratios (bottom panel) and cumulative mixing ratios (top panel) during 5 plume transects made < 20 km downwind from the Taylor Creek Fire, OR during WE-CAN.

The TC fire was sampled shortly after injection into the free troposphere with little to no regional smoke impacts, resulting in clearly defined plume edges that can be seen in Figure 4.1 by the rapid FA enhancement upon entry into the plumes. However, when exiting the plumes, the PTR-ToF trace shows a distinct tail indicative of FA being initially retained in the inlet before flushing out in the 60–90 seconds after returning to background air. This is further illustrated by the cumulative mixing ratio plot in Figure 4.1, where the integrated mixing ratios for both instruments near agreement just before sampling the proceeding plume. At the end of the shown sampling period the total I⁻ CIMS and PTR-ToF integrated FA mixing ratios are 3655 ppb and 3277 ppb respectively, resulting in an I⁻ CIMS to PTR-ToF ratio of 1.1. This indicates that the two measurements agree within their stated uncertainty when the residual FA in the PTR-ToF inlet is accounted for, and the sampling concentrations are sufficiently high. Comparison of emission ratios calculated from each instrument using plume integrated excess mixing ratios and plume exit times adjusted + 20 seconds to capture most of the FA tails during

85

WE-CAN, further confirm agreement between the two instruments with an average I^- CIMS to PTR-ToF ratio of 1.4 ± 0.3. Due to most other sampling periods having either more poorly defined plume edges, elevated background signals from regional smoke mixing, and/or not having enough time between consecutive transects, we are unable to accurately extend this analysis to other fires. However, it is likely that inlet losses decrease the PTR-ToF measured FA in most plumes sampled during WE-CAN.

The lack of a similar inlet artifact in the I^- CIMS measurement is likely explained by a few things. First, inlet material and size differ slightly between the two instruments with the most notable difference being that the I^- CIMS inlet is significantly shorter than the one used by the PTR-ToF, resulting in residence times < 0.7 s and 2 s respectively. Second, the I^- CIMS fast zeroing strategy (seen as the data gaps in the I^- CIMS trace in Figure 4.1) results in a FA background-subtracted signal that minimizes the effects of adsorption and desorption from walls and surfaces in the instrument (Palm et al., 2019). Consequently, this points to the importance of the instrument's inlet configuration and background correction procedures for the most accurate measurement of FA in environments with rapid concentration changes.

Although inlet retention explains a large part of the disagreement of FA measured by the two instruments while sampling smoke plumes with high, rapidly changing concentrations, the average flight integrated I^- CIMS to PTR-ToF formic acid mixing ratio (2.1 ± 0.47) indicates that the I^- CIMS measured $\sim 2 \times$ more FA than the PTR-ToF across all research flights (Figure S4.3). Further comparison of ~4 hours of clean free-troposphere samples during WE-CAN gives an integrated I^- CIMS to PTR-ToF FA ratio of 2.5, indicating that much of the disagreement between the two FA measurements is during sampling periods with relatively low concentrations. This likely represent that the PTR-ToF zeros contained residual FA due to desorption from the instrument/inlet surfaces and incomplete oxidation in the catalyst generated zero air. Consequently, too high of a background signal was subtracted resulting in the mixing ratios being biased

slightly low, especially when sampling relatively clean air. The I⁻ CIMS likely avoided similar complications by using pure N_2 to perform instrument zeros.

In addition to uncertainty in the formic acid sensitivities from calibration errors, the FA sensitivity in I⁻ CIMS also is strongly dependent on IMR temperature (Robinson et al., 2021), which was not directly controlled or logged during WE-CAN. To test if IMR temperature may play a role in the observed disagreement, we compared the I⁻ CIMS to PTR-ToF FA mixing ratios as a function of cabin temperature measured at the I⁻ CIMS instrument rack for all research flights. The least squares regression suggests a weak negative correlation (slope = -1.3, r^2 = 0.16) between the I-CIM *vs.* PTR-ToF FA mixing ratio and cabin temperature, with the ratio approaching 1:1 at the highest temperatures. The improved agreement between the two instruments at higher cabin temperatures may reflect the I⁻ CIMS sensitivity decreasing slightly with increasing IMR temperature, consistent with Robinson et al. (2021), though the lack of direct IMR temperature measurements makes this analysis highly uncertain.

The observed disagreement between the two instruments then, is likely due to a combination of factors including uncertainty in the formic acid sensitivity due to its humidity and temperature dependence, potential instrument drift between the laboratory calibrations and field measurements, inlet losses, and differences in background correction procedures. To improve future formic acid measurements made by I⁻ CIMS and PTR-ToF, more frequent FA calibrations need to be done in the field, while inlet artifacts should be better quantified. In this work we report formic acid mixing ratios measured by I⁻ CIMS due to its lower detection limit and lack of apparent inlet artifacts. However, due to the high uncertainty in the FA measurements, PTR-ToF mixing ratios are included to provide further constraints on the measurement uncertainty where appropriate.

4.6 Emissions of formic and acetic acid from WE-CAN sampled fires

Emission ratios (ERs) and emission factors (EFs) were calculated for 31 WE-CAN emission transects of 24 individual fires as described in Permar et al. (2021). Here, emission transects are defined as the nearest transect of a well-defined smoke plume that is traceable to a single emission source sampled 27–130 minutes downwind from the fire. Although these transects represent the freshest smoke sampled during the campaign, this is sufficient time for substantial secondary formation to have occurred (Akagi et al., 2012, 2012; Hobbs et al., 2003; Lindaas et al., 2021c; Peng et al., 2020). Consequently, FA and AA ERs and EFs during WE-CAN represent their combined production and loss before being sampled by the research aircraft, which may be more appropriate for the spatial and temporal resolution of many CTMs (Lonsdale et al., 2020). Normalized excess mixing ratios (NEMRs) were calculated using the background corrected plume integrated mixing ratios of a VOC to CO (ppb VOC ppm_{CO}^{-1}) for each emission and subsequent down-wind plume transect. ERs were used to calculate EFs, expressed as grams of VOC emitted per kilogram of burned fuel, using the carbon mass balance method (Yokelson et al., 1999, 1996) with the total emitted carbon as the sum of CO_2, CO, CH_4, organic carbon, black carbon, and 161 VOCs (Permar et al., 2021). Fuels burned during WE-CAN were primarily those characteristic of mixed conifer forests.

Literature values were compiled from 16 different papers, reporting 330 FA and 289 for AA ERs and EFs. Approximately half of were retrieved from the Smoke Emissions Reference Application (SERA) (Prichard et al., 2020). Average FA and AA ERs and EFs for the literature described in this work are summarized in Table S4.1 and represent a variety of burned fuels, which were broadly grouped as conifer forest (147 FA and 122 AA EFs), mixed hardwood forest (17, 23), shrubland (53, 38), grassland (36, 31), crop residue (46, 47), and organic soil/peat (31, 28). Table S4.1 also includes modified combustion efficiency (MCE) when available, instrumentation used, region of fuels burned, and whether the data are from a laboratory or field study (Akagi et al., 2012; Bertschi et al., 2003; Christian et al., 2003; Goode et al., 2000; Koss et al., 2018; McKenzie et al., 1995; Müller et al., 2016; Stockwell et al., 2015; Yokelson et al., 2003, 1999).

Figure 4.2 shows formic and acetic acid ERs for each of the 24 fires sampled during WE-CAN (green points) along with literature values (box-and-whisker plots). During WE-CAN, the average formic acid ER was found to be 9.5 ppb ppm$_{CO}^{-1}$ (range 3.4–18.9 ppb ppm$_{CO}^{-1}$), which is 3.5 times higher than the literature average of 2.7 ppb ppm$_{CO}^{-1}$ (range 0.2–13.4) calculated from 168 data points reported for 10 of the 16 studies in Table S4.1. We note that although FA ERs calculated from PTR-ToF measurements are slightly lower than I⁻ CIMS, both are generally higher than the 75th percentile of literature values.

One possible explanation for the higher ERs observed during WE-CAN is that a significant amount of FA has been produced in the plumes prior to being intercepted by the C-130, discussed in more detail in Section 4.7. To estimate how much FA may have been formed before being sampled, we estimate t_0 emission ratios from the least squares regression of NEMRs *vs.* physical age for three of the 5 pseudo-Lagrangian sampled smoke plumes shown in Figure 4.4 with $r^2 > 0.82$. FA NEMRs at t_0 range 5.7–7.4 ppb ppm$_{CO}^{-1}$, which is still approximately 2–3 time higher than the literature average. Consequently, while many of the FA ERs measured during WE-CAN likely reflect some plume aging, near field production alone is not enough to explain all of the disagreement. Given that ERs calculated using both I⁻ CIMS and PTR-ToF measurements agree within their stated uncertainty when inlet retention is accounted for (Section 4.5), it is likely that the ERs observed during WE-CAN also generally represent higher FA emissions from the wildfires sampled that season than has been observed in the literature.

In contrast, AA ERs measured during WE-CAN mostly fall within the 25th–75th percentiles of literature values (Figure 4.2), with good agreement between their averages (WE-CAN 11.5 ppb ppm$_{CO}^{-1}$, range 6.4–16.7 ppb ppm$_{CO}^{-1}$; literature 15.5 ppb ppm$_{CO}^{-1}$, range 0.9–85.6 ppb ppm$_{CO}^{-1}$).

Figure S4.4 shows that EFs follow the same trend as the ERs, with the WE-CAN average EF of 1.5 g kg^{-1} (range 0.5–2.5 g kg^{-1}) also ~3.5 times higher than the literature average of 0.4 g kg^{-1} (range 0.002–4.2 g kg^{-1}). Similarly, WE-CAN AA ERs are within the 25th to 75th percentile of literature values, with good agreement between their averages (WE-CAN 2.4 g kg^{-1}, range 1.2–3.3 g kg^{-1}; literature 2.5 g kg^{-1}, range 0.1–14.0).
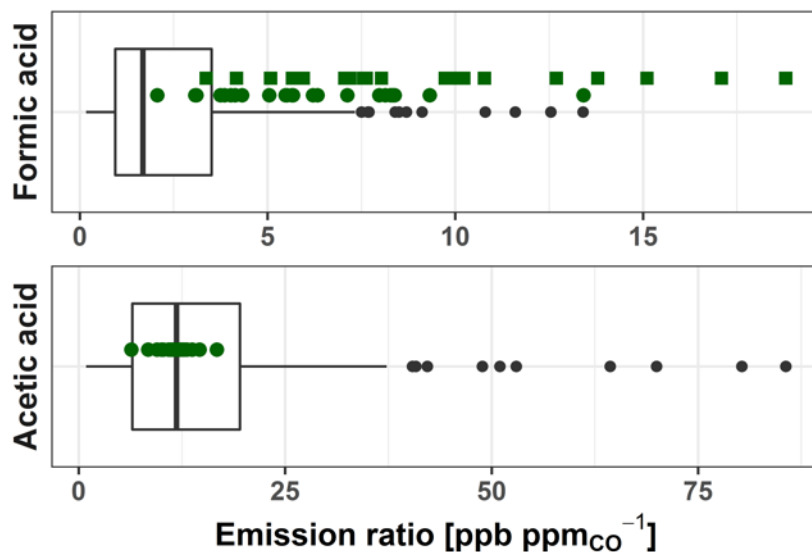
Figure 4.2: Emission ratios of formic and acetic acid from WE-CAN PTR-ToF observations (green points), I$^-$ CIMS FA (green squares), and literature values (box-and-whisker). The box and whisker plots reported include literature ERs from all studies in Table S4.1, representing a variety of fuels (168 data points for formic acid and 156 for acetic acid). Boxes represent the 25th and 75th percentiles, vertical lines as median, whiskers as $1.5 \times$ the interquartile range, and black points as $> 1.5 \times$ interquartile range.

To examine if the observed organic acid emission variability is related to burning condition, we compare their EFs to the modified combustion efficiency, which is a simple proxy used to describe the degree of flaming versus smoldering combustion in a fire. MCE is defined as,

$$MCE = \frac{\Delta CO_2}{\Delta CO_2 + \Delta CO} \tag{4.1}$$

where ΔCO_2 and ΔCO are the excess CO$_2$ and CO mixing ratios. An MCE near 1 corresponds to pure flaming combustion, while MCEs of 0.65–0.85 represents pure

smoldering (Akagi et al., 2011). During WE-CAN, MCEs ranged between 0.86–0.94, while those in previous studies in our literature review have a larger range of 0.68–0.99, with most MCEs < 0.84 corresponding to combustion of peat and organic soils. Figure 4.3 shows the correlations of formic and acetic acid EFs vs MCE for both WE-CAN sampled fires and literature values with soil/peat fuels removed. We note that their inclusion has little effect on the FA correlations, while only slightly improving the AA correlation coefficients. WE-CAN and literature FA EFs have little to no observed dependence on MCE, with r^2 of 0.03 and 0.12 respectively. Using PTR-ToF FA data slightly improves the r^2 to 0.05. In contrast, AA EFs have a modest negative correlation with MCE with $r^2 = 0.52$ during WE-CAN and $r^2 = 0.19$ for literature values.
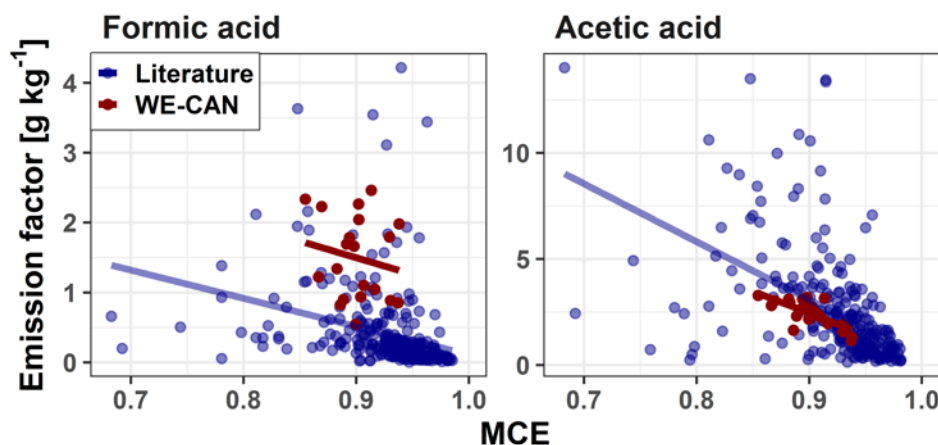
Figure 4.3: Correlations of formic acid (left) and acetic acid (right) EFs versus MCE for both WE-CAN (red points) and literature values (blue points). The least square regression for each group is shown in corresponding colors. For FA, the line of best fit for WE-CAN data is y = -4.8x + 5.7 (r^2=0.03) and y = -6.0x + 6.0 (r^2=0.12) for literature values. For AA, the line of best fit for WE-CAN data is y = -20.7x + 21.1 (r^2=0.52) and y = -27.1x + 27.4 (r^2=0.19) for literature values.

To determine if the type of fuel burned influenced FA or AA emissions, we compare WE-CAN and literature EFs between the six fuel categories described above. For each organic acid we use a Tukey's range test to evaluate if the 95 % confidence interval (CI) of emission factors for each fuel type overlap. For FA, the Tukey range test p-values are

> 0.05 for comparisons between all fuel types except with shrubland, indicating overlap in the 95 % CI for most fuels. This suggests that FA EF for shrubland, mainly consisting of chaparral vegetation types in our literature review, have statistically significant different EFs from the other 5 fuel categories. Alternatively, no statistical difference was found between any of the other categories. Coupled with the lack of correlation with MCE, this suggests that a single FA EF of 0.47 ± 0.62 g kg^{-1} and ER of 3.4 ± 3.5 ppb ppm$_{CO}$$^{-1}$ (average of WE-CAN and literature values) best describes most BB emissions, though a fuel specific EF for shrubland fuels (0.13 ± 0.14 g kg^{-1}) may be more accurate.

AA EFs between coniferous forests, mixed hardwood forests, shrubland, and grassland similarly show no statistically significant fuel related difference. However, organic soil/peat and crop residue both have p-values < 0.05 when compared to the other four fuels, suggesting that MCE and fuel dependent EFs may be needed to best describe AA EFs. Given that AA shows some dependence on MCE, it is possible that the differences between crop residue and organic soil/peat EFs compared to EFs for the other fuel categories is in part due to combustion efficiency. For example, organic soil/peat combustion is generally dominated by smoldering (MCE = 0.68–0.92 in this work), which would result in higher EFs (Figure 4.3). Box plots of FA and AA EFs for each fuel category are shown in Figure S4.5.

4.7 Near field acid production during WE-CAN

Formic and acetic acid concentrations varied widely during WE-CAN with maximum mixing ratios of 98 ppb and 89 ppb respectively. The maximum FA NEMR observed in smoke aged ~13 hours is 71 ppb ppm$_{CO}$$^{-1}$, which is $12 \times$ higher than the campaign average ER. This suggests a maximum FA production rate of 4.7 ppb ppm$_{CO}$$^{-1}$ h^{-1} in aged smoke sampled during WE-CAN. This is approximately half of the maximum NEMR observed during ATom in smoke sampled off the African coast estimated to have been aged 1-10 days (140 ppb ppm$_{CO}$$^{-1}$), though is similar to many other plumes intercepted during that campaign (Chen et al., 2019). Conversely, the maximum AA NEMR (17 ppb ppm$_{CO}$$^{-1}$) was observed in the same ~13 hour aged plume to be 5.5 ppb ppm$_{CO}$$^{-1}$, which is within 3σ of the campaign average ER.

Figure 4.4 shows FA and AA NEMRs as a function of smoke plume age for 5 fires with more than 10 plume transects sampled in a pseudo-Lagrangian fashion during WE-CAN. In the first 8 hours of plume aging FA is rapidly produced at an average rate of 2.7 ppb ppm$_{CO}^{-1}$ h^{-1}. This is in good agreement with FA production seen in other studies including 2.6–3 ppb ppm$_{CO}^{-1}$ h^{-1} in smoke from boreal forest fires (Goode et al., 2000), 1.6 ppb ppm$_{CO}^{-1}$ h^{-1} from BB in the Yucatan, Mexico (R. J. Yokelson et al., 2009), and 0.9 ppb ppm$_{CO}^{-1}$ h^{-1} in chaparral fires (Akagi et al., 2012). We hypothesize that the rapid FA production observed during WE-CAN is at least in part responsible for the higher FA EFs and ERs discussed in Section 4.6.

During WE-CAN, AA NEMRs remain relatively constant in the first 8 hours of plume aging, increasing by a statistically insignificant 0.3 ppb ppm$_{CO}^{-1}$ h^{-1} (p=0.13, r^2= 0.03, Figure 4.4). Given the relatively long atmospheric lifetime of AA (~2-3 days) (Lee et al., 2021; Paulot et al., 2011), it is unlikely that a significant amount was removed from the plume in the 8 hours of aging shown here. Consequently, these results suggest that most of the observed AA in the nearfield is from primary emissions, though photochemical production may still be an important source in more aged smoke.

Previous work has used the Framework for 0-D modeling (F0AM) (Wolfe et al., 2016) to simulate the Taylor Creek (TC) fire sampled during WE-CAN due to it being a well isolated plume with pseudo Lagrangian samples performed just after injection into the free troposphere (Garofalo et al., 2019; Lindaas et al., 2021a; Palm et al., 2021, 2020; Peng et al., 2021, 2020; Permar et al., 2023). Here, we the same F0AM model run as originally described in Peng et al. (2021) with updated VOC emissions per Permar et al. (2023). Briefly, F0AM was initialized using 49 VOCs, NO, NO$_2$, HONO, O$_3$, and CO. For VOCs measured by PTR-ToF, potential interfering isomers were removed so that the model was initialized based on the proportion of the mass attributed only to the given species following Koss et al. (2018) Physical parameters such as photolysis frequencies, temperature, and pressure were constrained to measured values at each model step with a

dilution correction factor based on CO observations. Model chemistry was simulated using the explicit Master Chemical Mechanism (F0AM+MCM), with an additional sensitivity test run using $3 \times$ emissions for all gases except FA and AA (F0AM+MCM$\times$3).

Figure 4.4 shows that neither F0AM+MCM or F0AM+MCM$\times$3 can reproduce the rapid FA formation observed in the TC plume, with modeled FA instead decreasing slightly with plume age. The model predicted loss rate for FA in the base run is ~0.3 ppb h^{-1} by reaction with OH, while there is minimal production (~0.01 ppb h^{-1}) from $C_4H_6O_3$ (MCM name HMML) and CH_2OO intermediates. Coupled with the model being insensitive to increased initial values, this represents more FA being removed in the model than is being produced and indicates that the MCM is missing a substantial amount of secondary FA production in BB smoke.

AA NEMRs in the TC plume are highly variable, likely representing changes in fire emissions or sampling different parts of the plume. Figure 4.4 shows that F0AM generally has good agreement with the observed AA NEMRs. Similar to FA, AA is also mainly lost in the model through reaction with OH at ~0.4 ppb h^{-1}, though with negligible production (<0.01 ppb h^{-1}) from CH_3CHOO and CH_3CO_3 radicals.
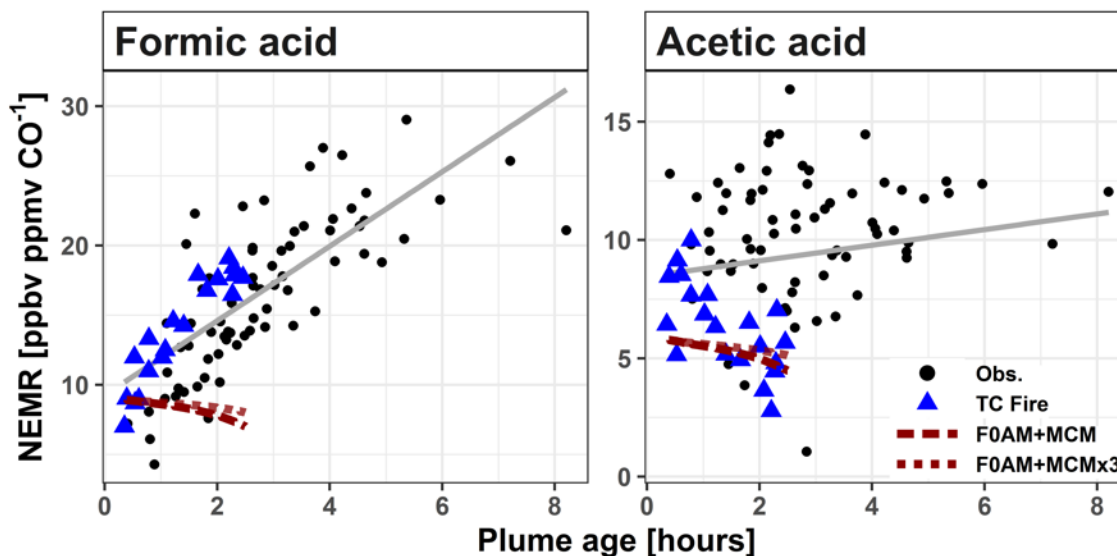
Figure 4.4: NEMRs of FA and AA for 5 research flights with more than 10 pseudo-Lagrangian transects. Least squares regression lines are shown in gray. Blue triangles are plume transects of the Taylor Creek fire corresponding to the red dashed F0AM+MCM and dotted F0AM+MCM×3 predicted NEMRs. During the first 8 hour of plume aging FA NEMR increased on average 2.7 ppb ppm$_{CO}^{-1}$ per hour ($r^2 = 0.58$, intercept = 9.3 ppb ppm$_{CO}^{-1}$), while AA has a statistically insignificant increase of 0.3 ppb ppm$_{CO}^{-1}$ per hour ($r^2 = 0.03$, intercept = 8.4 ppb ppm$_{CO}^{-1}$).

A current lack of understanding of the major FA and AA precursors is one of the largest hurdles to accurately modeling their evolution in smoke. To evaluate potential VOC precursors, NEMRs for both acids measured in the same 5 wildfires as described above were compared to NEMRs of 152 VOCs measured during WE-CAN using least squares regression. FA was found to have statistically significant negative correlations (p-value < 0.05, $r^2 > 0.10$) with 94 VOCs, which collectively account for ~54 % of the total emitted VOC mass and ~94 % of the calculated VOC OH reactivity (Permar et al., 2023, 2021). As the simplest organic acid, FA is known to be an oxidation product of many different VOCs (Alwe et al., 2019; Chaliyakunnel et al., 2016; Chen et al., 2019; Millet et al., 2015; Yuan et al., 2015), which is further demonstrated by its significant negative correlation with most reactive species measured during WE-CAN.

The three species most strongly correlated to FA are shown in Figures 4.5a, 4.5b, and 4.5c: $C_3H_4O_2$ (methyl glyoxal + acrylic acid, r^2=0.60), styrene (r^2=0.50), and 3-

methylfuran (r^2=0.46). Additionally, Figures 4.5d and 4.5e further demonstrate that FA is well correlated to two of the most important contributors to plume OH reactivity (OHR). While the strong correlation of FA NEMRs with these 5 VOCs do not directly indicate that they are FA precursors, they do demonstrate how FA is likely being produced by many species currently not well studied in the literature. Isoprene, ethene, and acetaldehyde are also shown due to being well known FA precursors (Figure 4.5f, 4.5g, and 4.5h). Of these, isoprene has the strongest negative correlation with FA during WE-CAN. Finally, Figure 4.5i and 4.5j show that FA is also well correlated with NO_x and O_3 in the near field, further indicating that FA production follows the overall plume oxidization. Taken together, it is difficult to identify specific species that are the most important precursors to FA in BB smoke due to it likely being formed through many different oxidation pathways.
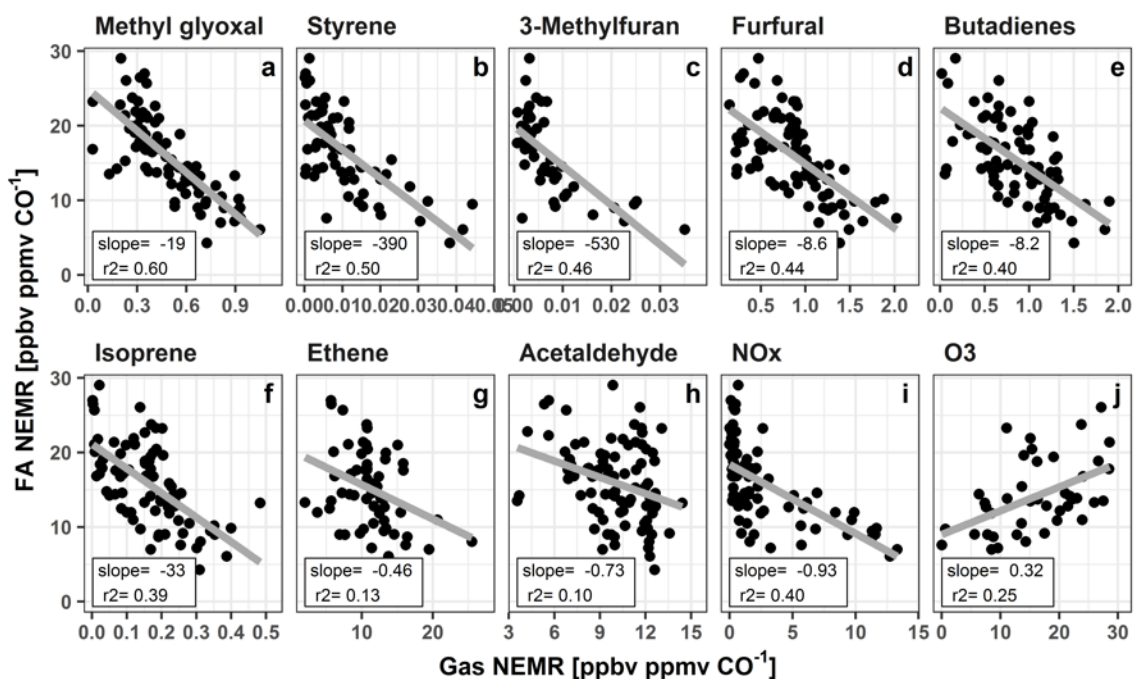
Figure 4.5: FA NEMRs compared to various gas phase species measured in 5 smoke plumes with more than 10 pseudo-Lagrangian plume transects. Slope and r^2 for the least squares regression of each species is shown at the bottom of each panel, while the gray lines are the best fit. Panels a, b, and c are the three VOCs with the strongest correlation to FA. Panels d and e represent two of the largest OH radical sinks in wildfire emissions.

96

Panels f, g, and h are known FA precursors, while i and j are representative of the overall plume oxidation.

Similar analysis with AA shows that it also is well correlated with a majority of BB VOCs, having statistically significant correlation with 105 species with $r^2 > 0.10$. These VOCs account for a similar amount of the total emitted VOC mass (~58 %) as FA, though represent less of the calculated plume VOC OHR (76 %). As AA does not show significant production or loss in the 8 hours of plume aging analyzed here (Figure 4.4), this likely represent AA being well correlated to lesser reactive species which have relatively unchanged NEMRs in the 8-hour plume aging shown here. This is demonstrated in Figure S4.6, where AA NEMRs are plotted versus a similar grouping of gases as in Figure 4.5. The three species with the strongest correlation with AA are shown in Figure S4.4.6a, b and c: $C_3H_6O_2$ (Hydroxyacetone + methyl acetate + Ethyl formate; $r^2=0.62$), $C_5H_8O_3$ (5-hydroxymethyl tetrahydro 2-furanone; $r^2=0.48$), and methyl propanoate ($r^2=0.45$). Like AA, these three species do not correlate with the physical plume age. Figure S4.6 also shows that AA has only modest correlation with the reactive VOCs furfural, butadiene, and isoprene ($r^2=0.14–0.20$) but is poorly correlated with ethene, acetaldehyde, NO_x, and O_3 ($r^2 < 0.1$). Consequently, this further supports the observation that negligible AA is production in the WE-CAN sample wildfire plumes and instead is mainly from primary emissions.

4.8 GEOS-Chem representation of FA and AA during WE-CAN and FIREX-AQ

Global chemical transport models typically have difficulty simulating formic and acetic acid mixing ratios, particularly in the presence of BB smoke. Here we investigate how the GEOS-Chem CTM represents FA and AA in different environments sampled during the WE-CAN and FIREX-AQ campaigns. For more accurate comparison, FIREX-AQ data is separated into its western and southeastern U.S. portions (FIREX-AQ-W and FIREX-AQ-SE), delimitated by the 105th meridian west. WE-CAN and FIREX-AQ data has also been averaged to 5 minutes to match the model resolution. GEOS-Chem was sampled along each flight track and reflects the simulated values during each corresponding campaign and sampling period.

Figure 4.6 shows the median FA vertical profiles of the full WE-CAN, FIREX-AQ-W, and FIREX-AQ-SE campaign flight tracks, along with the corresponding median GEOS-Chem simulated FA mixing ratios. The figure shows that GEOS-Chem generally underestimates the vertical distribution of FA observed during WE-CAN (-92 %; normalized mean bias to I⁻ CIMS, NMB) and above 450 hPa during FIREX-AQ-W (-77 % NMB) and FIREX-AQ-SE (-39). However, GEOS-Chem does significantly better simulating FA at high altitudes during FIREX-AQ-W (-27 %). Interestingly, GEOS-Chem overestimates FA mixing ratios compared to I⁻ CIMS measurements below 450 hPa in the southeastern U.S. (179 %), though the model is still much lower than the co-deployed PTR-ToF measurements. Figure S4.7 shows a similar underestimation for acetic acid mixing ratios, with NMB ranging -93 % to -99 % in both high and low altitude WE-CAN and FIREX-AQ-W samples (Figure S4.7).
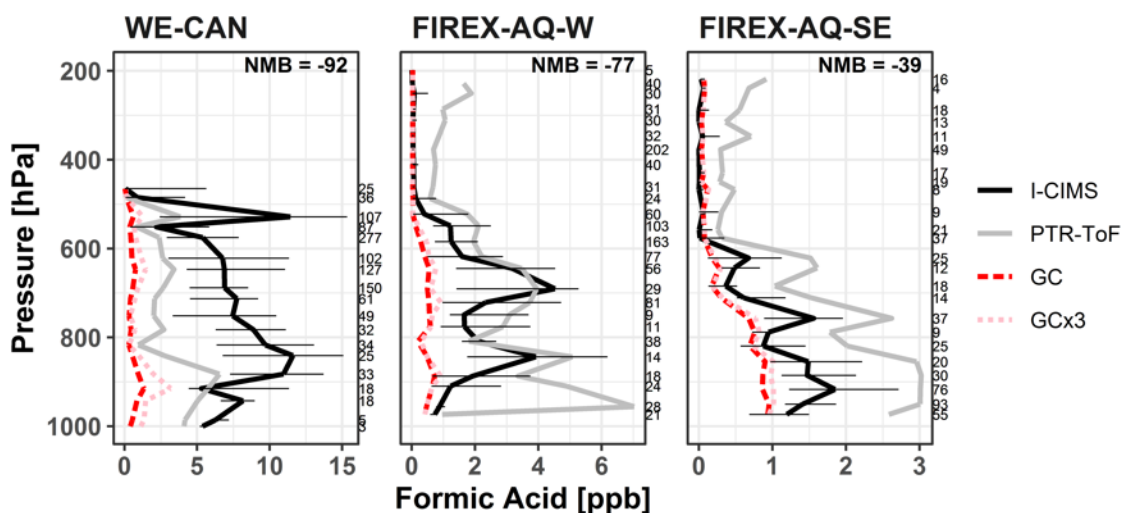
Figure 4.6. Vertical profiles of the median formic acid mixing ratio measured during the full WE-CAN and FIREX-AQ field campaigns, binned at 33 hPa. Black and gray lines correspond to the measurements made by I⁻ CIMS and PTR-ToF. Red dashed lines correspond to GEOS-Chem with GFAS BB emissions (GC) and the pink dotted lines are GEOS-Chem with 3 × GFAS BB emissions (GC×3). Error bars are the 25th and 75th percentiles of the I⁻ CIMS measurement. The number of samples in each altitude bin are shown on the right of the plots, while the normalized mean bias (NMB) to the I⁻ CIMS measurement above 450 hPa is shown at the top.

There are a few possible explanations for why GEOS-Chem underestimates FA and AA during the two campaigns, including: incorrect or missing emissions, sampling bias, and/or missing secondary chemistry from BB and biogenic precursors. As recent model developments have improved GEOS-Chem representation of the free troposphere (Chen et al., 2019) and biogenic sources, we hypothesize that BB is likely a key reason that GEOS-Chem underestimates FA and AA mixing ratio during WE-CAN and FIREX-AQ-W, discussed more below.

4.8.1. Model emissions

Emission inventories as implemented in GEOS-Chem may be biased low by a factor of three or more in the western U.S. due to underestimating the total biomass burned (Jin et al., 2022). To explore if underestimated BB emissions can explain the low model bias, GEOS-Chem was also initiated with $3 \times$ GFAS BB emissions as a sensitivity test. Figure S4.8 shows that GOES-Chem with base GFAS emissions underestimates CO during WE-CAN, FIREX-AQ-W, and FIREX-AQ-SE, with model representation in the western U.S. improved by the $3 \times$ GFAS model run, in good agreement with Jin et al. (2022). Similarly, though benzene and acetone are better represented by the model using base GFAS emissions, the $3 \times$ GFAS emission simulation generally improves model agreement. Despite this, Figure 4.6 and Figure S4.7 show that increasing BB emissions by a factor of 3 only slightly increases the median model predicted FA and AA mixing ratios, decreasing the NMB by ~5 % in all cases. Given that increasing BB emissions has minimal impact on the amount of FA or AA predicted by the model, that ERs calculated from the model match those observed during WE-CAN, and that GEOS-Chem is not significantly missing fire detections during both campaigns (Jin et al., 2022), underestimated BB emission alone cannot account for the low model bias. Additionally, as the $3 \times$ GFAS run also increases emissions for all BB implemented species, the relatively small acid enhancement further indicates that the model is likely missing secondary formation pathways rather than primary emissions of known precursor species.

4.8.2. Sampling bias

The WE-CAN and FIREX-AQ aircraft campaigns were focused on sampling BB smoke whenever possible. As GEOS-Chem was run at $0.25° \times 0.3125°$ (~25 km) resolution, the low model bias may in part also reflect dilution of narrow smoke plumes over the model grid. Though some error is in inherent in the model comparisons due to this sampling bias, Figure S4.9 shows that the observed FA:CO and FA:acetone ratios are higher than predicted by GEOS-Chem for WE-CAN and FIREX-AQ-W, with model FA:benzene ratios also low during WE-CAN. Alternatively, the model captures all the FA:tracer ratios well during FIREX-AQ-SE. As these tracers are generally well represented in the model (Figure S4.8), the low acid:tracer ratios in the western U.S. further indicate that the low model bias for FA and AA is primarily due to missing sources rather than from dilution in across the model grid. Additionally, the improved representation in the southeastern U.S. suggests that the model is simulating deciduous forest emissions well and consequently BB smoke or coniferous forest emissions are likely the cause of the low model bias in the western U.S.

4.8.3. Representation in different environments:

As the low FA and AA bias in GEOS-Chem cannot be explained by emissions and sampling bias alone, it is likely due to missing secondary chemistry in the model. To further investigate potential model deficiencies, we examine how GOES-Chem represents FA and AA in different environments sampled during the campaigns. Here, smoke impacted sampling periods are defined as those with hydrogen cyanide (HCN) > 250 ppt and acetonitrile (CH_3CN) > 200 ppt, while periods below this threshold are discussed as low/no-smoke. However, due to widespread regional smoke during the fire season, the low/no-smoke samples likely still represent some BB influence. In addition to this coarse filter, clean free troposphere samples were also defined for both campaigns based on HCN < 250 ppt, CH_3CN < 150 ppt, and altitudes < 624 hPa (~4000 m above sea level, representing the maximum boundary layer height as determined from vertical temperature profiles). Finally, WE-CAN data was further classified as being wildfire emissions, representing all the emission transects discussed in Section 4.6.

Figure 4.7 shown the vertical profiles for the median observed and modeled FA in the different environments defined above. It shows that GEOS-Chem underestimates the median FA mixing ratio most significantly in smoke impacted samples, doing slightly better during low/no smoke periods in the western U.S. Alternatively, GEOS-CHEM does well simulating FA mixing ratios in the free troposphere during all three periods, in good agreement with recent work Chen et al. (2019). This is particularly evident in FIREX-AQ-W free troposphere samples, which agree nearly 1:1 with the model. Similarly, the model also does very well simulating median FA mixing ratios in the low/no smoke southeast U.S. samples (NMB -40 %). This period is of note due to the region not being heavily impacted by smoke during this time, which in turn suggest that the model is accurately simulating FA from biogenic sources in the southeast U.S. correctly.

Although GEOS-Chem does better simulating FA during low/no smoke samples than in smoke, the improvement is only modest with NMB decreasing by < 10 %. This may point to the widespread smoke impacts in the western U.S. during fire season, where a pool of longer-lived oxygenated species may exist in the region. However, it could also indicate that the model is missing secondary chemistry from biogenic precursors, which would likely be different than those most responsible for FA in the southeastern U.S. For example, isoprene oxidation is thought to be one of the main contributors to FA formation above deciduous forests (Millet et al., 2015), while in coniferous forests emissions are typically dominated by monoterpenes and 2-methyl-3-buten-2-ol (MBO) (Hunter et al., 2017).
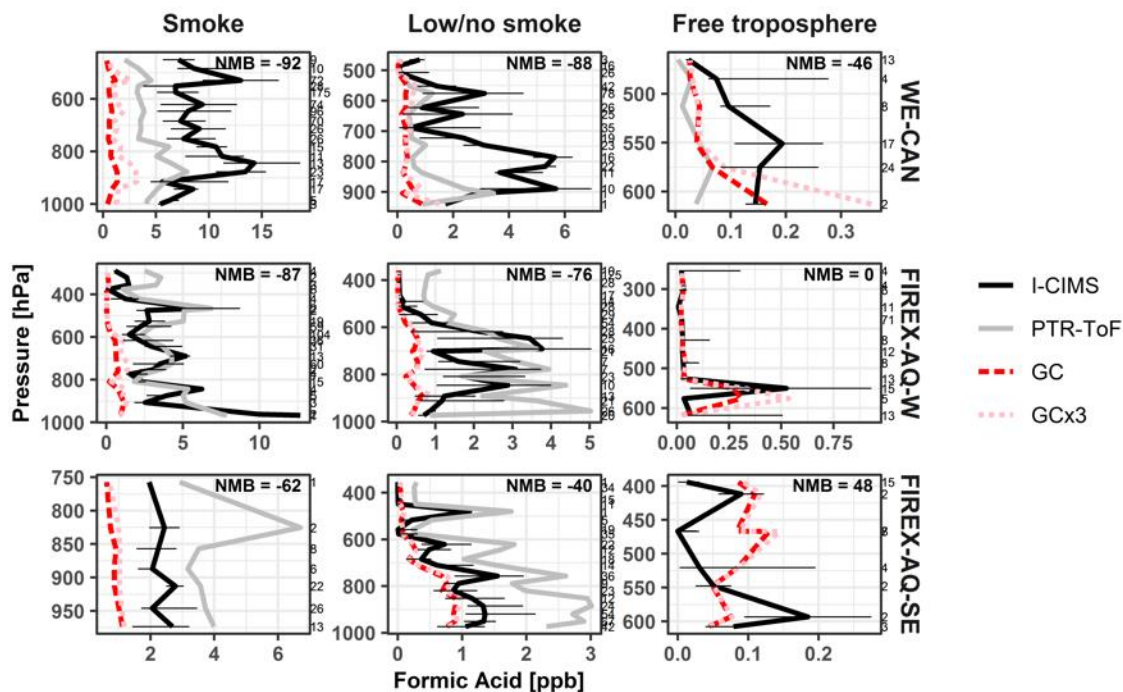
Figure 4.7. Vertical profiles of the median formic acid mixing ratio measured during the WE-CAN field campaign for smoke impacted, low/no smoke, and free troposphere sampling periods. Pressures are binned at 33 hPa. Black and gray lines correspond to the measurements made by I⁻ CIMS and PTR-ToF. Red dashed lines correspond to GEOS-Chem with GFAS BB emissions (GC) and the pink dotted lines are GEOS-Chem with 3 × GFAS BB emissions (GC×3). Error bars are the 25th and 75th percentile of the I⁻ CIMS measurement.

A similar trend can be seen for acetic acid in Figure S4.10, where GEOS-Chem underestimates AA in both smoke-impacted and low/no smoke environments during all three sampling periods. However, unlike FA, the NMB between smoke and low/no smoke conditions is nearly equal, ranging -92 % to -95 %. Additionally, although AA is well captured by the model in the clean troposphere during WE-CAN (NMB -45 %), it is biased low during both portions of FIREX-AQ (NMB -92 %). Given that there is little production of AA in the fresh BB plumes sampled during WE-CAN (Section 4.7), it is unlikely that secondary sources from BB smoke alone are enough to explain the low model bias. Additionally, the underrepresentation cannot be accounted for by BB emission, as the AA emission ratio in GFAS was updated to reflect the WE-CAN average while the 3 × GFAS initialized run only slightly increases the modeled AA. It is likely

then that the low model bias for AA is related to missing secondary production from biogenic precursor in both the western and southeastern U.S.

5 Conclusions and future directions

Emission factors and emission ratios were determined for 161 isomeric and individual VOCs, measured by four complimentary instruments during the WE-CAN field campaign. Instrument comparisons of 45 co-measured VOC species found that 36 agree within combined instrument uncertainties (< 60 %), while disagreement between measurements is likely due to unknown isomers or fragments detected by PTR-ToF-MS in fire smoke. Emissions data was calculated based on 31 near fire transects of 24 unique wildfires, nearly doubling the number of measured VOC EFs and ERs for wildfires compared to the most recent synthesis study, while also doubling the total number of western U.S. airborne samples for near-field fire emissions. In turn, the large number of emission samples provides much needed statistical constraints on the variability of wildfire VOC emissions and allows us to further explore potential explanations for the natural fire-to-fire variance, which can largely be explained by combustion efficiency for approximately half of the total emitted VOC mass measured during WE-CAN.

Using the metric of OH reactivity, we then assess which VOCs are the major OH sinks in western U.S. wildfire emissions, smoke aged > 3 days, smoke-impacted and low/no smoke urban atmospheres, and the clean free troposphere. Wildfire emissions were found to have a much more diverse group of VOCs that significantly contribute to plume OH reactivity compared to more traditionally studied biogenic and anthropogenic sources. As smoke plumes age, oxidation of primarily emitted VOCs results in OVOCs and CO becoming the dominate OH sink, with formaldehyde, acetic acid, and acetaldehyde being the largest individual contributors to the total OHR in smoke aged > 3 days. We then evaluate how well current iterations of the GEOS-Chem CTM and MCM represent the field-calculated OHR for wildfire emissions. The 21 species implemented in GEOS-Chem were found to only account of ~50 % of the field calculated OHR, indicating that even if the model emissions estimates are correct, it will miss half of the emitted VOC

OHR. This missing reactivity in the model may partly explain why GEOS-Chem systematically overestimate global mean OH concentrations. Consequently, it is recommended that furan-containing species, butadienes, and monoterpenes (collectively accounting for 62 % of the non-implemented VOC OHR) be implemented to improve model performance. Conversely, the much more detailed MCM was found to simulate chemistry for species contributing ~90 % of the field calculated OHR, indicating that most known VOC OH sinks are included in the model. These analyses highlight the most important VOC species for daytime BB plume oxidation, providing a roadmap for which individual VOCs and groups should be prioritized in next-generation air quality models to better predict the downwind air quality and subsequent public health impacts of BB smoke.

Formic acid and acetic acid play an important role in regulating free acidity in the free troposphere but are typically underestimated by CTMs when compared to field observations. One challenge is that measurements of FA by two commonly used mass spectrometers, PTR-ToF-MS and I$^-$CIMS, have high uncertainty due to having humidity dependent sensitivities, inlet artifacts, and base line issues. During WE-CAN FA ERs and EFs were found to be 3.5 times higher than literature values, due in part to its rapid formation of 2.7 ppb ppm$_{CO}^{-1}$ h^{-1} in smoke plumes. Conversely, WE-CAN AA emissions were found to agree withing the 25th and 75th percentiles of literature values, with no apparent formation in the plume aging time sampled during the campaign. GOES-Chem simulations with updated FA and AA chemistry were run for the WE-CAN and FIREX-AQ campaigns periods and compared to field observations. For both campaigns, FA and AA were found to be biased low in the model by ~90 %. As the model does well capturing emissions during the campaign and simulating FA mixing ratios over no/low smoke impacted southeast U.S. forests, it is likely that much of this disagreement is driven by missing secondary production from BB emissions.

The breadth of the WE-CAN VOC dataset leaves many avenues available for future study. For example, there is still much to be learned about how the overall oxidation state

of VOCs change within a plume, and how that is related to the proportion of species fragmenting vs. functionalizing. Beyond looking at the bulk chemistry, there are many individual VOCs whose evolution within smoke plumes has not been described or assessed for accurate model representation. Furans are an important example of this, as they make up a significant part of the OH sink in smoke plumes but have only recently been implemented in detailed chemical mechanisms. Analytically, though we leverage VOC speciation based on emissions sampled during laboratory burning experiments, it is unknown how the fractional contribution of isomers to PTR-ToF-MS ion masses changes as smoke ages. This leads to additional uncertainty in our analysis of aged smoke during the campaign and indicates a need for more speciated measurements co-deployed with PTR-ToF-MS in aged smoke. Additionally, to improve our understanding of FA and other compounds that 'stick' in sample inlets, more attention needs to be given to inlet design and instrument zeros.

The body of research encompassed in this dissertation expands our understanding of VOC emissions from wildfires, providing the most comprehensive set of VOC EFs and ERs measured in wildfire smoke to date. In turn, this work will allow for further validation of emission inventories based on real-world fire-to-fire variability. By leveraging the VOC emissions data reported here, we also determine the most important species for daytime plume OH chemistry, providing a roadmap for future model develop. Finally, this work provides much needed observational constraints on formic and acetic acid in wildfire smoke such that they can be better represented in CTMs.

References

Akagi, S.K., Burling, I.R., Mendoza, A., Johnson, T.J., Cameron, M., Griffith, D.W.T., Paton-Walsh, C., Weise, D.R., Reardon, J., Yokelson, R.J., 2014. Field measurements of trace gases emitted by prescribed fires in southeastern US pine forests using an open-path FTIR system. Atmospheric Chem. Phys. 14, 199–215. https://doi.org/10.5194/acp-14-199-2014

Akagi, S.K., Craven, J.S., Taylor, J.W., McMeeking, G.R., Yokelson, R.J., Burling, I.R., Urbanski, S.P., Wold, C.E., Seinfeld, J.H., Coe, H., Alvarado, M.J., Weise, D.R., 2012. Evolution of trace gases and particles emitted by a chaparral fire in California. Atmospheric Chem. Phys. 12, 1397–1421. https://doi.org/10.5194/acp-12-1397-2012

Akagi, S.K., Yokelson, R.J., Burling, I.R., Meinardi, S., Simpson, I., Blake, D.R., McMeeking, G.R., Sullivan, A., Lee, T., Kreidenweis, S., Urbanski, S., Reardon, J., Griffith, D.W.T., Johnson, T.J., Weise, D.R., 2013. Measurements of reactive trace gases and variable O3 formation rates in some South Carolina biomass burning plumes. Atmospheric Chem. Phys. 13, 1141–1165. https://doi.org/10.5194/acp-13-1141-2013

Akagi, S.K., Yokelson, R.J., Wiedinmyer, C., Alvarado, M.J., Reid, J.S., Karl, T., Crounse, J.D., Wennberg, P.O., 2011. Emission factors for open and domestic biomass burning for use in atmospheric models. Atmospheric Chem. Phys. 11, 4039–4072. https://doi.org/10.5194/acp-11-4039-2011

Alwe, H.D., Millet, D.B., Chen, X., Raff, J.D., Payne, Z.C., Fledderman, K., 2019. Oxidation of Volatile Organic Compounds as the Major Source of Formic Acid in a Mixed Forest Canopy. Geophys. Res. Lett. 46, 2940–2948. https://doi.org/10.1029/2018GL081526

Andreae, M.O., 2019. Emission of trace gases and aerosols from biomass burning – an updated assessment. Atmospheric Chem. Phys. 19, 8523–8546. https://doi.org/10.5194/acp-19-8523-2019

Andreae, M.O., Merlet, P., 2001. Emission of trace gases and aerosols from biomass burning. Glob. Biogeochem. Cycles 15, 955–966. https://doi.org/10.1029/2000GB001382

Andreae, M.O., Talbot, R.W., Andreae, T.W., Harriss, R.C., 1988. Formic and acetic acid over the central Amazon region, Brazil: 1. Dry season. J. Geophys. Res. Atmospheres 93, 1616–1624. https://doi.org/10.1029/JD093iD02p01616

Andrews, S.J., Carpenter, L.J., Apel, E.C., Atlas, E., Donets, V., Hopkins, J.R., Hornbrook, R.S., Lewis, A.C., Lidster, R.T., Lueb, R., Minaeian, J., Navarro, M., Punjabi, S., Riemer, D., Schauffler, S., 2016. A comparison of very short lived halocarbon (VSLS) and DMS aircraft measurements in the tropical west Pacific from CAST, ATTREX and CONTRAST. Atmospheric Meas. Tech. 9, 5213–5225. https://doi.org/10.5194/amt-9-5213-2016

Apel, E.C., Emmons, L.K., Karl, T., Flocke, F., Hills, A.J., Madronich, S., Lee-Taylor, J., Fried, A., Weibring, P., Walega, J., Richter, D., Tie, X., Mauldin, L., Campos, T., Weinheimer, A., Knapp, D., Sive, B., Kleinman, L., Springston, S., Zaveri, R., Ortega, J., Voss, P., Blake, D., Baker, A., Warneke, C., Welsh-Bon, D., de Gouw, J., Zheng, J., Zhang, R., Rudolph, J., Junkermann, W., Riemer, D.D., 2010. Chemical evolution of volatile organic compounds in the outflow of the Mexico City Metropolitan area. Atmospheric Chem. Phys. 10, 2353–2375. https://doi.org/10.5194/acp-10-2353-2010

Apel, E.C., Hills, A.J., Lueb, R., Zindel, S., Eisele, S., Riemer, D.D., 2003. A fast-GC/MS system to measure C2 to C4 carbonyls and methanol aboard aircraft. J. Geophys. Res. Atmospheres 108, 8794. https://doi.org/10.1029/2002JD003199

Apel, E.C., Hornbrook, R.S., Hills, A.J., Blake, N.J., Barth, M.C., Weinheimer, A., Cantrell, C., Rutledge, S.A., Basarab, B., Crawford, J., Diskin, G., Homeyer, C.R., Campos, T., Flocke, F., Fried, A., Blake, D.R., Brune, W., Pollack, I., Peischl, J., Ryerson, T., Wennberg, P.O., Crounse, J.D., Wisthaler, A., Mikoviny, T., Huey, G., Heikes, B., O'Sullivan, D., Riemer, D.D., 2015. Upper tropospheric ozone production from lightning NOx-impacted convection: Smoke ingestion case study from the DC3 campaign. J. Geophys. Res. Atmospheres 120, 2505–2523. https://doi.org/10.1002/2014JD022121

Atkinson, R., Arey, J., 2003. Atmospheric Degradation of Volatile Organic Compounds. Chem. Rev. 103, 4605–4638. https://doi.org/10.1021/cr0206420

Baasandorj, M., Millet, D.B., Hu, L., Mitroo, D., Williams, B.J., 2015. Measuring acetic and formic acid by proton-transfer-reaction mass spectrometry: sensitivity, humidity dependence, and quantifying interferences. Atmospheric Meas. Tech. 8, 1303–1321. https://doi.org/10.5194/amt-8-1303-2015

Bacher, C., Tyndall, G.S., Orlando, J.J., 2001. The Atmospheric Chemistry of Glycolaldehyde. J. Atmospheric Chem. 39, 171–189. https://doi.org/10.1023/A:1010689706869

Baker, K.R., Woody, M.C., Tonnesen, G.S., Hutzell, W., Pye, H.O.T., Beaver, M.R., Pouliot, G., Pierce, T., 2016. Contribution of regional-scale fire events to ozone and PM2.5 air quality estimated by photochemical modeling approaches. Atmos. Environ. 140, 539–554. https://doi.org/10.1016/j.atmosenv.2016.06.032

Baltensperger, U., Kalberer, M., Dommen, J., Paulsen, D., Alfarra, M.R., Coe, H., Fisseha, R., Gascho, A., Gysel, M., Nyeki, S., Sax, M., Steinbacher, M., Prevot, A.S.H., Sjögren, S., Weingartner, E., Zenobi, R., 2005. Secondary organic aerosols from anthropogenic and biogenic precursors. Faraday Discuss 130, 265–278. https://doi.org/10.1039/B417367H

Benedict, K.B., Prenni, A.J., El-Sayed, M.M.H., Hecobian, A., Zhou, Y., Gebhart, K.A., Sive, B.C., Schichtel, B.A., Collett, J.L., 2020. Volatile organic compounds and ozone at four national parks in the southwestern United States. Atmos. Environ. 239, 117783. https://doi.org/10.1016/j.atmosenv.2020.117783

Benedict, K.B., Zhou, Yong, Sive, B.C., Prenni, A.J., Gebhart, K.A., Fischer, E.V., Evanoski-Cole, A., Sullivan, A.P., Callahan, S., Schichtel, B.A., Mao, H., Zhou, Ying, Collett Jr., J.L., 2019. Volatile organic compounds and ozone in Rocky Mountain National Park during FRAPPÉ. Atmospheric Chem. Phys. 19, 499–521. https://doi.org/10.5194/acp-19-499-2019

Bertschi, I., Yokelson, R.J., Ward, D.E., Babbitt, R.E., Susott, R.A., Goode, J.G., Hao, W.M., 2003. Trace gas and particle emissions from fires in large diameter and belowground biomass fuels. J. Geophys. Res. Atmospheres 108. https://doi.org/10.1029/2002JD002100

Bey, I., Jacob, D.J., Yantosca, R.M., Logan, J.A., Field, B.D., Fiore, A.M., Li, Q., Liu, H.Y., Mickley, L.J., Schultz, M.G., 2001. Global modeling of tropospheric chemistry with assimilated meteorology: Model description and evaluation. J. Geophys. Res. Atmospheres 106, 23073–23095. https://doi.org/10.1029/2001JD000807

Bossolasco, A., Faragó, E.P., Schoemaecker, C., Fittschen, C., 2014. Rate constant of the reaction between CH3O2 and OH radicals. Chem. Phys. Lett. 593, 7–13. https://doi.org/10.1016/j.cplett.2013.12.052

Bourgeois, I., Peischl, J., Neuman, J.A., Brown, S.S., Thompson, C.R., Aikin, K.C., Allen, H.M., Angot, H., Apel, E.C., Baublitz, C.B., Brewer, J.F., Campuzano-Jost, P., Commane, R., Crounse, J.D., Daube, B.C., DiGangi, J.P., Diskin, G.S., Emmons, L.K., Fiore, A.M., Gkatzelis, G.I., Hills, A., Hornbrook, R.S., Huey, L.G., Jimenez, J.L., Kim, M., Lacey, F., McKain, K., Murray, L.T., Nault, B.A., Parrish, D.D., Ray, E., Sweeney, C., Tanner, D., Wofsy, S.C., Ryerson, T.B., 2021. Large contribution of biomass burning emissions to ozone throughout the global remote troposphere. Proc. Natl. Acad. Sci. 118, e2109628118. https://doi.org/10.1073/pnas.2109628118

Bowman, D.M.J.S., Williamson, G.J., Abatzoglou, J.T., Kolden, C.A., Cochrane, M.A., Smith, A.M.S., 2017. Human exposure and sensitivity to globally extreme wildfire events. Nat. Ecol. Evol. 1, 0058. https://doi.org/10.1038/s41559-016-0058

Brune, W.H., Ren, X., Zhang, L., Mao, J., Miller, D.O., Anderson, B.E., Blake, D.R., Cohen, R.C., Diskin, G.S., Hall, S.R., Hanisco, T.F., Huey, L.G., Nault, B.A., Peischl, J., Pollack, I., Ryerson, T.B., Shingler, T., Sorooshian, A., Ullmann, K., Wisthaler, A., Wooldridge, P.J., 2018. Atmospheric oxidation in the presence of clouds during the Deep Convective Clouds and Chemistry (DC3) study. Atmospheric Chem. Phys. 18, 14493–14510. https://doi.org/10.5194/acp-18-14493-2018

Bruns, E.A., Slowik, J.G., El Haddad, I., Kilic, D., Klein, F., Dommen, J., Temime-Roussel, B., Marchand, N., Baltensperger, U., Prévôt, A.S.H., 2017. Characterization of gas-phase organics using proton transfer reaction time-of-flight mass spectrometry: fresh and aged residential wood combustion emissions. Atmospheric Chem. Phys. 17, 705–720. https://doi.org/10.5194/acp-17-705-2017

Buysse, C.E., Kaulfus, A., Nair, U., Jaffe, D.A., 2019. Relationships between Particulate Matter, Ozone, and Nitrogen Oxides during Urban Smoke Events in the Western US. Environ. Sci. Technol. 53, 12519–12528. https://doi.org/10.1021/acs.est.9b05241

Cady-Pereira, K.E., Chaliyakunnel, S., Shephard, M.W., Millet, D.B., Luo, M., Wells, K.C., 2014. HCOOH measurements from space: TES retrieval algorithm and observed global distribution. Atmospheric Meas. Tech. 7, 2297–2311. https://doi.org/10.5194/amt-7-2297-2014

Canagaratna, M.R., Jimenez, J.L., Kroll, J.H., Chen, Q., Kessler, S.H., Massoli, P., Hildebrandt Ruiz, L., Fortner, E., Williams, L.R., Wilson, K.R., Surratt, J.D., Donahue, N.M., Jayne, J.T., Worsnop, D.R., 2015. Elemental ratio measurements of organic compounds using aerosol mass spectrometry: characterization, improved calibration, and implications. Atmospheric Chem. Phys. 15, 253–272. https://doi.org/10.5194/acp-15-253-2015

Carter, T.S., Heald, C.L., Jimenez, J.L., Campuzano-Jost, P., Kondo, Y., Moteki, N., Schwarz, J.P., Wiedinmyer, C., Darmenov, A.S., da Silva, A.M., Kaiser, J.W., 2020. How emissions uncertainty influences the distribution and radiative impacts of smoke from fires in North America. Atmospheric Chem. Phys. 20, 2073–2097. https://doi.org/10.5194/acp-20-2073-2020

Carter, T.S., Heald, C.L., Kroll, J.H., Apel, E.C., Blake, D., Coggon, M., Edtbauer, A., Gkatzelis, G., Hornbrook, R.S., Peischl, J., Pfannerstill, E.Y., Piel, F., Reijrink, N.G., Ringsdorf, A., Warneke, C., Williams, J., Wisthaler, A., Xu, L., 2022. An Improved Representation of Fire Non-Methane Organic Gases (NMOGs) in Models: Emissions to Reactivity. Atmospheric Chem. Phys. Discuss. 2022, 1–34. https://doi.org/10.5194/acp-2022-438

Chaliyakunnel, S., Millet, D.B., Wells, K.C., Cady-Pereira, K.E., Shephard, M.W., 2016. A Large Underestimate of Formic Acid from Tropical Fires: Constraints from Space-Borne Measurements. Environ. Sci. Technol. 50, 5631–5640. https://doi.org/10.1021/acs.est.5b06385

Chebbi, A., Carlier, P., 1996. Carboxylic acids in the troposphere, occurrence, sources, and sinks: A review. Atmos. Environ. 30, 4233–4249. https://doi.org/10.1016/1352-2310(96)00102-1

Chen, X., Millet, D.B., Singh, H.B., Wisthaler, A., Apel, E.C., Atlas, E.L., Blake, D.R., Bourgeois, I., Brown, S.S., Crounse, J.D., de Gouw, J.A., Flocke, F.M., Fried, A., Heikes, B.G., Hornbrook, R.S., Mikoviny, T., Min, K.-E., Müller, M., Neuman, J.A., O'Sullivan, D.W., Peischl, J., Pfister, G.G., Richter, D., Roberts, J.M., Ryerson, T.B., Shertz, S.R., Thompson, C.R., Treadaway, V., Veres, P.R., Walega, J., Warneke, C., Washenfelder, R.A., Weibring, P., Yuan, B., 2019. On the sources and sinks of atmospheric VOCs: an integrated analysis of recent aircraft campaigns over North America. Atmospheric Chem. Phys. 19, 9097–9123. https://doi.org/10.5194/acp-19-9097-2019

Christian, T.J., Kleiss, B., Yokelson, R.J., Holzinger, R., Crutzen, P.J., Hao, W.M., Saharjo, B.H., Ward, D.E., 2003. Comprehensive laboratory measurements of biomass-burning emissions: 1. Emissions from Indonesian, African, and other fuels. J. Geophys. Res. Atmospheres 108. https://doi.org/10.1029/2003JD003704

Coggon, M.M., Lim, C.Y., Koss, A.R., Sekimoto, K., Yuan, B., Gilman, J.B., Hagan, D.H., Selimovic, V., Zarzana, K.J., Brown, S.S., Roberts, J.M., Müller, M., Yokelson, R., Wisthaler, A., Krechmer, J.E., Jimenez, J.L., Cappa, C., Kroll, J.H., de Gouw, J., Warneke, C., 2019. OH chemistry of non-methane organic gases (NMOGs) emitted from laboratory and ambient biomass burning smoke: evaluating the influence of furans and oxygenated aromatics on ozone and secondary NMOG formation. Atmospheric Chem. Phys. 19, 14875–14899. https://doi.org/10.5194/acp-19-14875-2019

Cope, J.D., Abellar, K.A., Bates, K.H., Fu, X., Nguyen, T.B., 2021. Aqueous Photochemistry of 2-Methyltetrol and Erythritol as Sources of Formic Acid and Acetic Acid in the Atmosphere. ACS Earth Space Chem. 5, 1265–1277. https://doi.org/10.1021/acsearthspacechem.1c00107

Crutzen, P.J., Andreae, M.O., 1990. Biomass Burning in the Tropics: Impact on Atmospheric Chemistry and Biogeochemical Cycles. Science 250, 1669–1678. https://doi.org/10.1126/science.250.4988.1669

de Gouw, J.A., Goldan, P.D., Warneke, C., Kuster, W.C., Roberts, J.M., Marchewka, M., Bertman, S.B., Pszenny, A.A.P., Keene, W.C., 2003. Validation of proton transfer reaction-mass spectrometry (PTR-MS) measurements of gas-phase organic compounds in the atmosphere during the New England Air Quality Study (NEAQS) in 2002. J. Geophys. Res. Atmospheres 108. https://doi.org/10.1029/2003JD003863

de Gouw, J.A., Warneke, C., 2007. Measurements of volatile organic compounds in the earth's atmosphere using proton-transfer-reaction mass spectrometry. Mass Spectrom. Rev. 26, 223–257. https://doi.org/10.1002/mas.20119

Decker, Z.C.J., Robinson, M.A., Barsanti, K.C., Bourgeois, I., Coggon, M.M., DiGangi, J.P., Diskin, G.S., Flocke, F.M., Franchin, A., Fredrickson, C.D., Gkatzelis, G.I., Hall, S.R., Halliday, H., Holmes, C.D., Huey, L.G., Lee, Y.R., Lindaas, J., Middlebrook, A.M., Montzka, D.D., Moore, R., Neuman, J.A., Nowak, J.B., Palm, B.B., Peischl, J., Piel, F., Rickly, P.S., Rollins, A.W., Ryerson, T.B., Schwantes, R.H., Sekimoto, K., Thornhill, L., Thornton, J.A., Tyndall, G.S., Ullmann, K., Van Rooy, P., Veres, P.R., Warneke, C., Washenfelder, R.A., Weinheimer, A.J., Wiggins, E., Winstead, E., Wisthaler, A., Womack, C., Brown, S.S., 2021a. Nighttime and daytime dark oxidation chemistry in wildfire plumes: an observation and model analysis of FIREX-AQ aircraft data. Atmospheric Chem. Phys. 21, 16293–16317. https://doi.org/10.5194/acp-21-16293-2021

Decker, Z.C.J., Wang, S., Bourgeois, I., Campuzano Jost, P., Coggon, M.M., DiGangi, J.P., Diskin, G.S., Flocke, F.M., Franchin, A., Fredrickson, C.D., Gkatzelis, G.I., Hall, S.R., Halliday, H., Hayden, K., Holmes, C.D., Huey, L.G., Jimenez, J.L., Lee, Y.R., Lindaas, J., Middlebrook, A.M., Montzka,

D.D., Neuman, J.A., Nowak, J.B., Pagonis, D., Palm, B.B., Peischl, J., Piel, F., Rickly, P.S., Robinson, M.A., Rollins, A.W., Ryerson, T.B., Sekimoto, K., Thornton, J.A., Tyndall, G.S., Ullmann, K., Veres, P.R., Warneke, C., Washenfelder, R.A., Weinheimer, A.J., Wisthaler, A., Womack, C., Brown, S.S., 2021b. Novel Analysis to Quantify Plume Crosswind Heterogeneity Applied to Biomass Burning Smoke. Environ. Sci. Technol. 55, 15646–15657. https://doi.org/10.1021/acs.est.1c03803

Decker, Z.C.J., Zarzana, K.J., Coggon, M., Min, K.-E., Pollack, I., Ryerson, T.B., Peischl, J., Edwards, P., Dubé, W.P., Markovic, M.Z., Roberts, J.M., Veres, P.R., Graus, M., Warneke, C., de Gouw, J., Hatch, L.E., Barsanti, K.C., Brown, S.S., 2019. Nighttime Chemical Transformation in Biomass Burning Plumes: A Box Model Analysis Initialized with Aircraft Observations. Environ. Sci. Technol. 53, 2529–2538. https://doi.org/10.1021/acs.est.8b05359

Di Carlo, P., Brune, W.H., Martinez, M., Harder, H., Lesher, R., Ren, X., Thornberry, T., Carroll, M.A., Young, V., Shepson, P.B., Riemer, D., Apel, E., Campbell, C., 2004. Missing OH Reactivity in a Forest: Evidence for Unknown Reactive Biogenic VOCs. Science 304, 722–725. https://doi.org/10.1126/science.1094392

Ferek, R.J., Reid, J.S., Hobbs, P.V., Blake, D.R., Liousse, C., 1998. Emission factors of hydrocarbons, halocarbons, trace gases and particles from biomass burning in Brazil. J. Geophys. Res. Atmospheres 103, 32107–32118. https://doi.org/10.1029/98JD00692

Ferracci, V., Heimann, I., Abraham, N.L., Pyle, J.A., Archibald, A.T., 2018. Global modelling of the total OH reactivity: investigations on the "missing" OH sink and its atmospheric implications. Atmospheric Chem. Phys. 18, 7109–7129. https://doi.org/10.5194/acp-18-7109-2018

Flannigan, M., Cantin, A.S., Groot, W.J. de, Wotton, M., Newbery, A., Gowman, L.M., 2013. Global wildland fire season severity in the 21st century. For. Ecol. Manag. 294, 54–61. https://doi.org/10.1016/j.foreco.2012.10.022

Fortner, E.C., Zheng, J., Zhang, R., Berk Knighton, W., Volkamer, R.M., Sheehy, P., Molina, L., André, M., 2009. Measurements of Volatile Organic Compounds Using Proton Transfer Reaction – Mass Spectrometry during the MILAGRO 2006 Campaign. Atmospheric Chem. Phys. 9, 467–481. https://doi.org/10.5194/acp-9-467-2009

Franco, B., Blumenstock, T., Cho, C., Clarisse, L., Clerbaux, C., Coheur, P.-F., De Mazière, M., De Smedt, I., Dorn, H.-P., Emmerichs, T., Fuchs, H., Gkatzelis, G., Griffith, D.W.T., Gromov, S., Hannigan, J.W., Hase, F., Hohaus, T., Jones, N., Kerkweg, A., Kiendler-Scharr, A., Lutsch, E., Mahieu, E., Novelli, A., Ortega, I., Paton-Walsh, C., Pommier, M., Pozzer, A., Reimer, D., Rosanka, S., Sander, R., Schneider, M., Strong, K., Tillmann, R., Van Roozendael, M., Vereecken, L., Vigouroux, C., Wahner, A., Taraborrelli, D., 2021. Ubiquitous atmospheric production of organic acids mediated by cloud droplets. Nature 593, 233–237. https://doi.org/10.1038/s41586-021-03462-x

Friedli, H.R., Atlas, E., Stroud, V.R., Giovanni, L., Campos, T., Radke, L.F., 2001. Volatile organic trace gases emitted from North American wildfires. Glob. Biogeochem. Cycles 15, 435–452. https://doi.org/10.1029/2000GB001328

Galloway, J.N., Likens, G.E., Keene, W.C., Miller, J.M., 1982. The composition of precipitation in remote areas of the world. J. Geophys. Res. Oceans 87, 8771–8786. https://doi.org/10.1029/JC087iC11p08771

Garofalo, L.A., Pothier, M.A., Levin, E.J.T., Campos, T., Kreidenweis, S.M., Farmer, D.K., 2019. Emission and Evolution of Submicron Organic Aerosol in Smoke from Wildfires in the Western United States. ACS Earth Space Chem. 3, 1237–1247. https://doi.org/10.1021/acsearthspacechem.9b00125

Gilman, J.B., Lerner, B.M., Kuster, W.C., Goldan, P.D., Warneke, C., Veres, P.R., Roberts, J.M., de Gouw, J.A., Burling, I.R., Yokelson, R.J., 2015. Biomass burning emissions and potential air quality impacts of volatile organic compounds and other trace gases from fuels common in the US. Atmospheric Chem. Phys. 15, 13915–13938. https://doi.org/10.5194/acp-15-13915-2015

Glasius, M., Wessel, S., Christensen, C.S., Jacobsen, J.K., Jørgensen, H.E., Klitgaard, K.C., Petersen, L., Rasmussen, J.K., Hansen, T.S., Lohse, C., Boaretto, E., Heinemeier, J., 2000. Sources to formic acid studied by carbon isotopic analysis and air mass characterization. Atmos. Environ. 34, 2471–2479. https://doi.org/10.1016/S1352-2310(99)00416-1

Goode, J.G., Yokelson, R.J., Ward, D.E., Susott, R.A., Babbitt, R.E., Davies, M.A., Hao, W.M., 2000. Measurements of excess O3, CO2, CO, CH4, C2H4, C2H2, HCN, NO, NH3, HCOOH, CH3COOH, HCHO, and CH3OH in 1997 Alaskan biomass burning plumes by airborne Fourier transform

infrared spectroscopy (AFTIR). J. Geophys. Res. Atmospheres 105, 22147–22166. https://doi.org/10.1029/2000JD900287

Groot, W.J. de, Flannigan, M.D., Cantin, A.S., 2013. Climate change impacts on future boreal fire regimes. For. Ecol. Manag. 294, 35–44. https://doi.org/10.1016/j.foreco.2012.09.027

Grutter, M., Glatthor, N., Stiller, G.P., Fischer, H., Grabowski, U., Höpfner, M., Kellmann, S., Linden, A., von Clarmann, T., 2010. Global distribution and variability of formic acid as observed by MIPAS-ENVISAT. J. Geophys. Res. Atmospheres 115. https://doi.org/10.1029/2009JD012980

Gueneron, M., Erickson, M.H., VanderSchelden, G.S., Jobson, B.T., 2015. PTR-MS fragmentation patterns of gasoline hydrocarbons. Int. J. Mass Spectrom. 379, 97–109. https://doi.org/10.1016/j.ijms.2015.01.001

Guérette, E.-A., Paton-Walsh, C., Desservettaz, M., Smith, T.E.L., Volkova, L., Weston, C.J., Meyer, C.P., 2018. Emissions of trace gases from Australian temperate forest fires: emission factors and dependence on modified combustion efficiency. Atmospheric Chem. Phys. 18, 3717–3735. https://doi.org/10.5194/acp-18-3717-2018

Haase, K.B., Keene, W.C., Pszenny, A.A.P., Mayne, H.R., Talbot, R.W., Sive, B.C., 2012. Calibration and intercomparison of acetic acid measurements using proton-transfer-reaction mass spectrometry (PTR-MS). Atmospheric Meas. Tech. 5, 2739–2750. https://doi.org/10.5194/amt-5-2739-2012

Hansen, R.F., Blocquet, M., Schoemaecker, C., Léonardis, T., Locoge, N., Fittschen, C., Hanoune, B., Stevens, P.S., Sinha, V., Dusanter, S., 2015. Intercomparison of the comparative reactivity method (CRM) and pump–probe technique for measuring total OH reactivity in an urban environment. Atmospheric Meas. Tech. 8, 4243–4264. https://doi.org/10.5194/amt-8-4243-2015

Hatch, L.E., Jen, C.N., Kreisberg, N.M., Selimovic, V., Yokelson, R.J., Stamatis, C., York, R.A., Foster, D., Stephens, S.L., Goldstein, A.H., Barsanti, K.C., 2019. Highly Speciated Measurements of Terpenoids Emitted from Laboratory and Mixed-Conifer Forest Prescribed Fires. Environ. Sci. Technol. 53, 9418–9428. https://doi.org/10.1021/acs.est.9b02612

Hatch, L.E., Yokelson, R.J., Stockwell, C.E., Veres, P.R., Simpson, I.J., Blake, D.R., Orlando, J.J., Barsanti, K.C., 2017. Multi-instrument comparison and compilation of non-methane organic gas emissions from biomass burning and implications for smoke-derived secondary organic aerosol precursors. Atmospheric Chem. Phys. 17, 1471–1489. https://doi.org/10.5194/acp-17-1471-2017

Heald, C.L., de Gouw, J., Goldstein, A.H., Guenther, A.B., Hayes, P.L., Hu, W., Isaacman-VanWertz, G., Jimenez, J.L., Keutsch, F.N., Koss, A.R., Misztal, P.K., Rappenglück, B., Roberts, J.M., Stevens, P.S., Washenfelder, R.A., Warneke, C., Young, C.J., 2020. Contrasting Reactive Organic Carbon Observations in the Southeast United States (SOAS) and Southern California (CalNex). Environ. Sci. Technol. 54, 14923–14935. https://doi.org/10.1021/acs.est.0c05027

Higuera, P.E., Shuman, B.N., Wolf, K.D., 2021. Rocky Mountain subalpine forests now burning more than any time in recent millennia. Proc. Natl. Acad. Sci. 118. https://doi.org/10.1073/pnas.2103135118

Hobbs, P.V., Sinha, P., Yokelson, R.J., Christian, T.J., Blake, D.R., Gao, S., Kirchstetter, T.W., Novakov, T., Pilewskie, P., 2003. Evolution of gases and particles from a savanna fire in South Africa. J. Geophys. Res. Atmospheres 108, 8485. https://doi.org/10.1029/2002JD002352

Holder, A.L., Gullett, B.K., Urbanski, S.P., Elleman, R., O'Neill, S., Tabor, D., Mitchell, W., Baker, K.R., 2017. Emissions from prescribed burning of agricultural fields in the Pacific Northwest. Atmos. Environ. 166, 22–33. https://doi.org/10.1016/j.atmosenv.2017.06.043

Hornbrook, R.S., Blake, D.R., Diskin, G.S., Fried, A., Fuelberg, H.E., Meinardi, S., Mikoviny, T., Richter, D., Sachse, G.W., Vay, S.A., Walega, J., Weibring, P., Weinheimer, A.J., Wiedinmyer, C., Wisthaler, A., Hills, A., Riemer, D.D., Apel, E.C., 2011. Observations of nonmethane organic compounds during ARCTAS; Part 1: Biomass burning emissions and plume enhancements. Atmospheric Chem. Phys. 11, 11103–11130. https://doi.org/10.5194/acp-11-11103-2011

Hunter, J.F., Day, D.A., Palm, B.B., Yatavelli, R.L.N., Chan, A.W.H., Kaser, L., Cappellin, L., Hayes, P.L., Cross, E.S., Carrasquillo, A.J., Campuzano-Jost, P., Stark, H., Zhao, Y., Hohaus, T., Smith, J.N., Hansel, A., Karl, T., Goldstein, A.H., Guenther, A., Worsnop, D.R., Thornton, J.A., Heald, C.L., Jimenez, J.L., Kroll, J.H., 2017. Comprehensive characterization of atmospheric organic carbon at a forested site. Nat. Geosci. 10, 748–753. https://doi.org/10.1038/ngeo3018

Jacob, D.J., 1986. Chemistry of OH in remote clouds and its role in the production of formic acid and peroxymonosulfate. J. Geophys. Res. Atmospheres 91, 9807–9826. https://doi.org/10.1029/JD091iD09p09807

110

Jaffe, D.A., O'Neill, S.M., Larkin, N.K., Holder, A.L., Peterson, D.L., Halofsky, J.E., Rappold, A.G., 2020. Wildfire and prescribed burning impacts on air quality in the United States. J. Air Waste Manag. Assoc. 70, 583–615. https://doi.org/10.1080/10962247.2020.1749731

Jaffe, D.A., Wigder, N.L., 2012. Ozone production from wildfires: A critical review. Atmos. Environ. 51, 1–10. https://doi.org/10.1016/j.atmosenv.2011.11.063

Jiang, J., Carter, W.P.L., Cocker, D.R., Barsanti, K.C., 2020. Development and Evaluation of a Detailed Mechanism for Gas-Phase Atmospheric Reactions of Furans. ACS Earth Space Chem. 4, 1254–1268. https://doi.org/10.1021/acsearthspacechem.0c00058

Jin, L., Permar, W., Selimovic, V., Ketcherside, D., Yokelson, R.J., Hornbrook, R.S., Apel, E.C., Ku, I.-T., Collett Jr., J.L., Sullivan, A.P., Jaffe, D.A., Pierce, J.R., Fried, A., Coggon, M.M., Gkatzelis, G.I., Warneke, C., Fischer, E.V., Hu, L., 2022. Constraining emissions of volatile organic compounds from western US wildfires with WE-CAN and FIREX-AQ airborne observations. EGUsphere 2022, 1–39. https://doi.org/10.5194/egusphere-2022-1107

Jolly, W., 2015. Climate-induced variations in global wildfire danger from 1979 to 2013. Nat. Commun. 6, 7537. https://doi.org/10.1038/ncomms8537

Juncosa Calahorrano, J.F., Lindaas, J., O'Dell, K., Palm, B.B., Peng, Q., Flocke, F., Pollack, I.B., Garofalo, L.A., Farmer, D.K., Pierce, J.R., Collett, J.L., Weinheimer, A., Campos, T., Hornbrook, R.S., Hall, S.R., Ullmann, K., Pothier, M.A., Apel, E.C., Permar, W., Hu, L., Hills, A.J., Montzka, D., Tyndall, G., Thornton, J.A., Fischer, E.V., 2021. Daytime Oxidized Reactive Nitrogen Partitioning in Western U.S. Wildfire Smoke Plumes. J. Geophys. Res. Atmospheres 126. https://doi.org/10.1029/2020JD033484

Kaiser, J.W., Heil, A., Andreae, M.O., Benedetti, A., Chubarova, N., Jones, L., Morcrette, J.-J., Razinger, M., Schultz, M.G., Suttie, M., van der Werf, G.R., 2012. Biomass burning emissions estimated with a global fire assimilation system based on observed fire radiative power. Biogeosciences 9, 527–554. https://doi.org/10.5194/bg-9-527-2012

Karl, T., Hansel, A., Cappellin, L., Kaser, L., Herdlinger-Blatt, I., Jud, W., 2012. Selective measurements of isoprene and 2-methyl-3-buten-2-ol based on NO^+ ionization mass spectrometry. Atmospheric Chem. Phys. 12, 11877–11884. https://doi.org/10.5194/acp-12-11877-2012

Keene, W.C., Galloway, J.N., Holden Jr., J.D., 1983. Measurement of weak organic acidity in precipitation from remote areas of the world. J. Geophys. Res. Oceans 88, 5122–5130. https://doi.org/10.1029/JC088iC09p05122

Kirchner, F., Jeanneret, F., Clappier, A., Krüger, B., van den Bergh, H., Calpini, B., 2001. Total VOC reactivity in the planetary boundary layer: 2. A new indicator for determining the sensitivity of the ozone production to VOC and NO x. J. Geophys. Res. Atmospheres 106, 3095–3110. https://doi.org/10.1029/2000JD900603

Koss, A., Yuan, B., Warneke, C., Gilman, J.B., Lerner, B.M., Veres, P.R., Peischl, J., Eilerman, S., Wild, R., Brown, S.S., Thompson, C.R., Ryerson, T., Hanisco, T., Wolfe, G.M., Clair, J.M.St., Thayer, M., Keutsch, F.N., Murphy, S., de Gouw, J., 2017. Observations of VOC emissions and photochemical products over US oil- and gas-producing regions using high-resolution $H_3O^{+\$}$ CIMS (PTR-ToF-MS). Atmospheric Meas. Tech. 10, 2941–2968. https://doi.org/10.5194/amt-10-2941-2017

Koss, A.R., Sekimoto, K., Gilman, J.B., Selimovic, V., Coggon, M.M., Zarzana, K.J., Yuan, B., Lerner, B.M., Brown, S.S., Jimenez, J.L., Krechmer, J., Roberts, J.M., Warneke, C., Yokelson, R.J., de Gouw, J., 2018. Non-methane organic gas emissions from biomass burning: identification, quantification, and emission factors from PTR-ToF during the FIREX 2016 laboratory experiment. Atmospheric Chem. Phys. 18, 3299–3319. https://doi.org/10.5194/acp-18-3299-2018

Kovacs, T.A., Brune, W.H., Harder, H., Martinez, M., Simpas, J.B., Frost, G.J., Williams, E., Jobson, T., Stroud, C., Young, V., Fried, A., Wert, B., 2003. Direct measurements of urban OH reactivity during Nashville SOS in summer 1999. J. Environ. Monit. 5, 68–74. https://doi.org/10.1039/B204339D

Kumar, V., Chandra, B.P., Sinha, V., 2018. Large unexplained suite of chemically reactive compounds present in ambient air due to biomass fires. Sci. Rep. 8, 626. https://doi.org/10.1038/s41598-017-19139-3

Larkin, N.K., Raffuse, S.M., Strand, T.M., 2014. Wildland fire emissions, carbon, and climate: U.S. emissions inventories. Wildland Fire Emiss. Carbon Clim. Sci. Overv. Knowl. Needs 317, 61–69. https://doi.org/10.1016/j.foreco.2013.09.012

Le Breton, M., McGillen, M.R., Muller, J.B.A., Bacak, A., Shallcross, D.E., Xiao, P., Huey, L.G., Tanner, D., Coe, H., Percival, C.J., 2012. Airborne observations of formic acid using a chemical ionization

mass spectrometer. Atmospheric Meas. Tech. 5, 3029–3039. https://doi.org/10.5194/amt-5-3029-2012

Lebegue, B., Schmidt, M., Ramonet, M., Wastine, B., Yver Kwok, C., Laurent, O., Belviso, S., Guemri, A., Philippon, C., Smith, J., Conil, S., 2016. Comparison of nitrous oxide (N$_2$O) analyzers for high-precision measurements of atmospheric mole fractions. Atmospheric Meas. Tech. 9, 1221–1238. https://doi.org/10.5194/amt-9-1221-2016

Lee, B.H., Lopez-Hilfiker, F.D., Mohr, C., Kurtén, T., Worsnop, D.R., Thornton, J.A., 2014. An Iodide-Adduct High-Resolution Time-of-Flight Chemical-Ionization Mass Spectrometer: Application to Atmospheric Inorganic and Organic Compounds. Environ. Sci. Technol. 48, 6309–6317. https://doi.org/10.1021/es500362a

Lee, B.H., Lopez-Hilfiker, F.D., Veres, P.R., McDuffie, E.E., Fibiger, D.L., Sparks, T.L., Ebben, C.J., Green, J.R., Schroder, J.C., Campuzano-Jost, P., Iyer, S., D'Ambro, E.L., Schobesberger, S., Brown, S.S., Wooldridge, P.J., Cohen, R.C., Fiddler, M.N., Bililign, S., Jimenez, J.L., Kurtén, T., Weinheimer, A.J., Jaegle, L., Thornton, J.A., 2018. Flight Deployment of a High-Resolution Time-of-Flight Chemical Ionization Mass Spectrometer: Observations of Reactive Halogen and Nitrogen Oxide Species. J. Geophys. Res. Atmospheres 123, 7670–7686. https://doi.org/10.1029/2017JD028082

Lee, X., Huang, D., Liu, Q., Liu, X., Zhou, H., Wang, Q., Ma, Y., 2021. Underrated primary biogenic origin and lifetime of atmospheric formic and acetic acid. Sci. Rep. 11, 7176. https://doi.org/10.1038/s41598-021-86542-2

Lelieveld, J., Gromov, S., Pozzer, A., Taraborrelli, D., 2016. Global tropospheric hydroxyl distribution, budget and reactivity. Atmospheric Chem. Phys. 16, 12477–12493. https://doi.org/10.5194/acp-16-12477-2016

Liang, Y., Weber, R.J., Misztal, P.K., Jen, C.N., Goldstein, A.H., 2022. Aging of Volatile Organic Compounds in October 2017 Northern California Wildfire Plumes. Environ. Sci. Technol. 56, 1557–1567. https://doi.org/10.1021/acs.est.1c05684

Liao, J., Wolfe, G.M., Hannun, R.A., St. Clair, J.M., Hanisco, T.F., Gilman, J.B., Lamplugh, A., Selimovic, V., Diskin, G.S., Nowak, J.B., Halliday, H.S., DiGangi, J.P., Hall, S.R., Ullmann, K., Holmes, C.D., Fite, C.H., Agastra, A., Ryerson, T.B., Peischl, J., Bourgeois, I., Warneke, C., Coggon, M.M., Gkatzelis, G.I., Sekimoto, K., Fried, A., Richter, D., Weibring, P., Apel, E.C., Hornbrook, R.S., Brown, S.S., Womack, C.C., Robinson, M.A., Washenfelder, R.A., Veres, P.R., Neuman, J.A., 2021. Formaldehyde evolution in US wildfire plumes during the Fire Influence on Regional to Global Environments and Air Quality experiment (FIREX-AQ). Atmospheric Chem. Phys. 21, 18319–18331. https://doi.org/10.5194/acp-21-18319-2021

Lill, E., Lindaas, J., Juncosa Calahorrano, J.F., Campos, T., Flocke, F., Apel, E.C., Hornbrook, R.S., Hills, A., Jarnot, A., Blake, N., Permar, W., Hu, L., Weinheimer, A., Tyndall, G., Montzka, D.D. e, Hall, S.R., Ullmann, K., Thornton, J., Palm, B.B., Peng, Q., Pollack, I., Fischer, E.V., 2022. Wildfire-driven changes in the abundance of gas-phase pollutants in the city of Boise, ID during summer 2018. Atmospheric Pollut. Res. 13, 101269. https://doi.org/10.1016/j.apr.2021.101269

Lindaas, J., Pollack, I.B., Calahorrano, J.J., O'Dell, K., Garofalo, L.A., Pothier, M.A., Farmer, D.K., Kreidenweis, S.M., Campos, T., Flocke, F., Weinheimer, A.J., Montzka, D.D., Tyndall, G.S., Apel, E.C., Hills, A.J., Hornbrook, R.S., Palm, B.B., Peng, Q., Thornton, J.A., Permar, W., Wielgasz, C., Hu, L., Pierce, J.R., Collett Jr., J.L., Sullivan, A.P., Fischer, E.V., 2021a. Empirical Insights Into the Fate of Ammonia in Western U.S. Wildfire Smoke Plumes. J. Geophys. Res. Atmospheres 126, e2020JD033730. https://doi.org/10.1029/2020JD033730

Lindaas, J., Pollack, I.B., Garofalo, L.A., Pothier, M.A., Farmer, D.K., Kreidenweis, S.M., Campos, T.L., Flocke, F., Weinheimer, A.J., Montzka, D.D., Tyndall, G.S., Palm, B.B., Peng, Q., Thornton, J.A., Permar, W., Wielgasz, C., Hu, L., Ottmar, R.D., Restaino, J.C., Hudak, A.T., Ku, I.-T., Zhou, Y., Sive, B.C., Sullivan, A., Collett Jr, J.L., Fischer, E.V., 2021b. Emissions of Reactive Nitrogen From Western U.S. Wildfires During Summer 2018. J. Geophys. Res. Atmospheres 126, e2020JD032657. https://doi.org/10.1029/2020JD032657

Lindaas, J., Pollack, I.B., Garofalo, L.A., Pothier, M.A., Farmer, D.K., Kreidenweis, S.M., Campos, T.L., Flocke, F., Weinheimer, A.J., Montzka, D.D., Tyndall, G.S., Palm, B.B., Peng, Q., Thornton, J.A., Permar, W., Wielgasz, C., Hu, L., Ottmar, R.D., Restaino, J.C., Hudak, A.T., Ku, I.-T., Zhou, Y., Sive, B.C., Sullivan, A., Collett Jr, J.L., Fischer, E.V., 2021c. Emissions of Reactive Nitrogen From Western U.S. Wildfires During Summer 2018. J. Geophys. Res. Atmospheres 126, e2020JD032657. https://doi.org/10.1029/2020JD032657

Link, M.F., Nguyen, T.B., Bates, K., Müller, J.-F., Farmer, D.K., 2020. Can Isoprene Oxidation Explain High Concentrations of Atmospheric Formic and Acetic Acid over Forests? ACS Earth Space Chem. 4, 730–740. https://doi.org/10.1021/acsearthspacechem.0c00010

Littell, J.S., McKenzie, D., Wan, H.Y., Cushman, S.A., 2018. Climate Change and Future Wildfire in the Western United States: An Ecological Approach to Nonstationarity. Earths Future 6, 1097–1111. https://doi.org/10.1029/2018EF000878

Liu, J.C., Pereira, G., Uhl, S.A., Bravo, M.A., Bell, M.L., 2015. A systematic review of the physical health impacts from non-occupational exposure to wildfire smoke. Environ. Res. 136, 120–132. https://doi.org/10.1016/j.envres.2014.10.015

Liu, X., Huey, L.G., Yokelson, R.J., Selimovic, V., Simpson, I.J., Müller, M., Jimenez, J.L., Campuzano-Jost, P., Beyersdorf, A.J., Blake, D.R., Butterfield, Z., Choi, Y., Crounse, J.D., Day, D.A., Diskin, G.S., Dubey, M.K., Fortner, E., Hanisco, T.F., Hu, W., King, L.E., Kleinman, L., Meinardi, S., Mikoviny, T., Onasch, T.B., Palm, B.B., Peischl, J., Pollack, I.B., Ryerson, T.B., Sachse, G.W., Sedlacek, A.J., Shilling, J.E., Springston, S., St. Clair, J.M., Tanner, D.J., Teng, A.P., Wennberg, P.O., Wisthaler, A., Wolfe, G.M., 2017. Airborne measurements of western U.S. wildfire emissions: Comparison with prescribed burning and air quality implications: Western U.S. Wildfire Emissions. J. Geophys. Res. Atmospheres 122, 6108–6129. https://doi.org/10.1002/2016JD026315

Lonsdale, C.R., Alvarado, M.J., Hodshire, A.L., Ramnarine, E., Pierce, J.R., 2020. Simulating the forest fire plume dispersion, chemistry, and aerosol formation using SAM-ASP version 1.0. Geosci. Model Dev. 13, 4579–4593. https://doi.org/10.5194/gmd-13-4579-2020

Lou, S., Holland, F., Rohrer, F., Lu, K., Bohn, B., Brauers, T., Chang, C.C., Fuchs, H., Häseler, R., Kita, K., Kondo, Y., Li, X., Shao, M., Zeng, L., Wahner, A., Zhang, Y., Wang, W., Hofzumahaus, A., 2010. Atmospheric OH reactivities in the Pearl River Delta – China in summer 2006: measurement and model results. Atmospheric Chem. Phys. 10, 11243–11260. https://doi.org/10.5194/acp-10-11243-2010

Mao, J., Ren, X., Brune, W.H., Olson, J.R., Crawford, J.H., Fried, A., Huey, L.G., Cohen, R.C., Heikes, B., Singh, H.B., Blake, D.R., Sachse, G.W., Diskin, G.S., Hall, S.R., Shetter, R.E., 2009. Airborne measurement of OH reactivity during INTEX-B. Atmospheric Chem. Phys. 9, 163–173. https://doi.org/10.5194/acp-9-163-2009

Mao, J., Ren, X., Chen, S., Brune, W.H., Chen, Z., Martinez, M., Harder, H., Lefer, B., Rappenglück, B., Flynn, J., Leuchner, M., 2010. Atmospheric oxidation capacity in the summer of Houston 2006: Comparison with summer measurements in other metropolitan studies. Atmos. Environ. 44, 4107–4115. https://doi.org/10.1016/j.atmosenv.2009.01.013

McClure, C.D., Jaffe, D.A., 2018. US particulate matter air quality improves except in wildfire-prone areas. Proc. Natl. Acad. Sci. 115, 7901–7906. https://doi.org/10.1073/pnas.1804353115

McKeen, S.A., Wotawa, G., Parrish, D.D., Holloway, J.S., Buhr, M.P., Hübler, G., Fehsenfeld, F.C., Meagher, J.F., 2002. Ozone production from Canadian wildfires during June and July of 1995. J. Geophys. Res. Atmospheres 107, ACH 7-1-ACH 7-25. https://doi.org/10.1029/2001JD000697

McKenzie, L.M., Hao, W.Min., Richards, G.N., Ward, D.E., 1995. Measurement and Modeling of Air Toxins from Smoldering Combustion of Biomass. Environ. Sci. Technol. 29, 2047–2054. https://doi.org/10.1021/es00008a025

Metzger, S., Mihalopoulos, N., Lelieveld, J., 2006. Importance of mineral cations and organics in gas-aerosol partitioning of reactive nitrogen compounds: case study based on MINOS results. Atmospheric Chem. Phys. 6, 2549–2567. https://doi.org/10.5194/acp-6-2549-2006

Millet, D.B., 2012. Natural atmospheric acidity. Nat. Geosci. 5, 8–9. https://doi.org/10.1038/ngeo1361

Millet, D.B., Alwe, H.D., Chen, X., Deventer, M.J., Griffis, T.J., Holzinger, R., Bertman, S.B., Rickly, P.S., Stevens, P.S., Léonardis, T., Locoge, N., Dusanter, S., Tyndall, G.S., Alvarez, S.L., Erickson, M.H., Flynn, J.H., 2018. Bidirectional Ecosystem–Atmosphere Fluxes of Volatile Organic Compounds Across the Mass Spectrum: How Many Matter? ACS Earth Space Chem. 2, 764–777. https://doi.org/10.1021/acsearthspacechem.8b00061

Millet, D.B., Baasandorj, M., Farmer, D.K., Thornton, J.A., Baumann, K., Brophy, P., Chaliyakunnel, S., de Gouw, J.A., Graus, M., Hu, L., Koss, A., Lee, B.H., Lopez-Hilfiker, F.D., Neuman, J.A., Paulot, F., Peischl, J., Pollack, I.B., Ryerson, T.B., Warneke, C., Williams, B.J., Xu, J., 2015. A large and ubiquitous source of atmospheric formic acid. Atmospheric Chem. Phys. 15, 6283–6304. https://doi.org/10.5194/acp-15-6283-2015

Millet, D.B., Guenther, A., Siegel, D.A., Nelson, N.B., Singh, H.B., de Gouw, J.A., Warneke, C., Williams, J., Eerdekens, G., Sinha, V., Karl, T., Flocke, F., Apel, E., Riemer, D.D., Palmer, P.I., Barkley, M., 2010. Global atmospheric budget of acetaldehyde: 3-D model analysis and constraints from in-situ and satellite observations. Atmospheric Chem. Phys. 10, 3405–3425. https://doi.org/10.5194/acp-10-3405-2010

Müller, J.-F., Stavrakou, T., Peeters, J., 2019. Chemistry and deposition in the Model of Atmospheric composition at Global and Regional scales using Inversion Techniques for Trace gas Emissions (MAGRITTE v1.1) – Part 1: Chemical mechanism. Geosci. Model Dev. 12, 2307–2356. https://doi.org/10.5194/gmd-12-2307-2019

Müller, M., Anderson, B.E., Beyersdorf, A.J., Crawford, J.H., Diskin, G.S., Eichler, P., Fried, A., Keutsch, F.N., Mikoviny, T., Thornhill, K.L., Walega, J.G., Weinheimer, A.J., Yang, M., Yokelson, R.J., Wisthaler, A., 2016. In situ measurements and modeling of reactive trace gases in a small biomass burning plume. Atmospheric Chem. Phys. 16, 3813–3824. https://doi.org/10.5194/acp-16-3813-2016

Murray, L.T., Fiore, A.M., Shindell, D.T., Naik, V., Horowitz, L.W., 2021. Large uncertainties in global hydroxyl projections tied to fate of reactive nitrogen and carbon. Proc. Natl. Acad. Sci. 118, e2115204118. https://doi.org/10.1073/pnas.2115204118

Naik, V., Voulgarakis, A., Fiore, A.M., Horowitz, L.W., Lamarque, J.-F., Lin, M., Prather, M.J., Young, P.J., Bergmann, D., Cameron-Smith, P.J., Cionni, I., Collins, W.J., Dalsøren, S.B., Doherty, R., Eyring, V., Faluvegi, G., Folberth, G.A., Josse, B., Lee, Y.H., MacKenzie, I.A., Nagashima, T., van Noije, T.P.C., Plummer, D.A., Righi, M., Rumbold, S.T., Skeie, R., Shindell, D.T., Stevenson, D.S., Strode, S., Sudo, K., Szopa, S., Zeng, G., 2013. Preindustrial to present-day changes in tropospheric hydroxyl radical and methane lifetime from the Atmospheric Chemistry and Climate Model Intercomparison Project (ACCMIP). Atmospheric Chem. Phys. 13, 5277–5298. https://doi.org/10.5194/acp-13-5277-2013

Ninneman, M., Jaffe, D.A., 2021. The impact of wildfire smoke on ozone production in an urban area: Insights from field observations and photochemical box modeling. Atmos. Environ. 267, 118764. https://doi.org/10.1016/j.atmosenv.2021.118764

Nölscher, A.C., Yañez-Serrano, A.M., Wolff, S., de Araujo, A.C., Lavrič, J.V., Kesselmeier, J., Williams, J., 2016. Unexpected seasonality in quantity and composition of Amazon rainforest air reactivity. Nat. Commun. 7, 10383. https://doi.org/10.1038/ncomms10383

O'Dell, K., Ford, B., Fischer, E.V., Pierce, J.R., 2019. Contribution of Wildland-Fire Smoke to US PM2.5 and Its Influence on Recent Trends. Environ. Sci. Technol. 53, 1797–1804. https://doi.org/10.1021/acs.est.8b05430

O'Dell, K., Hornbrook, R.S., Permar, W., Levin, E.J.T., Garofalo, L.A., Apel, E.C., Blake, N.J., Jarnot, A., Pothier, M.A., Farmer, D.K., Hu, L., Campos, T., Ford, B., Pierce, J.R., Fischer, E.V., 2020. Hazardous Air Pollutants in Fresh and Aged Western US Wildfire Smoke and Implications for Long-Term Exposure. Environ. Sci. Technol. 54, 11838–11847. https://doi.org/10.1021/acs.est.0c04497

Ottmar, R.D., 2014. Wildland fire emissions, carbon, and climate: Modeling fuel consumption. Wildland Fire Emiss. Carbon Clim. Sci. Overv. Knowl. Needs 317, 41–50. https://doi.org/10.1016/j.foreco.2013.06.010

Pagonis, D., Sekimoto, K., de Gouw, J., 2019. A Library of Proton-Transfer Reactions of H3O+ Ions Used for Trace Gas Detection. J. Am. Soc. Mass Spectrom. 30, 1330–1335. https://doi.org/10.1007/s13361-019-02209-3

Palm, B.B., Liu, X., Jimenez, J.L., Thornton, J.A., 2019. Performance of a new coaxial ion–molecule reaction region for low-pressure chemical ionization mass spectrometry with reduced instrument wall interactions. Atmospheric Meas. Tech. 12, 5829–5844. https://doi.org/10.5194/amt-12-5829-2019

Palm, B.B., Peng, Q., Fredrickson, C.D., Lee, B.H., Garofalo, L.A., Pothier, M.A., Kreidenweis, S.M., Farmer, D.K., Pokhrel, R.P., Shen, Y., Murphy, S.M., Permar, W., Hu, L., Campos, T.L., Hall, S.R., Ullmann, K., Zhang, X., Flocke, F., Fischer, E.V., Thornton, J.A., 2020. Quantification of organic aerosol and brown carbon evolution in fresh wildfire plumes. Proc. Natl. Acad. Sci. 117, 29469–29477. https://doi.org/10.1073/pnas.2012218117

Palm, B.B., Peng, Q., Hall, S.R., Ullmann, K., Campos, T.L., Weinheimer, A., Montzka, D., Tyndall, G., Permar, W., Hu, L., Flocke, F., Fischer, E.V., Thornton, J.A., 2021. Spatially Resolved

Photochemistry Impacts Emissions Estimates in Fresh Wildfire Plumes. Geophys. Res. Lett. 48, e2021GL095443. https://doi.org/10.1029/2021GL095443

Pan, X., Ichoku, C., Chin, M., Bian, H., Darmenov, A., Colarco, P., Ellison, L., Kucsera, T., da Silva, A., Wang, J., Oda, T., Cui, G., 2020. Six global biomass burning emission datasets: intercomparison and application in one global aerosol model. Atmospheric Chem. Phys. 20, 969–994. https://doi.org/10.5194/acp-20-969-2020

Paulot, F., Wunch, D., Crounse, J.D., Toon, G.C., Millet, D.B., DeCarlo, P.F., Vigouroux, C., Deutscher, N.M., González Abad, G., Notholt, J., Warneke, T., Hannigan, J.W., Warneke, C., de Gouw, J.A., Dunlea, E.J., De Mazière, M., Griffith, D.W.T., Bernath, P., Jimenez, J.L., Wennberg, P.O., 2011. Importance of secondary sources in the atmospheric budgets of formic and acetic acids. Atmospheric Chem. Phys. 11, 1989–2013. https://doi.org/10.5194/acp-11-1989-2011

Peng, Q., Palm, B.B., Fredrickson, C.D., Lee, B.H., Hall, S.R., Ullmann, K., Campos, T., Weinheimer, A.J., Apel, E.C., Flocke, F., Permar, W., Hu, L., Garofalo, L.A., Pothier, M.A., Farmer, D.K., Ku, I.-T., Sullivan, A.P., Collett, J.L., Fischer, E., Thornton, J.A., 2021. Observations and Modeling of NOx Photochemistry and Fate in Fresh Wildfire Plumes. ACS Earth Space Chem. 5, 2652–2667. https://doi.org/10.1021/acsearthspacechem.1c00086

Peng, Q., Palm, B.B., Melander, K.E., Lee, B.H., Hall, S.R., Ullmann, K., Campos, T., Weinheimer, A.J., Apel, E.C., Hornbrook, R.S., Hills, A.J., Montzka, D.D., Flocke, F., Hu, L., Permar, W., Wielgasz, C., Lindaas, J., Pollack, I.B., Fischer, E.V., Bertram, T.H., Thornton, J.A., 2020. HONO Emissions from Western U.S. Wildfires Provide Dominant Radical Source in Fresh Wildfire Smoke. Environ. Sci. Technol. 54, 5954–5963. https://doi.org/10.1021/acs.est.0c00126

Permar, W., Jin, L., Peng, Q., O'Dell, K., Lill, E., Selimovic, V., Yokelson, R.J., Hornbrook, R.S., Hills, A.J., Apel, E.C., Ku, I.-T., Zhou, Y., Sive, B.C., Sullivan, A.P., Collett, J.L., Palm, B.B., Thornton, J.A., Flocke, F., Fischer, E.V., Hu, L., 2023. Atmospheric OH reactivity in the western United States determined from comprehensive gas-phase measurements during WE-CAN. Environ. Sci. Atmospheres. https://doi.org/10.1039/D2EA00063F

Permar, W., Wang, Q., Selimovic, V., Wielgasz, C., Yokelson, R.J., Hornbrook, R.S., Hills, A.J., Apel, E.C., Ku, I.-T., Zhou, Y., Sive, B.C., Sullivan, A.P., Collett Jr, J.L., Campos, T.L., Palm, B.B., Peng, Q., Thornton, J.A., Garofalo, L.A., Farmer, D.K., Kreidenweis, S.M., Levin, E.J.T., DeMott, P.J., Flocke, F., Fischer, E.V., Hu, L., 2021. Emissions of Trace Organic Gases From Western U.S. Wildfires Based on WE-CAN Aircraft Measurements. J. Geophys. Res. Atmospheres 126, e2020JD033838. https://doi.org/10.1029/2020JD033838

Pommier, M., Clerbaux, C., Coheur, P.-F., 2017. Determination of enhancement ratios of HCOOH relative to CO in biomass burning plumes by the Infrared Atmospheric Sounding Interferometer (IASI). Atmospheric Chem. Phys. 17, 11089–11105. https://doi.org/10.5194/acp-17-11089-2017

Prichard, S.J., O'Neill, S.M., Eagle, P., Andreu, A.G., Drye, B., Dubowy, J., Urbanski, S., Strand, T.M., 2020. Wildland fire emission factors in North America: synthesis of existing data, measurement needs and management applications. Int. J. Wildland Fire 29, 132. https://doi.org/10.1071/WF19066

R Core Team, 2019. R: A Language and Environment for Statistical Computing. R Foundation for Statistical Computing, Vienna, Austria.

Reid, C.E., Brauer, M., Johnston, F.H., Jerrett, M., Balmes, J.R., Elliott, C.T., 2016. Critical Review of Health Impacts of Wildfire Smoke Exposure. Environ. Health Perspect. 124, 1334–1343. https://doi.org/10.1289/ehp.1409277

Ren, X., Harder, H., Martinez, M., Lesher, R.L., Oliger, A., Simpas, J.B., Brune, W.H., Schwab, J.J., Demerjian, K.L., He, Y., Zhou, X., Gao, H., 2003. OH and HO2 Chemistry in the urban atmosphere of New York City. Atmos. Environ. 37, 3639–3651. https://doi.org/10.1016/S1352-2310(03)00459-X

Ridley, B.A., Grahek, F.E., 1990. A Small, Low Flow, High Sensitivity Reaction Vessel for NO Chemiluminescence Detectors. J. Atmospheric Ocean. Technol. 7, 307–311. https://doi.org/10.1175/1520-0426(1990)007<0307:ASLFHS>2.0.CO;2

Ridley, B.A., Grahek, F.E., Walega, J.G., 1992. A Small High-Sensitivity, Medium-Response Ozone Detector Suitable for Measurements from Light Aircraft. J. Atmospheric Ocean. Technol. 9, 142–148. https://doi.org/10.1175/1520-0426(1992)009<0142:ASHSMR>2.0.CO;2

Roberts, J.M., Stockwell, C.E., Yokelson, R.J., de Gouw, J., Liu, Y., Selimovic, V., Koss, A.R., Sekimoto, K., Coggon, M.M., Yuan, B., Zarzana, K.J., Brown, S.S., Santin, C., Doerr, S.H., Warneke, C., 2020. The nitrogen budget of laboratory-simulated western US wildfires during the FIREX 2016

Fire Lab study. Atmospheric Chem. Phys. 20, 8807–8826. https://doi.org/10.5194/acp-20-8807-2020

Robinson, M.A., Decker, Z.C.J., Barsanti, K.C., Coggon, M.M., Flocke, F.M., Franchin, A., Fredrickson, C.D., Gilman, J.B., Gkatzelis, G.I., Holmes, C.D., Lamplugh, A., Lavi, A., Middlebrook, A.M., Montzka, D.M., Palm, B.B., Peischl, J., Pierce, B., Schwantes, R.H., Sekimoto, K., Selimovic, V., Tyndall, G.S., Thornton, J.A., Van Rooy, P., Warneke, C., Weinheimer, A.J., Brown, S.S., 2021. Variability and Time of Day Dependence of Ozone Photochemistry in Western Wildfire Plumes. Environ. Sci. Technol. 55, 10280–10290. https://doi.org/10.1021/acs.est.1c01963

Rocca, M.E., Brown, P.M., MacDonald, L.H., Carrico, C.M., 2014. Climate change impacts on fire regimes and key ecosystem services in Rocky Mountain forests. For. Ecol. Manag. 327, 290–305. https://doi.org/10.1016/j.foreco.2014.04.005

RStudio Team, 2020. RStudio: Integrated Development Environment for R. RStudio, PBC., Boston, MA.

Russo, R.S., Zhou, Y., White, M.L., Mao, H., Talbot, R., Sive, B.C., 2010. Multi-year (2004–2008) record of nonmethane hydrocarbons and halocarbons in New England: seasonal variations and regional sources. Atmospheric Chem. Phys. 10, 4909–4929. https://doi.org/10.5194/acp-10-4909-2010

Safieddine, S.A., Heald, C.L., Henderson, B.H., 2017. The global nonmethane reactive organic carbon budget: A modeling perspective. Geophys. Res. Lett. 44, 3897–3906. https://doi.org/10.1002/2017GL072602

Sanchez, D., Seco, R., Gu, D., Guenther, A., Mak, J., Lee, Y., Kim, D., Ahn, J., Blake, D., Herndon, S., Jeong, D., Sullivan, J.T., Mcgee, T., Park, R., Kim, S., 2021. Contributions to OH reactivity from unexplored volatile organic compounds measured by PTR-ToF-MS – a case study in a suburban forest of the Seoul metropolitan area during the Korea–United States Air Quality Study (KORUS-AQ) 2016. Atmospheric Chem. Phys. 21, 6331–6345. https://doi.org/10.5194/acp-21-6331-2021

Santín, C., Doerr, S.H., Preston, C.M., González-Rodríguez, G., 2015. Pyrogenic organic matter production from wildfires: a missing sink in the global carbon cycle. Glob. Change Biol. 21, 1621–1633. https://doi.org/10.1111/gcb.12800

Schwarz, J.P., Gao, R.S., Spackman, J.R., Watts, L.A., Thomson, D.S., Fahey, D.W., Ryerson, T.B., Peischl, J., Holloway, J.S., Trainer, M., Frost, G.J., Baynard, T., Lack, D.A., de Gouw, J.A., Warneke, C., Del Negro, L.A., 2008. Measurement of the mixing state, mass, and optical size of individual black carbon particles in urban and biomass burning emissions. Geophys. Res. Lett. 35. https://doi.org/10.1029/2008GL033968

Sekimoto, K., Koss, A.R., Gilman, J.B., Selimovic, V., Coggon, M.M., Zarzana, K.J., Yuan, B., Lerner, B.M., Brown, S.S., Warneke, C., Yokelson, R.J., Roberts, J.M., de Gouw, J., 2018. High- and low-temperature pyrolysis profiles describe volatile organic compound emissions from western US wildfire fuels. Atmospheric Chem. Phys. 18, 9263–9281. https://doi.org/10.5194/acp-18-9263-2018

Sekimoto, K., Li, S.-M., Yuan, B., Koss, A., Coggon, M., Warneke, C., de Gouw, J., 2017. Calculation of the sensitivity of proton-transfer-reaction mass spectrometry (PTR-MS) for organic trace gases using molecular properties. Int. J. Mass Spectrom. 421, 71–94. https://doi.org/10.1016/j.ijms.2017.04.006

Selimovic, V., Yokelson, R.J., McMeeking, G.R., Coefield, S., 2020. Aerosol Mass and Optical Properties, Smoke Influence on O3, and High NO3 Production Rates in a Western U.S. City Impacted by Wildfires. J. Geophys. Res. Atmospheres 125, e2020JD032791. https://doi.org/10.1029/2020JD032791

Selimovic, V., Yokelson, R.J., McMeeking, G.R., Coefield, S., 2019. In situ measurements of trace gases, PM, and aerosol optical properties during the 2017 NW US wildfire smoke event. Atmospheric Chem. Phys. 19, 3905–3926. https://doi.org/10.5194/acp-19-3905-2019

Selimovic, V., Yokelson, R.J., Warneke, C., Roberts, J.M., de Gouw, J., Reardon, J., Griffith, D.W.T., 2018. Aerosol optical properties and trace gas emissions by PAX and OP-FTIR for laboratory-simulated western US wildfires during FIREX. Atmospheric Chem. Phys. 18, 2929–2948. https://doi.org/10.5194/acp-18-2929-2018

Shaw, M.F., Sztáray, B., Whalley, L.K., Heard, D.E., Millet, D.B., Jordan, M.J.T., Osborn, D.L., Kable, S.H., 2018. Photo-tautomerization of acetaldehyde as a photochemical source of formic acid in the troposphere. Nat. Commun. 9, 2584. https://doi.org/10.1038/s41467-018-04824-2

Shirley, T.R., Brune, W.H., Ren, X., Mao, J., Lesher, R., Cardenas, B., Volkamer, R., Molina, L.T., Molina, M.J., Lamb, B., Velasco, E., Jobson, T., Alexander, M., 2006. Atmospheric oxidation in the Mexico

City Metropolitan Area (MCMA) during April 2003. Atmospheric Chem. Phys. 6, 2753–2765. https://doi.org/10.5194/acp-6-2753-2006

Sinha, V., Williams, J., Lelieveld, J., Ruuskanen, T.M., Kajos, M.K., Patokoski, J., Hellen, H., Hakola, H., Mogensen, D., Boy, M., Rinne, J., Kulmala, M., 2010. OH Reactivity Measurements within a Boreal Forest: Evidence for Unknown Reactive Emissions. Environ. Sci. Technol. 44, 6614–6620. https://doi.org/10.1021/es101780b

Slusher, D.L., Huey, L.G., Tanner, D.J., Flocke, F.M., Roberts, J.M., 2004. A thermal dissociation–chemical ionization mass spectrometry (TD-CIMS) technique for the simultaneous measurement of peroxyacyl nitrates and dinitrogen pentoxide. J. Geophys. Res. Atmospheres 109. https://doi.org/10.1029/2004JD004670

Snow, J.A., Heikes, B.G., Shen, H., O'Sullivan, D.W., Fried, A., Walega, J., 2007. Hydrogen peroxide, methyl hydroperoxide, and formaldehyde over North America and the North Atlantic. J. Geophys. Res. Atmospheres 112, 122. https://doi.org/10.1029/2006JD007746

Španěl, P., Diskin, A.M., Wang, T., Smith, D., 2003. A SIFT study of the reactions of H3O+, NO+ and O2+ with hydrogen peroxide and peroxyacetic acid. Int. J. Mass Spectrom. 228, 269–283. https://doi.org/10.1016/S1387-3806(03)00214-8

Stavrakou, T., Müller, J.-F., Peeters, J., Razavi, A., Clarisse, L., Clerbaux, C., Coheur, P.-F., Hurtmans, D., De Mazière, M., Vigouroux, C., Deutscher, N.M., Griffith, D.W.T., Jones, N., Paton-Walsh, C., 2012. Satellite evidence for a large source of formic acid from boreal and tropical forests. Nat. Geosci. 5, 26–30. https://doi.org/10.1038/ngeo1354

Stockwell, C.E., Veres, P.R., Williams, J., Yokelson, R.J., 2015. Characterization of biomass burning emissions from cooking fires, peat, crop residue, and other fuels with high-resolution proton-transfer-reaction time-of-flight mass spectrometry. Atmospheric Chem. Phys. 15, 845–865. https://doi.org/10.5194/acp-15-845-2015

Stockwell, C.E., Yokelson, R.J., Kreidenweis, S.M., Robinson, A.L., DeMott, P.J., Sullivan, R.C., Reardon, J., Ryan, K.C., Griffith, D.W.T., Stevens, L., 2014. Trace gas emissions from combustion of peat, crop residue, domestic biofuels, grasses, and other fuels: configuration and Fourier transform infrared (FTIR) component of the fourth Fire Lab at Missoula Experiment (FLAME-4). Atmospheric Chem. Phys. 14, 9727–9754. https://doi.org/10.5194/acp-14-9727-2014

Thames, A.B., Brune, W.H., Miller, D.O., Allen, H.M., Apel, E.C., Blake, D.R., Bui, T.P., Commane, R., Crounse, J.D., Daube, B.C., Diskin, G.S., DiGangi, J.P., Elkins, J.W., Hall, S.R., Hanisco, T.F., Hannun, R.A., Hintsa, E., Hornbrook, R.S., Kim, M.J., McKain, K., Moore, F.L., Nicely, J.M., Peischl, J., Ryerson, T.B., St. Clair, J.M., Sweeney, C., Teng, A., Thompson, C.R., Ullmann, K., Wennberg, P.O., Wolfe, G.M., 2020. Missing OH reactivity in the global marine boundary layer. Atmospheric Chem. Phys. 20, 4013–4029. https://doi.org/10.5194/acp-20-4013-2020

Travis, K.R., Heald, C.L., Allen, H.M., Apel, E.C., Arnold, S.R., Blake, D.R., Brune, W.H., Chen, X., Commane, R., Crounse, J.D., Daube, B.C., Diskin, G.S., Elkins, J.W., Evans, M.J., Hall, S.R., Hintsa, E.J., Hornbrook, R.S., Kasibhatla, P.S., Kim, M.J., Luo, G., McKain, K., Millet, D.B., Moore, F.L., Peischl, J., Ryerson, T.B., Sherwen, T., Thames, A.B., Ullmann, K., Wang, X., Wennberg, P.O., Wolfe, G.M., Yu, F., 2020. Constraining remote oxidation capacity with ATom observations. Atmospheric Chem. Phys. 20, 7753–7781. https://doi.org/10.5194/acp-20-7753-2020

Trentmann, J., Yokelson, R.J., Hobbs, P.V., Winterrath, T., Christian, T.J., Andreae, M.O., Mason, S.A., 2005. An analysis of the chemical processes in the smoke plume from a savanna fire. J. Geophys. Res. Atmospheres 110. https://doi.org/10.1029/2004JD005628

Urbanski, S., 2014. Wildland fire emissions, carbon, and climate: Emission factors. For. Ecol. Manag. 317, 51–60. https://doi.org/10.1016/j.foreco.2013.05.045

U.S. Environmental Protection Agency, 2020. 2017 National Emissions Inventory (NEI) Technical Support Document (TSD).

van der Werf, G.R., Randerson, J.T., Giglio, L., van Leeuwen, T.T., Chen, Y., Rogers, B.M., Mu, M., van Marle, M.J.E., Morton, D.C., Collatz, G.J., Yokelson, R.J., Kasibhatla, P.S., 2017. Global fire emissions estimates during 1997–2016. Earth Syst. Sci. Data 9, 697–720. https://doi.org/10.5194/essd-9-697-2017

Veres, P., Gilman, J.B., Roberts, J.M., Kuster, W.C., Warneke, C., Burling, I.R., de Gouw, J., 2010. Development and validation of a portable gas phase standard generation and calibration system for volatile organic compounds. Atmospheric Meas. Tech. 3, 683–691. https://doi.org/10.5194/amt-3-683-2010

Vlasenko, A., Macdonald, A.. M., Sjostedt, S.J., Abbatt, J.P.D., 2010. Formaldehyde measurements by Proton transfer reaction – Mass Spectrometry (PTR-MS): correction for humidity effects. Atmospheric Meas. Tech. 3, 1055–1062. https://doi.org/10.5194/amt-3-1055-2010

Warneke, C., Veres, P., Holloway, J.S., Stutz, J., Tsai, C., Alvarez, S., Rappenglueck, B., Fehsenfeld, F.C., Graus, M., Gilman, J.B., de Gouw, J.A., 2011. Airborne formaldehyde measurements using PTR-MS: calibration, humidity dependence, inter-comparison and initial results. Atmospheric Meas. Tech. 4, 2345–2358. https://doi.org/10.5194/amt-4-2345-2011

Westerling, A.L., 2016. Increasing western US forest wildfire activity: sensitivity to changes in the timing of spring. Philos. Trans. R. Soc. B Biol. Sci. 371, 20150178. https://doi.org/10.1098/rstb.2015.0178

Westerling, A.L., 2006. Warming and Earlier Spring Increase Western U.S. Forest Wildfire Activity. Science 313, 940–943. https://doi.org/10.1126/science.1128834

Westerling, A.L., Turner, M.G., Smithwick, E.A.H., Romme, W.H., Ryan, M.G., 2011. Continued warming could transform Greater Yellowstone fire regimes by mid-21st century. Proc. Natl. Acad. Sci. 108, 13165–13170. https://doi.org/10.1073/pnas.1110199108

Wickham, H., 2016. ggplot2: Elegant Graphics for Data Analysis. Springer-Verlag New York.

Wickham, H., François, R., Henry, L., Müller, K., 2019. dplyr: A Grammar of Data Manipulation.

Wiedinmyer, C., Akagi, S.K., Yokelson, R.J., Emmons, L.K., Al-Saadi, J.A., Orlando, J.J., Soja, A.J., 2011. The Fire INventory from NCAR (FINN): a high resolution global model to estimate the emissions from open burning. Geosci. Model Dev. 4, 625–641. https://doi.org/10.5194/gmd-4-625-2011

Wolfe, G.M., Hanisco, T.F., Arkinson, H.L., Blake, D.R., Wisthaler, A., Mikoviny, T., Ryerson, T.B., Pollack, I., Peischl, J., Wennberg, P.O., Crounse, J.D., St. Clair, J.M., Teng, A., Huey, L.G., Liu, X., Fried, A., Weibring, P., Richter, D., Walega, J., Hall, S.R., Ullmann, K., Jimenez, J.L., Campuzano-Jost, P., Bui, T.P., Diskin, G., Podolske, J.R., Sachse, G., Cohen, R.C., 2022. Photochemical evolution of the 2013 California Rim Fire: synergistic impacts of reactive hydrocarbons and enhanced oxidants. Atmospheric Chem. Phys. 22, 4253–4275. https://doi.org/10.5194/acp-22-4253-2022

Wolfe, G.M., Marvin, M.R., Roberts, S.J., Travis, K.R., Liao, J., 2016. The Framework for 0-D Atmospheric Modeling (F0AM) v3.1. Geosci. Model Dev. 9, 3309–3319. https://doi.org/10.5194/gmd-9-3309-2016

Wyche, K.P., Monks, P.S., Ellis, A.M., Cordell, R.L., Parker, A.E., Whyte, C., Metzger, A., Dommen, J., Duplissy, J., Prevot, A.S.H., Baltensperger, U., Rickard, A.R., Wulfert, F., 2009. Gas phase precursors to anthropogenic secondary organic aerosol: detailed observations of 1,3,5-trimethylbenzene photooxidation. Atmospheric Chem. Phys. 9, 635–665. https://doi.org/10.5194/acp-9-635-2009

Xu, L., Crounse, J.D., Vasquez, K.T., Allen, H., Wennberg, P.O., Bourgeois, I., Brown, S.S., Campuzano-Jost, P., Coggon, M.M., Crawford, J.H., DiGangi, J.P., Diskin, G.S., Fried, A., Gargulinski, E.M., Gilman, J.B., Gkatzelis, G.I., Guo, H., Hair, J.W., Hall, S.R., Halliday, H.A., Hanisco, T.F., Hannun, R.A., Holmes, C.D., Huey, L.G., Jimenez, J.L., Lamplugh, A., Lee, Y.R., Liao, J., Lindaas, J., Neuman, J.A., Nowak, J.B., Peischl, J., Peterson, D.A., Piel, F., Richter, D., Rickly, P.S., Robinson, M.A., Rollins, A.W., Ryerson, T.B., Sekimoto, K., Selimovic, V., Shingler, T., Soja, A.J., Clair, J.M.S., Tanner, D.J., Ullmann, K., Veres, P.R., Walega, J., Warneke, C., Washenfelder, R.A., Weibring, P., Wisthaler, A., Wolfe, G.M., Womack, C.C., Yokelson, R.J., 2021. Ozone chemistry in western U.S. wildfire plumes. Sci. Adv. 7, eabl3648. https://doi.org/10.1126/sciadv.abl3648

Yang, Y., Shao, M., Wang, X., Nölscher, A.C., Kessel, S., Guenther, A., Williams, J., 2016. Towards a quantitative understanding of total OH reactivity: A review. Atmos. Environ. 134, 147–161. https://doi.org/10.1016/j.atmosenv.2016.03.010

Yokelson, R.J., Bertschi, I.T., Christian, T.J., Hobbs, P.V., Ward, D.E., Hao, W.M., 2003. Trace gas measurements in nascent, aged, and cloud-processed smoke from African savanna fires by airborne Fourier transform infrared spectroscopy (AFTIR). J. Geophys. Res. Atmospheres 108. https://doi.org/10.1029/2002JD002322

Yokelson, R.J., Burling, I.R., Gilman, J.B., Warneke, C., Stockwell, C.E., de Gouw, J., Akagi, S.K., Urbanski, S.P., Veres, P., Roberts, J.M., Kuster, W.C., Reardon, J., Griffith, D.W.T., Johnson, T.J., Hosseini, S., Miller, J.W., Cocker III, D.R., Jung, H., Weise, D.R., 2013. Coupling field and laboratory measurements to estimate the emission factors of identified and unidentified trace gases for prescribed fires. Atmospheric Chem. Phys. 13, 89–116. https://doi.org/10.5194/acp-13-89-2013

Yokelson, R.J., Christian, T.J., Karl, T.G., Guenther, A., 2008. The tropical forest and fire emissions experiment: laboratory fire measurements and synthesis of campaign data. Atmos Chem Phys 19.

Yokelson, R J, Crounse, J.D., DeCarlo, P.F., Karl, T., Urbanski, S., Atlas, E., Campos, T., Shinozuka, Y., Kapustin, V., Clarke, A.D., Weinheimer, A., Knapp, D.J., Montzka, D.D., Holloway, J., Weibring, P., Flocke, F., Zheng, W., Toohey, D., Wennberg, P.O., Wiedinmyer, C., Mauldin, L., Fried, A., Richter, D., Walega, J., Jimenez, J.L., Adachi, K., Buseck, P.R., Hall, S.R., Shetter, R., 2009. Emissions from biomass burning in the Yucatan. Atmos Chem Phys 28.

Yokelson, R. J., Crounse, J.D., DeCarlo, P.F., Karl, T., Urbanski, S., Atlas, E., Campos, T., Shinozuka, Y., Kapustin, V., Clarke, A.D., Weinheimer, A., Knapp, D.J., Montzka, D.D., Holloway, J., Weibring, P., Flocke, F., Zheng, W., Toohey, D., Wennberg, P.O., Wiedinmyer, C., Mauldin, L., Fried, A., Richter, D., Walega, J., Jimenez, J.L., Adachi, K., Buseck, P.R., Hall, S.R., Shetter, R., 2009. Emissions from biomass burning in the Yucatan. Atmospheric Chem. Phys. 9, 5785–5812. https://doi.org/10.5194/acp-9-5785-2009

Yokelson, R.J., Goode, J.G., Ward, D.E., Susott, R.A., Babbitt, R.E., Wade, D.D., Bertschi, I., Griffith, D.W.T., Hao, W.M., 1999. Emissions of formaldehyde, acetic acid, methanol, and other trace gases from biomass fires in North Carolina measured by airborne Fourier transform infrared spectroscopy. J. Geophys. Res. Atmospheres 104, 30109–30125. https://doi.org/10.1029/1999JD900817

Yokelson, R.J., Griffith, D.W.T., Ward, D.E., 1996. Open-path Fourier transform infrared studies of large-scale laboratory biomass fires. J. Geophys. Res. Atmospheres 101, 21067–21080. https://doi.org/10.1029/96JD01800

Yoshino, A., Sadanaga, Y., Watanabe, K., Kato, S., Miyakawa, Y., Matsumoto, J., Kajii, Y., 2006. Measurement of total OH reactivity by laser-induced pump and probe technique—comprehensive observations in the urban atmosphere of Tokyo. Atmos. Environ. 40, 7869–7881. https://doi.org/10.1016/j.atmosenv.2006.07.023

Yuan, B., Koss, A.R., Warneke, C., Coggon, M., Sekimoto, K., de Gouw, J.A., 2017. Proton-Transfer-Reaction Mass Spectrometry: Applications in Atmospheric Sciences. Chem. Rev. 117, 13187–13229. https://doi.org/10.1021/acs.chemrev.7b00325

Yuan, B., Veres, P.R., Warneke, C., Roberts, J.M., Gilman, J.B., Koss, A., Edwards, P.M., Graus, M., Kuster, W.C., Li, S.-M., Wild, R.J., Brown, S.S., Dubé, W.P., Lerner, B.M., Williams, E.J., Johnson, J.E., Quinn, P.K., Bates, T.S., Lefer, B., Hayes, P.L., Jimenez, J.L., Weber, R.J., Zamora, R., Ervens, B., Millet, D.B., Rappenglück, B., de Gouw, J.A., 2015. Investigation of secondary formation of formic acid: urban environment vs. oil and gas producing region. Atmospheric Chem. Phys. 15, 1975–1993. https://doi.org/10.5194/acp-15-1975-2015

Yuan, B., Warneke, C., Shao, M., de Gouw, J.A., 2014. Interpretation of volatile organic compound measurements by proton-transfer-reaction mass spectrometry over the deepwater horizon oil spill. Int. J. Mass Spectrom. 358, 43–48. https://doi.org/10.1016/j.ijms.2013.11.006

Yue, X., Mickley, L.J., Logan, J.A., Kaplan, J.O., 2013. Ensemble projections of wildfire activity and carbonaceous aerosol concentrations over the western United States in the mid-21st century. Atmos. Environ. 77, 767–780. https://doi.org/10.1016/j.atmosenv.2013.06.003

Zhang, F., Wang, J., Ichoku, C., Hyer, E.J., Yang, Z., Ge, C., Su, S., Zhang, X., Kondragunta, S., Kaiser, J.W., Wiedinmyer, C., Silva, A. da, 2014. Sensitivity of mesoscale modeling of smoke direct radiative effect to the emission inventory: a case study in northern sub-Saharan African region. Environ. Res. Lett. 9, 075002. https://doi.org/10.1088/1748-9326/9/7/075002

Zheng, W., Flocke, F.M., Tyndall, G.S., Swanson, A., Orlando, J.J., Roberts, J.M., Huey, L.G., Tanner, D.J., 2011. Characterization of a thermal decomposition chemical ionization mass spectrometer for the measurement of peroxy acyl nitrates (PANs) in the atmosphere. Atmospheric Chem. Phys. 11, 6529–6547. https://doi.org/10.5194/acp-11-6529-2011

Zhou, Y., Shively, D., Mao, H., Russo, R.S., Pape, B., Mower, R.N., Talbot, R., Sive, B.C., 2010. Air Toxic Emissions from Snowmobiles in Yellowstone National Park. Environ. Sci. Technol. 44, 222–228. https://doi.org/10.1021/es9018578

Appendix a: supplemental figures
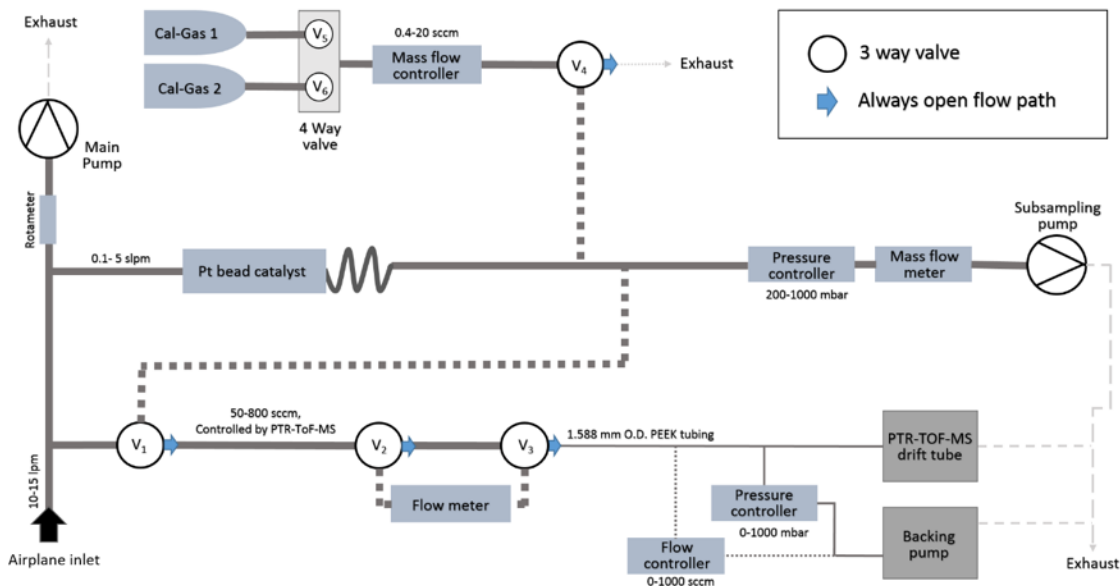
Figure S2.1. Schematic of PTR-ToF-MS inlet configuration, zero air generator, and in flight calibration system during WE-CAN. All tubing is 3.175 mm I.D. PFA tubing except where shown to decrease to 1.588 mm O.D. PEEK tubing. The flow path during sampling is shown with the solid lines with typical flow rates indicated, while the dashed lines represent flow pathways used during calibration and instrument backgrounds.
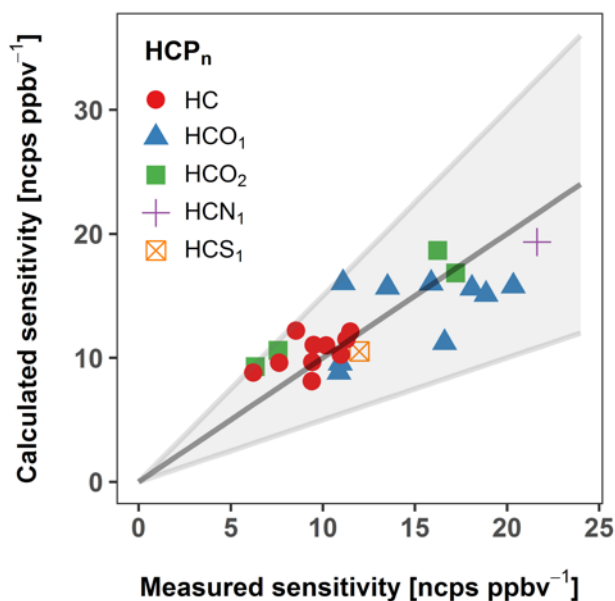
Figure S2.2. Measured sensitivities for species directly calibrated using standard gases during WE-CAN, compared to sensitivities calculated using molecular properties following Sekimoto et al. (2017). Calibrated VOCs are shown by their elemental

compositions, HCPn, where HC stands for the hydrocarbon part and Pn represents the species and number of electronegative atoms in the compound. Thus, HC represents species only containing hydrogen and carbon (alkynes, terpenes, aromatics), HCO1 represents species with one oxygen (alcohols, ketones, aldehydes, furans), HCO2 represents two oxygens (formic acid, acetic acid, and furaldehydes), HCN1 is acetonitrile, and HCS1 is dimethyl sulfide. The shaded regions represent ±50 % uncertainty from the one-to-one line (dark grey). Directly calibrated species include methanol, propyne, acetonitrile, acetaldehyde, formic acid, 1-butene, acetone, acetic acid, dimethyl sulfide, furan, isoprene, methyl vinyl ketone, methacrolein, methyl ethyl ketone, benzene, 2-methyl furan, toluene, 2-furfural (furaldehyde), 3-hexanone, ethylbenzene, m-xylene, 5-methyl furfural, C9 aromatics (1,3,5-trimethylbenzene and 1,2,4-trimethylbenzene), 1,2,3,5-tetramethylbenzene, and α-pinene.
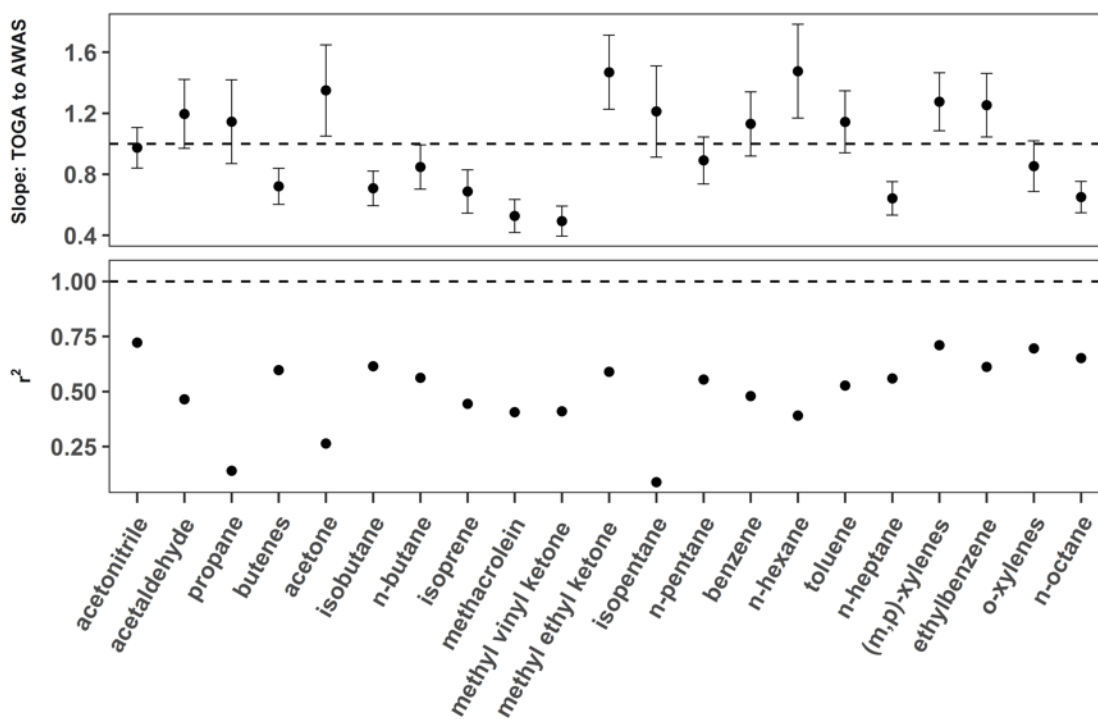
Figure S2.3. Slope and correlation coefficients (r^2) of the reduced major axis regression of TOGA versus AWAS emission ratios, for 15 'unique fires' used in this work. Slopes < 1 mean that TOGA measured values are higher than AWAS values. Error bars show the standard error of the slope. AWAS measured 3-methylpentane ~10x higher than TOGA and has been removed from the plot to preserve the y-axis scale. The poor slope comparison is partially due to the fact that 3-methylpentane is enhanced only slightly in the wildfires compared to the other observed alkanes. Butenes include TOGA isobutene and 1-butene compared with AWAS 1-butene, cis-2-butene, and trans-2-butene. NCPS: normalized counts per second
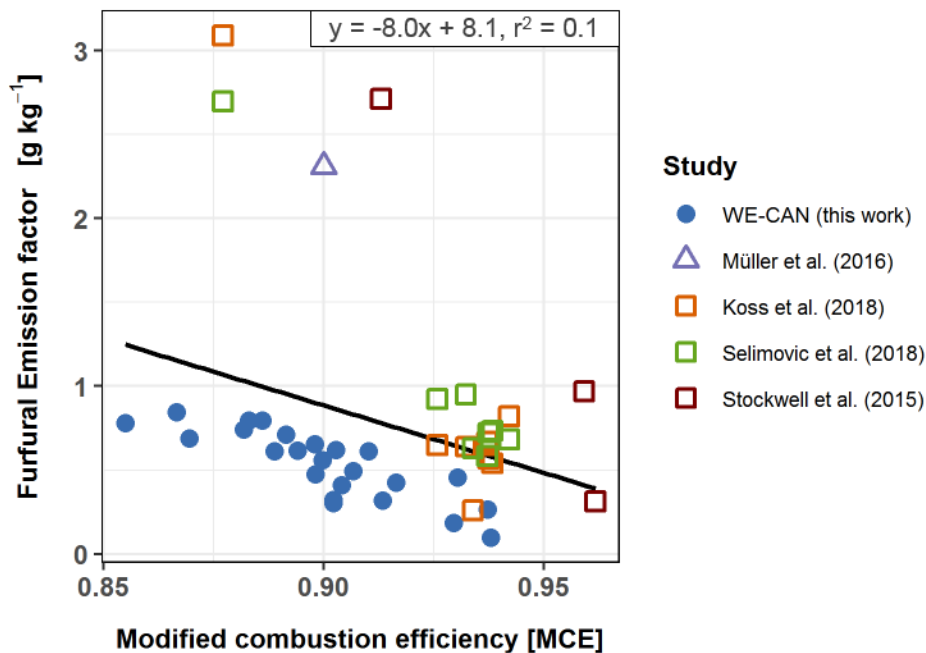
Figure S2.4. Correlations of WE-CAN furfural EFs versus MCE, along with EFs for one field campaigns (Müller et al., 2016) and coniferous fuels measured during three laboratory burns (Koss et al., 2018; Selimovic et al., 2018; Stockwell et al., 2015). The black line represents the least squares regression for all studies.
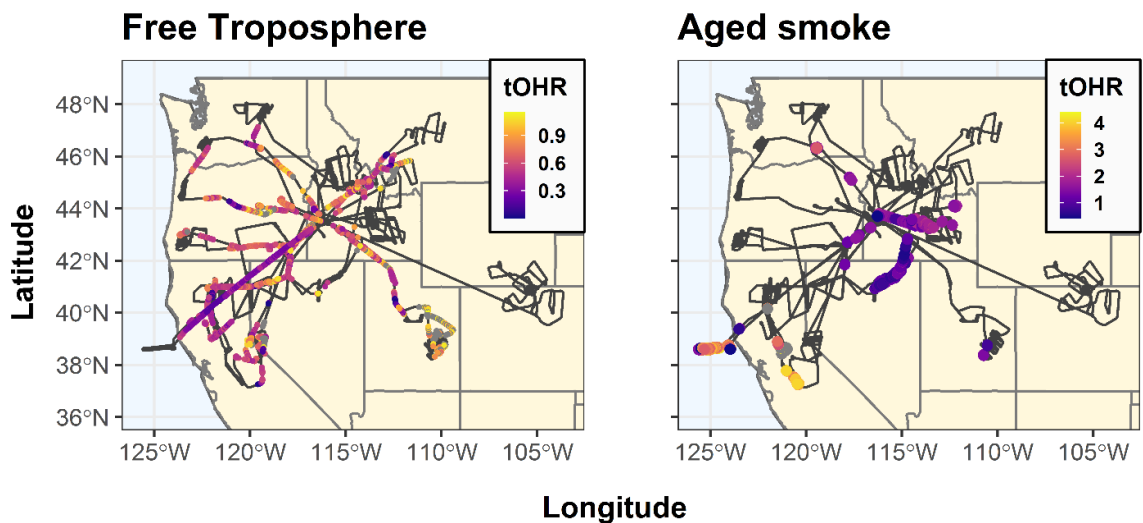
Figure S3.1: WE-CAN research flight tracks colored by the total calculated OH reactivity (tOHR, s^{-1}) for free troposphere and aged smoke sampling periods. The maximum total OH reactivity is limited to the 95th percentile.
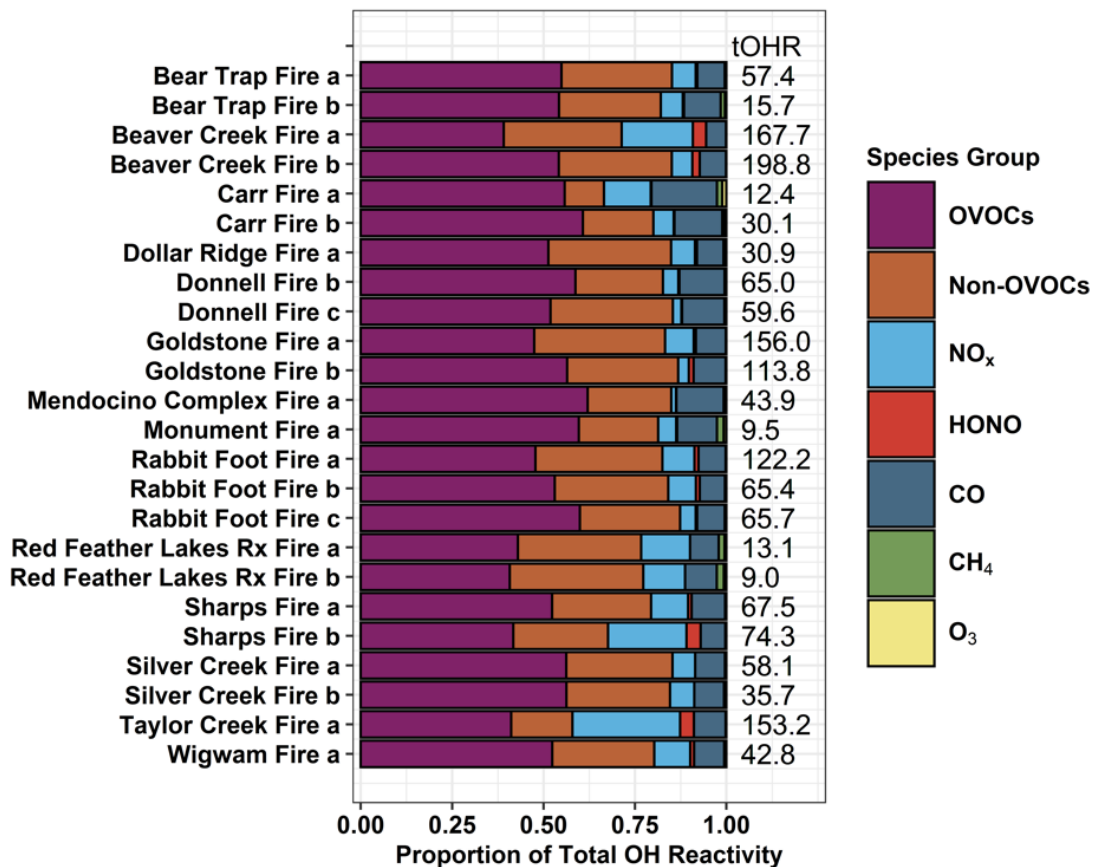
Figure S3.2. Total gas OH reactivity profiles for 24 fires reported in this work. Emission transects of the same fire completed more than 30 minutes apart are treated as separate fires and denoted with a, b, etc. Average total calculated OH reactivities (s-1) are shown for each transect to the right of the bars.
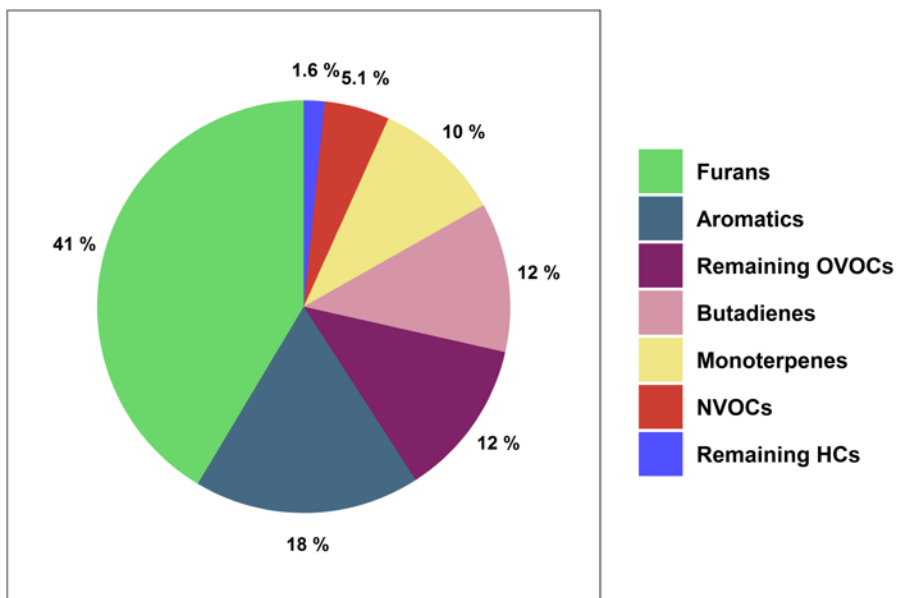
Figure S3.3. The proportion of VOC groups comprising the non-implemented VOC OHR fraction shown in Figure 4c. These groups represent those species that were measured during WE-CAN but are not implemented for biomass burning in the GEOS-Chem CTM.
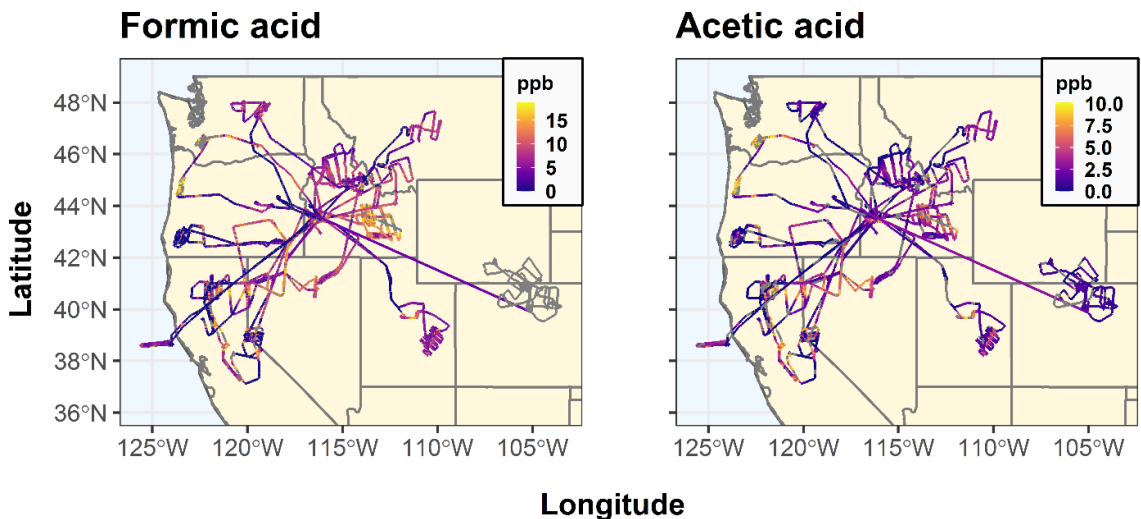
Figure S4.1. Flight tracks for WE-CAN research flights colored by formic acid (I⁻ CIMS) and acetic acid (PTR-ToF) mixing ratios (ppb). Maximum concentrations are limited to the 95th percentile.
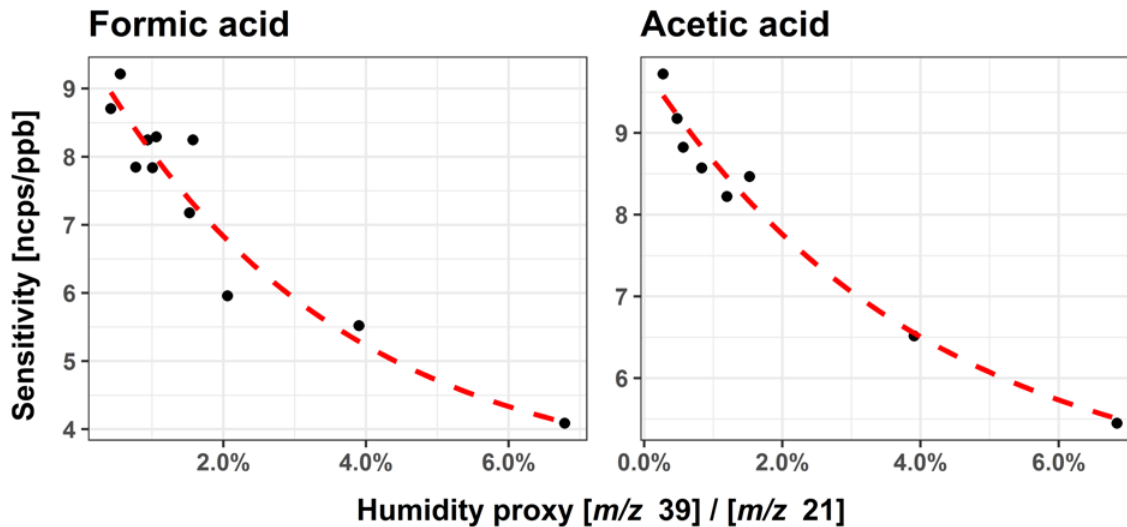
Figure S4.2. Formic and acetic acid sensitivity in PTR-ToF as a function of the internal humidity proxy $H_2O \cdot H_3O^+$ to H_3O^+ ([m/z 39]/[m/z 21]). The line of best fit is shown in red, corresponding to: 6.5e^(-29.1*([m/z 39]/[m/z 21])) + 3.2) for FA and 5.3e^(-24.3*([m/z 39]/[m/z 21])) + 4.5) for AA.
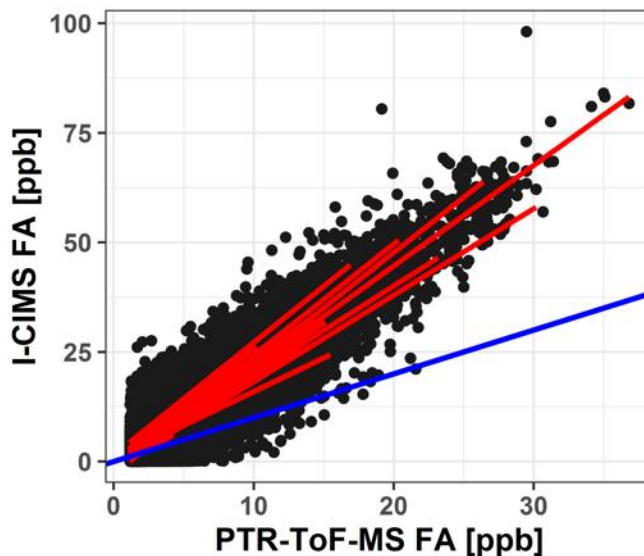
Figure S4.3. Correlations between I⁻ CIMS and PTR-ToF 1 Hz FA measurements during WE-CAN for all research flights, filtered to remove cloud sampling. The blue line represents 1:1 agreement while the red lines are the total least squares regression for each research flight.
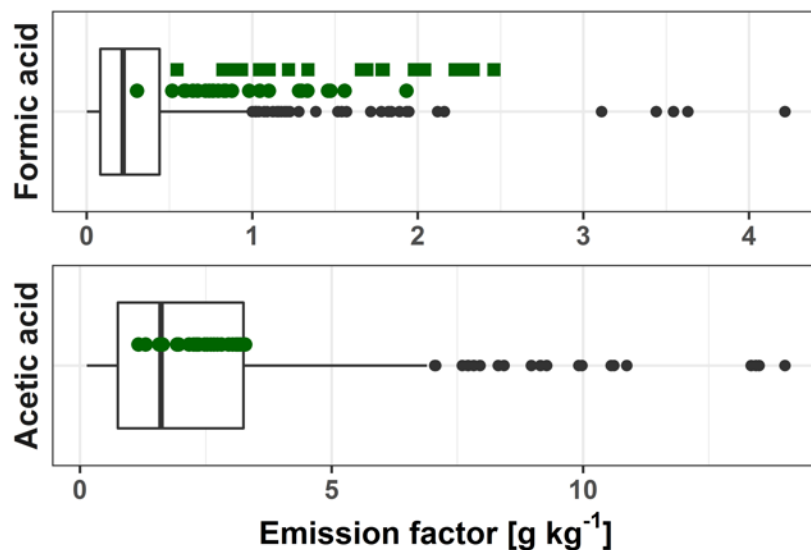
Figure S4.4. Emission factors of formic and acetic acid from WE-CAN PTR-ToF observations (green points), I⁻ CIMS (green squares), and literature values (box-and-whisker). The box and whisker plots reported include literature EFs from all studies in Table S1 (330 data points for formic acid and 289 for acetic acid). Boxes represent the 25th and 75th percentiles, vertical lines as median, whiskers as 1.5 × the interquartile range, and black points as > 1.5 × interquartile range.
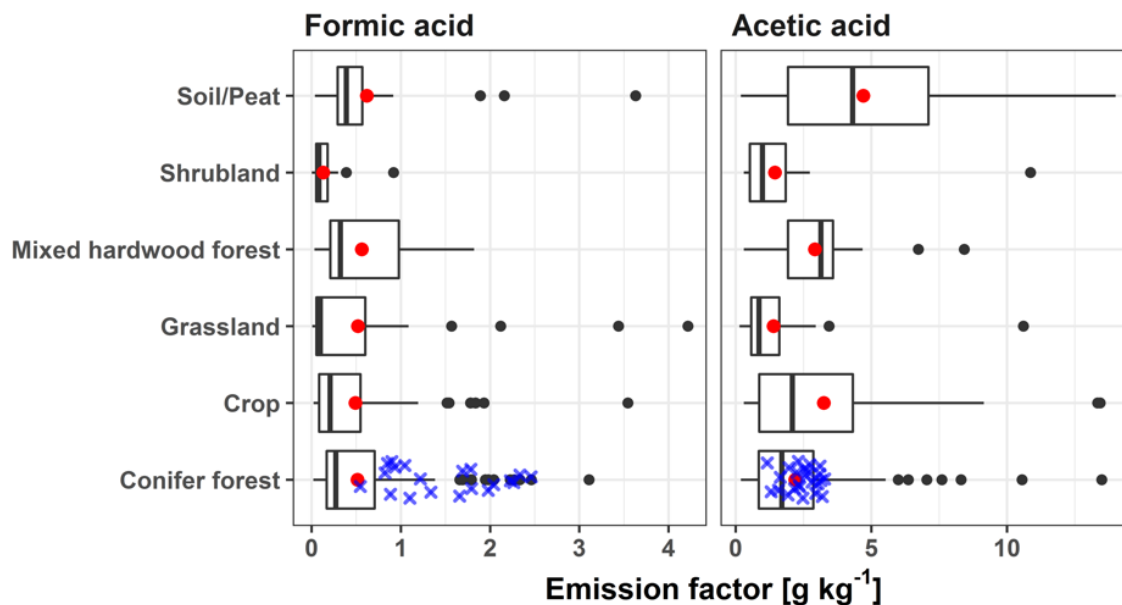
Figure S4.5. Box-and-whisker plot of WE-CAN and literature EFs by the type of fuel burned. Red points are the literature mean for the data represented by the boxes, blue "x" are WE-CAN measured EFs.
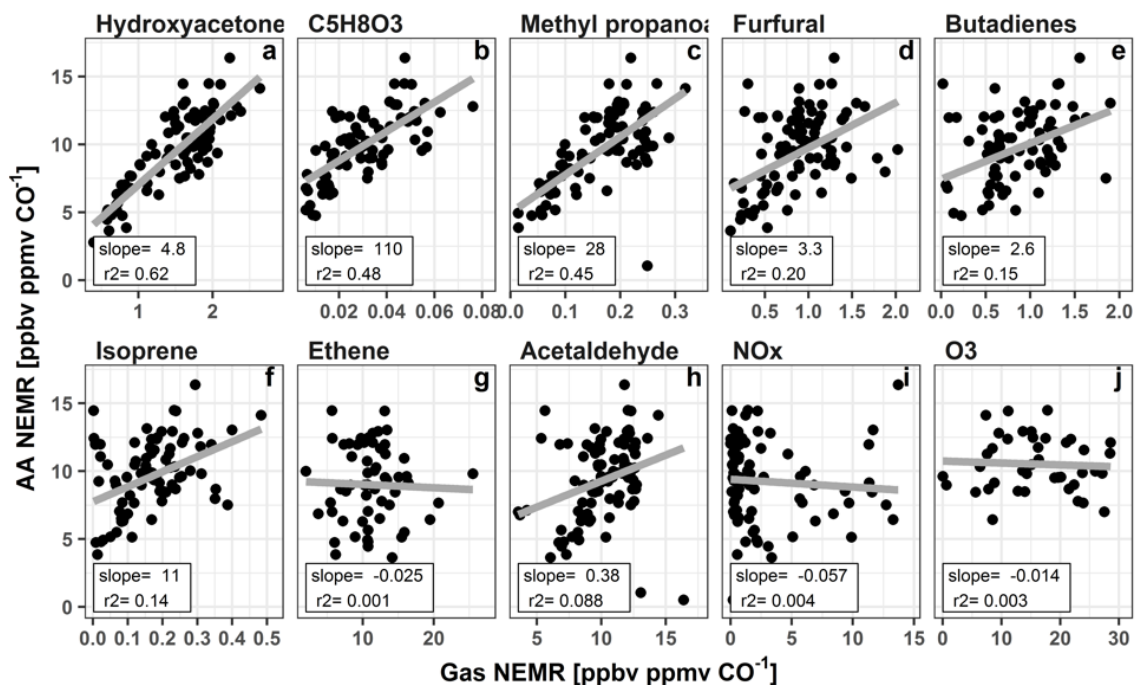
Figure S4.6. AA NEMRs compared to various gas phase species measured in 5 smoke plumes with more than 10 pseudo-Lagrangian plume transects. Slope and r2 for the least squares regression of each species is shown at the bottom of each panel, while the gray lines are the best fit. Panels a, b, and c are the three VOCs with the strongest correlation to AA. Panels d and e represent two of largest OH radical sinks in wildfire emissions. Panels f, g, and h are known organic acid precursors, while h and i are representative of the overall plume oxidation.
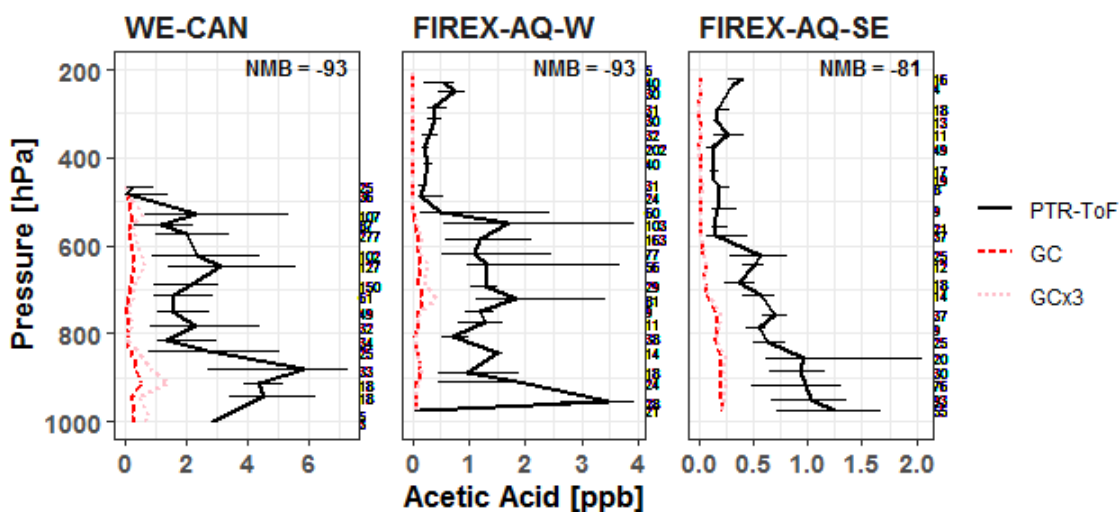
Figure S4.7. Vertical profiles of the median acetic acid mixing ratio measured during the full WE-CAN and FIREX-AQ field campaigns, binned at 33 hPa. Black and gray lines

correspond to the measurements made PTR-ToF with error bars representing the 25th and 75th percentile of measurements. Red dashed lines correspond to GEOS-Chem with GFAS BB emissions (GC) and the pink dotted lines are GEOS-Chem with $3 \times$ GFAS BB emissions (GC×3). The number of samples in each altitude bin are shown on the right of each plot, while the normalized mean bias (NMB) to the PTR-ToF measurement above 450 hPa is shown at the top.
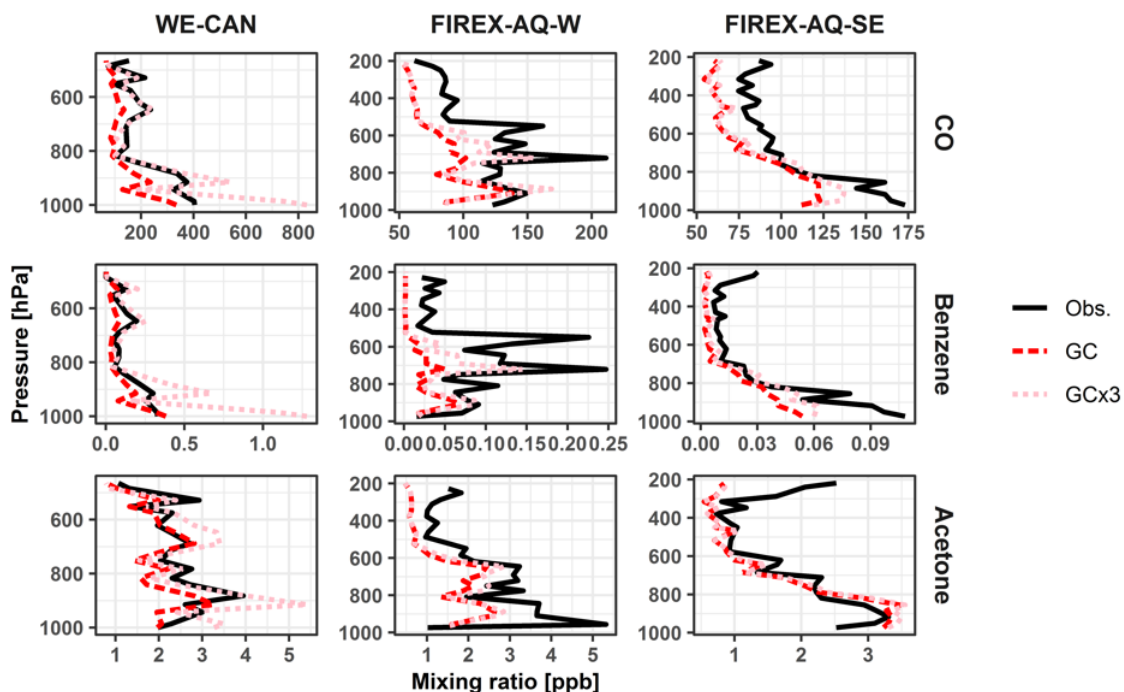
Figure S4.8. Vertical profiles of the median CO, benzene, and acetone mixing ratios measured during the full WE-CAN and FIREX-AQ field campaigns, binned at 33 hPa. Black lines correspond to the observations while red dashed lines correspond to GEOS-Chem with GFAS BB emissions (GC) and the pink dotted lines are GEOS-Chem with 3 × GFAS BB emissions (GC×3).
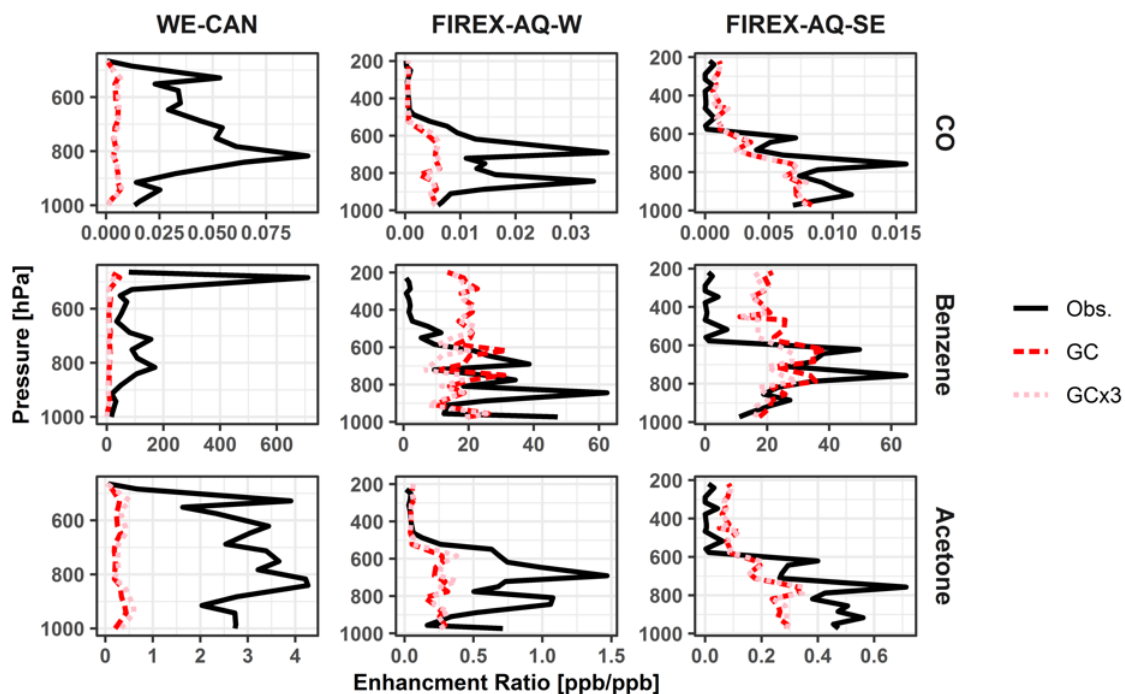
Figure S4.9. Vertical profiles of the median formic acid enhancement ratios to CO, benzene, and acetone during the full WE-CAN and FIREX-AQ field campaigns, binned at 33 hPa. Black lines correspond to the observations while red dashed lines correspond to GEOS-Chem with GFAS BB emissions (GC) and the pink dotted lines are GEOS-Chem with 3 × GFAS BB emissions (GC×3).

Appendix b: supplemental tables

Table S2.1. Summary of measurements used in this work. VOC contributors for PTR-ToF-MS ions and isomeric fractional contributions are from Koss et al. (2018) except for green colored contributions which were determined from WE-CAN data using TOGA speciated measurements. VOCs that are reported for additional speciation information but were not used in the total carbon or total emissions calculations are shown in italics. PTR-ToF-MS VOCs with direct calibrations are shown in red, while the remaining were calculated using the method described by Sekimoto et al. (2017).

Dominant isotopologue exact mass (da)	Protonated mass (m/z)	Chemical formula	VOC contributor	Isomeric fractional contribution to PTR-ToF-MS ion signal	PTR-ToF-MS calibration factor (ncps/ppb)	Insturment	Measurment uncertainty (%)	Functional group
43.990	-	CO2	CO2			PICARRO		
27.995	-	CO	CO			QCL		
16.031	-	CH4	CH4			PICARRO		
26.016	26.016	C2H2	Ethyne			AWAS	10.0	alkyne
27.011	27.011	HCN	Hydrogen cyanide			TOGA	20.0	nitrile
28.031	28.031	C2H4	Ethene			AWAS	10.0	alkene
30.011	31.018	CH2O	Formaldehyde	1.00	13.2	PTR-ToF-MS	40.0	aldehyde
30.047	30.047	C2H6	Ethane			AWAS	10.0	alkane
32.026	33.033	CH4O	Methanol	1.00	16.3	PTR-ToF-MS	15.0	alcohol
41.027	42.034	C2H3N	Acetonitrile	1.00	21.6	PTR-ToF-MS	15.0	nitrile
42.047	42.047	C3H6	Propene			AWAS	10.0	alkene
43.006	44.013	HNCO	Isocyanic acid	1.00	10.5	PTR-ToF-MS	50.0	nitrile
43.042	44.049	C2H5N	Ethenamine	1.00	12.3	PTR-ToF-MS	50.0	amine
44.026	45.033	C2H4O	Acetaldehyde	1.00	18.9	PTR-ToF-MS	15.0	aldehyde
44.063	44.063	C3H8	Propane			TOGA	NA	alkane
45.021	46.029	CH3NO	Formamide	1.00	18.0	PTR-ToF-MS	50.0	amide
46.005	46.005	CH2O2	Formic acid			I- CIMS	0.0	acid
46.042	46.042	C2H6O	Ethanol			TOGA	30.0	alcohol
49.992	49.992	CH3Cl	Methyl chloride			TOGA	20.0	haloalkane

52.031	53.039	C4H4	1-Buten-3-yne	0.87	8.5	PTR-ToF-MS	50.0	alkene
52.031	53.039	C4H4	Fragments	0.13	NA	PTR-ToF-MS	NA	
53.027	54.034	C3H3N	Acrylonitrile	1.00	20.1	PTR-ToF-MS	50.0	nitrile
54.011	55.018	C3H2O	2-Propynal	1.00	15.3	PTR-ToF-MS	50.0	aldehyde
54.047	55.054	C4H6	1,3-Butadiene	0.82	9.1	PTR-ToF-MS	50.0	diene
54.047	55.054	C4H6	1,2-Butadiene	0.01	8.6	PTR-ToF-MS	50.0	diene
55.055	55.054	C4H7	Fragments	0.17	NA	PTR-ToF-MS	NA	
55.042	56.049	C3H5N	Propanenitrile	1.00	19.7	PTR-ToF-MS	50.0	nitrile
56.026	56.026	C3H4O	Acrolein			TOGA	30.0	alkenal
56.063	57.070	C4H8	Butenes	0.59	6.2	PTR-ToF-MS	15.0	alkene
57.070	57.070	C4H9	Fragments	0.41	NA	PTR-ToF-MS	NA	
56.063	*56.063*	*C4H8*	*Isobutene, 1-Butene*			*TOGA*	*20.0*	*alkene*
57.021	58.029	C2H3NO	Methyl isocyanate	0.50	15.2	PTR-ToF-MS	50.0	nitrile
57.021	58.029	C2H3NO	Hydroxyacetonitrile	0.50	13.0	PTR-ToF-MS	50.0	nitrile
57.058	58.065	C3H7N	Propene amine	1.00	9.5	PTR-ToF-MS	50.0	amine
58.005	59.013	C2H2O2	Glyoxal	1.00	20.9	PTR-ToF-MS	50.0	aldehyde
58.042	59.049	C3H6O	Acetone	0.83	20.1	PTR-ToF-MS	15.0	ketone
58.042	59.049	C3H6O	Propanal	0.17	15.1	PTR-ToF-MS	50.0	aldehyde
58.042	*58.042*	*C3H6O*	*Acetone*			*TOGA*	*20.0*	*ketone*
58.042	*58.042*	*C3H6O*	*Propanal*			*TOGA*	*30.0*	*aldehyde*
58.078	58.078	C4H10	n-Butane			TOGA	15.0	alkane
58.078	58.078	C4H10	Isobutane			TOGA	15.0	alkane
59.037	60.044	C2H5NO	Acetamide	1.00	17.9	PTR-ToF-MS	50.0	amide
59.073	60.081	C3H9N	Trimethylamine	1.00	9.0	PTR-ToF-MS	50.0	amine
60.021	61.028	C2H4O2	Acetic acid	0.67	7.6	PTR-ToF-MS	30.0	acid
60.021	61.028	C2H4O2	Glycolaldehyde (=hydroxyacetaldehyde)	0.33	14.4	PTR-ToF-MS	50.0	aldehyde
60.058	60.058	C3H8O	Isopropanol			TOGA	30.0	alcohol
61.016	62.024	CH3NO2	Nitromethane	1.00	17.9	PTR-ToF-MS	50.0	nitroalkane
62.019	62.019	C2H6S	Dimethyl sulfide			AWAS	10.0	sulfide
65.027	66.034	C4H3N	Cyanoallene isomers	1.00	19.2	PTR-ToF-MS	50.0	nitrile
66.047	67.054	C5H6	1,3-Cyclopentadiene	0.22	8.9	PTR-ToF-MS	50.0	cycloalkene

67.055	67.054	C5H7	Fragments	0.78	NA	PTR-ToF-MS	NA	
67.042	68.049	C4H5N	Pyrrole	0.57	11.5	PTR-ToF-MS	50.0	N-heterocycle
67.042	68.049	C4H5N	Butene nitrile isomers	0.43	19.2	PTR-ToF-MS	50.0	nitrile
67.042	*67.042*	*C4H5N*	*Methacrylonitrile*			*TOGA*	*50.0*	*nitrile*
67.990	68.997	C3O2	Carbon suboxide	1.00	7.6	PTR-ToF-MS	50.0	ketone
68.026	69.033	C4H4O	Furan	1.00	10.9	PTR-ToF-MS	15.0	furan
68.063	68.063	C5H8	Isoprene			*TOGA*	*15.0*	*diene*
69.058	70.065	C4H7N	Butane nitrile	0.61	18.9	PTR-ToF-MS	50.0	nitrile
69.058	70.065	C4H7N	Dihydropyrrole	0.39	12.6	PTR-ToF-MS	50.0	N-heterocycle
70.005	71.013	C3H2O2	Propiolic acid	1.00	10.1	PTR-ToF-MS	50.0	acid
70.042	71.049	C4H6O	Methyl vinyl ketone	0.60	15.9	PTR-ToF-MS	15.0	ketone
70.042	71.049	C4H6O	Methacrolein	0.28	11.1	PTR-ToF-MS	15.0	ketone
70.042	71.049	C4H6O	2-Butenal (=crotonaldehyde)	0.13	18.7	PTR-ToF-MS	50.0	alkenal
70.042	*70.042*	*C4H6O*	*Methyl vinyl ketone*			*TOGA*	*20.0*	*ketone*
70.042	*70.042*	*C4H6O*	*Methacrolein*			*TOGA*	*20.0*	*ketone*
70.042	*70.042*	*C4H6O*	*2-Butenal*			*TOGA*	*30.0*	*alkenal*
70.078	71.086	C5H10	Pentene, Methylbutenes	0.69	9.3	PTR-ToF-MS	50.0	alkene
71.086	71.086	C5H11	Fragments	0.31	NA	PTR-ToF-MS	NA	
70.078	*70.078*	*C5H10*	*Cyclopentane*			*AWAS*	*10.0*	*cyclo-alkane*
71.073	72.081	C4H9N	Buteneamines, Tetrahydropyrole	1.00	10.0	PTR-ToF-MS	50.0	amine
72.021	73.028	C3H4O2	Pyruvaldehyde (=methyl glyoxal)	0.50	18.3	PTR-ToF-MS	50.0	aldehyde
72.021	73.028	C3H4O2	Acrylic acid	0.50	10.2	PTR-ToF-MS	50.0	acid
72.058	73.065	C4H8O	Methyl ethyl ketone	0.85	18.1	PTR-ToF-MS	15.0	ketone
72.058	73.065	C4H8O	2-Methyl propanal	0.14	15.9	PTR-ToF-MS	50.0	aldehyde
72.058	73.065	C4H8O	Butanal	0.01	15.3	PTR-ToF-MS	50.0	aldehyde
72.058	*72.058*	*C4H8O*	*Methyl ethyl ketone*			*TOGA*	*20.0*	*ketone*
72.058	*72.058*	*C4H8O*	*Butanal*			*TOGA*	*30.0*	*aldehyde*
72.094	72.094	C5H12	n-Pentane			TOGA	15.0	alkane
72.094	72.094	C5H12	Isopentane			TOGA	15.0	alkane
73.016	74.024	C2H3NO2	Nitroethene	1.00	17.7	PTR-ToF-MS	50.0	nitroalkane
74.037	75.044	C3H6O2	Hydroxyacetone	0.50	8.1	PTR-ToF-MS	50.0	ketone

74.037	75.044	C3H6O2	Methyl acetate	0.35	10.7	PTR-ToF-MS	50.0	ester
74.037	75.044	C3H6O2	Ethyl formate	0.14	11.7	PTR-ToF-MS	50.0	ester
75.032	76.039	C2H5NO2	Nitroethane, Ethyl nitrite	1.00	17.5	PTR-ToF-MS	50.0	nitroalkane
75.944	75.944	CS2	Carbon disulfide			TOGA	50.0	sulfide
78.047	79.054	C6H6	Benzene	0.95	9.4	PTR-ToF-MS	15.0	aromatic
78.047	79.054	C6H6	Fragments	0.05	NA	PTR-ToF-MS	NA	
79.042	80.049	C5H5N	Pentadienenitriles	0.56	19.3	PTR-ToF-MS	50.0	nitrile
79.042	80.049	C5H5N	Pyridine	0.44	13.2	PTR-ToF-MS	50.0	N-heterocycle
80.026	81.033	C5H4O	2,4-Cyclopentadiene-1-one	0.42	17.0	PTR-ToF-MS	50.0	ketone
80.026	81.033	C5H4O	Fragments	0.58	NA	PTR-ToF-MS	NA	
81.058	82.065	C5H7N	Pentenenitriles	0.67	19.4	PTR-ToF-MS	50.0	nitrile
81.058	82.065	C5H7N	Methylpyrroles	0.33	12.6	PTR-ToF-MS	50.0	N-heterocycle
82.042	83.049	C5H6O	2-Methylfuran	0.51	10.9	PTR-ToF-MS	15.0	furan
82.042	83.049	C5H6O	3-Methyl furan	0.10	9.9	PTR-ToF-MS	50.0	furan
82.042	83.049	C5H6O	Fragments	0.37	NA	PTR-ToF-MS	NA	
82.042	*82.042*	*C5H6O*	*2-Methylfuran*			*TOGA*	*20.0*	*furan*
82.042	*82.042*	*C5H6O*	*3-Methylfuran*			*TOGA*	*20.0*	*furan*
82.078	82.078	C6H10	2,2-Dimethylbutane			AWAS	10.0	alkane
83.073	84.081	C5H9N	Pentanenitriles	1.00	20.4	PTR-ToF-MS	50.0	nitrile
83.953	83.953	CH2Cl2	Dichloromethane			TOGA	15.0	haloalkane
84.021	85.028	C4H4O2	2(3H)-Furanone	0.81	11.3	PTR-ToF-MS	50.0	ester
84.058	85.065	C5H8O	3-Methyl-3-buten-2-one	0.37	16.0	PTR-ToF-MS	50.0	ketone
84.058	85.065	C5H8O	Cyclopentanone	0.18	17.6	PTR-ToF-MS	50.0	ketone
84.058	85.065	C5H8O	Fragments	0.45	NA	PTR-ToF-MS	NA	
84.094	84.094	C6H12	Cyclohexane			AWAS	10.0	cyclo-alkane
86.037	87.044	C4H6O2	2,3-Butanedione	0.87	8.4	PTR-ToF-MS	50.0	dione
86.037	87.044	C4H6O2	Methyl acrylate	0.05	11.4	PTR-ToF-MS	50.0	ester
86.037	87.044	C4H6O2	Fragments	0.08	NA	PTR-ToF-MS	NA	
86.073	87.080	C5H10O	3-Methyl-2-butanone	0.43	16.0	PTR-ToF-MS	50.0	ketone
86.073	87.080	C5H10O	2-Pentanone	0.32	15.2	PTR-ToF-MS	50.0	ketone
86.073	87.080	C5H10O	3-Pentanone	0.21	15.7	PTR-ToF-MS	50.0	ketone

86.073	87.080	C5H10O	2-Methylbutanal, 3-Methylbutanal	0.04	15.0	PTR-ToF-MS	50.0	aldehyde
86.073	*86.073*	*C5H10O*	*2-Methyl-3-buten-2-ol*			*TOGA*	*30.0*	*alcohol*
86.110	86.110	C6H14	n-Hexane			AWAS	10.0	alkane
86.110	86.110	C6H14	3-Methylpentane			AWAS	10.0	alkane
88.016	89.023	C3H4O3	Pyruvic acid	1.00	13.6	PTR-ToF-MS	50.0	acid
88.052	89.060	C4H8O2	Methyl propanoate	1.00	11.3	PTR-ToF-MS	50.0	ester
89.048	90.055	C3H7NO2	Nitropropanes	1.00	18.1	PTR-ToF-MS	50.0	nitroalkane
90.047	90.047	C7H16	2,4-Dimethylpentane			AWAS	10.0	alkane
91.042	92.049	C6H5N	Ethylnylpyrrole	1.00	12.7	PTR-ToF-MS	50.0	N-heterocycle
92.063	93.070	C7H8	Toluene	1.00	10.6	PTR-ToF-MS	15.0	aromatic
93.021	94.029	C5H3NO	3-Furancarbonitrile	0.70	16.5	PTR-ToF-MS	50.0	furan
93.021	94.029	C5H3NO	2-Furancarbonitrile	0.30	16.5	PTR-ToF-MS	50.0	furan
93.058	94.065	C6H7N	2-Methylpyridine	0.93	12.2	PTR-ToF-MS	50.0	N-heterocycle
93.058	94.065	C6H7N	3-Methylpyridine	0.07	14.1	PTR-ToF-MS	50.0	N-heterocycle
93.942	93.942	CH3Br	Methyl bromide			TOGA	20.0	haloalkane
94.042	95.049	C6H6O	Phenol	1.00	10.6	PTR-ToF-MS	50.0	aromatic
96.021	97.028	C5H4O2	2-Furfural (=furaldehyde)	0.84	16.2	PTR-ToF-MS	15.0	furan
96.021	97.028	C5H4O2	3-Furfural	0.04	18.5	PTR-ToF-MS	50.0	furan
96.021	97.028	C5H4O2	Fragments	0.11	NA	PTR-ToF-MS	NA	
96.058	97.065	C6H8O	C2-Substituted furan isomers	0.46	10.3	PTR-ToF-MS	50.0	furan
96.058	97.065	C6H8O	2,5-Dimethylfuran	0.44	10.3	PTR-ToF-MS	50.0	furan
96.058	97.065	C6H8O	2-Ethylfuran	0.10	10.3	PTR-ToF-MS	50.0	furan
97.089	98.096	C6H11N	4-Methylpentanenitrile	1.00	18.6	PTR-ToF-MS	50.0	nitrile
97.969	97.969	C2H4Cl2	1,2-Dichloroethane			TOGA	50.0	haloalkane
98.000	99.008	C4H2O3	Maleic anhydride	1.00	14.7	PTR-ToF-MS	50.0	furan
98.037	99.044	C5H6O2	2-Furanmethanol	0.34	12.3	PTR-ToF-MS	50.0	furan
98.037	99.044	C5H6O2	Fragments	0.66	NA	PTR-ToF-MS	NA	
98.073	99.080	C6H10O	C6H10O Ketones	0.74	16.1	PTR-ToF-MS	50.0	ketone
98.073	99.080	C6H10O	Methylcyclopentanone, Cyclohexanone	0.26	17.4	PTR-ToF-MS	50.0	cycloketone
98.110	98.110	C7H14	Methylcyclohexane			AWAS	10.0	cyclo-alkane
100.016	101.023	C4H4O3	Dihydrofurandione	1.00	15.8	PTR-ToF-MS	50.0	anhydride

100.052	101.060	C5H8O2	Methyl methacrylate	0.69	11.6	PTR-ToF-MS	50.0	ester
100.052	101.060	C5H8O2	Fragments	0.31	NA	PTR-ToF-MS	NA	
100.089	101.096	C6H12O	Hexanones	0.53	13.5	PTR-ToF-MS	15.0	ketone
100.089	101.096	C6H12O	Hexanal	0.47	14.5	PTR-ToF-MS	50.0	aldehyde
100.125	100.125	C7H16	n-Heptane			AWAS	10.0	alkane
100.125	100.125	C7H16	2-Methylhexane			AWAS	10.0	alkane
100.125	100.125	C7H16	3-Methylhexane			AWAS	10.0	alkane
100.125	100.125	C7H16	2,3-Dimethylpentane			AWAS	10.0	alkane
102.032	103.039	C4H6O3	Acetic anhydride	1.00	15.1	PTR-ToF-MS	50.0	anhydride
103.042	104.049	C7H5N	Benzonitrile	1.00	20.9	PTR-ToF-MS	50.0	nitrile
104.063	104.063	C8H8	Styrene			TOGA	40.0	aromatic
105.043	105.043	C3H7NO3	Isopropyl nitrate			TOGA	15.0	nitrate-ester
105.043	105.043	C3H7NO3	n-Propyl nitrate			TOGA	15.0	nitrate-ester
105.058	106.065	C7H7N	Vinylpyridine	1.00	13.0	PTR-ToF-MS	50.0	N-heterocycle
106.042	107.049	C7H6O	Benzaldehyde	1.00	16.7	PTR-ToF-MS	50.0	aromatic
106.078	107.086	C8H10	(m,p)-Xylenes	0.46	9.5	PTR-ToF-MS	15.0	aromatic
106.078	107.086	C8H10	Ethylbenzene	0.36	5.3	PTR-ToF-MS	15.0	aromatic
106.078	107.086	C8H10	o-Xylene	0.18	11.0	PTR-ToF-MS	50.0	aromatic
106.078	106.078	C8H10	(m,p)-Xylenes			TOGA	20.0	aromatic
106.078	106.078	C8H10	Ethylbenzene			TOGA	20.0	aromatic
106.078	106.078	C8H10	o-Xylene			TOGA	20.0	aromatic
108.021	109.028	C6H4O2	Quinone (=p-benzoquinone)	1.00	11.0	PTR-ToF-MS	50.0	ketone
108.058	109.065	C7H8O	2-Methylphenol (=o-cresol)	0.50	11.7	PTR-ToF-MS	50.0	alcohol
108.058	109.065	C7H8O	Anisol	0.50	11.4	PTR-ToF-MS	50.0	ether
110.037	111.044	C6H6O2	5-Methyl furfural	0.50	17.2	PTR-ToF-MS	15.0	furan
110.037	111.044	C6H6O2	Benzene diols (=catechol, resorcinol)	0.50	12.1	PTR-ToF-MS	50.0	alcohol
110.073	111.080	C7H10O	C3 Furans	0.55	10.9	PTR-ToF-MS	50.0	furan
110.073	111.080	C7H10O	Fragments	0.45	NA	PTR-ToF-MS	NA	
111.032	112.039	C5H5NO2	Dihydroxy pyridine	0.50	16.6	PTR-ToF-MS	50.0	N-heterocycle
111.032	112.039	C5H5NO2	Methyl maleimide	0.50	16.6	PTR-ToF-MS	50.0	N-heterocycle
112.008	112.008	C6H5Cl	Chlorobenzene			TOGA	15.0	haloalkane

112.016	113.023	C5H4O3	5-Hydroxy 2-furfural/2-furoic acid	1.00	13.9	PTR-ToF-MS	50.0	acid
112.052	113.060	C6H8O2	2-Hydroxy-3-methyl-2-cyclopenten-1-one	1.00	12.2	PTR-ToF-MS	50.0	cycloketone
112.089	113.096	C7H12O	Ethylcyclopentanone	1.00	16.4	PTR-ToF-MS	50.0	ketone
113.011	114.019	C4H3NO3	Nitrofuran	1.00	16.6	PTR-ToF-MS	50.0	furan
114.032	115.039	C5H6O3	5-Hydroxymethyl-2[3H]-furanone	0.50	14.8	PTR-ToF-MS	50.0	ester
114.068	115.075	C6H10O2	C6 1-DBE esters	0.54	12.5	PTR-ToF-MS	50.0	ester
114.068	115.075	C6H10O2	C6 Diones	0.46	10.8	PTR-ToF-MS	50.0	dione
114.104	115.112	C7H14O	Heptanal	0.63	14.7	PTR-ToF-MS	50.0	aldehyde
114.104	115.112	C7H14O	2,4-Dimethyl-3-pentanone	0.24	15.5	PTR-ToF-MS	50.0	ketone
114.104	115.112	C7H14O	Heptanone	0.13	15.4	PTR-ToF-MS	50.0	ketone
114.141	114.141	C8H18	2,2,4-Trimethylpentane			AWAS	10.0	alkane
114.141	114.141	C8H18	n-Octane			AWAS	10.0	alkane
114.141	114.141	C8H18	2-Methylheptane			AWAS	10.0	alkane
114.141	114.141	C8H18	2,3,4-Trimethylpentane			AWAS	10.0	alkane
114.141	114.141	C8H18	3-Methylheptane			AWAS	10.0	alkane
116.047	117.055	C5H8O3	5-Hydroxymethyl tetrahydro 2-furanone, 5-Hydroxy tetrahydro 2-furfural	1.00	14.8	PTR-ToF-MS	50.0	furan
116.084	117.091	C6H12O2	C6 Esters	1.00	12.5	PTR-ToF-MS	50.0	ester
117.058	118.065	C8H7N	Benzeneacetonitrile	1.00	18.7	PTR-ToF-MS	50.0	aromatic
117.914	117.914	CHCl3	Chloroform			TOGA	15.0	haloalkane
118.042	119.049	C8H6O	Benzofuran	1.00	11.2	PTR-ToF-MS	50.0	furan
118.078	119.086	C9H10	Methyl styrenes	0.84	11.5	PTR-ToF-MS	50.0	aromatic
118.078	119.086	C9H10	Indane	0.13	11.4	PTR-ToF-MS	50.0	aromatic
118.078	119.086	C9H10	Propenyl benzenes	0.03	11.4	PTR-ToF-MS	50.0	aromatic
119.058	119.058	C4H9NO3	Isobutyl nitrate, 2-Butyl nitrate			TOGA	30.0	nitrate-ester
120.058	121.065	C8H8O	Tolualdehyde	1.00	13.5	PTR-ToF-MS	50.0	aromatic
120.094	121.101	C9H12	C9 Aromatics	1.00	11.3	PTR-ToF-MS	15.0	aromatic
120.094	120.094	C9H12	1,2,3-Trimethylbenzene			AWAS	10.0	aromatic
120.094	120.094	C9H12	1,2,4-Trimethylbenzene			AWAS	10.0	aromatic
120.094	120.094	C9H12	4-Ethyltoluene			AWAS	10.0	aromatic
120.094	120.094	C9H12	3-Ethyltoluene			AWAS	10.0	aromatic

136

120.094	120.094	C9H12	2-Ethyltoluene			AWAS	10.0	aromatic
120.094	120.094	C9H12	Isopropylbenzene			AWAS	10.0	aromatic
120.094	120.094	C9H12	n-Propylbenzene			AWAS	10.0	aromatic
120.094	120.094	C9H12	1,3,5-Trimethylbenzene			AWAS	10.0	aromatic
122.037	123.044	C7H6O2	2-Hydroxybenzaldehyde (=salicylaldehyde)	1.00	12.6	PTR-ToF-MS	50.0	aromatic
122.073	123.080	C8H10O	C2 Phenols	0.50	12.2	PTR-ToF-MS	50.0	alcohol
122.073	123.080	C8H10O	Methyl anisol	0.50	13.6	PTR-ToF-MS	50.0	aromatic
124.016	125.023	C6H4O3	Hydroxy benzoquinone	1.00	14.9	PTR-ToF-MS	50.0	aromatic
124.052	125.060	C7H8O2	Guaiacol (=2-methoxyphenol)	1.00	12.7	PTR-ToF-MS	50.0	aromatic
126.032	127.039	C6H6O3	5-(Hydroxymethyl)-2-furfural	1.00	15.0	PTR-ToF-MS	50.0	furan
128.157	128.157	C9H20	n-Nonane			AWAS	10.0	alkane
131.930	131.930	C2H3Cl3	1,1,1-Trichloroethane			TOGA	20.0	haloalkane
132.058	133.065	C9H8O	Methylbenzofuran	1.00	11.8	PTR-ToF-MS	50.0	furan
132.094	133.101	C10H12	Ethyl styrene	0.50	11.9	PTR-ToF-MS	50.0	aromatic
132.094	133.101	C10H12	Methylpropenylbenzenes, bButenylbenzenes	0.50	11.9	PTR-ToF-MS	50.0	aromatic
134.073	135.080	C9H10O	3-Methylacetophenone	1.00	13.9	PTR-ToF-MS	50.0	aromatic
134.110	135.117	C10H14	C10 Aromatics	0.92	11.5	PTR-ToF-MS	15.0	aromatic
135.117	135.117	C10H15	Fragments	0.08	NA	PTR-ToF-MS	NA	
136.052	137.060	C8H8O2	Methyl benzoic acid	1.00	13.2	PTR-ToF-MS	50.0	aromatic
136.125	137.132	C10H16	Camphene	0.38	12.1	PTR-ToF-MS	50.0	terpene
136.125	137.132	C10H16	α-Pinene	0.33	5.1	PTR-ToF-MS	15.0	terpene
136.125	137.132	C10H16	β-Pinene, Myrcene	0.21	12.1	PTR-ToF-MS	50.0	terpene
136.125	137.132	C10H16	Tricyclene	0.07	12.1	PTR-ToF-MS	50.0	terpene
136.125	136.125	C10H16	Camphene			TOGA	20.0	monoterpene
136.125	136.125	C10H16	α-Pinene			TOGA	20.0	monoterpene
136.125	136.125	C10H16	β-Pinene, Myrcene			TOGA	30.0	monoterpene
136.125	136.125	C10H16	Tricyclene			TOGA	20.0	monoterpene
137.048	138.055	C7H7NO2	Nitrotoluene	1.00	21.2	PTR-ToF-MS	50.0	aromatic
138.068	139.075	C8H10O2	2-Methoxy-4-methylphenol (=creosol)	1.00	13.3	PTR-ToF-MS	50.0	aromatic
141.928	141.928	CH3I	Methyl iodide			TOGA	50.0	haloalkane

142.078	143.086	C11H10	Methylnaphthalene	1.00	12.3	PTR-ToF-MS	50.0	aromatic
144.042	145.050	C6H8O4	Product of levoglucosan dehydration (pyrolysis)	1.00	15.3	PTR-ToF-MS	50.0	alcohol
146.073	147.080	C10H10O	Dimethylbenzofuran	1.00	12.4	PTR-ToF-MS	50.0	furan
148.089	149.096	C10H12O	Methyl chavicol (=estragole)	1.00	14.3	PTR-ToF-MS	50.0	aromatic
148.125	149.132	C11H16	C11 Aromatics	1.00	12.5	PTR-ToF-MS	50.0	aromatic
150.068	151.075	C9H10O2	Vinyl guaiacol	1.00	13.8	PTR-ToF-MS	50.0	aromatic
152.047	153.055	C8H8O3	Vanillin	1.00	15.4	PTR-ToF-MS	50.0	aromatic
152.120	153.127	C10H16O	Oxygenated monoterpenes	0.70	14.6	PTR-ToF-MS	50.0	terpene
152.120	153.127	C10H16O	Camphor	0.30	17.3	PTR-ToF-MS	50.0	cycloketone
154.063	155.070	C8H10O3	Syringol	1.00	15.5	PTR-ToF-MS	50.0	aromatic
154.136	155.143	C10H18O	Cineole	1.00	14.7	PTR-ToF-MS	50.0	O-heterocycle
154.136	155.143	C10H18O	Other oxygenated monoterpenes	0.00	14.7	PTR-ToF-MS	50.0	terpene
156.094	157.101	C12H12	1,3-Dimethylnaphthalene	1.00	12.8	PTR-ToF-MS	50.0	aromatic
156.151	157.159	C10H20O	Decanal	1.00	15.4	PTR-ToF-MS	50.0	aldehyde
162.141	163.148	C12H18	C12 aromatics	1.00	13.0	PTR-ToF-MS	50.0	aromatic
164.084	165.091	C10H12O2	Eugenol, Isoeugenol	1.00	14.5	PTR-ToF-MS	50.0	ester
176.157	177.164	C13H20	C13 aromatics	1.00	13.4	PTR-ToF-MS	50.0	aromatic
204.188	205.195	C15H24	Sesquiterpenes	1.00	14.3	PTR-ToF-MS	50.0	terpene
			Black carbon (BC)			SP2	40.0	
			Organic carbon (OC)			HR-AMS	35.0	

Table S2.2. WE-CAN Campaign-averaged Emission Ratios, Emission Factors, and VOC Mass Fractions.

VOC contributor[a]	Exact mass[b], Da	Chemical formula	N[c]	ER to CO, ppb ppm^{-1} (σ)	EF, g kg^{-1} (σ)	VOC mass fraction %
Carbon dioxide	43.99	CO_2	24	9520.00 (2500.00)	1413.00 (61.00)	-
Carbon monoxide	27.995	CO	24	1000.00 (-)	99.30 (20.00)	-
Methane	16.031	CH_4	24	102.00 (17.00)	5.93 (1.80)	-
Ethyne[e]	26.016	C_2H_2	16	3.50 (1.80)	0.31 (0.17)	1.20 (0.71)
Hydrogen cyanide[d]	27.011	HCN	15	4.30 (1.70)	0.43 (0.17)	1.70 (0.79)
Ethene[e]	28.031	C_2H_4	16	16.00 (9.10)	1.50 (1.00)	5.90 (4.20)
Formaldehyde	30.011	CH_2O	24	18.00 (3.30)	1.90 (0.43)	7.30 (2.50)
Ethane[e]	30.047	C_2H_6	16	10.00 (6.70)	1.10 (0.84)	4.30 (3.40)
Methanol	32.026	CH_4O	24	13.00 (2.00)	1.50 (0.39)	5.80 (2.10)
Acetonitrile	41.027	C_2H_3N	24	2.10 (0.99)	0.31 (0.15)	1.20 (0.65)
Propene[e]	42.047	C_3H_6	16	4.90 (3.60)	0.74 (0.62)	2.90 (2.50)
Isocyanic acid	43.006	HNCO	24	1.10 (0.35)	0.16 (0.036)	0.61 (0.21)
Ethenamine	43.042	C_2H_5N	24	0.072 (0.034)	0.011 (0.0058)	0.043 (0.025)
Acetaldehyde	44.026	C_2H_4O	24	11.00 (1.60)	1.70 (0.43)	6.30 (2.30)
Propane[d]	44.063	C_3H_8	15	2.70 (0.92)	0.46 (0.18)	1.80 (0.84)
Formamide	45.021	CH_3NO	24	0.23 (0.08)	0.037 (0.014)	0.14 (0.066)
Formic acid[f]	46.005	CH_2O_2	20	9.50 (4.20)	1.50 (0.60)	5.70 (2.70)
Ethanol[d]	46.042	C_2H_6O	13	0.19 (0.17)	0.035 (0.04)	0.13 (0.16)
Methyl chloride[d]	49.992	CH_3Cl	15	0.092 (0.047)	0.017 (0.0089)	0.067 (0.038)
1-Buten-3-yne	52.031	C_4H_4	24	0.28 (0.088)	0.052 (0.018)	0.20 (0.087)
Acrylonitrile	53.027	C_3H_3N	24	0.23 (0.076)	0.044 (0.015)	0.17 (0.074)
2-Propynal	54.011	C_3H_2O	24	0.20 (0.089)	0.037 (0.015)	0.14 (0.07)
1,3-Butadiene, 1,2-Butadiene	54.047	C_4H_6	24	1.40 (0.38)	0.27 (0.096)	1.00 (0.46)
Propanenitrile	55.042	C_3H_5N	24	0.19 (0.087)	0.037 (0.018)	0.14 (0.077)
Acrolein[d]	56.026	C_3H_4O	15	1.90 (0.66)	0.40 (0.18)	1.50 (0.79)
Butenes	56.063	C_4H_8	24	1.30 (0.52)	0.26 (0.12)	1.00 (0.52)
Isobutene, 1-Butene[d]	56.063	C_4H_8	15	1.30 (0.78)	0.28 (0.17)	-
Methyl isocyanate, Hydroxyacetonitrile	57.021	C_2H_3NO	24	0.16 (0.03)	0.033 (0.0087)	0.13 (0.047)

Propeneamines	57.058	C_3H_7N	24	0.087 (0.035)	0.018 (0.0082)	0.07 (0.037)
Glyoxal	58.005	$C_2H_2O_2$	22	0.028 (0.023)	0.0054 (0.0045)	0.021 (0.018)
Acetone, Propanal	58.042	C_3H_6O	24	4.10 (0.64)	0.84 (0.22)	3.20 (1.20)
Acetone[d]	58.042	C_3H_6O	15	2.90 (1.40)	0.65 (0.38)	-
Propanal[d]	58.042	C_3H_6O	15	0.81 (0.30)	0.18 (0.07)	-
n-Butane[d]	58.078	C_4H_{10}	15	0.56 (0.26)	0.12 (0.061)	0.48 (0.27)
Isobutane[d]	58.078	C_4H_{10}	15	0.17 (0.088)	0.038 (0.019)	0.14 (0.084)
Acetamide	59.037	C_2H_5NO	24	0.19 (0.046)	0.04 (0.012)	0.15 (0.061)
Trimethylamine	59.073	C_3H_9N	24	0.026 (0.0085)	0.0054 (0.002)	0.021 (0.0095)
Acetic acid, Glycolaldehyde (=hydroxyacetaldehyde)	60.021	$C_2H_4O_2$	24	11.00 (2.10)	2.40 (0.61)	9.40 (3.40)
Isopropanol[d]	60.058	C_3H_8O	14	0.032 (0.021)	0.0074 (0.0058)	0.028 (0.024)
Nitromethane	61.016	CH_3NO_2	24	0.38 (0.10)	0.078 (0.0085)	0.30 (0.085)
Dimethyl sulfide[e]	62.019	C_2H_6S	9	0.41 (0.37)	0.08 (0.083)	0.31 (0.33)
Cyanoallene isomers	65.027	C_4H_3N	24	0.0074 (0.0055)	0.0017 (0.0012)	0.0064 (0.0049)
1,3-Cyclopentadiene	66.047	C_5H_6	24	0.048 (0.018)	0.011 (0.0049)	0.044 (0.022)
Pyrrole, Butenenitrile isomers	67.042	C_4H_5N	24	0.16 (0.091)	0.039 (0.021)	0.15 (0.089)
Methacrylonitrile[d]	67.042	C_4H_5N	15	0.056 (0.043)	0.014 (0.011)	-
Carbon suboxide	67.99	C_3O_2	21	0.037 (0.024)	0.0084 (0.0054)	0.032 (0.023)
Furan	68.026	C_4H_4O	24	1.70 (0.60)	0.43 (0.19)	1.70 (0.85)
Isoprene[d]	68.063	C_5H_8	15	0.31 (0.39)	0.082 (0.095)	0.31 (0.37)
Butanenitriles, Dihydropyrrole	69.058	C_4H_7N	24	0.081 (0.04)	0.02 (0.01)	0.077 (0.044)
Propiolic acid	70.005	$C_3H_2O_2$	23	0.044 (0.029)	0.011 (0.0071)	0.041 (0.029)
Methyl vinyl ketone, Methacrolein, 2-Butenal (=crotonaldehyde)	70.042	C_4H_6O	24	1.60 (0.51)	0.39 (0.15)	1.50 (0.71)
Methyl vinyl ketone[d]	70.042	C_4H_6O	15	0.75 (0.45)	0.20 (0.12)	-
Methacrolein[d]	70.042	C_4H_6O	15	0.37 (0.26)	0.097 (0.067)	-
2-Butenal[d]	70.042	C_4H_6O	15	0.15 (0.075)	0.041 (0.02)	-
Pentenes, Methylbutenes	70.078	C_5H_{10}	24	0.06 (0.03)	0.015 (0.0084)	0.059 (0.036)
Cyclopentane[e]	70.078	C_5H_{10}	16	0.014 (0.0088)	0.0035 (0.0025)	-
Buteneamines, Tetrahydropyrrole	71.073	C_4H_9N	21	0.014 (0.011)	0.0036 (0.003)	0.014 (0.012)
Pyruvaldehyde (=methyl glyoxal), Acrylic acid	72.021	$C_3H_4O_2$	24	0.84 (0.26)	0.22 (0.082)	0.83 (0.39)

Compound	Mass	Formula	n			
Methyl ethyl ketone, 2-Methylpropanal, Butanal	72.058	C_4H_8O	24	0.82 (0.17)	0.21 (0.063)	0.81 (0.32)
Methyl ethyl ketone[d]	72.058	C_4H_8O	15	0.73 (0.27)	0.20 (0.075)	-
Butanal[d]	72.058	C_4H_8O	15	0.19 (0.079)	0.053 (0.023)	-
n-Pentane[d]	72.094	C_5H_{12}	15	0.21 (0.094)	0.057 (0.028)	0.22 (0.12)
Isopentane[d]	72.094	C_5H_{12}	15	0.069 (0.043)	0.019 (0.012)	0.073 (0.05)
Nitroethene	73.016	$C_2H_3NO_2$	24	0.038 (0.013)	0.0099 (0.0037)	0.038 (0.017)
Hydroxyacetone, Methyl acetate, Ethyl formate	74.037	$C_3H_6O_2$	24	2.10 (0.57)	0.57 (0.20)	2.20 (0.97)
Nitroethane, Ethyl nitrite	75.032	$C_2H_5NO_2$	24	0.045 (0.012)	0.012 (0.0042)	0.047 (0.02)
Carbon disulfide[d]	75.944	CS_2	15	0.0016 (0.0012)	4.5e-04 (3.1e-04)	0.0017 (0.0013)
Benzene	78.047	C_6H_6	24	1.80 (0.24)	0.50 (0.14)	1.90 (0.73)
Pentadienenitriles, Pyridine	79.042	C_5H_5N	24	0.13 (0.025)	0.037 (0.01)	0.14 (0.055)
2,4-Cyclopentadiene-1-one	80.026	C_5H_4O	24	0.092 (0.052)	0.027 (0.017)	0.11 (0.07)
Pentenenitriles, Methylpyrroles	81.058	C_5H_7N	24	0.069 (0.039)	0.02 (0.011)	0.077 (0.048)
2-Methylfuran, 3-Methylfuran	82.042	C_5H_6O	24	0.92 (0.38)	0.28 (0.13)	1.10 (0.58)
2-Methylfuran[d]	82.042	C_5H_6O	12	0.15 (0.09)	0.047 (0.03)	-
3-Methylfuran[d]	82.042	C_5H_6O	14	0.03 (0.021)	0.0097 (0.0071)	-
2,2-Dimethylbutane[e]	82.078	C_6H_{10}	14	0.055 (0.037)	0.015 (0.011)	0.058 (0.043)
Pentanenitriles	83.073	C_5H_9N	24	0.071 (0.037)	0.021 (0.011)	0.08 (0.047)
Dichloromethane[d]	83.953	CH_2Cl_2	14	0.0088 (0.0064)	0.0029 (0.0022)	0.011 (0.009)
2(3H)-Furanone	84.021	$C_4H_4O_2$	24	1.10 (0.28)	0.32 (0.11)	1.20 (0.54)
3-Methyl-3-buten-2-one, Cyclopentanone	84.058	C_5H_8O	24	0.28 (0.099)	0.087 (0.038)	0.33 (0.17)
Cyclohexane[e]	84.094	C_6H_{12}	6	0.026 (0.043)	0.008 (0.014)	0.031 (0.055)
2,3-Butanedione, Methyl acrylate	86.037	$C_4H_6O_2$	24	1.70 (0.52)	0.53 (0.21)	2.00 (0.97)
3-Methyl-2-butanone, 2-Pentanone, 3-Pentanone, 2-Methylbutanal, 3-Methylbutanal	86.073	$C_5H_{10}O$	24	0.20 (0.058)	0.062 (0.023)	0.24 (0.11)
2-Methyl-3-buten-2-ol[d]	86.073	$C_5H_{10}O$	13	0.018 (0.01)	0.0061 (0.0036)	-
n-Hexane[e]	86.11	C_6H_{14}	15	0.13 (0.10)	0.04 (0.036)	0.15 (0.14)
3-Methylpentane[e]	86.11	C_6H_{14}	12	0.034 (0.019)	0.01 (0.0065)	0.039 (0.027)
Pyruvic acid	88.016	$C_3H_4O_3$	22	0.063 (0.026)	0.019 (0.008)	0.074 (0.036)
Methyl propanoate	88.052	$C_4H_8O_2$	24	0.25 (0.094)	0.081 (0.036)	0.31 (0.16)

Nitropropanes	89.048	$C_3H_7NO_2$	23	0.0074 (0.0033)	0.0024 (0.0012)	0.0092 (0.0052)
2,4-Dimethylpentane[e]	90.047	C_7H_{16}	7	0.0076 (0.0094)	0.0023 (0.003)	0.0086 (0.012)
Ethylnylpyrrole	91.042	C_6H_5N	24	0.028 (0.0068)	0.0091 (0.0026)	0.035 (0.014)
Toluene	92.063	C_7H_8	24	1.20 (0.33)	0.42 (0.16)	1.60 (0.74)
3-Furancarbonitrile, 2-Furancarbonitrile	93.021	C_5H_3NO	24	0.026 (0.0087)	0.0088 (0.0037)	0.034 (0.017)
2-Methylpyridine, 3-Methylpyridine	93.058	C_6H_7N	24	0.10 (0.026)	0.035 (0.012)	0.13 (0.057)
Methyl bromide[d]	93.942	CH_3Br	14	0.0029 (0.002)	1e-03 (7.1e-04)	0.0039 (0.0029)
Phenol	94.042	C_6H_6O	24	0.98 (0.34)	0.33 (0.13)	1.30 (0.60)
2-Furfural (=furaldehyde), 3-Furfural	96.021	$C_5H_4O_2$	24	1.50 (0.44)	0.53 (0.21)	2.00 (0.97)
C_2-Substituted furan isomers, 2,5-Dimethylfuran, 2-Ethylfuran	96.058	C_6H_8O	24	0.57 (0.25)	0.20 (0.096)	0.77 (0.42)
4-Methylpentanenitrile	97.089	$C_6H_{11}N$	24	0.025 (0.014)	0.0088 (0.0047)	0.034 (0.02)
1,2-Dichloroethane[d]	97.969	$C_2H_4Cl_2$	10	0.002 (0.0022)	8.2e-04 (9.1e-04)	0.0032 (0.0036)
Maleic anhydride	98	$C_4H_2O_3$	24	0.44 (0.28)	0.14 (0.072)	0.55 (0.31)
2-Furanmethanol	98.037	$C_5H_6O_2$	24	0.25 (0.10)	0.09 (0.043)	0.34 (0.19)
$C_6H_{10}O$ Ketones, Methylcyclopentanone, Cyclohexanone	98.073	$C_6H_{10}O$	24	0.096 (0.033)	0.034 (0.015)	0.13 (0.066)
Methylcyclohexane[e]	98.11	C_7H_{14}	13	0.05 (0.059)	0.018 (0.022)	0.07 (0.088)
Dihydrofurandione	100.016	$C_4H_4O_3$	23	0.16 (0.059)	0.055 (0.019)	0.21 (0.092)
Methyl methacrylate	100.052	$C_5H_8O_2$	24	0.31 (0.098)	0.11 (0.045)	0.44 (0.21)
Hexanones, Hexanal	100.089	$C_6H_{12}O$	23	0.036 (0.011)	0.013 (0.0056)	0.05 (0.025)
n-Heptane[e]	100.125	C_7H_{16}	16	0.13 (0.13)	0.046 (0.05)	0.18 (0.20)
2-Methylhexane[e]	100.125	C_7H_{16}	9	0.057 (0.11)	0.021 (0.042)	0.079 (0.16)
3-Methylhexane[e]	100.125	C_7H_{16}	5	0.04 (0.046)	0.016 (0.018)	0.06 (0.072)
2,3-Dimethylpentane[e]	100.125	C_7H_{16}	10	0.011 (0.019)	0.0039 (0.0075)	0.015 (0.029)
Acetic anhydride	102.032	$C_4H_6O_3$	24	0.12 (0.04)	0.044 (0.02)	0.17 (0.088)
Benzonitrile	103.042	C_7H_5N	24	0.15 (0.053)	0.055 (0.022)	0.21 (0.10)
Styrene[d]	104.063	C_8H_8	15	0.045 (0.028)	0.018 (0.012)	0.07 (0.048)
Isopropyl nitrate[d]	105.043	$C_3H_7NO_3$	13	0.0033 (0.0014)	0.0013 (5.5e-04)	0.0049 (0.0025)
n-Propyl nitrate	105.043	$C_3H_7NO_3$	4	0.0015 (6.5e-04)	5.3e-04 (2.4e-04)	0.002 (0.0011)
Vinylpyridine	105.058	C_7H_7N	24	0.022 (0.0092)	0.0085 (0.0038)	0.033 (0.017)

Compound	Mass	Formula	n	Value 1	Value 2	Value 3
Benzaldehyde	106.042	C_7H_6O	24	0.22 (0.043)	0.084 (0.026)	0.32 (0.13)
C_8 Aromatics	106.078	C_8H_{10}	24	0.53 (0.17)	0.21 (0.08)	0.79 (0.37)
(m,p)-Xylenes[d]	106.078	C_8H_{10}	15	0.16 (0.077)	0.065 (0.033)	-
Ethylbenzene[d]	106.078	C_8H_{10}	15	0.12 (0.046)	0.05 (0.022)	-
o-Xylene[d]	106.078	C_8H_{10}	15	0.062 (0.028)	0.025 (0.012)	-
Quinone (=p-benzoquinone)	108.021	$C_6H_4O_2$	24	0.20 (0.049)	0.077 (0.02)	0.30 (0.11)
2-Methylphenol (=o-Cresol), Anisol	108.058	C_7H_8O	24	0.57 (0.25)	0.23 (0.11)	0.87 (0.49)
5-Methylfurfural, Benzene diols (=catechol, resorcinol)	110.037	$C_6H_6O_2$	24	0.62 (0.24)	0.25 (0.12)	0.96 (0.52)
C_3 Furans	110.073	$C_7H_{10}O$	24	0.11 (0.052)	0.046 (0.024)	0.18 (0.10)
Dihydroxy pyridine, Methyl maleimide	111.032	$C_5H_5NO_2$	24	0.06 (0.017)	0.024 (0.0084)	0.092 (0.04)
Chlorobenzene[d]	112.008	C_6H_5Cl	14	4.5e-04 (2.4e-04)	2e-04 (1.3e-04)	7.5e-04 (5.2e-04)
5-Hydroxy-2-furfural/2-furoic acid	112.016	$C_5H_4O_3$	24	0.32 (0.07)	0.12 (0.031)	0.48 (0.17)
2-Hydroxy-3-methyl-2-cyclopenten-1-one	112.052	$C_6H_8O_2$	24	0.29 (0.13)	0.12 (0.061)	0.46 (0.26)
Ethylcyclopentanone	112.089	$C_7H_{12}O$	24	0.034 (0.016)	0.014 (0.007)	0.053 (0.03)
Nitrofuran	113.011	$C_4H_3NO_3$	24	0.013 (0.0044)	0.0051 (0.0019)	0.019 (0.0088)
5-Hydroxymethyl-2[3H]-furanone	114.032	$C_5H_6O_3$	24	0.063 (0.024)	0.026 (0.011)	0.098 (0.049)
C_6 1-DBE esters, C_6 Diones	114.068	$C_6H_{10}O_2$	24	0.093 (0.032)	0.039 (0.017)	0.15 (0.076)
Heptanal, 2,4-Dimethyl-3-pentanone, Heptanone	114.104	$C_7H_{14}O$	24	0.017 (0.0048)	0.0072 (0.0025)	0.027 (0.012)
2,2,4-Trimethylpentane[e]	114.141	C_8H_{18}	13	0.071 (0.046)	0.028 (0.018)	0.11 (0.073)
n-Octane[e]	114.141	C_8H_{18}	15	0.052 (0.038)	0.021 (0.017)	0.082 (0.07)
2-Methylheptane[e]	114.141	C_8H_{18}	14	0.034 (0.11)	0.015 (0.048)	0.056 (0.18)
2,3,4-Trimethylpentane[e]	114.141	C_8H_{18}	3	0.015 (0.021)	0.0067 (0.01)	0.026 (0.04)
3-Methylheptane[e]	114.141	C_8H_{18}	6	0.017 (0.022)	0.0074 (0.01)	0.028 (0.04)
5-Hydroxymethyl tetrahydro 2-furanone, 5-Hydroxy tetrahydro 2-furfural	116.047	$C_5H_8O_3$	24	0.08 (0.038)	0.034 (0.019)	0.13 (0.08)
C_6 Esters	116.084	$C_6H_{12}O_2$	24	0.028 (0.015)	0.011 (0.0062)	0.044 (0.026)
Benzeneacetonitrile	117.058	C_8H_7N	24	0.023 (0.0071)	0.0096 (0.0034)	0.037 (0.016)
Chloroform[d]	117.914	$CHCl_3$	7	7.5e-04 (5.9e-04)	3.6e-04 (2.9e-04)	0.0014 (0.0012)
Benzofuran	118.042	C_8H_6O	24	0.096 (0.028)	0.041 (0.015)	0.16 (0.072)

Methylstyrenes, Indane, Propenylbenzenes	118.078	C_9H_{10}	24	0.086 (0.041)	0.037 (0.019)	0.14 (0.081)
Isobutyl nitrate, 2-Butyl nitrate[d]	119.058	$C_4H_9NO_3$	7	0.0047 (0.0029)	0.0019 (0.0011)	0.0073 (0.0048)
Tolualdehydes	120.058	C_8H_8O	24	0.19 (0.053)	0.082 (0.03)	0.31 (0.14)
C_9 Aromatics	120.094	C_9H_{12}	24	0.16 (0.064)	0.069 (0.031)	0.26 (0.14)
1,2,3-Trimethylbenzene[e]	120.094	C_9H_{12}	16	0.19 (0.23)	0.089 (0.11)	-
1,2,4-Trimethylbenzene[e]	120.094	C_9H_{12}	15	0.17 (0.21)	0.076 (0.099)	-
4-Ethyltoluene[e]	120.094	C_9H_{12}	14	0.10 (0.15)	0.045 (0.071)	-
3-Ethyltoluene[e]	120.094	C_9H_{12}	14	0.079 (0.098)	0.034 (0.046)	-
2-Ethyltoluene[e]	120.094	C_9H_{12}	14	0.058 (0.11)	0.025 (0.051)	-
Isopropylbenzene[e]	120.094	C_9H_{12}	13	0.03 (0.054)	0.013 (0.025)	-
n-Propylbenzene[e]	120.094	C_9H_{12}	12	0.015 (0.0084)	0.0064 (0.0039)	-
1,3,5-Trimethylbenzene[e]	120.094	C_9H_{12}	7	0.0085 (0.0069)	0.0036 (0.0027)	-
2-Hydroxybenzaldehyde (=salicylaldehyde)	122.037	$C_7H_6O_2$	24	0.15 (0.041)	0.065 (0.023)	0.25 (0.11)
C_2 Phenols, Methyl anisol	122.073	$C_8H_{10}O$	24	0.22 (0.11)	0.10 (0.057)	0.39 (0.24)
Hydroxybenzoquinone	124.016	$C_6H_4O_3$	24	0.098 (0.052)	0.045 (0.026)	0.17 (0.11)
Guaiacol (=2-methoxyphenol)	124.052	$C_7H_8O_2$	24	0.58 (0.32)	0.27 (0.17)	1.00 (0.70)
5-(Hydroxymethyl)-2-furfural	126.032	$C_6H_6O_3$	24	0.14 (0.047)	0.064 (0.026)	0.24 (0.12)
n-Nonane[e]	128.156	C_9H_{20}	15	0.033 (0.024)	0.015 (0.012)	0.058 (0.048)
1,1,1-Trichloroethane[d]	131.93	$C_2H_3Cl_3$	12	4.3e-04 (6.5e-04)	2.1e-04 (3.2e-04)	8.2e-04 (0.0012)
Methylbenzofurans	132.058	C_9H_8O	24	0.094 (0.036)	0.046 (0.021)	0.17 (0.092)
Ethyl styrenes, Methylpropenylbenzenes, Butenylbenzenes	132.094	$C_{10}H_{12}$	24	0.083 (0.053)	0.04 (0.026)	0.15 (0.11)
3-Methylacetophenone	134.073	$C_9H_{10}O$	24	0.092 (0.034)	0.045 (0.019)	0.17 (0.086)
C_{10} Aromatics	134.11	$C_{10}H_{14}$	24	0.081 (0.039)	0.04 (0.021)	0.15 (0.09)
Methylbenzoic acid	136.052	$C_8H_8O_2$	24	0.13 (0.047)	0.066 (0.029)	0.25 (0.13)
Monoterpenes	136.125	$C_{10}H_{16}$	24	0.41 (0.30)	0.21 (0.15)	0.79 (0.61)
Camphene[d]	136.125	$C_{10}H_{16}$	15	0.03 (0.021)	0.016 (0.011)	-
α-Pinene[d]	136.125	$C_{10}H_{16}$	15	0.026 (0.02)	0.014 (0.012)	-
β-Pinene, Myrcene[d]	136.125	$C_{10}H_{16}$	10	0.021 (0.014)	0.011 (0.0079)	-
Tricyclene[d]	136.125	$C_{10}H_{16}$	15	0.0047 (0.0032)	0.0025 (0.0018)	-

Nitrotoluene	137.048	$C_7H_7NO_2$	23	0.014 (0.0057)	0.0071 (0.0034)	0.027 (0.015)
2-Methoxy-4-methylphenol (=creosol)	138.068	$C_8H_{10}O_2$	24	0.27 (0.18)	0.14 (0.11)	0.54 (0.44)
Methyl iodide[d]	141.928	CH_3I	15	0.0014 (7e-04)	7.7e-04 (5.2e-04)	0.0029 (0.0022)
Methylnaphthalene	142.078	$C_{11}H_{10}$	24	0.096 (0.041)	0.05 (0.024)	0.19 (0.10)
Product of levoglucosan dehydration (pyrolysis)	144.042	$C_6H_8O_4$	24	0.078 (0.052)	0.042 (0.03)	0.16 (0.12)
Dimethylbenzofuran	146.073	$C_{10}H_{10}O$	24	0.095 (0.047)	0.051 (0.028)	0.20 (0.12)
Methyl chavicol (=estragole)	148.089	$C_{10}H_{12}O$	24	0.046 (0.026)	0.025 (0.015)	0.097 (0.062)
C_{11} Aromatics	148.125	$C_{11}H_{16}$	24	0.025 (0.013)	0.014 (0.0074)	0.052 (0.031)
Vinyl guaiacol	150.068	$C_9H_{10}O_2$	24	0.063 (0.041)	0.036 (0.025)	0.14 (0.10)
Vanillin	152.047	$C_8H_8O_3$	18	0.04 (0.041)	0.022 (0.023)	0.083 (0.092)
Oxygenated monoterpenes, Camphor	152.12	$C_{10}H_{16}O$	24	0.045 (0.027)	0.025 (0.014)	0.094 (0.059)
Syringol	154.063	$C_8H_{10}O_3$	24	0.03 (0.011)	0.017 (0.0067)	0.065 (0.031)
Cineole, Other oxygenated monoterpenes	154.136	$C_{10}H_{18}O$	24	0.0048 (0.0029)	0.0027 (0.0017)	0.01 (0.0071)
1,3-Dimethylnaphthalene	156.094	$C_{12}H_{12}$	24	0.051 (0.027)	0.03 (0.018)	0.12 (0.074)
Decanal	156.151	$C_{10}H_{20}O$	21	0.0067 (0.0031)	0.0037 (0.0017)	0.014 (0.0076)
C_{12} Aromatics	162.141	$C_{12}H_{18}$	24	0.01 (0.0061)	0.0062 (0.0036)	0.024 (0.015)
Eugenol, Isoeugenol	164.084	$C_{10}H_{12}O_2$	24	0.032 (0.021)	0.02 (0.014)	0.076 (0.058)
C_{13} Aromatics	176.156	$C_{13}H_{20}$	24	0.013 (0.0065)	0.0085 (0.0047)	0.033 (0.02)
Sesquiterpenes	204.188	$C_{15}H_{24}$	23	0.038 (0.038)	0.029 (0.028)	0.11 (0.11)
Black carbon[g]	-	-	24	4.95 (2.00)[i]	0.389 (0.17)	-
Organic carbon[h]	-	-	24	145.00 (23.00)[i]	11.60 (3.30)	-
Total VOC emissions				**148.26 (29.61)**	**26.11 (6.92)**	

Note. Uncertainties are reported as the standard deviation (1σ) of the campaign average, representing fire-to-fire variability. The corresponding campaign average MCE is 0.90. [a]VOC contributors to PTR-ToF-MS measured ion masses are assigned based on Koss et al. (2018) and listed in order of most abundant isomeric contribution. Italicized VOC contributors are shown for speciation purposes but not included in the total carbon term of the carbon mass balance nor total emissions calculations (Section 2.3.6). [b]Dominant/Primary isotopologue exact mass. [c]Number of emission transects sampled more than 30 minutes apart. [d]Trace organic gas analyzer (TOGA). [e]Advanced whole air sampler (AWAS). [f]Iodide-adduct time-of-flight chemical-ionization mass (I⁻ CIMS). [g]Single particle soot photometer (SP2). [h]High-resolution aerosol mass spectrometer (HR-AMS). [i]$\mu g\ sm^{-3}\ ppm^{-1}_{CO}$.

Table S2.3. Emission pass start and stop times for the 24 'unique fires' used in this work. Times are reported in UTC. Enter and exit times correspond to when the C-130 entered and exited a smoke plume used for the emission analysis in this work. Emission transects > 30 minutes apart are treated as 'unique fires' and denoted with a, b, c, etc. 'Unique fires' with multiple emission transects that were averaged together are shown as pass 1, pass 2, etc.

Fire	Flight	Date	Pass 1		Pass 2		Pass 3		Pass 4		Pass 5	
			Enter	Exit	Enter	Exit	Enter	Exit	Enter	Exit	Enter	Exit
Carr Fire a	RF02	2018-07-26	21:52:15	21:54:10								
Carr Fire b	RF02	2018-07-26	22:36:05	22:39:45								
Taylor Creek Fire a	RF03	2018-07-30	22:47:40	22:48:40	22:51:30	22:52:45						
Sharps Fire a	RF04	2018-07-31	20:39:25	20:41:40	20:54:15	20:55:30						
Sharps Fire b	RF04	2018-08-01	00:03:20	00:05:40								
Rabbit Foot Fire a	RF06	2018-08-04	01:32:20	01:33:30								
Donnell Fire b	RF07	2018-08-06	22:38:50	22:40:30								
Donnell Fire c	RF07	2018-08-07	00:19:10	00:22:55	00:23:10	00:24:20						
Bear Trap Fire a	RF09	2018-08-09	21:22:15	21:24:00								
Bear Trap Fire b	RF09	2018-08-09	23:00:40	23:05:25								
Dollar Ridge Fire b	RF09	2018-08-10	00:16:20	00:18:00								
Rabbit Foot Fire b	RF10	2018-08-13	21:43:15	21:45:20								
Goldstone Fire a	RF10	2018-08-13	22:08:30	22:11:00								
Wigwam Fire a	RF10	2018-08-13	22:49:00	22:50:15								
Monument Fire a	RF10	2018-08-13	22:51:10	22:52:50								
Rabbit Foot Fire c	RF11	2018-08-15	20:44:20	20:46:10	20:53:50	20:59:25	21:06:20	21:09:55	21:27:55	21:32:25	21:37:50	21:43:00
Beaver Creek Fire a	RF11	2018-08-15	21:55:05	21:56:25								
Beaver Creek Fire b	RF11	2018-08-16	00:29:20	00:31:25								
Goldstone Fire b	RF11	2018-08-16	00:49:00	00:50:30								
Mendocino Complex Fire a	RF13	2018-08-21	00:14:40	00:20:45								
Red Feather Lakes Rx Fire a	RF18	2018-09-10	20:23:15	20:24:15								
Red Feather Lakes Rx Fire b	RF18	2018-09-10	22:26:05	22:26:35								
Silver Creek Fire a	RF19	2018-09-13	21:16:47	21:18:00								
Silver Creek Fire b	RF19	2018-09-13	21:18:15	21:19:00								

Table S2.4. Linear regression statistics for EF vs. MCE correlations for the 151 VOCs with EFs measured in at least 10 of the 24 'unique fires'.

Dominant isotopologue exact mass (da)	Chemical formula	VOC contributor	slope	Intercept	r^2	p-value	n^a
43.990	CO2	Carbon dioxide					
27.995	CO	Carbon monoxide					
16.031	CH4	Methane	-79.54	77.53	0.87	0.000	24
26.016	C2H2	Ethyne[e]	-1.43	1.60	0.03	0.520	16
27.011	HCN	Hydrogen cyanide[d]	-3.80	3.83	0.20	0.096	15
28.031	C2H4	Ethene[e]	-17.63	17.44	0.13	0.175	16
30.011	CH2O	Formaldehyde	-13.80	14.33	0.47	0.000	24
30.047	C2H6	Ethane[e]	-20.61	19.70	0.25	0.047	16
32.026	CH4O	Methanol	-15.23	15.21	0.69	0.000	24
41.027	C2H3N	Acetonitrile	-2.61	2.65	0.14	0.073	24
42.047	C3H6	Propene[e]	-14.52	13.85	0.23	0.062	16
43.006	HNCO	Isocyanic acid	0.17	0.01	0.01	0.642	24
43.042	C2H5N	Ethenamine	-0.16	0.15	0.33	0.003	24
44.026	C2H4O	Acetaldehyde	-16.81	16.79	0.70	0.000	24
44.063	C3H8	Propane[d]	-4.89	4.84	0.29	0.040	15
45.021	CH3NO	Formamide	-0.38	0.38	0.33	0.003	24
46.005	CH2O2	Formic acid[f]	-4.77	5.79	0.03	0.441	20
46.042	C2H6O	Ethanol[d]	-0.96	0.89	0.26	0.073	13
49.992	CH3Cl	Methyl chloride[d]	-0.15	0.15	0.12	0.214	15
52.031	C4H4	1-Buten-3-yne	-0.56	0.56	0.44	0.000	24
53.027	C3H3N	Acrylonitrile	-0.35	0.35	0.23	0.019	24
54.011	C3H2O	2-Propynal	-0.13	0.15	0.03	0.417	24
54.047	C4H6	1,3-Butadiene, 1,2-Butadiene	-3.62	3.53	0.65	0.000	24
55.042	C3H5N	Propanenitrile	-0.29	0.30	0.12	0.091	24
56.026	C3H4O	Acrolein[d]	-5.89	5.67	0.44	0.007	15
56.063	C4H8	Butenes	-3.85	3.73	0.49	0.000	24
56.063	C4H8	*Isobutene, 1-Butene*[d]					
57.021	C2H3NO	Methyl isocyanate, Hydroxyacetonitrile	-0.32	0.32	0.62	0.000	24

57.058	C3H7N	Propeneamines	-0.27	0.26	0.48	0.000	24
58.005	C2H2O2	Glyoxal	0.05	-0.04	0.05	0.311	22
58.042	C3H6O	Acetone, Propanal	-8.12	8.15	0.62	0.000	24
58.042	C3H6O	*Acetone*[d]					
58.042	C3H6O	*Propanal*[d]					
58.078	C4H10	n-Butane[d]	-1.44	1.42	0.22	0.075	15
58.078	C4H10	Isobutane[d]	-0.36	0.36	0.14	0.168	15
59.037	C2H5NO	Acetamide	-0.33	0.33	0.33	0.003	24
59.073	C3H9N	Trimethylamine	-0.05	0.05	0.26	0.011	24
60.021	C2H4O2	Acetic acid, glycolaldehyde (=hydroxyacetaldehyde)	-20.67	21.05	0.52	0.000	24
60.058	C3H8O	Isopropanol[d]	-0.15	0.14	0.27	0.056	14
61.016	CH3NO2	Nitromethane	0.06	0.03	0.02	0.521	24
62.019	C2H6S	Dimethyl sulfide[e]					
65.027	C4H3N	Cyanoallene isomers	-0.01	0.01	0.03	0.449	24
66.047	C5H6	1,3-Cyclopentadiene	-0.16	0.16	0.48	0.000	24
67.042	C4H5N	Pyrrole, Butenenitrile isomers	-0.29	0.30	0.09	0.157	24
67.042	C4H5N	*Methacrylonitrile*[d]					
67.990	C3O2	Carbon suboxide	0.03	-0.02	0.01	0.614	21
68.026	C4H4O	Furan	-7.45	7.14	0.69	0.000	24
68.063	C5H8	Isoprene[d]	-1.11	1.08	0.05	0.403	15
69.058	C4H7N	Butanenitriles, Dihydropyrrole	-0.19	0.19	0.15	0.065	24
70.005	C3H2O2	Propiolic acid	0.01	0.00	0.00	0.911	23
70.042	C4H6O	Methyl vinyl ketone, Methacrolein, 2-Butenal (=crotonaldehyde)	-5.06	4.95	0.51	0.000	24
70.042	C4H6O	*Methyl vinyl ketone*[d]					
70.042	C4H6O	*Methacrolein*[d]					
70.042	C4H6O	*2-Butenal*[d]					
70.078	C5H10	Pentenes & methylbutenes	-0.25	0.24	0.41	0.001	24
70.078	C5H10	*Cyclopentane*[e]					
71.073	C4H9N	Buteneamines, tetrahydropyrrole	-0.04	0.04	0.05	0.321	21
72.021	C3H4O2	Pyruvaldehyde (=methyl glyoxal), Acrylic acid	-2.82	2.76	0.53	0.000	24
72.058	C4H8O	Methyl ethyl ketone, 2-Methylpropanal, Butanal	-2.26	2.25	0.59	0.000	24
72.058	C4H8O	*Methyl ethyl ketone*[d]					

72.058	C4H8O	*Butanal*[d]					
72.094	C5H12	n-Pentane[d]	-0.72	0.70	0.26	0.052	15
72.094	C5H12	Isopentane[d]	-0.24	0.23	0.16	0.142	15
73.016	C2H3NO2	Nitroethene	-0.09	0.09	0.26	0.012	24
74.037	C3H6O2	Hydroxyacetone, Methyl acetate, Ethyl formate	-7.74	7.53	0.65	0.000	24
75.032	C2H5NO2	Nitroethane, ethyl nitrite	-0.15	0.15	0.57	0.000	24
75.944	CS2	Carbon disulfide[d]	0.00	0.00	0.00	0.893	15
78.047	C6H6	Benzene	-6.20	6.08	0.91	0.000	24
79.042	C5H5N	Pentadienenitriles, Pyridine	-0.41	0.41	0.71	0.000	24
80.026	C5H4O	2,4-Cyclopentadiene-1-one	-0.53	0.51	0.45	0.000	24
81.058	C5H7N	Pentenenitriles, Methylpyrroles	-0.21	0.21	0.15	0.061	24
82.042	C5H6O	2-Methylfuran, 3-Methylfuran	-4.73	4.54	0.58	0.000	24
82.042	C5H6O	*2-Methylfuran*[d]					
82.042	C5H6O	*3-Methylfuran*[d]					
82.078	C6H10	2,2-Dimethylbutane[e]	-0.13	0.13	0.06	0.395	14
83.073	C5H9N	Pentanenitriles	-0.14	0.15	0.08	0.186	24
83.953	CH2Cl2	Dichloromethane[d]	-0.04	0.04	0.10	0.267	14
84.021	C4H4O2	2(3H)-Furanone	-4.07	3.99	0.61	0.000	24
84.058	C5H8O	3-Methyl-3-buten-2-one, Cyclopentanone	-1.46	1.40	0.68	0.000	24
84.094	C6H12	Cyclohexane[e]					
86.037	C4H6O2	2,3-Butanedione, Methyl acrylate	-7.85	7.59	0.63	0.000	24
86.073	C5H10O	3-Methyl-2-butanone, 2-Pentanone, 3-Pentanone, 2-Methylbutanal, 3-Methylbutanal	-0.84	0.82	0.61	0.000	24
86.073	C5H10O	*2-Methyl-3-buten-2-ol*[d]					
86.110	C6H14	n-Hexane[e]	-0.98	0.93	0.31	0.031	15
86.110	C6H14	3-Methylpentane[e]	-0.11	0.11	0.13	0.257	12
88.016	C3H4O3	Pyruvic acid	-0.11	0.12	0.10	0.162	22
88.052	C4H8O2	Methyl propanoate	-1.19	1.15	0.50	0.000	24
89.048	C3H7NO2	Nitropropanes	-0.03	0.03	0.31	0.006	23
90.047	C7H16	2,4-Dimethylpentane[e]					
91.042	C6H5N	Ethylnylpyrrole	-0.08	0.08	0.41	0.001	24
92.063	C7H8	Toluene	-6.73	6.48	0.82	0.000	24
93.021	C5H3NO	3-Furancarbonitrile, 2-Furancarbonitrile	-0.13	0.13	0.60	0.000	24

93.058	C6H7N	2-Methylpyridine, 3-Methylpyridine	-0.46	0.45	0.70	0.000	24
93.942	CH3Br	Methyl bromide[d]	-0.01	0.01	0.08	0.340	14
94.042	C6H6O	Phenol	-4.08	4.01	0.46	0.000	24
96.021	C5H4O2	2-Furfural (=furaldehyde), 3-Furfural	-8.25	7.96	0.71	0.000	24
96.058	C6H8O	C2-substituted furan isomers, 2,5-Dimethylfuran, 2-Ethylfuran	-3.30	3.17	0.53	0.000	24
97.089	C6H11N	4-methylpentanenitrile	-0.07	0.07	0.09	0.152	24
97.969	C2H4Cl2	1,2-Dichloroethane[d]	-0.03	0.02	0.22	0.172	10
98.000	C4H2O3	Maleic anhydride	0.56	-0.36	0.03	0.441	24
98.037	C5H6O2	2-Furanmethanol	-1.54	1.48	0.58	0.000	24
98.073	C6H10O	C6H10O ketones, Methylcyclopentanone, Cyclohexanone	-0.57	0.55	0.68	0.000	24
98.110	C7H14	Methylcyclohexane[e]	-0.37	0.35	0.12	0.243	13
100.016	C4H4O3	Dihydrofurandione	-0.29	0.31	0.11	0.125	23
100.052	C5H8O2	Methyl methacrylate	-1.54	1.50	0.53	0.000	24
100.089	C6H12O	Hexanones, Hexanal	-0.20	0.19	0.61	0.000	23
100.125	C7H16	n-Heptane[e]	-0.76	0.73	0.10	0.247	16
100.125	C7H16	2-Methylhexane[e]					
100.125	C7H16	3-Methylhexane[e]					
100.125	C7H16	2,3-Dimethylpentane[e]	-0.08	0.07	0.06	0.512	10
102.032	C4H6O3	Acetic anhydride	-0.75	0.72	0.65	0.000	24
103.042	C7H5N	Benzonitrile	-0.70	0.68	0.44	0.000	24
104.063	C8H8	Styrene[d]	-0.30	0.29	0.26	0.050	15
105.043	C3H7NO3	Isopropyl nitrate[d]	-0.01	0.01	0.08	0.356	13
105.043	C3H7NO3	n-propyl nitrate					
105.058	C7H7N	Vinylpyridine	-0.12	0.11	0.42	0.001	24
106.042	C7H6O	Benzaldehyde	-1.07	1.05	0.78	0.000	24
106.078	C8H10	C8 Aromatics	-3.09	2.99	0.67	0.000	24
106.078	C8H10	(m,p)-Xylene[d]					
106.078	C8H10	Ethylbenzene[d]					
106.078	C8H10	o-Xylene[d]					
108.021	C6H4O2	Quinone (=p-Benzoquinone)	-0.45	0.48	0.23	0.019	24
108.058	C7H8O	2-Methylphenol (=o-cresol), Anisol	-3.99	3.82	0.58	0.000	24
110.037	C6H6O2	5-Methylfurfural, Benzene diols (=catechol, resorcinol)	-4.50	4.30	0.65	0.000	24

Mass	Formula	Name					
110.073	C7H10O	C$_3$ Furans	-0.87	0.83	0.60	0.000	24
111.032	C5H5NO2	Dihydroxy pyridine, Methyl maleimide	-0.32	0.31	0.67	0.000	24
112.008	C6H5Cl	Chlorobenzene[d]	0.00	0.00	0.16	0.164	14
112.016	C5H4O3	5-Hydroxy-2-furfural/2-furoic acid	-0.89	0.92	0.36	0.002	24
112.052	C6H8O2	2-Hydroxy-3-methyl-2-cyclopenten-1-one	-2.25	2.15	0.62	0.000	24
112.089	C7H12O	Ethylcyclopentanone	-0.21	0.20	0.39	0.001	24
113.011	C4H3NO3	Nitrofuran	-0.03	0.04	0.15	0.065	24
114.032	C5H6O3	5-hydroxymethyl-2[3H]-furanone	-0.31	0.30	0.36	0.002	24
114.068	C6H10O2	C$_6$ 1-DBE esters, C$_6$ Diones	-0.66	0.63	0.68	0.000	24
114.104	C7H14O	Heptanal, 2,4-Dimethyl-3-pentanone, Heptanone	-0.09	0.09	0.59	0.000	24
114.141	C8H18	2,2,4-Trimethylpentane[e]	-0.15	0.42	0.02	0.622	13
114.141	C8H18	n-Octane[e]	-0.44	0.41	0.27	0.046	15
114.141	C8H18	2-Methylheptane[e]	-0.43	0.16	0.04	0.518	14
114.141	C8H18	2,3,4-Trimethylpentane[e]					
114.141	C8H18	3-Methylheptane[e]					
116.047	C5H8O3	5-hydroxymethyl tetrahydro 2-furanone, 5-hydroxy tetrahydro 2-furfural	-0.63	0.60	0.51	0.000	24
116.084	C6H12O2	C$_6$ Esters	-0.09	0.09	0.10	0.140	24
117.058	C8H7N	Benzeneacetonitrile	-0.11	0.11	0.48	0.000	24
117.914	CHCl3	Chloroform[d]					
118.042	C8H6O	Benzofuran	-0.62	0.60	0.73	0.000	24
118.078	C9H10	Methylstyrenes, Indane, Propenylbenzenes	-0.55	0.53	0.38	0.001	24
119.058	C4H9NO3	Isobutyl nitrate, 2-butyl nitrate[d]					
120.058	C8H8O	Tolualdehydes	-1.19	1.15	0.72	0.000	24
120.094	C9H12	C$_9$ Aromatics	-1.04	1.01	0.51	0.000	24
120.094	C9H12	*1,2,3-Trimethylbenzene[e]*					
120.094	C9H12	*1,2,4-Trimethylbenzene[e]*					
120.094	C9H12	*4-Ethyltoluene[e]*					
120.094	C9H12	*3-Ethyltoluene[e]*					
120.094	C9H12	*2-Ethyltoluene[e]*					
120.094	C9H12	*Isopropylbenzene[e]*					
120.094	C9H12	*n-Propylbenzene[e]*					
120.094	C9H12	*1,3,5-Trimethylbenzene[e]*					

122.037	C7H6O2	2-Hydroxybenzaldehyde (=Salicylaldehyde)	-0.84	0.82	0.63	0.000	24
122.073	C8H10O	C_2 Phenols, Methyl anisol	-2.01	1.91	0.56	0.000	24
124.016	C6H4O3	Hydroxybenzoquinone	-0.80	0.76	0.42	0.001	24
124.052	C7H8O2	Guaiacol (=2-methoxyphenol)	-6.08	5.75	0.60	0.000	24
126.032	C6H6O3	5-(Hydroxymethyl)-2-furfural	-0.88	0.86	0.53	0.000	24
128.157	C9H20	n-Nonane[e]	-0.26	0.25	0.20	0.098	15
131.930	C2H3Cl3	1,1,1-Trichloroethane[d]	0.00	0.00	0.01	0.784	12
132.058	C9H8O	Methylbenzofurans	-0.77	0.74	0.62	0.000	24
132.094	C10H12	Ethyl styrenes, Methylpropenylbenzenes, Butenylbenzenes	-0.68	0.65	0.30	0.006	24
134.073	C9H10O	3-Methylacetophenone	-0.71	0.68	0.62	0.000	24
134.110	C10H14	C_{10} Aromatics	-0.72	0.69	0.54	0.000	24
136.052	C8H8O2	Methylbenzoic acid	-1.13	1.08	0.69	0.000	24
136.125	C10H16	Monoterpenes	-3.58	3.43	0.26	0.011	24
136.125	C10H16	Camphene[d]					
136.125	C10H16	a-Pinene[d]					
136.125	C10H16	b-Pinene, Myrcene[d]					
136.125	C10H16	Tricyclene[d]					
137.048	C7H7NO2	Nitrotoluene	-0.11	0.10	0.46	0.000	23
138.068	C8H10O2	2-Methoxy-4-methylphenol (= creosol)	-3.65	3.43	0.53	0.000	24
141.928	CH3I	Methyl iodide[d]	-0.02	0.02	0.40	0.011	15
142.078	C11H10	Methylnaphthalene	-0.84	0.80	0.57	0.000	24
144.042	C6H8O4	Product of levoglucosan dehydration (pyrolysis)	-0.77	0.73	0.29	0.006	24
146.073	C10H10O	Dimethylbenzofuran	-0.92	0.88	0.50	0.000	24
148.089	C10H12O	Methyl chavicol (estragole)	-0.42	0.41	0.38	0.001	24
148.125	C11H16	C_{11} Aromatics	-0.23	0.22	0.44	0.001	24
150.068	C9H10O2	Vinyl guaiacol	-0.79	0.75	0.46	0.000	24
152.047	C8H8O3	Vanillin	-0.37	0.35	0.11	0.173	18
152.120	C10H16O	Oxygenated monoterpenes, Camphor	-0.25	0.25	0.15	0.063	24
154.063	C8H10O3	Syringol	-0.23	0.22	0.52	0.000	24
154.136	C10H18O	Cineole, Other oxygenated monoterpenes	-0.03	0.03	0.11	0.112	24
156.094	C12H12	1,3-Dimethylnaphthalene	-0.64	0.61	0.59	0.000	24
156.151	C10H20O	Decanal	-0.05	0.05	0.29	0.012	21

162.141	C12H18	C$_{12}$ Aromatics		-0.08	0.08	0.24	0.016	24
164.084	C10H12O2	Eugenol + isoeugenol		-0.44	0.42	0.44	0.000	24
176.157	C13H20	C$_{13}$ Aromatics		-0.16	0.15	0.52	0.000	24
204.188	C15H24	Sesquiterpenes		-0.42	0.40	0.09	0.166	23

Table S3.1. VOC species used in this work, including the instrument each species was measured by, the isomeric fractional contributions to the PTR-ToF-MS measured ion, measurement uncertainty, and weighted rate constants for the reaction with the OH radical.

Formula	Dominant isotopologue mass (da)	VOC contributor	Instrument	Fractional contribution to PTR-ToF-MS ion signal	Uncertainty (%)	k_{OH} (10^{-12} cm^3 molecule^{-1} s^{-1})
C$_2$H$_2$	26.0157	Ethyne	AWAS		10	1
HCN	27.0109	Hydrogen cyanide	CIMS		30	0
C$_2$H$_4$	28.0313	Ethene	AWAS		10	7.8
CH$_2$O	30.0106	Formaldehyde	PTR	1	40	8.5
C$_2$H$_6$	30.0470	Ethane	AWAS		10	0.24
CH$_4$O	32.0262	Methanol	PTR	1	15	0.8
C$_2$H$_3$N	41.0265	Acetonitrile	PTR	1	15	0
C$_3$H$_6$	42.0470	Propene	PTR	0.62	50	30
C$_3$H$_6$	42.0470	Fragments	PTR	0.38		
HNCO	43.0058	Isocyanic acid	PTR	1	50	0
C$_2$H$_5$N	43.0422	Ethenamine	PTR	1	50	0.2
C$_2$H$_4$O	44.0262	Acetaldehyde	PTR	1	15	15
C$_3$H$_8$	44.0626	Propane	TOGA		30	1.09
CH$_3$NO	45.0215	Formamide	PTR	1	50	1.5
CH$_2$O$_2$	46.0055	Formic acid	CIMS		30	0.4
C$_2$H$_6$O	46.0419	Ethanol	TOGA		30	3.2
HONO	47.0007	HONO	CIMS		30	6
C$_4$H$_4$	52.0313	1-Buten-3-yne	PTR	0.87	50	20

C_4H_4		Fragments	PTR	0.13		
C_3H_3N	53.0265	Acrylonitrile	PTR	1	50	4
C_3H_2O	54.0106	2-Propynal	PTR	1	50	20
C_4H_6	54.0470	1,3-Butadiene	PTR	0.82	50	58.8
C_4H_6	54.0470	1,2-Butadiene	PTR	0.01	50	58.8
C_4H_7		Fragments	PTR	0.17		
C_3H_5N	55.0422	Propanenitrile	PTR	1	50	0.3
C_3H_4O	56.0262	Acrolein	TOGA		30	20
C_4H_8	56.0626	Butenes	PTR	0.59	15	31.8
C_4H_9		Fragments	PTR	0.41		
C_2H_3NO	57.0215	Methyl isocyanate	PTR	0.5	50	0.1
C_2H_3NO	57.0215	Hydroxyacetonitrile	PTR	0.5	50	0.1
C_3H_7N	57.0578	Propene amine	PTR	1	50	15
$C_2H_2O_2$	58.0055	Glyoxal	PTR	1	50	11
C_3H_6O	58.0419	Acetone	PTR	0.83	20	0.2
C_3H_6O	58.0419	Propanal	PTR	0.17	20	0.2
C_4H_{10}	58.0783	Isobutane	TOGA		15	2.3
C_4H_{10}	58.0783	n-Butane	TOGA		15	2.4
C_2H_5NO	59.0371	Acetamide	PTR	1	50	8.6
C_3H_9N	59.0735	Trimethylamine	PTR	1	50	60
$C_2H_4O_2$	60.0211	Acetic acid	PTR	0.67	40	3.7
$C_2H_4O_2$	60.0211	Glycolaldehyde (=hydroxyacetaldehyde)	PTR	0.33	40	3.7
C_3H_8O	60.0575	Isopropanol	TOGA		30	5.7
CH_3NO_2	61.0164	Nitromethane	PTR	1	50	0
C_2H_6S	62.0190	Dimethyl sulfide	AWAS		10	6
C_4H_3N	65.0265	Cyanoallene isomers	PTR	1	50	4
C_5H_6	66.0470	1,3-Cyclopentadiene	PTR	0.22	50	92
C_5H_7		Fragments	PTR	0.78		
C_4H_5N	67.0422	Pyrrole	PTR	0.57	50	111.4
C_4H_5N	67.0422	Butene nitrile isomers	PTR	0.43	50	111.4
C_3O_2	67.9898	Carbon suboxide	PTR	1	50	1.5

Formula	Mass	Name	Instrument			
C_4H_4O	68.0262	Furan	TOGA		40	40
C_5H_8	68.0626	Isoprene	PTR	0.63	20	100
C_4H_7N	69.0578	Butane nitrile	PTR	0.61	50	7.7
C_4H_7N	69.0578	Dihydropyrrole	PTR	0.39	50	7.7
$C_3H_2O_2$	70.0055	Propiolic acid	PTR	1	50	26
C_4H_6O	70.0419	Methyl vinyl ketone	PTR	0.6	20	24.8
C_4H_6O	70.0419	Methacrolein	PTR	0.28	20	24.8
C_4H_6O	70.0419	2-Butenal (=crotonaldehyde)	PTR	0.13	20	24.8
C_5H_{10}	70.0783	Pentene, Methylbutenes	PTR	0.69	50	57.2
C_5H_{11}		Fragments	PTR	0.31		
C_4H_9N	71.0735	Buteneamines, Tetrahydropyrole	PTR	1	50	25
$C_3H_4O_2$	72.0211	Pyruvaldehyde (=methyl glyoxal)	PTR	0.5	50	21.1
$C_3H_4O_2$	72.0211	Acrylic acid	PTR	0.5	50	21.1
C_4H_8O	72.0575	Methyl ethyl ketone	PTR	0.85	20	5.5
C_4H_8O	72.0575	2-Methyl propanal	PTR	0.14	20	5.5
C_4H_8O	72.0575	Butanal	PTR	0.01	20	5.5
C_5H_{12}	72.0939	n-Pentane	TOGA		15	3.9
C_5H_{12}	72.0939	Isopentane	TOGA		15	3.9
$C_2H_3NO_2$	73.0164	Nitroethene	PTR	1	50	1.2
$C_3H_6O_2$	74.0368	Hydroxyacetone	PTR	0.5	50	2.2
$C_3H_6O_2$	74.0368	Methyl acetate	PTR	0.35	50	2.2
$C_3H_6O_2$	74.0368	Ethyl formate	PTR	0.14	50	2.2
$C_2H_5NO_2$	75.0320	Nitroethane, Ethyl nitrite	PTR	1	50	0.1
CS_2	75.9441	Carbon disulfide	TOGA		50	1.98
C_6H_6	78.0470	Benzene	PTR	0.95	15	1.2
C_6H_6		Fragments	PTR	0.05		
C_5H_5N	79.0422	Pentadienenitriles	PTR	0.56	50	5.6
C_5H_5N	79.0422	Pyridine	PTR	0.44	50	5.6
C_5H_4O	80.0262	2,4-Cyclopentadiene-1-one	PTR	0.42	50	20
C_5H_4O		Fragments	PTR	0.58		
C_5H_7N	81.0578	Pentenenitriles	PTR	0.67	50	62.7

C_5H_7N	81.0578	Methylpyrroles	PTR	0.33	50	62.7
C_5H_6O	82.0419	2-Methylfuran	TOGA		20	100
C_5H_6O	82.0419	3-Methyl furan	TOGA		20	100
C_6H_{10}	82.0783	2,2-Dimethylbutane	AWAS		10	5.95
C_5H_9N	83.0735	Pentanenitriles	PTR	1	50	0.5
$C_4H_4O_2$	84.0211	2(3H)-Furanone	PTR	0.81	50	44.5
C_5H_8O	84.0575	3-Methyl-3-buten-2-one	PTR	0.37	50	11.5
C_5H_8O	84.0575	Cyclopentanone	PTR	0.18	50	11.5
C_5H_8O		Fragments	PTR	0.45		
C_6H_{12}	84.0939	Cyclohexane	AWAS		10	7.2
$C_4H_6O_2$	86.0368	2,3-Butanedione	PTR	0.87	50	0.8
$C_4H_6O_2$	86.0368	Methyl acrylate	PTR	0.05	50	0.8
$C_4H_6O_2$		Fragments	PTR	0.08		
$C_5H_{10}O$	86.0732	3-Methyl-2-butanone	PTR	0.43	50	7.9
$C_5H_{10}O$	86.0732	2-Pentanone	PTR	0.32	50	7.9
$C_5H_{10}O$	86.0732	3-Pentanone	PTR	0.21	50	7.9
$C_5H_{10}O$	86.0732	2-Methylbutanal, 3-Methylbutanal	PTR	0.04	50	7.9
C_6H_{14}	86.1096	n-Hexane	AWAS		10	5.4
C_6H_{14}	86.1096	3-Methylpentane	AWAS		10	5.45
$C_3H_4O_3$	88.0160	Pyruvic acid	PTR	1	50	0.1
$C_4H_8O_2$	88.0524	Methyl propanoate	PTR	1	50	0.9
$C_3H_7NO_2$	89.0477	Nitropropanes	PTR	1	50	1.2
C_7H_{16}	90.0470	2,4-Dimethylpentane	AWAS		10	6.89
C_6H_5N	91.0422	Ethylnylpyrrole	PTR	1	50	145
C_7H_8	92.0626	Toluene	PTR	1	15	5.6
C_5H_3NO	93.0215	3-Furancarbonitrile	PTR	0.7	50	40
C_5H_3NO	93.0215	2-Furancarbonitrile	PTR	0.3	50	40
C_6H_7N	93.0578	2-Methylpyridine	PTR	0.93	50	2.6
C_6H_7N	93.0578	3-Methylpyridine	PTR	0.07	50	2.6
C_6H_6O	94.0419	Phenol	CIMS		30	28
$C_5H_4O_2$	96.0211	2-Furfural (=furaldehyde)	PTR	0.84	20	35.6

Formula	Mass	Name	Method			
$C_5H_4O_2$	96.0211	3-Furfural	PTR	0.04	20	35.6
$C_5H_4O_2$		Fragments	PTR	0.11		
C_6H_8O	96.0575	C2-Substituted furan isomers	PTR	0.46	50	132
C_6H_8O	96.0575	2,5-Dimethylfuran	PTR	0.44	50	132
C_6H_8O	96.0575	2-Ethylfuran	PTR	0.1	50	132
$C_6H_{11}N$	97.0891	4-Methylpentanenitrile	PTR	1	50	5
$C_4H_2O_3$	98.0004	Maleic anhydride	PTR	1	50	1.4
$C_5H_6O_2$	98.0368	2-Furanmethanol	PTR	0.34	50	13.6
$C_5H_6O_2$		Fragments	PTR	0.66		
$C_6H_{10}O$	98.0732	C6H10O Ketones	PTR	0.74	50	6.4
$C_6H_{10}O$	98.0732	Methylcyclopentanone, Cyclohexanone	PTR	0.26	50	6.4
C_7H_{14}	98.1096	Methylcyclohexane	AWAS		10	11
$C_4H_4O_3$	100.0160	Dihydrofurandione (=succinic anhydride)	PTR	1	50	20
$C_5H_8O_2$	100.0524	Methyl methacrylate	PTR	0.69	50	30.3
$C_5H_8O_2$		Fragments	PTR	0.31		
$C_6H_{12}O$	100.0888	Hexanones	PTR	0.53	30	18.6
$C_6H_{12}O$	100.0888	Hexanal	PTR	0.47	30	18.6
C_7H_{16}	100.1252	n-Heptane	AWAS		10	7.11
C_7H_{16}	100.1252	2-Methylhexane	AWAS		10	6.7
C_7H_{16}	100.1252	3-Methylhexane	AWAS		10	6.3
C_7H_{16}	100.1252	2,3-Dimethylpentane	AWAS		10	6.89
$C_4H_6O_3$	102.0317	Acetic anhydride	PTR	1	50	43
C_7H_5N	103.0422	Benzonitrile	PTR	1	50	1
C_8H_8	104.0626	Styrene	TOGA		40	58
$C_3H_7NO_3$	105.0426	Isopropyl nitrate	TOGA		15	0.42
$C_3H_7NO_3$	105.0426	n-Propyl nitrate	TOGA		15	0.73
C_7H_7N	105.0578	Vinylpyridine	PTR	1	50	57
C_7H_6O	106.0419	Benzaldehyde	PTR	1	50	12
C_8H_{10}	106.0783	(m,p)-Xylenes	PTR	0.46	20	13.2
C_8H_{10}	106.0783	Ethylbenzene	PTR	0.36	20	13.2
C_8H_{10}	106.0783	o-Xylene	PTR	0.18	20	13.2

$C_6H_4O_2$	108.0211	Quinone (=p-benzoquinone)	PTR	1	50	4.6
C_7H_8O	108.0575	2-Methylphenol (=o-cresol)	PTR	0.5	50	26.2
C_7H_8O	108.0575	Anisol	PTR	0.5	50	26.2
$C_6H_6O_2$	110.0368	5-Methyl furfural	PTR	0.5	30	80.1
$C_6H_6O_2$	110.0368	Benzene diols (=catechol, resorcinol)	PTR	0.5	30	80.1
$C_7H_{10}O$	110.0732	C3 Furans	PTR	0.55	50	23.3
$C_7H_{10}O$		Fragments	PTR	0.45		
$C_5H_5NO_2$	111.0320	Dihydroxy pyridine	PTR	0.5	50	10.3
$C_5H_5NO_2$	111.0320	Methyl maleimide	PTR	0.5	50	10.3
$C_5H_4O_3$	112.0160	5-Hydroxy 2-furfural/2-furoic acid	PTR	1	50	49
$C_6H_8O_2$	112.0524	2-Hydroxy-3-methyl-2-cyclopenten-1-one	PTR	1	50	57
$C_7H_{12}O$	112.0888	Ethylcyclopentanone	PTR	1	50	10
$C_4H_3NO_3$	113.0113	Nitrofuran	PTR	1	50	40
$C_5H_6O_3$	114.0317	5-Hydroxymethyl-2[3H]-furanone	PTR	0.5	50	100
$C_6H_{10}O_2$	114.0681	C6 1-DBE esters	PTR	0.54	50	20
$C_6H_{10}O_2$	114.0681	C6 Diones	PTR	0.46	50	20
$C_7H_{14}O$	114.1045	Heptanal	PTR	0.63	50	21.4
$C_7H_{14}O$	114.1045	2,4-Dimethyl-3-pentanone	PTR	0.24	50	21.4
$C_7H_{14}O$	114.1045	Heptanone	PTR	0.13	50	21.4
C_8H_{18}	114.1409	2,2,4-Trimethylpentane	TOGA		15	5.4
C_8H_{18}	114.1409	n-Octane	AWAS		10	8.11
C_8H_{18}	114.1409	2-Methylheptane	AWAS		10	12.2
C_8H_{18}	114.1409	2,3,4-Trimethylpentane	AWAS		10	6.5
C_8H_{18}	114.1409	3-Methylheptane	AWAS		10	14
$C_5H_8O_3$	116.0473	5-Hydroxymethyl tetrahydro 2-furanone, 5-Hydroxy tetrahydro 2-furfural	PTR	1	50	5
$C_6H_{12}O_2$	116.0837	C6 Esters	PTR	1	50	6
C_8H_7N	117.0578	Benzeneacetonitrile	PTR	1	50	1.2
C_8H_6O	118.0419	Benzofuran	PTR	1	50	37
C_9H_{10}	118.0783	Methyl styrenes	PTR	0.84	50	50.4
C_9H_{10}	118.0783	Indane	PTR	0.13	50	50.4

C_9H_{10}	118.0783	Propenyl benzenes	PTR	0.03	50	50.4
C_8H_8O	120.0575	Tolualdehyde	PTR	1	50	16
C_9H_{12}	120.0939	C9 Aromatics	PTR	1	15	22
$C_7H_6O_2$	122.0368	2-Hydroxybenzaldehyde	PTR	1	50	38
$C_8H_{10}O$	122.0732	C2 Phenols	PTR	0.5	50	46.6
$C_8H_{10}O$	122.0732	Methyl anisol	PTR	0.5	50	46.6
$C_6H_4O_3$	124.0160	Hydroxy benzoquinone	PTR	1	50	4.6
$C_7H_8O_2$	124.0524	Guaiacol (=2-methoxyphenol)	PTR	1	50	75
$C_6H_6O_3$	126.0317	5-(Hydroxymethyl)-2-furfural	PTR	1	50	100
C_9H_{20}	128.1565	n-Nonane	AWAS		10	9.7
C_9H_8O	132.0575	Methylbenzofuran	PTR	1	50	37
$C_{10}H_{12}$	132.0939	Ethyl styrene	PTR	0.5	50	33
$C_{10}H_{12}$	132.0939	Methylpropenylbenzenes, Butenylbenzenes	PTR	0.5	50	33
$C_9H_{10}O$	134.0732	3-Methylacetophenone	PTR	1	50	4.5
$C_{10}H_{14}$	134.1096	C10 Aromatics	PTR	0.92	15	9.5
$C_{10}H_{15}$		Fragments	PTR	0.8		
$C_8H_8O_2$	136.0524	Methyl benzoic acid	PTR	1	50	12
$C_{10}H_{16}$	136.1252	Camphene	PTR	0.38	40	162.8
$C_{10}H_{16}$	136.1252	α-Pinene	PTR	0.33	40	162.8
$C_{10}H_{16}$	136.1252	β-Pinene, Myrcene	PTR	0.21	40	162.8
$C_{10}H_{16}$	136.1252	Tricyclene	PTR	0.07	40	162.8
$C_7H_7NO_2$	137.0477	Nitrotoluene	PTR	1	50	0.1
$C_8H_{10}O_2$	138.0681	2-Methoxy-4-methylphenol (=creosol)	PTR	1	50	100
$C_{11}H_{10}$	142.0783	Methylnaphthalene	PTR	1	50	50
$C_6H_8O_4$	144.0423	Product of levoglucosan dehydration (pyrolysis)	PTR	1	50	4.6
$C_{10}H_{10}O$	146.0732	Dimethylbenzofuran	PTR	1	50	37
$C_{10}H_{12}O$	148.0888	Methyl chavicol (=estragole)	PTR	1	50	50
$C_{11}H_{16}$	148.1252	C11 Aromatics	PTR	1	50	50
$C_9H_{10}O_2$	150.0681	Vinyl guaiacol	PTR	1	50	100
$C_8H_8O_3$	152.0473	Vanillin	PTR	1	50	85

$C_{10}H_{16}O$	152.1201	Oxygenated monoterpenes	PTR	0.7	50	4.3
$C_{10}H_{16}O$	152.1201	Camphor	PTR	0.3	50	4.3
$C_8H_{10}O_3$	154.0630	Syringol	PTR	1	50	100
$C_{10}H_{18}O$	154.1358	Cineole	PTR	1	50	25
$C_{10}H_{18}O$	154.1358	Other oxygenated monoterpenes	PTR	0	50	25
$C_{12}H_{12}$	156.0939	1,3-Dimethylnaphthalene	PTR	1	50	60
$C_{10}H_{20}O$	156.1514	Decanal	PTR	1	50	13
$C_{12}H_{18}$	162.1409	C12 aromatics	PTR	1	50	113
$C_{10}H_{12}O_2$	164.0837	Eugenol, Isoeugenol	PTR	1	50	100
$C_{13}H_{20}$	176.1565	C13 aromatics	PTR	1	50	113
$C_{15}H_{24}$	204.1878	Sesquiterpenes	PTR	1	50	300

Table S3.2. Global Fire Assimilation System version 1.2 (GFAS) emission inventory estimates for the 21 biomass burning VOC species and CO implemented in GEOS-Chem version 13.3.2. GFAS emissions were retrieved for July–September 2018 over the western U.S. domain (36° N-127° W, 49.5° N-105° W). Note that GFAS ERs for lumped aldehydes, MEK, formic acid, and acetic acid were updated based on Permar et al. (2021)

GEOS-Chem Species	Formula	k_{OH}	Total emissions (Gg carbon)
CO	CO	0.14	1690
Ethane	C_2H_6	0.25	19
Propane	C_3H_8	1.09	6.37
Lumped C≥4 alkanes	-	4.2	7.95
Ethene	C_2H_4	8.5	42
Lumped C≥3 alkenes	-	30.7	35
Methanol	CH_4O	0.9	34
Ethanol	C_2H_6O	3.2	0.47
Benzene	C_6H_6	1.22	17
Toluene	C_7H_8	5.6	12
Xylenes	C_8H_{10}	13.2	1.26

Compound	Formula		
Isoprene	C₅H₈	100	2.46
Formaldehyde	CH₂O	8.95	25
Acetaldehyde	C₂H₄O	15	19
Lumped C≥3 aldehydes	-	18.7	4.82
Dimethyl sulfide	C₂H₆S	6	0.59
Acetone	C₃H₆O	0.2	17
Methyl Ethyl Ketone	C₄H₈O	1.2	4.65
Methacrolein	C₄H₆O	2.8	2.35
Glycolaldehyde	C₂H₄O₂	1.2	9.14
Formic acid	CH₂O₂	0.4	15.12
Acetic acid	C₂H₄O₂	3.7	29.18

Table S3.3. Initialization values used for the Framework for 0-D Atmospheric Modeling of the Taylor Creek Fire.

Compound	Formula	Taylor Creek Fire (ppb)
CO	CO	5670.68
NO	NO	6.76
NO₂	NO₂	58.86
HONO	HONO	64.49
Ozone	O₃	31.75
Furan	C₄H₄O	6.33
Benzene	C₆H₆	8.10
HNO₃	HNO₃	21.00
Guaiacol	C₇H₈O₂	1.05

PAN	$C_2H_3NO_5$	6.90
Isoprene	C_5H_8	1.19
Ethene	C_2H_4	82.53
Catechol	$C_6H_6O_2$	1.00
2-Methylfuran	C_5H_6O	1.56
Methylfurfural	$C_6H_6O_2$	1.00
Dimethylfuran	C_6H_8O	0.67
Syringol	$C_8H_{10}O_3$	0.07
3-Methylfuran	C_5H_6O	0.31
Formaldehye	CH_2O	126.05
Acetaldehyde	C_2H_4O	53.88
Acetone	C_3H_6O	14.34
Propanal	C_3H_6O	2.94
MVK	C_4H_6O	4.90
MACR	C_4H_6O	2.29
PPN	$C_3H_5NO_5$	0.84
Phenol	C_6H_6O	4.23
o-Xylene	C_8H_{10}	0.29
α-Pinene	$C_{10}H_{16}$	0.34
p-Xylene	C_8H_{10}	0.75
Cresol	C_7H_8O	1.81
1-Butene	C_4H_8	5.03
n-Butane	C_4H_{10}	0.90
Ethylbenzene	C_8H_{10}	0.59
1,2,3-Trimethylbenzene	C_9H_{12}	0.42
Styrene	C_8H_8	1.59

Benzaldehyde	C_7H_6O	1.07
n-Pentane	C_5H_{12}	1.05
n-Hexane	C_6H_{14}	0.22
n-Heptane	C_7H_{16}	0.18
n-Octane	C_8H_{18}	0.11
3-Methyl-1-butene	C_5H_{10}	0.27
1-Hexene	C_6H_{12}	1.69
β-Pinene	$C_{10}H_{16}$	0.22
Acrolein	C_3H_4O	5.50
2-Butenal	C_4H_6O	1.06
Butanal	C_4H_8O	0.27
Pentanal	$C_5H_{10}O$	0.38
Propene	C_3H_6	17.43
Butadiene	C_4H_6	7.27
Glyoxal	$C_2H_2O_2$	0.29
Sesquiterpenes	$C_{15}H_{24}$	0.02
Methylglyoxal	$C_3H_4O_2$	2.63
Biacetyl	$C_4H_6O_2$	2.43
Formic acid	CH_2O_2	51.1
Acetic acid	$C_2H_4O_2$	32.09
Acetol	$C_3H_6O_2$	2.91
Furfural (=furaldehyde)	$C_5H_4O_2$	7.34

Table S4.1. Average EFs and MCE with 1σ standard deviations reported for previous literature, along with if the study came from field or laboratory campaigns, the dominant fuels burned, and instrumentation used. Unreported values are indicated with a "-", while no standard deviation is shown for single measurements. Instrumentation acronyms include Airborne Fourier Transfer InfraRed (AFTIR) spectrometer, Open-path Fourier Transfer InfraRed (OP-FTIR) spectrometer, Proton Transfer Reaction Mass spectrometer (PTR-MS), and gas chromatography flame ionization detector (GC-MS).

Study	Formic Acid (g/kg)	Acetic acid (g/kg)	MCE	Type	Dominant fuel regions	Instrument
Akagi et al., 2013	0.08 ± 0.03	1.91 ± 0.95	0.91 ± 0.04	Field	South Carolina USA	AFTIR
Bertschi et al., 2003	1.23 ± 1.16	4.87 ± 3.01	0.87 ± 0.02	Laboratory	Montana USA and Zambia Africa	OP-FTIR
Burling et al., 2010	0.18 ± 0.23	1.57 ± 2.17	0.94 ± 0.03	Laboratory	Southeast and Southwest USA	OP-FTIR
Burling et al., 2011	0.09 ± 0.08	1.67 ± 1.59	0.91 ± 0.05	Field	North Carolina and Southwest USA	AFTIR
Christian et al., 2003	0.66 ± 0.59	8.35 ± 4.32	0.88 ± 0.05	Laboratory	Indonesia and Africa	OP-FTIR/PTR-MS
Goode et al., 1999	0.57 ± 0.46	1.28 ± 0.62	0.96 ± 0.01	Laboratory	Grass fires	OP-FTIR
Goode et al., 2000	1.13 ± 0.36	2.55 ± 0.78	0.92 ± 0.01	Field	Alaska USA	AFTIR
Koss et al., 2018	0.28 ± 0.22	-	0.93 ± 0.04	Laboratory	Western USA	PTR-ToF-MS
McKenzie et al., 1995	0.53 ± 0.4	2.64 ± 2.49	-	Laboratory	Montana USA	GC-MS
Müller et al., 2016	0.13	0.47	0.9	Field	Georgia USA	PTR-ToF-MS
Selimovic et al., 2018	0.28 ± 0.25	1.92 ± 1.62	0.93 ± 0.04	Laboratory	Western USA	OP-FTIR
Stockwell et al., 2015	0.28 ± 0.36	2.55 ± 3.07	0.94 ± 0.06	Laboratory	Mixed global	PTR-ToF-MS
Yokelson et al., 1999	3.11	1.17	0.93	Field	North Carolina USA	AFTIR
Yokelson et al., 2003	0.58 ± 0.19	2.37 ± 1.05	0.94 ± 0.02	Field	African savanna	AFTIR
Yokelson et al., 2007	0.59 ± 0.48	3.43 ± 0.44	0.91 ± 0.02	Field	Tropical and Amazon forests	AFTIR
Yokelson et al., 2011	1.34 ± 1.24	3.2 ± 2.52	0.92 ± 0.03	Field	Mexico	AFTIR